Doctoral Dissertation
Doctoral Program in Electrical, Electronics and Communications Engineering (36^{th}cycle)

Next Generation Grid-Tied Inverters with Virtual Synchronous Machine Features for Grid Services and Grid Support

By

Vincenzo Mallemaci

******

Supervisor(s):
Prof. Radu Bojoi, Supervisor
Prof. Enrico Carpaneto, Co-Supervisor

Doctoral Examination Committee:
Prof. Paolo Mattavelli, Referee, Università di Padova
Prof. Giovanni De Carne, Referee, Karlsruhe Institute of Technology

Politecnico di Torino
2024

Declaration

I hereby declare that, the contents and organization of this dissertation constitute my own original work and does not compromise in any way the rights of third parties, including those relating to the security of personal data.

Vincenzo Mallemaci
2024

* This dissertation is presented in partial fulfillment of the requirements for **Ph.D. degree** in the Graduate School of Politecnico di Torino (ScuDo).

rist Pú

Acknowledgements

La dedica di questa tesi di Dottorato è *rist Þú*, letteralmente *Incidilo* in islandese. È un monito che esorta ognuno di noi ad incidere sulla propria pelle ogni incontro avvenuto nella nostra vita, perchè da ognuno di essi, positivo o negativo che sia, possiamo trarre qualcosa per crescere umanamente e professionalmente. Seguendo questo monito, voglio incidere e quindi ringraziare tutte le persone che hanno fatto parte di questo percorso chiamato Dottorato, e più in generale per tutti i miei ormai più di 9 anni al Politecnico.

Grazie innanzitutto al mio tutore Radu Bojoi, per essere stata una guida seria e di esempio. Ringrazio il mio co-tutore Enrico Carpaneto per le conoscenze che mi ha trasmesso. Grazie a Fabio, il mio "terzo tutore", per avermi ascoltato e aiutato in tutto questo percorso.

Grazie a tutti i ragazzi del laboratorio, rimasti o andati via, dai più grandi ai più *freschi*. Chi in un modo, chi nell'altro, avete reso anche le giornate più storte un po' più facili. Grazie Stefano per tutte le cose fatte insieme e grazie a Federico, Alessia e Alessandro perchè ho imparato più io da voi che voi da me. Grazie Enrico, prima amico e poi collega. A Luisa i ringraziamenti non piacciono, quindi ti scrivo *Ciat*.

Fuori dalle mura del laboratorio, grazie agli amici di casa e di Torino, del Poli e dell'Einaudi, per tutti questi anni in cui ci siete sempre stati.

Grazie Do, per la parte di strada che abbiamo fatto insieme.

Grazie mamma e papà per aver supportato ogni mia scelta, giusta o sbagliata che fosse, senza condizionamenti e sempre con un *Forza*. Grazie Salvo, un pezzo di famiglia a Torino. Grazie a tutta la mia famiglia, lontana da 9 anni ma sempre nel cuore.

Infine, grazie Giusi. Un raggio di sole apparso all'improvviso.

Abstract

Currently, synchronous machines (SMs) employed in thermoelectric and hydroelectric power plants ensure the stability of the grid frequency and voltage by providing ancillary services, such as inertial response, active and reactive power regulation, and fault support. However, with the ongoing decommissioning of thermoelectric power plants, particularly coal-based ones, the number of synchronous generators on the grid is decreasing. Additionally, renewable energy plants, such as those using solar and wind power, inherently lack inertial support because they connect to the grid through static power electronic converters. This reduction in total power system inertia poses a risk to grid frequency and voltage stability. Consequently, newest grid codes mandate that even power electronics-interfaced renewable energy sources provide grid services. For this purpose, control algorithms based on the Virtual Synchronous Machine (VSM) concept enable grid-connected converters to mimic conventional SMs and guarantee essential grid services. The goal of this PhD thesis is to develop control strategies that integrate the Virtual Synchronous Machine (VSM) control concept to provide grid services (such as virtual inertia) and grid support in compliance with the most recent grid codes. The thesis is divided into two main parts.

The first part provides a theoretical and experimental assessment for the main VSM topologies available in the literature. It begins by discussing the key aspects of grid-connected converters and defines the differences between grid-following, grid-forming and VSM, which are often sources of confusion in the literature. It then presents a literature review of the main VSM topologies. Each topology is implemented following a common tuning strategy. Their inertial behavior, frequency regulation and support capability during faults are compared using a common setup to highlight the differences and similarities between the various topologies. The beneficial effect of inertial response is then demonstrated using a dynamic network. The focus then shifts to the behavior of VSMs under non-ideal grid conditions. The thesis proposes a method to predict the response of the main VSM topologies to grid harmonics and imbalances. Some topologies can improve grid voltage quality by acting as harmonic/unbalance sinks, while

others may deteriorate it. The thesis also demonstrates how the harmonic/unbalance sink capability of grid-forming VSMs is limited by the effect of dead time, making the dead-time compensation essential to guarantee the correct sink performance.

The second part of the thesis focuses on the S-VSC, the VSM developed at the Politecnico di Torino. The peculiarity of this solution is its operation as a virtual compensator rather than as a virtual generator, like most VSMs from the literature. Its principle of operation as a grid-feeding VSM was demonstrated in previous works. This thesis extends the S-VSC algorithm to grid-forming operation, demonstrating its validity for the control of converters connected to microgrids that operate both in grid-connected and in island mode. The following chapter adopts the μ-analysis as a tool to evaluate the robust stability of the S-VSC against system uncertainties. The thesis also demonstrates that a converter functioning as a compensator is more robust than one functioning as a generator, both as a single grid-connected converter and in parallel with another. The final chapter shows that implementing the S-VSC algorithm into a battery charger control can enable battery chargers to provide ancillary services to the grid.

Contents

Chapter 1

Motivation and Goal of the Work

1.1 Renewable Energy Sources

Renewable energy sources offer a sustainable alternative to fossil fuels, mitigating climate change while fostering energy independence and economic growth.

In the last decade, the amount of energy produced from wind and solar sources has grown exponentially and it is supposed to spread more and more, as shown from the analysis and forecast of Figs. 1.1, 1.2, 1.3, 1.4 [1–3].

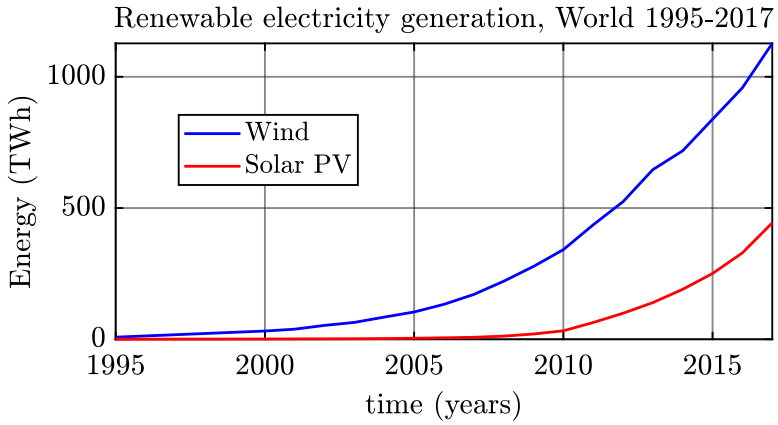

Fig. 1.1 Renewable electricity generation by Wind and Solar PV, World 1995-2017. Source: IEA [1].

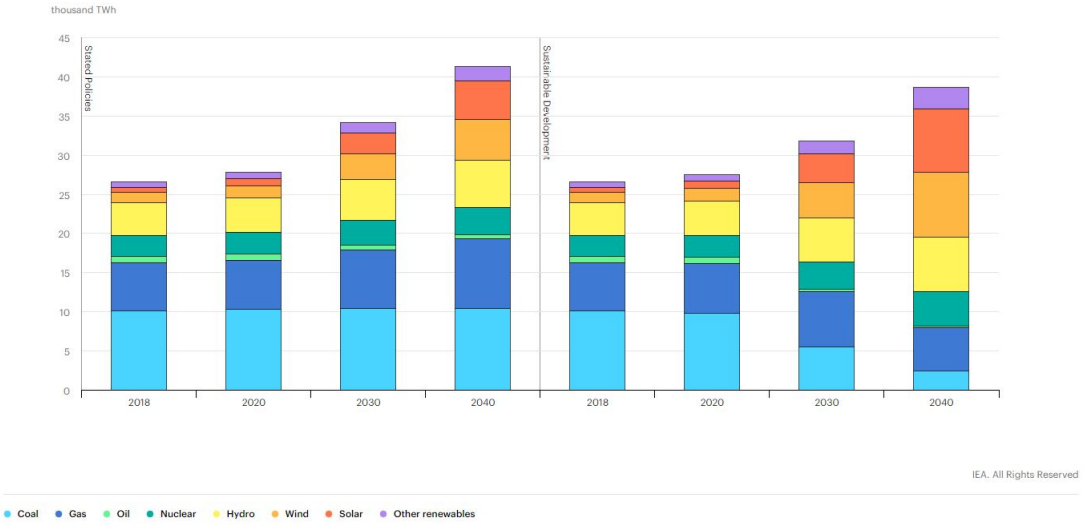

Fig. 1.2 Electricity generation by fuel and scenario, 2018-2040 (entire world). Source: IEA [1].

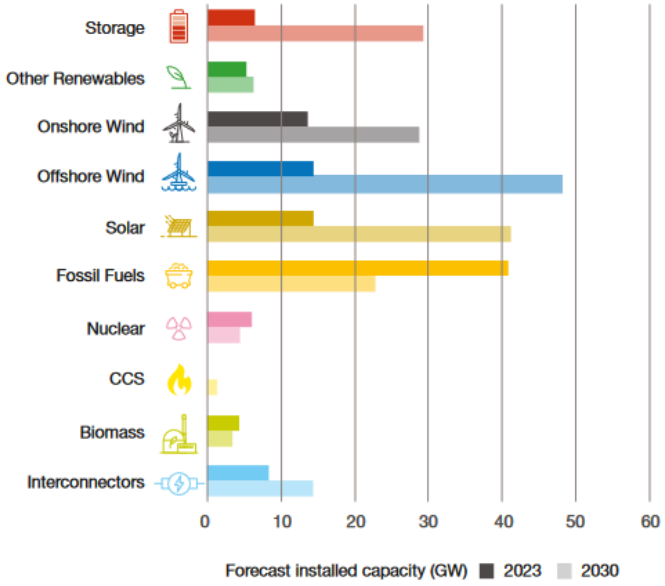

Fig. 1.3 Generation mix now and forecast for 2030 in Great Britain. Source: National Grid ESO [2].

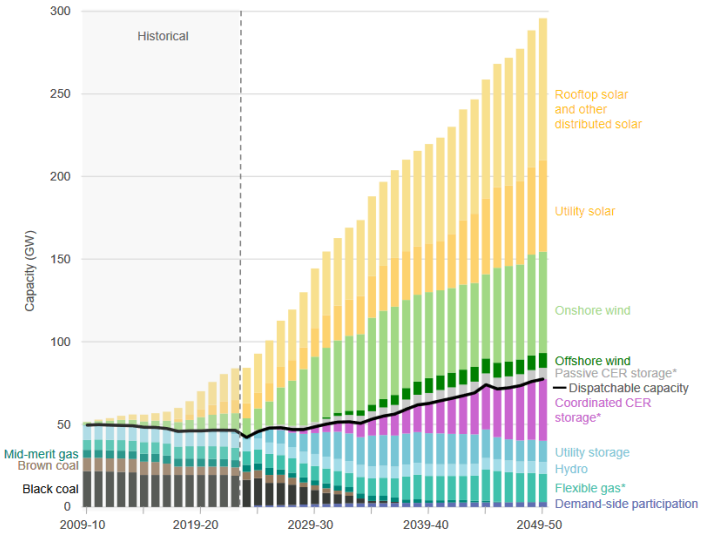

Fig. 1.4 Generation mix now and forecast in Australia. Source: Australian Energy Market Operator (AEMO) [3].

Solar Energy

Solar power harnesses the abundant energy emitted by the sun through photovoltaic (PV) panels or concentrated solar power (CSP) systems. PV panels convert sunlight directly into electricity, while CSP systems use mirrors or lenses to concentrate solar energy for electricity generation or heat production. Advancements in solar technology have strongly reduced costs, making solar power increasingly competitive with conventional energy sources. Rooftop solar installations empower homeowners and businesses to generate their own electricity, reducing reliance on centralized power grids and lowering utility bills [4].

Wind Energy

Wind energy exploits the kinetic energy of the wind to generate electricity using wind turbines. Onshore and offshore wind farms capture the power of the wind, converting it into electricity. Wind power has experienced rapid growth globally, driven by technological advancements, favorable policies, and declining costs. Wind turbines can be deployed across diverse landscapes, from open plains to coastal waters, providing a scalable solution for the renewable energy transition [5].

1.2 Integration of Renewable Energy Sources

Solar and wind renewable energy sources are interfaced to the grid through static power electronics converters. For instance, photovoltaic (PV) plants generate electrical energy in the form of direct current (dc). Typically, two conversion stages are utilized to connect PV plant to the grid: a first dc/dc stage and a second dc/ac converter, commonly referred to as inverter. One of the most commonly used control algorithms for photovoltaic applications is the Maximum Power Point Tracking (MPPT) algorithm [6]. By continuously adjusting the operating point of the PV system to track the point of maximum power output, the MPPT algorithm ensures optimal energy harvesting from the solar source, achieving efficiency levels of around 98%.

A simplified scheme of the system under study is illustrated in Fig. 1.5.

The successful penetration of solar and wind energy into the grid relies on the proper design and control of power electronic converters.

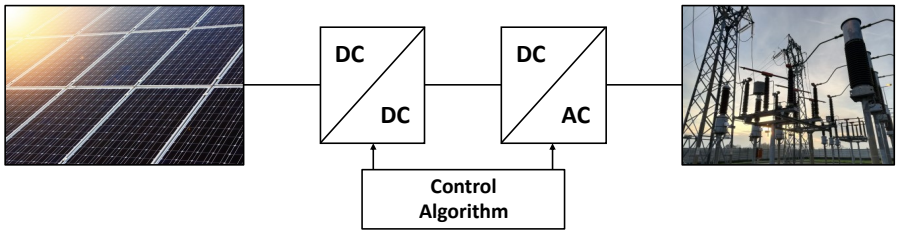

Fig. 1.5 Conventional scheme of connection between PV plant and grid.

1.3 Stability of the Electric Grid: Present and Future Challenges

1.3.1 Working principle of the Electric Grid

The electric grid ensures the balance between electricity demand and supply by maintaining the grid frequency as close as possible to its nominal value [7]. This is achieved through the alternators of hydroelectric and thermoelectric power plants (fossil fuel-based), which historically undergo a three-phase frequency regulation process during load transients, as depicted in Fig. 1.6.

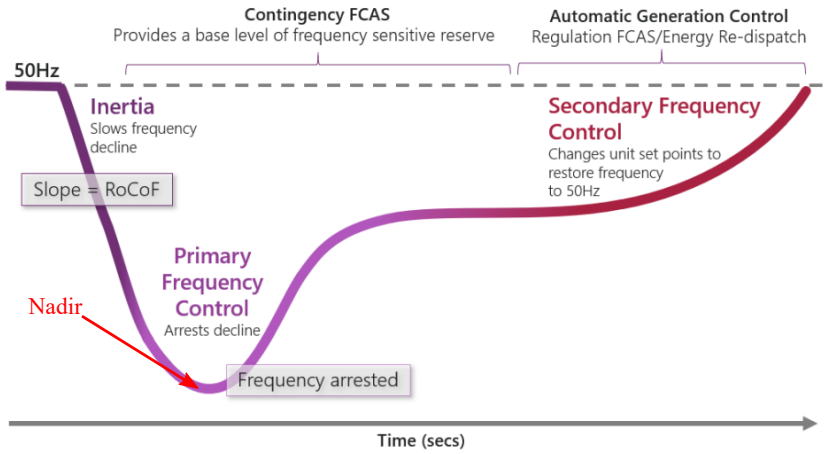

Fig. 1.6 Frequency profile and frequency control steps after a generation reduction. Source: [8].

During a power imbalance, kinetic energy stored in alternators plays a crucial role: when power demand increases, the rotors slow down and inject inertial active power into the grid. This inertial response enables synchronous generators (SGs) to raise the Nadir (minimum frequency value) and reduce the Rate of Change of Frequency (ROCOF), thereby minimizing the likelihood of triggering frequency protection relays. Following these initial seconds (1-4 s), primary frequency regulation adjusts the power output from sources such as water flow to match the new load conditions, a process typically taking a few minutes. Finally, secondary frequency control restores the frequency setpoint for a grid section (e.g., a country), managed centrally over a timescale of tens of minutes [7].

The inertial response and frequency control are essential components of the ancillary services that rotating power plants must deliver to maintain grid stability [9–12].

1.3.2 Opportunities of Renewable Energy Sources

Distributed Energy Production

Distributed energy production decentralizes electricity generation, empowering communities, businesses, and individuals to produce their own energy locally. The benefits of Distributed Energy can be summarized as follows [13, 14]:

- **Resilience**: Distributed energy systems enhance grid resilience by reducing reliance on centralized infrastructure vulnerable to outages and disruptions;

- **Energy Independence**: By generating their own electricity, consumers can reduce dependence on external energy sources and volatile fuel prices;
- **Environmental Sustainability**: Distributed energy production promotes renewable sources, reducing greenhouse gas emissions and environmental degradation.

Some of the promising solutions technologies and solutions are [13, 14]:

- **Solar Rooftop**: Rooftop solar installations enable homeowners and businesses to generate their own electricity, often through net metering arrangements that allow surplus energy to be fed back into the grid;
- **Microgrids**: Microgrids are localized grids that can operate independently (islanded) or connected to the main grid, incorporating renewable energy sources, energy storage, and smart grid technologies;
- **Distributed Storage**: Battery storage systems allow consumers to store excess energy for later use, improving grid stability, and enabling greater integration of intermittent renewables.

1.3.3 Limitations of Renewable Energy Sources

While distributed energy production offers numerous benefits, it also presents challenges that must be addressed to realize its full potential. Indeed, renewable power generators (RPGs) lack inherent inertial features due to their static power converters, which have no rotating mechanical parts [10, 15, 16]. Until recently, RPGs only injected power based on conventional control algorithms like MPPT, with ancillary services provided by SGs. However, the planned decommissioning of thermoelectric power plants (especially coal-based ones) will reduce the number of SGs connected to the grid, leading to decreased total system inertia. This decrease results in higher ROCOF and lower Nadir during power imbalances, and reduced grid frequency stability. Consequently, the increasing penetration of converter-interfaced RPGs could jeopardize grid stability unless they also provide ancillary services, particularly inertial behavior [10–12, 15]. Therefore, integrating distributed energy resources (DERs) into the existing grid requires upgrades to infrastructure, regulatory frameworks and grid management systems. Smart grid technologies, demand response programs, advanced monitoring and control systems are essential for optimizing grid operations and managing variable renewable generation.

1.3.4 Example of case study

An important incident is the 2016 blackout in South Australia (SA) [17]. Tornadoes damaged three transmission lines, resulting in a series of six voltage dips occurring in a time span of about two minutes. Consequently, the active power production of wind power plants decreased because their control systems were unable to manage the voltage dips. This led to a surge in imported power into SA, causing an overload that triggered a trip in the interconnection with a neighboring region. The load shedding protections in SA did not activate promptly due to the rapid frequency decline, as depicted in Fig. 1.7.

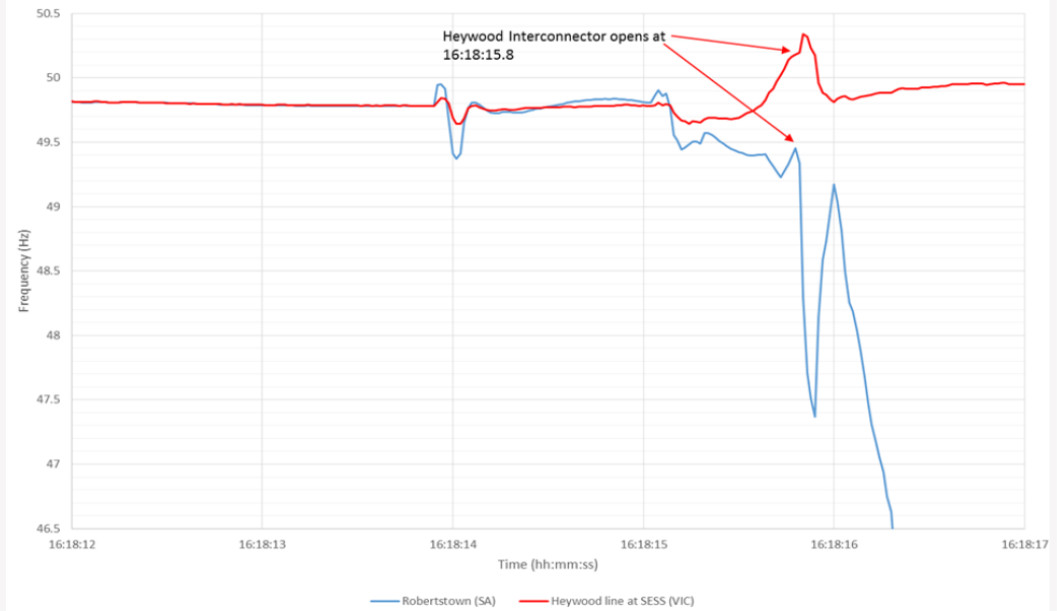

Fig. 1.7 Frequency profile after SA grid separation. Source: [17].

The SA power system became isolated from the rest of the network, and the resulting power imbalance caused the blackout. Two main conclusions can be drawn from this event:

- Increased inertia is necessary to reduce the ROCOF, facilitating the activation of protection relays;
- Enhanced control systems are required to enable renewable energy sources (RES) to withstand multiple fault events, allowing them to contribute to frequency regulation even after grid faults.

As a more general concept, the decommissioning of thermoeletric power plants together with the penetration of converter-interfaced renewable energy sources will reduce the total

power system inertia, compromising both the grid frequency and the voltage stability. A report of ENTSO-E proposes a forecast of the Total System Inertia (TSI) reduction in Europe, as illustrated in Fig. 1.8 [10]. As it can be observed, several national per unit TSI constant inertia H are expected to fall below the value of 2 s (compared with a traditional value of about 5–6 s). At least two Synchronous Areas (SAs), Great Britain, Ireland, and a number of individual countries' contribution within Continental Europe are expected to fall within this category (see countries in red), highlighting their need to prepare their strategy and possibly also start taking action.

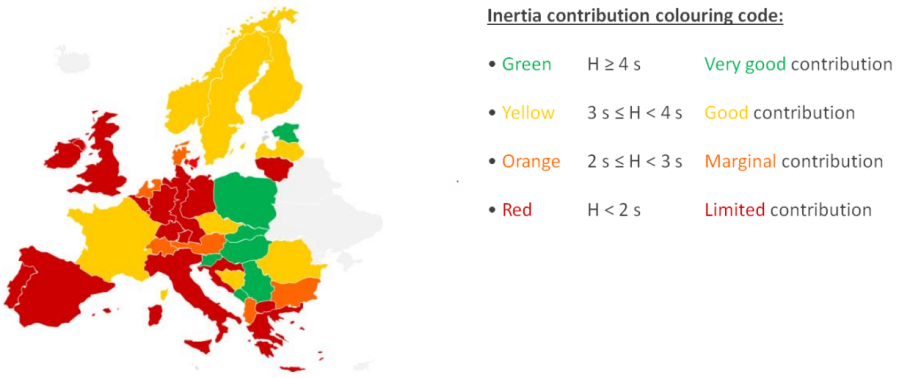

Fig. 1.8 Indicating contribution of each TSO to the TSI constant (source: TYNDP 2016 reflecting 2030 scenario) [10].

The frequency instability due to the total system inertia reduction is just one of the future issues related to the transition from fossil fuels to renewable energy sources. The safe operation of the power system is indeed guaranteed by several ancillary services [10]:

- Frequency regulation (in terms of inertia and active power control);
- Voltage regulation (in terms of reactive power control);
- Grid support during faults (injection of reactive short circuit current);
- Harmonics and Imbalance compensation (harmonic/unbalance sink capability);
- Island Capability.

RPGs cannot provide these features because their power converters are static and lack rotating mechanical parts. Additionally, conventional control techniques are inadequate for addressing this issue. Consequently, RPGs can only inject power according to the MPPT algorithm, leaving ancillary services to be supplied by traditional synchronous

generators. This limitation restricts the use of renewable sources, as their increased presence would reduce grid stability.

In conclusion, more advanced control strategies are required to make power electronics-interfaces renewable power plants able to support the electric grid and enhance the grid voltage and frequency stability, thus facilitating the penetration of renewable energy sources into the power system.

1.4 The Concept of Virtual Synchronous Machine

According to recent grid codes and pilot projects initiated by various Transmission System Operators (TSOs), renewable power generators (RPGs) will soon be required to provide ancillary services such as inertial behavior, reactive support, and harmonic compensation [18, 10, 19, 20].

It has been demonstrated that power electronic converters can fulfill these roles effectively. For instance, droop control-based inverters are used for inertial support and frequency control [21], STATCOMs provide reactive support, and active filters are employed for harmonic compensation [22]. A promising approach to achieve these functionalities comprehensively is to configure static converters to emulate synchronous generators. This approach ensures they can provide inertial support, active and reactive power regulation, and harmonic compensation. By emulating an alternator, a converter can inherit the beneficial aspects of synchronous generators while potentially overcoming some of their limitations. Unlike physical inertia, which is fixed in generators, the inertia constant in a converter emulating an alternator is virtual and adjustable according to application requirements.

Numerous solutions have been proposed over the past 15 years under the Virtual Synchronous Machine (VSM) concept [23, 24], each offering unique capabilities and applications.

1.5 Goal of the Thesis

The goal of this PhD thesis is to develop control strategies that integrate the Virtual Synchronous Machine (VSM) concept to make grid-connected converters able to provide grid services (such as virtual inertia) and grid support.

1.6 Thesis Outline & Main Contributions

The thesis is divided into two main parts.

The first part (Chapters 2, 3 and 4) focuses on general aspects of Virtual Synchronous Machines. It starts with a general introduction on grid-connected converters to define a clear nomenclature in Chapter 2, underlying the differences between grid-following, grid-forming and VSM converters as discussed in [C1]. Next, the thesis provides a review of the most common VSM topologies available in the literature in Chapter 3 based on the work presented in [J4]. The main aspects and differences are highlighted with a focus on the inertial contribution of ten different VSM models and the grid support capability of four VSMs [J4], [C1]. Finally, Chapter 4 focuses on the behavior of VSMs under non-ideal grid voltage conditions (i.e., voltage unbalances and distortions), proposing a method to validate their harmonic and unbalance sink capability, published in [J3]. Moreover, Chapter 4 demonstrates how the inverter dead-time effect limits the harmonic and unbalance sink capability of grid-forming VSMs as in [C3] and [J2].

The second part (Chapters 5, 6 and 7) focuses on the Simplified Virtual Synchronous Compensator (S-VSC), the VSM developed at the Politecnico di Torino, with a threefold goal:

- Extend the original S-VSC control algorithm proposed in [25] to the grid-forming operation (Chapters 5) as in [C4] and [J1];
- Demonstrates the higher robustness of the virtual compensator behavior over the virtual generator mode operation (Chapters 6) [C2];
- Integrate the virtual compensator concept as an add-on feature into an ultra fast battery charger prototype to make electric vehicles chargers able to provide ancillary services as well (Chapters 7) [J8].

The thesis ends with Chapters 8, outlining the main conclusions and the future works. The main contributions of the PhD thesis can be summarized, per chapter, as follows:

Chapter 3: Virtual Synchronous Machines

- Comprehensive comparison of ten different VSMs topologies implemented on a common experimental setup:
  - Common tuning procedure to guarantee a fair comparison [J4];

  - Highlight the main implementation issues [J4];
  - Review of typologies with experimental results of the inertial contribution and the grid fault support [J4], [C1];
  - Highlight the negligible differences between grid-following and grid-forming VSMs in supporting the grid [C1].

Chapter 4: VSMs behavior under non-ideal conditions

- General method to foresee the behavior of the main VSM typologies under non-ideal grid voltage conditions [J3]:
  - The method quantifies the harmonic/unbalance sink capability of the VSM under study with no need of implementing the VSM control;
  - The method is easily applicable to any other VSM solution.
- Demonstration of the limited harmonic/unbalance sink capability of grid-forming VSMs due to the inverter dead-time [J2]:
  - The inverter dead-time worsens the harmonic/unbalance sink capability;
  - The inverter dead-time must be compensated to match the expected theoretical behavior.

Chapter 5: Grid-Forming S-VSC

- The original S-VSC control algorithm is extended to the grid-forming operation [J1]:
  - S-VSC can operate both as grid-following and grid-forming, either connected to the grid or in island operation. Therefore, the S-VSC is a suitable solution for the control of inverter-based microgrids;
  - The transition from the grid-following to the grid-forming operation is smooth and it does not need communication with the breaker interfacing the microgrid with the rest of the grid;
  - The S-VSC can withstand to grid faults both in grid-connected and in island operation.

Chapter 6: Robust Stability Analysis of the S-VSC

- Study of the robust stability analysis of a VSM through the μ-analysis:
  - Demonstration of the higher robustness of the virtual synchronous compensator (VSC) approach over the virtual synchronous generator (VSG) one for different grid conditions, sizes of the systems and tuning parameters [C2];
  - For the first time in the literature, the theoretical outcomes of the μ-analysis of grid-connected converters are experimentally validated [C2];
  - Considering a system of a grid-forming converter operating in parallel to a grid-following converter and the grid, the thesis demonstrates that if the grid-following converter operates as a VSC, the system is more robust against grid impedance uncertainties with respect to the VSG mode operation.

Chapter 7: VSMs integrated in battery chargers

- Ultra-fast battery chargers can provide ancillary services as well. The S-VSC control is included in the conventional charger control as an add-on feature to support the grid during grid contingencies, while preserving the normal operation of the charger [J8].

1.7 List of Publications

The PhD research activity led to the publication of the following papers:

Journals

[J1] V. **Mallemaci**, F. Mandrile, E. Carpaneto and R. Bojoi, "Simplified Virtual Synchronous Compensator With Grid–Forming Capability," in IEEE Transactions on Industry Applications, vol. 59, no. 5, pp. 6203-6219, Sept.-Oct. 2023, doi: 10.1109/TIA.2023.3285523.

[J2] V. **Mallemaci**, F. Mandrile, E. Carpaneto and R. Bojoi, "Dead–Time Effect on Two–Level Grid–Forming Virtual Synchronous Machines," in IEEE Transactions on Industry Applications, vol. 59, no. 5, pp. 6103-6112, Sept.-Oct. 2023, doi: 10.1109/TIA.2023.3281535.

[J3] V. **Mallemaci**, F. Mandrile, E. Carpaneto and R. Bojoi, "General Method to Foresee the Behavior of Virtual Synchronous Machines Working With Distorted and Unbalanced Voltage Conditions," in IEEE Transactions on Industrial Electronics, vol. 70, no. 10, pp. 9709-9719, Oct. 2023, doi: 10.1109/TIE.2022.3222642.

[J4] V. **Mallemaci**, F. Mandrile, S. Rubino, A. Mazza, E. Carpaneto, R. Bojoi, A comprehensive comparison of Virtual Synchronous Generators with focus on virtual inertia and frequency regulation, Electric Power Systems Research, Volume 201, 2021, 107516, ISSN 0378-7796, https://doi.org/10.1016/j.epsr.2021.107516.

Conferences

[C1] V. **Mallemaci**, F. Mandrile, A. Camboni, E. Carpaneto and R. Bojoi, "Grid-Following Virtual Synchronous Machines: a valid solution fulfilling the newest grid codes regarding the reactive grid support during faults," 2024 IEEE 22nd Mediterranean Electrotechnical Conference (MELECON), Porto, Portugal, 2024, pp. 1169-1174, doi: 10.1109/MELECON56669.2024.10608672.

[C2] V. **Mallemaci**, S. Pugliese, F. Mandrile, E. Carpaneto, R. Bojoi and M. Liserre, "Robust Stability Analysis of the Simplified Virtual Synchronous Compensator for Grid Services and Grid Support," 2023 IEEE Energy Conversion Congress and Exposition (ECCE), Nashville, TN, USA, 2023, pp. 1188-1195, doi: 10.1109/ECCE53617.2023.10362442.

[C3] V. **Mallemaci**, F. Mandrile, E. Carpaneto and R. Bojoi, "Dead-Time Effect on Two-Level Voltage Source Virtual Synchronous Machines," 2022 IEEE Energy Conversion Congress and Exposition (ECCE), Detroit, MI, USA, 2022, pp. 01-07, doi: 10.1109/ECCE50734.2022.9947625.

[C4] V. **Mallemaci**, E. Carpaneto and R. Bojoi, "Grid-Forming Inverter with Simplified Virtual Synchronous Compensator Providing Grid Services and Grid Support," 2021 24th International Conference on Electrical Machines and Systems (ICEMS), Gyeongju, Korea, Republic of, 2021, pp. 2323-2328,
doi: 10.23919/ICEMS52562.2021.9634289.

Finally, as complementary activities, I collaborated as a co-author of the following papers and co-supervisor of two Master Thesis:

Journals

[J5] F. Mandrile, V. **Mallemaci**, E. Carpaneto and R. Bojoi, "Lead-Lag Filter-Based Damping of Virtual Synchronous Machines," in IEEE Transactions on Industry Applications, vol. 59, no. 6, pp. 6900-6913, Nov.-Dec. 2023, doi: 10.1109/TIA.2023.3293779.

[J6] F. Reißner, V. **Mallemaci**, F. Mandrile, I. R. Bojoi and G. Weiss, "Virtual Friction Subjected to Communication Delays in a Microgrid of Virtual Synchronous Machines," in IEEE Journal of Emerging and Selected Topics in Power Electronics, vol. 11, no. 4, pp. 3910-3923, Aug. 2023, doi: 10.1109/JESTPE.2023.3276019.

[J7] F. Reissner, V. **Mallemaci**, F. Mandrile, R. Bojoi and G. Weiss, "Virtual Friction: Experimental Validation in a Microgrid of 3 Virtual Synchronous Machines," 2022 IEEE 23rd Workshop on Control and Modeling for Power Electronics (COMPEL), Tel Aviv, Israel, 2022, pp. 1-6, doi: 10.1109/COMPEL53829.2022.9830008.

[J8] Mandrile, F.; Cittanti, D.; **Mallemaci**, V.; Bojoi, R. Electric Vehicle Ultra-Fast Battery Chargers: A Boost for Power System Stability? World Electr. Veh. J. 2021, 12, 16. https://doi.org/10.3390/wevj12010016.

Conferences

[C5] A. Roveri, F. Mandrile, V. **Mallemaci** and R. Bojoi, "Discontinuous PWM Modulation for Active Power Filters Operating in Disturbed Environments," 2023 IEEE Energy Conversion Congress and Exposition (ECCE), Nashville, TN, USA, 2023, pp. 6429-6436, doi: 10.1109/ECCE53617.2023.10362487.

[C6] A. Roveri, V. **Mallemaci**, F. Mandrile and R. Bojoi, "Power Decoupling Method for Grid Inertial Support Provided by Ultra-Fast Bidirectional Chargers," 2023 IEEE Energy Conversion Congress and Exposition (ECCE), Nashville, TN, USA, 2023, pp. 6544-6546, doi: 10.1109/ECCE53617.2023.10362280.

[C7] D. Cittanti, V. **Mallemaci**, F. Mandrile, S. Rubino, R. Bojoi and A. Boglietti, "PWM-Induced Losses in Electrical Machines: An Impedance-Based Estimation Method," 2021 24th International Conference on Electrical Machines and Systems (ICEMS), Gyeongju, Korea, Republic of, 2021, pp. 548-553, doi: 10.23919/ICEMS52562.2021.9634438.

[C8] F. Mandrile, V. **Mallemaci**, E. Carpaneto and R. Bojoi, "A Lead-Lag Filter for Virtual Synchronous Machines with Improved Electromechanical Damping," 2021 IEEE Energy Conversion Congress and Exposition (ECCE), Vancouver, BC, Canada, 2021, pp. 583-589, doi: 10.1109/ECCE47101.2021.9595825.

Master Thesis Co-Supervised

[T1] F. Campanelli, Control of a Microgrid based on Virtual Synchronous Machine Technology, 2023. Supervisors: F. Mandrile, V. **Mallemaci** (Politecnico di Torino).

[T2] F. Mussinatto, Active Power Filter for Power Quality improvement of Power Converters Functional Testing Lines, 2021. Supervisors: R. Bojoi, F. Mandrile, V. **Mallemaci** (Politecnico di Torino), F. Pagani, A. Roveri (Prima Electro S.p.A).

Chapter 2

Grid-tied Converters

Grid-tied converters can play a fundamental role in enhancing the reliability of the grid by facilitating the integration of renewable energy sources and electric vehicle battery chargers. Grid converters serve as key components in modern grid infrastructure, offering enhanced control capabilities and seamless integration of renewable energy sources. The higher is the penetration of converter-interfaced renewable energy sources, the higher is the number of needed requirements, as highlighted in the white paper published by the Australian Electricity Market Operator (Fig.2.1 [15]).

The chapter will start with the main requirements prescribed by the Italian and Great Britain Transmission System Operators (TSOs) and the Universal Interoperability for grid-Forming Inverters (UNIFI) Consortium co-led by the National Renewable Energy Laboratory (NREL). Next, the chapter describes the general aspects of grid-tied converters to define a clear nomenclature, by focusing on the definitions of grid-following (GFL) and grid-forming (GFM) converters.

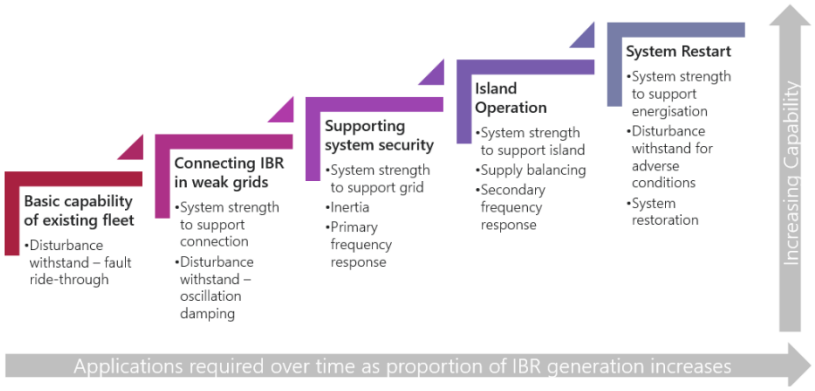

Fig. 2.1 Increasing requirements of grid-tied converters according to the penetration level. Source: Australian Electricity Market Operator [15].

2.1 Requirements from Grid Codes

The electric system is undergoing a revolutionary transformation, driven primarily by the increasing penetration of RPGs and the expansion of distributed generation. Each year, authorities and organizations worldwide are updating guidelines to facilitate the integration of RES. A milestone was reached in 2016, when the European Commission established a network code on requirements for grid connection of generators [26], for both conventional and renewable energy sources.

In this context, frequency and voltage regulations hold a central position. Moreover, grid codes prescribe specific requirements also for the harmonic content and the phase unbalance of the voltage at the point of connection to the grid. For each requirement, the main guidelines defined by Italian and Great Britain TSOs will be described. The following guidelines are directly extracted from the TSOs grid codes.

2.1.1 Terna: Italian TSO

The main aspects of the Terna's grid code [27] regarding RESs can be found in the annexes A18 (for wind power plants) [28], A68 (photovoltaic power plants) [29] and A79 (electrochemical storage systems) [30]. Since Terna is a TSO, the guidelines refer to plants either directly connected to the transmission power system, or indirectly connected by means of a portion of grid with a nominal voltage equal or higher than 110 kV. The main topics of the annexes are:

- The general features of the power plant and the required operating range for the connection to the High Voltage (HV) power system;
- The characteristics of the managing and regulation systems which plants have to provide in normal and emergency conditions.

According to the grid code, inverters have to be designed, built and employed in order to stay connected to the grid even during emergency conditions and grid restore, within specific operating limits. They are defined in terms of voltage, frequency and ROCOF:

$$85\,\%\mathrm{V_n} \leq V \leq 115\,\%\mathrm{V_n} \tag{2.1}$$

$$47.5\,\mathrm{Hz} \leq f \leq 51.5\,\mathrm{Hz} \tag{2.2}$$

$$\frac{df}{dt} \leq 2.5\,\mathrm{Hz/s} \tag{2.3}$$

where:

- V_n is the nominal voltage ($\mathrm{V_{rms}}$);
- V is the voltage at the connection point ($\mathrm{V_{rms}}$);
- f is the grid frequency (Hz);
- $\frac{df}{dt}$ is the derivative of frequency, measured at least on 5 cycles (100 ms).

Active Power Regulation

The active power regulation is necessary to control the frequency. The active power regulation curve for wind and PV plants is proposed in Fig. 2.2. According to the grid code, the wind and PV plants must be suitable to provide a frequency regulation as performed by conventional synchronous generators. Three kinds of modes are defined:

- Frequency Sensitive Mode (FSM);
- Limited Frequency Sensitive Mode Under-Frequency (LFSM-U);
- Limited Frequency Sensitive Mode Over-Frequency (LFSM-O).

The frequency regulation law is the following:

$$f - f_n = -s \cdot (P - P_n)$$
$$\Delta f = -s \cdot \Delta P \tag{2.4}$$

where:

- f is the output frequency (Hz);
- f_n is the nominal frequency (Hz);
- s is the active droop coefficient (Hz/W);
- P is the output active power (W);
- P_n is the nominal active power (W).

According to the frequency range, s assumes a different value.

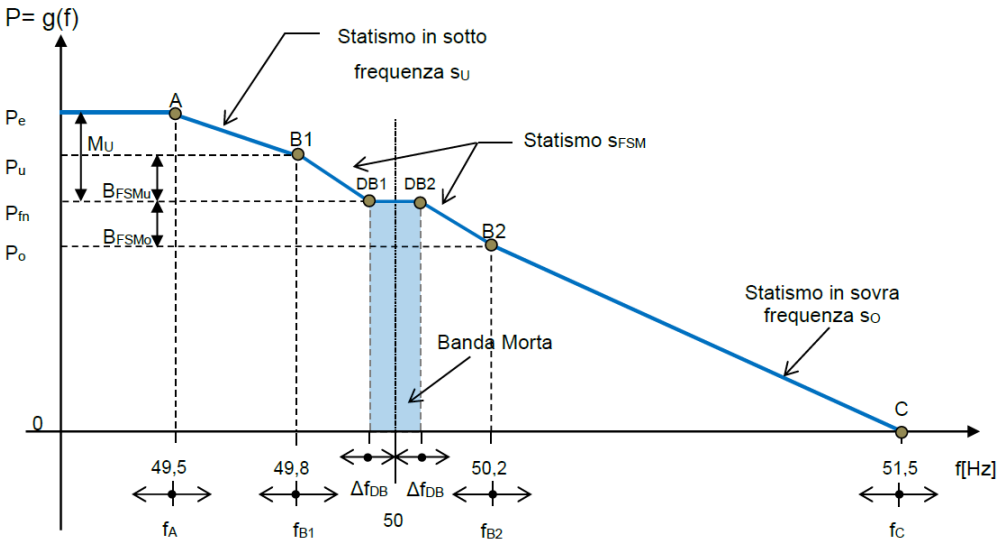

Fig. 2.2 Active Power Regulation Curve for Wind and PV plants. Source: [28, 29]

FSM is the frequency regulation performed around the nominal frequency value. It is implemented in the interval $[f_{B1}, f_{B2}]$ shown in Fig. 2.2. It is actuated according to an active droop coefficient indicated with s_{FSM}. In this case, the maximum insensibility value must be 10 mHz. Moreover, a dead-band in the interval [0,500] mHz is requested.

LFSM-U is the law to follow when the frequency is lower than the nominal value, in the interval $[f_A, f_{B1}]$. In this case the active droop coefficient is s_U.

FSM-O is the modality actuated when the frequency is in the interval $[f_{B2}, f_C]$. Here the active droop coefficient is s_O and it is chosen in order to zero the injected active power when the upper limit of frequency (51.5 Hz) is reached.

Voltage Regulation

The capability to be insensible to voltage variations is requested, within specific limits. The common expression of this feature is Fault Ride Through (FRT). In Fig. 2.3, two curves are proposed with the time limits: Under Fault Ride Through (UFRT) curve and Over Fault Ride Through (OFRT) curve. The allowed and forbidden working areas are highlighted in the figure.

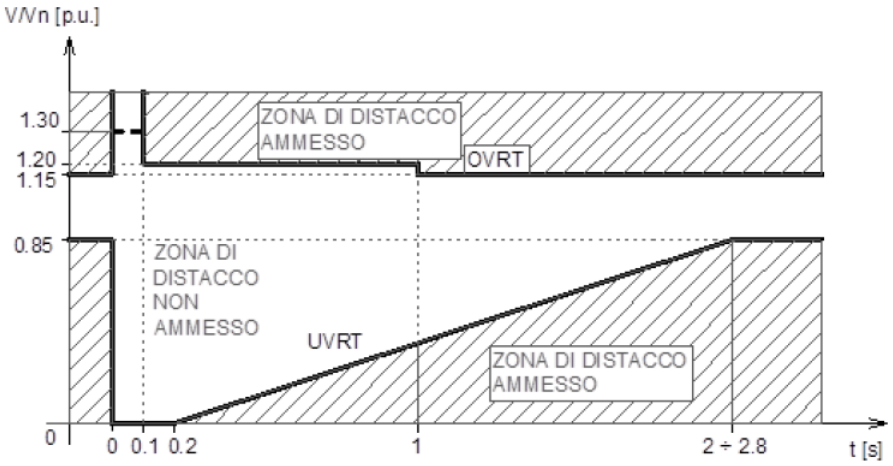

Fig. 2.3 FRT Curves for Wind and PV plants. Source: [28, 29]

Harmonic Distortion

The harmonic current emissions of the Storage Plant must be such that the maximum level of total harmonic distortion of the current (THDI), calculated up to the 50th harmonic, and the individual harmonic currents, based on the nominal current of the Storage Plant at the Point of Connection (PdC), do not exceed the values indicated in the Tables below, according to the voltage level and in compliance with IEEE 519 [18, 31].

Harmonic emissions from the Storage Plant must be limited such that the maximum level of total harmonic distortion (THDV) of the voltage (calculated up to the 50th

harmonic) at the connection point of the Storage Plant shall not exceed the following values:

- THDV ≤ 2.5% for networks at nominal voltage below 220 kV;
- THDV ≤ 1.5% for networks with nominal voltage greater than or equal to 220 kV.

When evaluating the plant emission limits, the following alternatives can be checked:

- The plant's emissions do not exceed the planning values; in this case, the plant can be connected without further arrangements;
- The plant's emissions are higher than the planning limits; in this case, the connection is conditioned on further compensation, such that the emissions are within 70% of the planning values.

Synthetic Inertia

The Italian TSO has still not defined the concept of Virtual Synchronous Machine. However, they started to introduce the concept of "synthetic inertia" in the Annex 79. The Grid Code prescribes, indeed, that the control system of storage plants with a nominal power equal to or greater than 10 MW must be equipped with a function called "synthetic inertia". This function emulates the inertia of synchronous rotating groups, modifying the active power exchange of the Storage Plant with the grid based on the frequency measurement and/or the frequency derivative (also in combination with logical operators). The schemes and implementation methods of this function, as well as the characteristics of the frequency measurement chain and its derivative, must be preliminary discussed and agreed upon with the Operator and documented in the plant's Operating Regulations [30].

2.1.2 National Grid ESO: Great Britain TSO

National Grid ESO is the electricity system operator for Great Britain. The latest version of the grid code prescribes the technical and design criteria and performance requirements for Power Generating Modules (which includes Electricity Storage Modules), Offshore Transmission System (OTSDUW) Data and High Voltage DC (HVDC) equipments [32, 2, 33].

Power Generating Modules

The Power Generating Modules are gathered into different types according to the voltage level and the maximum capacity as follows [32]:

- Type A: Voltage $<$ 110 kV and Maximum Capacity between 0.8 kW and 1 MW;
- Type B: Voltage $<$ 110 kV and Maximum Capacity between 1 MW and 10 MW;
- Type C: Voltage $<$ 110 kV and Maximum Capacity between 10 MW and 50 MW;
- Type D: Voltage $\geq$ 110 kV and Maximum Capacity $>$ 50 MW.

Grid frequency variations

The frequency of the National Electricity Transmission System is nominally 50Hz and must be controlled within the range of 49.5 - 50.5 Hz under normal conditions, except during exceptional circumstances such as System Restoration. In such cases, the system frequency may rise to 52 Hz or fall to 47 Hz. The design of User's Plant and Apparatus, as well as OTSDUW Plant and Apparatus, must enable their operation within this frequency range as specified in Table 2.1.

Table 2.1 National Grid ESO frequency range requirements [32].

Frequency Range (Hz)	**Requirement**
51.5-52	Operation for a period of at least 15 minutes is required each time the Frequency is above 51.5 Hz
51-51.5	Operation for a period of at least 90 minutes is required each time the Frequency is above 51 Hz
49-51	Continuous operation is required
47.5-49	Operation for a period of at least 90 minutes is required each time the Frequency is below 49 Hz
47-47.5	Operation for a period of at least 20 seconds is required each time the Frequency is below 47.5 Hz

For the avoidance of doubt, disconnection, by frequency or speed based relays is notpermitted within the frequency range 47.5 Hz to 51.5 Hz.

Grid Voltage Variations

The normal operating voltage ranges of the National Electricity Transmission System are summarized in Figure 2.4.

National Electricity Transmission System Nominal Voltage	Normal Operating Range		Time period for Operation
	Voltage (percentage of Nominal Voltage)	Pu (1pu relates to the Nominal Voltage)	
Greater than 300kV	V -10% to +5% V +5% to +10%	0.90pu- 1.05pu 1.05pu- 1.10pu	Unlimited 15 minutes
110kV up to 300kV	V ±10%	0.90- 1.10pu	Unlimited
Below 110kV	±6%	0.94pu- 1.06pu	Unlimited

Fig. 2.4 Grid voltage variation requirements [33].

Voltage Waveform Quality

All Plant and Apparatus connected to the National Electricity Transmission System should be capable of withstanding the following distortions of the voltage waveform in respect of harmonic content and phase unbalance [32]:

- **Harmonic Content**: the Electromagnetic Compatibility Levels for harmonic distortion on the Onshore Transmission System from all sources under both Planned Outage and fault outage conditions, (unless abnormal conditions prevail) shall comply with Engineering Recommendation G5. The Electromagnetic Compatibility Levels for harmonic distortion on an Offshore Transmission System will be defined in relevant Bilateral Agreements [32];
- **Phase Unbalance**: under Planned Outage conditions, the weekly 95 percentile of Phase (Voltage) Unbalance, calculated in accordance with IEC 61000-4-30 and IEC 61000-3-13, on the National Electricity Transmission System for voltages above 150kV should remain, in England and Wales, below 1.5%, and in Scotland, below 2%, and for voltages of 150kV and below, across GB below 2%, unless abnormal conditions prevail and Offshore (or in the case of OTSDUW, OTSDUW Plant and Apparatus) will be defined in relevant Bilateral Agreements. The Phase Unbalance is calculated from the ratio of root mean square (rms) of negative phase sequence voltage to rms of positive phase sequence voltage, based on 10-minute average values, in accordance with IEC 61000-4-30 [32].

Active Power

Each Power Generating Module and HVDC Equipment must be capable of [32]:

a) continuously maintaining constant active power output for system frequency changes within the range 50.5 Hz to 49.5 Hz;

b) maintaining its active power output at a level not lower than the figure determined by the linear relationship shown in Fig. 2.5 for system frequency changes within the range 49.5 to 47 Hz for all ambient temperatures up to and including 25° C, such that if the system frequency drops to 47 Hz the active power output does not decrease by more than 5%;

c) To clarify, concerning a Power Generating Module, including a DC Connected Power Park Module utilizing an Intermittent Power Source where mechanical power input varies over time, the requirement specifies that: 1) The Active Power output must be unaffected by system frequency under point (a) of the list; 2) the Active Power output should not decrease with system frequency beyond the specified amount in (b) above;

d) At the Grid Entry Point or User System Entry Point, The Active Power output under steady-state conditions from any Power Generating Module or HVDC Equipment directly connected to the National Electricity Transmission System, or in the case of OTSDUW, the Active Power transfer at the Interface Point from any OTSDUW Plant and Apparatus, should not be influenced by voltage variations within the normal operating range specified above by more than the change in Active Power losses at reduced or increased voltage.

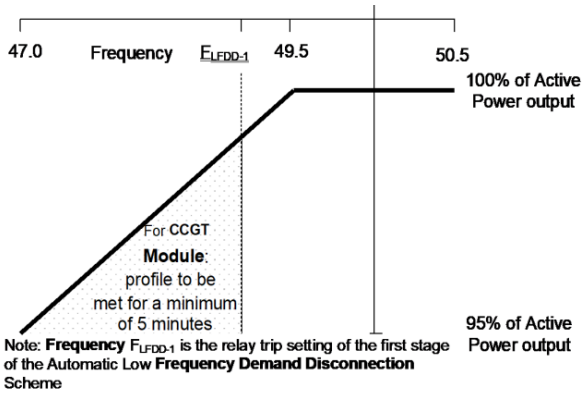

Fig. 2.5 Active Power Output with falling frequency for Power Generating Modules and HVDC Systems and Electricity Storage Modules when operating in an exporting mode of operation [32].

Reactive Power

When operating at Maximum Capacity all Type B Power Park Modules must be capable of continuous operation at any points between the limits of 0.95 Power Factor lagging and 0.95 Power Factor leading at the Grid Entry Point or User System Entry Point unless otherwise agreed with The Company or relevant Network Operator. At Active Power output levels other than Maximum Capacity, each Power Park Module must be capable of continuous operation at any point between the Reactive Power capability limits identified on the HV Generator Performance Chart unless otherwise agreed with The Company or Network Operator.

All Type C and Type D Power Park Modules, HVDC Converters at a HVDC Converter Station including Remote End HVDC Converters or OTSDUW Plant and Apparatus, shall be capable of satisfying the Reactive Power capability requirements at the Grid Entry Point or User System Entry Point (or Interface Point Capacity in the case of OTSUW Plant and Apparatus or HVDC Interface Point in the case of Remote End HVDC Converter Stations) as defined in Fig. 2.6 when operating below Maximum Capacity. With all Plant in service, the Reactive Power limits will reduce linearly below 50% Active Power output as shown in Fig. 2.6 unless the requirement to maintain the Reactive Power limits defined at Maximum Capacity (or Interface Point Capacity in the case of OTSDUW Plant and Apparatus) under absorbing Reactive Power conditions down to 20% Active Power output has been specified by The Company. These Reactive Power limits will be reduced pro rata to the amount of Plant in service [32].

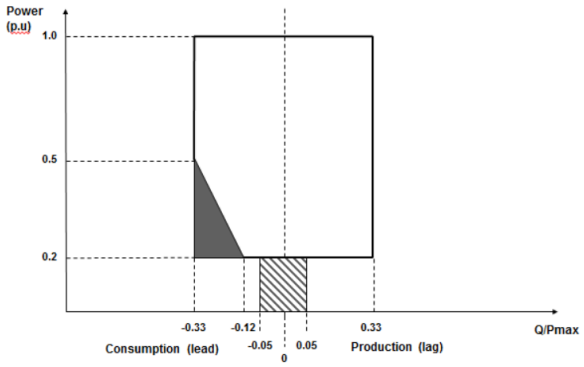

Fig. 2.6 Reactive power capability curve [32].

Fault Ride Through Capability

The Fault Ride Through (FRT) Capability refers to the ability of Power Generating Modules (including DC Connected Power Park Modules) and HVDC Systems to remain connected to the system and continue operating during periods of low voltage at the Grid Entry Point or User System Entry Point resulting from secured faults.

The FRT requirements differ according to the topology of the generating unit (i.e., offshore or onshore, rotating or converter-interfaced). Two examples are proposed in the following [32].

- For voltage dips on the LV Side of the Offshore Platform which last up to 140ms in duration, the fault ride through requirement is defined by Fig. 2.7. V/VN is the ratio of the voltage at the LV side of the Offshore Platform to the nominal voltage of the LV side of the Offshore Platform. The purpose of this requirement is to translate the conditions caused by a balanced or unbalanced fault which occurs on the Onshore Transmission System (which may include the Interface Point) at the LV Side of the Offshore Platform [32];
- Requirements applicable to Offshore Power Park Modules subject to Voltage which occur on The LV Side Of The Offshore Platform greater than 140ms in duration. In addition to the previous requirement, the FRT requirements applicable for Offshore Power Park Modules during balanced voltage dips which occur at the LV Side of the Offshore Platform and have durations greater than 140ms and up to 3 minutes are defined in Fig. 2.8 and termed the voltage–duration profile. This profile is not a voltage-time response curve that would be obtained by plotting the transient voltage response at the LV Side of the Offshore Platform to a disturbance. Rather,

each point on the profile (i.e. the heavy black line) represents a voltage level and an associated time duration which connected Offshore Power Park Modules must withstand or ride through [32].

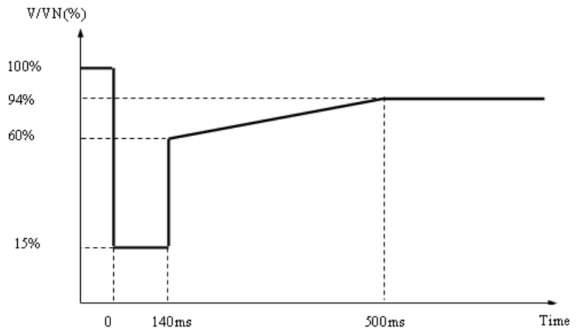

Fig. 2.7 Fault Ride Through capability curve of example 1 [32].

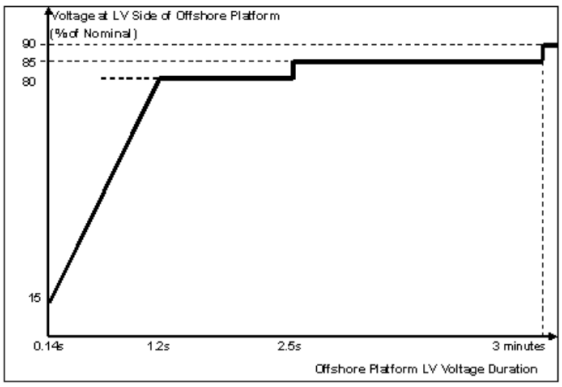

Fig. 2.8 Fault Ride Trough capability curve of example 2 [32].

Grid-Forming/Virtual Synchronous Machine

On January 2022, National Grid ESO approved the GC0137 grid code modification named "Minimum Specification Required for Provision of GB Grid Forming (GBGF) Capability (formerly Virtual Synchronous Machine (VSM) Capability)" [33]. This is one of the first grid code modification which introducing the concept of VSM. However, in the grid code modification there is a pervasive treatment of the grid-forming and VSM concepts as synonymous, although the VSM concept is inherently independent of whether it operates in a grid-following or grid-forming mode, as it will be clarified along the thesis. Nevertheless, this subsection aims at summarizing the main requirements of VSMs prescribed by National Grid ESO.

The Technical Performance requirements are described in the list below and are extracted from [33, 32]. The Grid Forming Plant has been categorized into two segments: GBGF-S (Grid Forming Plant derived from a Synchronous Generator) and GBGF-I (Grid Forming Plant derived from a Power Electronic Converter). This division became necessary due to slight variations in requirements between the two types of plants. For instance, owners of GBGF-S plants are not expected to perform certain tests or analyses because the dynamic performance characteristics of these plants are well-established. The proposer considers it unnecessary and inefficient to conduct such tests in these cases [33].

- **Active Control Based Power**: the Active Power output supplied by a Grid Forming Plant through controlled means (be it manual or automatic) of the positive phase sequence Root Mean Square Active Power produced at fundamental System Frequency by the control system of a Grid Forming Unit. For GBGF-I, this is equivalent to a Synchronous Generating Unit with a traditional governor coupled to its prime mover. Active Control Based Power includes Active Power changes that results from a change to the Grid Forming Plant Owners available set points that have a 5 Hz limit on the bandwidth of the provided response. Active Control Based Power also includes Active Power components produced by the normal operation of a Grid Forming Plant that comply with the Engineering Recommendation P28 limits. These Active Power components do not have a 5 Hz limit on the bandwidth of the provided response. Active Control Based Power does not include Active Power components proportional to System Frequency, slip or deviation that provide damping power to emulate the natural damping function provided by a real Synchronous Generating Unit [33].

- **Active Phase Jump Power**: it consists in the transient injection or absorption of Active Power from a Grid Forming Plant to the Total System as a result of changes in the phase angle between the Internal Voltage Source of the Grid Forming Plant and the Grid Entry Point or User System Entry Point. The technical requirements prescribe that in the event of a disturbance or fault on the Total System, a Grid Forming Plant will instantaneously (within 5ms) inject or absorb Active Phase Jump Power to the Total System as a result of the phase angle change. For GBGF-I as a minimum value this is up to the Phase Jump Angle Limit Power. Active Phase Jump Power is an inherent capability of a Grid Forming Plant that starts to respond naturally, within less than 5 ms and can have frequency components of over 1000 Hz [33].

- **Active Damping Power**: the Active Damping Power is the damped response of a Grid Forming Plant to an oscillation between the voltage at the Grid Entry Point or User System Entry Point and the voltage of the Internal Voltage Source of the Grid Forming Plant. For the avoidance of doubt, Active Damping Power is an inherent capability of a Grid Forming Plant that starts to respond naturally, within less than 5ms to low frequency oscillations in the System Frequency [33].

- **Active Inertia Power**: the injection or absorption of Active Power by a Grid Forming Plant to or from the Total System during a System Frequency change. The transient injection or absorption of Active Power from a Grid Forming Plant to the Total System as a result of the ROCOF value at the Grid Entry Point or User System Entry Point. This requires a sufficient energy storage capacity of the Grid Forming Plant to meet the Grid Forming Capability requirements specified in ECC.6.3.19 [33]. For the avoidance of doubt, this includes the rotational inertial energy of the complete drive train of a Synchronous Generating Unit. Active Inertia Power is an inherent capability of a Grid Forming Plant to respond naturally, within less than 5ms, to changes in the System Frequency. The Active Inertia Power has a slower frequency response compared with Active Phase Jump Power [33].

- **Control Based Reactive Power**: the Reactive Power supplied by a Grid Forming Plant through controlled means based on operator adjustment selectable setpoints [33].

- **GBGF Fast Fault Current Injection**: the ability of a Grid Forming Plant to supply reactive current, that starts to be delivered into the Total System in less than 5ms when the voltage falls below 90% of its nominal value at the Grid Entry Point or User System Entry Point [33].

- **Grid Forming Active Power**: Grid Forming Active Power is the inherent Active Power produced by Grid Forming Plant that includes Active Inertia Power plus Active Phase Jump Power plus Active Damping Power [33].

- **Grid Forming Capability**: it is (but not limited to) the capability a Power Generating Module, HVDC Converter (which could form part of an HVDC System), Generating Unit, Power Park Module, DC Converter, OTSDUW Plant and Apparatus, Electricity Storage Module, Dynamic Reactive Compensation Equipment or any Plant and Apparatus (including a smart load) whose supplied Active Power is directly proportional to the difference between the magnitude and phase of its Internal Voltage Source and the magnitude and phase of the voltage at the

Grid Entry Point or User System Entry Point and the sine of the Load Angle. As a consequence, Plant and Apparatus which has a Grid Forming Capability has a frequency of rotation of the Internal Voltage Source which is the same as the System Frequency for normal operation, with only the Load Angle defining the relative position between the two. In the case of a GBGF-I, a Grid Forming Unit forming part of a GBGF-I shall be capable of sustaining a voltage at its terminals irrespective of the voltage at the Grid Entry Point or User System Entry Point for normal operating conditions. For GBGF-I, the control system, which determines the amplitude and phase of the Internal Voltage Source, shall have a response to the voltage and System Frequency at the Grid Entry Point or User System Entry Point) with a bandwidth that is less than a defined value as shown by the control system's NFP Plot. Exceptions to this requirement are only allowed during transients caused by System faults, voltage dips/surges and/or step or ramp changes in the phase angle which are large enough to cause damage to the Grid Forming Plant via excessive currents [33].

- **Voltage Jump Reactive Power**: it consists in the transient Reactive Power injected or absorbed from a Grid Forming Plant to the Total System as a result of either a step or ramp change in the difference between the voltage magnitude and/or phase of the voltage of the Internal Voltage Source of the Grid Forming Plant and Grid Entry Point or User System Entry Point. The technical requirements prescribe that he transient Reactive Power injected or absorbed from a Grid Forming Plant to the Total System as a result of either a step or ramp change in the difference between the voltage magnitude and/or phase of the voltage of the Internal Voltage Source of the Grid Forming Plant and Grid Entry Point or User System Entry Point. In the event of a voltage magnitude and phase change at the Grid Entry Point or User System Entry Point, a Grid Forming Plant will instantaneously (within 5ms) supply Voltage Jump Reactive Power to the Total System as a result of the voltage magnitude change [33].

2.1.3 UNIFI Specifications for Grid-Forming Converters

As outlined in the previous subsections, grid codes prescribe the requirements of grid-tied converters to support the grid. Moreover, in the past years, several international projects suggested fundamental requirements to guarantee the acceptable power system operation with high penetration of grid-tied converters [34, 35, 16]. In the following, this thesis summarizes the specifications prescribed by the Universal Interoperability for

grid-Forming Inverters (UNIFI) Consortium co-led by the National Renewable Energy Laboratory (NREL) [16].

Grid-Forming Control

According to the UNIFI, a proper GFM control maintains an internal voltage phasor that is constant or nearly constant in the sub-transient to transient time frame (i.e., 0-5 cycles) [16]. Therefore, the GFM converter will almost immediately respond to changes in the external system and attempt to keep the converter control during grid perturbations to maintain the grid stability. Moreover, the voltage phasor is controlled to synchronize to the other devices in the grid while regulating the active and reactive power to support the grid.

Performance Requirements for Operation Within Normal Grid Operating Conditions

Normal operations for power systems are defined by operation within a narrow range around nominal voltage and frequency, with the ability to go outside of those ranges for short periods of time. The requirements within normal operating conditions are fully described in [16] and summarized here as follows:

- **Autonomously Support the Grid**: as GFL, GFM converters have to autonomously respond to changes (both transient and steady state) in their locally measured signals (e.g., terminals of the converter or point of interconnection voltage, current, and frequency) to support the local power system;
- **Dispatchability of Power Output**: when operating as part of an interconnected grid, a GFM plant's steady state power output, within the normal range of voltage magnitude and frequency, should be dispatchable either through system operator control or by a locally determined goal, based upon a market clearing solution, like a GFL converter;
- **Provide Positive Damping of Voltage and Frequency Oscillations**: it is expected that a GFM converter will present a non-negative resistance or damping to the grid within a frequency range of common grid electrical resonances to prevent the initiation of any adverse interactions or oscillations;

- **Active and Reactive Power Sharing across Generation Resources**: a GFM converter has to autonomously share power with other generation resources using the principles of droop akin to the operation of conventional synchronous generators or GFL converters;
- **Operation in Grids with Low System Strengths**: a GFM converter is expected to operate stably when connected to a power system with low system strength. The system strength is a term used to describe how fast a system's voltage and frequency change after a disturbance. The strength metrics are:
  - Short Circuit Ratio (SCR);
  - Rate of change of frequency (ROCOF) during grid disturbances;
  - Critical clearing time (CCT) of short-circuit faults to ensure stable operation after fault clearance;
  - Rate of change of voltage in response to changes in current injection to the grid (i.e., apparent source impedance).
- **Operation Under System Unbalance**: a GFM converter should not actively oppose or prevent the flow of negative sequence current for small levels of voltage unbalance. If the provision of large amounts of negative sequence current introduces stress to equipment, reduction or limitation of the magnitude of the current may be allowed after discussion with the system operator.

Performance Requirements for Operation Outside Normal Conditions

Abnormal conditions on the power system (e.g., temporary and permanent faults, oscillations, generation loss, load loss, blackouts) are characterized by voltage and frequency excursions outside of the normal operating ranges. The requirements outside normal operating conditions are fully described in [16] and summarized here as follows:

- **Ride-through Behavior**: a GFM converter must ride-through events that result in operations outside normal limits by injecting current during and after a voltage sag to aid in voltage recovery. The injected current must oppose to the change in voltage at each converter terminal subject to physical limitations of the converter unit. It is expected that the converter will continue to inject current within its ratings. The purpose of current injection is to support system-wide stability subject to hardware equipment limitations and capabilities;

- **Response to Symmetrical Faults**: during symmetrical faults, a GFM converter is expected to maintain a balanced internal voltage to the extent possible within its physical limits. The GFM converter should inject current to oppose the change in voltage;
- **Response to Asymmetrical Faults**: during asymmetrical faults, a GFM converter is expected to maintain a balanced voltage to the extent possible within its physical limits. This naturally results in the GFM converter outputting unbalanced currents, including negative sequence currents;
- **Response to Abnormal Frequency**: as long as the frequency does not exceed the must-not-trip region defined by system planner or by IEEE 1547-2018 [36] or IEEE 2800-2022 [37] or other applicable requirements or standards, a GFM converter is expected to modulate active power as required during and after a frequency excursion event to aid in frequency recovery and stability;
- **Response to Phase Jumps and Voltage Steps**: a GFM converter is expected to absorb or inject active and/or reactive power to resist changes in positive sequence voltage phase angle and is expected to do so unless it exceeds an equipment limit. Similarly, a GFM converter is expected to absorb or inject reactive/active power to reduce changes in the positive sequence voltage magnitude.

Additional GFM Capabilities

This subsection collects additional capabilities that UNIFI suggests to implement in coordination with the system operator, as follows:

- **Intentional Islanding**: a GFM converter that is designed to maintain an intentional island is expected to be capable of maintaining a stable voltage and frequency when intentional islanding occurs. This capability depends on certain conditions listed in detail in [16]. Once the operation of the island has stabilized, the GFM plant's voltage and frequency operating ranges should be adequately set to allow continuous operation over the load range of the island without tripping on over-voltage and/or frequency protection settings as defined by the system planner or by applicable standards or respective protection studies;
- **Black Start and System Restoration**: some GFM converters can be designed and programmed to provide black start services. If implemented, these black start

services should be coordinated with system operators to help in system restoration from black-out conditions. The suggested step-by-step procedure to properly perform the black start service is detailed in [16];

- **Regulating Voltage Harmonics**: the harmonic distortion of the line-to-neutral voltage waveforms produced by a GFM plant should comply with the requirements of the system planner. As a result, a GFM converter may inject harmonic currents at its point of interconnection to aid in reducing the amplitude of voltage harmonics induced by other power system components;
- **Secondary Voltage and Frequency Signal Response**: GFM plants that are expected to participate in secondary control, should be able to receive an external signal that enables power flow control from a system operator. This is known as the secondary control signal since the unit or plant receives an external signal to adjust power output. Once it receives new setpoints, the GFM plant is expected to operate (within the GFM converter's limits) at the new steady state condition within the time specified by the system operator.

2.2 General Structure

The general scheme under study consists of a grid-tied converter connected to the grid trough an LCL (or LC) filter as shown in Fig.2.9. The inverter is supplied by an ideal dc source as the focus of the work is the control of the dc/ac converter. Therefore, the dc part of the system is considered ideal.

In this system, e_g is the three phase grid voltage, v_{PCC} is the three phase PCC phase voltage, v_g is the three phase measured phase voltage (measured at the filter capacitors), i_g is the three phase grid current and i_i is the three phase measured inverter current.

The Point of Common Coupling (PCC) defines the connection between the inverter and the grid.

The filter consists of an inverter-side inductor L_f (with an equivalent series resistance R_f), a filter capacitor C_f with a damping resistor R_d and a grid-side inductor L_{fg} (with an equivalent series resistance R_{fg}). The grid is modeled as an equivalent Thevenin circuit with a grid inductance L_g, and, according to the tests, also a grid resistance R_g.

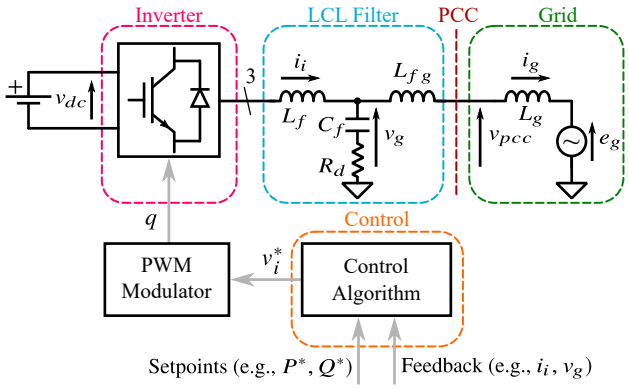

Fig. 2.9 Scheme of the system under study.

The inverter commands q are generated by the PWM modulator, which receives the voltage reference v_i^*. This is retrieved by the control algorithm of the converter.

2.3 Grid-Following and Grid-Forming Converters

2.3.1 Grid-Following

A grid-following converter is a grid-tied converter controlled as a current source. It needs a method to synchronize to the grid (e.g., PLL) [38]. It can exchange active and reactive power to the grid according to either the grid supporting or the grid feeding approach. It cannot operate in island mode as a GFM. In grid supporting operation, the converter can contribute to the voltage amplitude and frequency regulation. The converter receives the voltage amplitude reference V^* and the frequency reference ω^* and participates at the grid voltage and frequency regulation according to a droop control law [27, 7]. The block scheme is depicted in Fig. 2.10a. The "Reference Current Generator" block consists of the droop control laws to retrieve the active and the reactive power references [7]. Then, they are divided by the measured voltage v_c to retrieve the reference current i_i^*. The typical application is a storage system.

In grid feeding operation, the converter exchanges active and reactive power according to external active and reactive references P^*, Q^* (coming from e.g., the MPPT algorithm) as depicted in Fig. 2.10b. The "Reference Current Generator" consists only on the division per the measured voltage to obtain the reference current. In both operations (i.e., supporting and feeding), a current regulator aims at canceling the error between the reference current i_i^* and the measured current i_i. This way, the actual current tracks

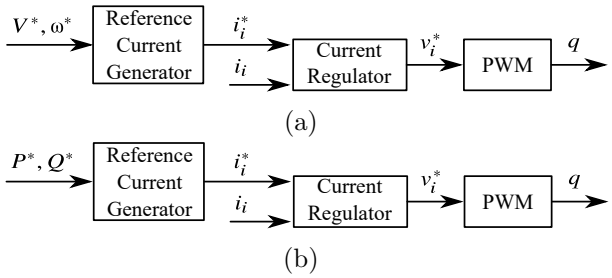

Fig. 2.10 (a) Grid supporting general block control scheme; (b) grid feeding general block control scheme.

the reference. The current regulator output is the desired (reference) inverter voltage v_i^* applied to the PWM modulator to retrieve the inverter commands q. Different types of current regulators are available in the literature. The most adopted solutions are the proportional integral (PI) and the proportional resonant (PRES) [38, 39]. Hence, a GFL converter includes a current regulator that easily controls the current, preventing the overcurrent protection from triggering during abnormal conditions.

Finally, the stability of grid-following converters is strictly related to the grid stiffness. The stiffer is the grid, the higher is the stability margin of the converter. Therefore, a grid-following converter well operates in case of stiff grids, while it shows stability issues in case of weak grid conditions [40, 41].

2.3.2 Grid-Forming

A grid-forming converter is a grid-tied converter controlled as a voltage source with given amplitude and frequency. The output voltage of the grid-forming control can be used as a reference for the rest of the system. The main goal of this control strategy is to make the power converter form the grid. It can operate both connected to the grid and in island mode (microgrid operation) [42–44]. In island operation, the converter imposes the voltage (in terms of amplitude and frequency) to supply loads in a microgrid configuration. In this case, a closed loop voltage control is necessary to cancel the error between the reference voltage and frequency and the actual values. An additional current regulator can be added to control the current (e.g., to limit the inverter current). Moreover, a GFM converter can perform the so-called black start: impose the voltage starting from a zero value (e.g., in case of restoring the grid after a fault). Next, in grid-connected operation, the converter behaves as a voltage source trying to impose the reference voltage. The weaker is the grid, the smaller will be the error between the reference voltage and the actual voltage. In grid-connected operation, the GFM can operate both with open and

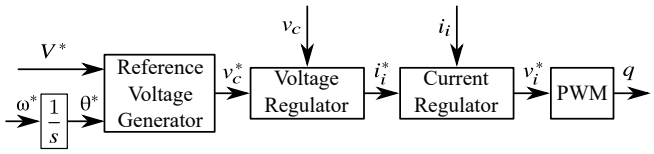

Fig. 2.11 Grid-forming general block control scheme with dual loop control.

closed loop voltage control. Moreover, it can operate either with a single voltage loop control or with a dual loop control. In the first case, a single voltage regulator controls the voltage v_c. In the second case, there are two cascaded regulators: inner current regulator to control the inverter current i_i; outer voltage regulator to control v_c [45]. The general block control scheme of the dual loop GFM converter is illustrated in Fig. 2.11.

Finally, even the stability of grid-forming converters is strictly related to the grid stiffness. The stiffer is the grid, the lower is the stability margin of the converter. Therefore, a grid-forming converter well operates in case of weak grids, while it shows stability issues in case of stiff grid conditions [40, 41].

Chapter 3

Virtual Synchronous Machines

This chapter reviews ten representative VSM models found in the literature. The VSM solutions are implemented based on their original structures as presented in their respective papers. However, to ensure a fair comparison under the same conditions, this thesis proposes a standardized parameter tuning procedure detailed in the following.

The VSM solutions studied and implemented in this thesis are listed in Table 3.1.

Table 3.1 List of VSM solutions.

Model	**Output Type**
Synchronverter [46–48]	Grid-Forming
Enhanced Synchronverter [49]	Grid-Following
Osaka [50, 51]	Grid-Forming
VISMA [52, 53]	Grid-Following
VISMA I [54, 55]	Grid-Following
VISMA II [56]	Grid-Forming
SPC [57, 58]	Grid-Following
VSYNC [59, 60]	Grid-Following
KHI [61]	Grid-Following
CVSM [62, 63]	Grid-Following
S-VSC [25, 64]	Grid-Following/Grid-Forming

The results of this chapter brought to the publication of [65] and [66]. Moreover, some of the results were obtained as part of a Master's Thesis [67].

3.1 General Aspects of the VSM models

This Section provides general information about the system on analysis and the tuning procedure of the VSM models.

A Virtual Synchronous Machine is a converter able to emulate the behavior of a conventional synchronous machine. In the following, the main elements of a generic VSM are listed. Each VSM solution can show differences for one or more parts. A general block control scheme of a generic VSM is depicted in Fig. 3.1. The main blocks are:

- Mechanical emulation (i.e., swing equation). The most representative element of a VSM solution is the implementation of the swing equation, i.e., the equation which describes the mechanical behavior of a synchronous machine. The swing equation of a synchronous machine is as follows [7]:

$$P_m - P_e = 2H\frac{d\omega_r}{dt} \tag{3.1}$$

  where P_m is the mechanical power from the prime motor (e.g., turbine), P_e is the electrical power, H is the inertia constant of the machine and ω_r is the rotor speed. The equation can be also written in terms of torque [7]. For a virtual machine, the equation becomes:

$$P_v^* - P_v = 2H\frac{d\omega_v}{dt} \tag{3.2}$$

$$\theta_v = \int \omega_v dt \tag{3.3}$$

  where ω_v is the virtual speed and θ_v is the virtual angle of the VSM.

- Virtual damping. The damping of the VSM can be implemented as a damping term on the swing equation or as a virtual damping flux of a virtual damping winding [68].

- Active droop control. To perform the active power regulation, a high-level proportional controller can be added [69]. The simplest damping method is the droop-based damping, where the damping term is proportional to the frequency deviation from a reference setpoint ω^* as follows:

$$P_v^* - P_v = 2H\frac{d\omega_v}{dt} + k_d(\omega_v - \omega^*) \tag{3.4}$$

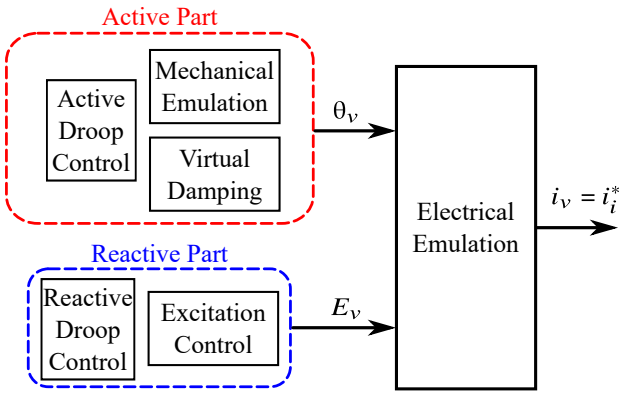

Fig. 3.1 General block scheme of a generic VSM.

- Excitation control. The excitation of the virtual machine is obtained through an integral (or proportional-integral) control of the reactive power. It provides the excitation flux and consequently the virtual electromotive force amplitude E_v [68, 70]:

$$E_v = \omega_v \int k_e \frac{Q_v^* - Q_v}{V_g} dt \tag{3.5}$$

- Reactive droop control. To perform the reactive power regulation, a high-level proportional controller can be added [64].

- Electrical emulation. The electrical part of the virtual machine can be emulated either using the electrical equations of a synchronous machine or by using a virtual impedance (or admittance). The virtual impedance (or admittance) can be arbitrary tuned for each frequency (i.e., fundamental, fifth harmonic, seventh,...) with the purpose of provide harmonic compensation:

  – Virtual impedance. The voltage reference v_i^* is obtained by subtracting the voltage drop on the tunable virtual impedance to the virtual electromotive force;

  – Virtual admittance. The tunable virtual admittance is used to retrieve the reference current from the difference between the virtual electromotive force and the measured voltage v_c. Next, the voltage reference v_i^* is obtained from the closed loop current control.

3.1.1 Scheme of the hardware on study

The reference hardware to study and implement the VSM solutions is shown in Fig. 3.2.

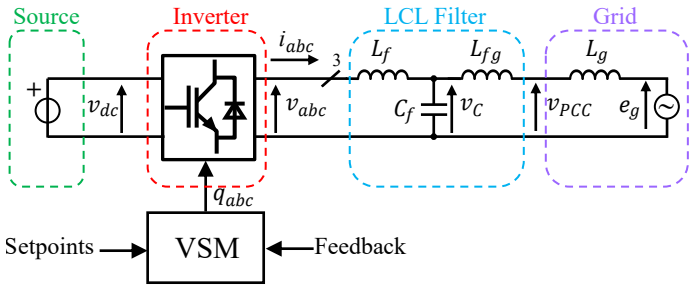

Fig. 3.2 Hardware block diagram for the considered VSM solutions [65].

The hardware is the same shown in Fig. 2.9. In this case, the inverter is controlled according to the VSM algorithm. The VSM block contains the whole control algorithm, including the grid synchronization procedure, the current control, the Pulse Width Modulation (PWM) and the measurements. The measured quantities to perform the VSM controls are the capacitor voltage v_C and the inverter current is i_{abc} [65].

3.1.2 Grid-Following and Grid-Forming VSMs

The literature is full of different VSMs algorithms belonging to different typologies depending on how the virtual electromotive force e_v (in terms of amplitude and phase) is employed:

- GFL VSMs: grid-following VSMs using a tunable virtual admittance Y_v to obtain the reference current as the difference between the virtual electromotive force e_v and the capacitor voltage v_c as follows:

$$i_i^* = i_v = Y_v(e_v - v_c) \tag{3.6}$$

  Then, the reference current i_i^* is provided as input of a current regulator to obtain the voltage reference v_i^*.

  In this thesis the current is controlled through a PI current regulator in rotating reference frame defined either by a PLL or the VSM, according to the model. The current regulator is tuned according to [38].

  The interface between the GFL VSM and the grid can be represented by the single-phase equivalent circuit shown in Fig. 3.3a. Here, L_g denotes the grid inductance, R_g represents the grid resistance, and C_f is the capacitance of the LCL filter.

Therefore, the virtual machine imposes its virtual electromotive force behind a virtual impedance to inject the desired reference current.

This kind of VSM embeds a current regulator. Therefore, during faults the current can be easily kept within safety limits. Moreover, a GFL VSM does not need a PLL to track the grid because the VSM inherently synchronizes to the grid through a power synchronization procedure [68]. Moreover, by adding an high level control, a GFL VSM can be enabled to operate even in island mode as in [64].

Some examples of this VSM typology are the SPC model [57] and the last version of the Synchronverter [49]. More recent models are [68, 71]. In this thesis, the SPC is the model adopted to experimentally test the performance of a GFL VSM against a voltage dip.

- GFM VSMs: in grid-forming VSMs the voltage reference v_i^* can:
  - Corresponds to the virtual electromotive force e_v, as happens for single open loop voltage control. Some examples are the original version of the Synchronverter [47] and the models in [50, 72];
  - Be calculated by subtracting the voltage drop across a tunable virtual impedance Z_v from the electromotive force e_v, as, for instance, for the VISMA II model: [56]:

$$v_i^* = e_v - Z_v i_v \tag{3.7}$$

  - Be retrieved from a dual loop control. The difference between the VSM electromotive force e_v and the voltage drop on a tunable virtual impedance Z_v is used as a voltage reference for the capacitor voltage reference v_c^*:

$$v_c^* = e_v - Z_v i_v \tag{3.8}$$

    Then, a cascaded dual loop control is employed. A first voltage loop control receives the reference voltage v_c^* and the actual voltage v_c to provide the inverter reference current i_i^*. Next, as it happens for GFL VSMs, the reference current is tracked by means of a current regulator whose output is v_i^*. An example of this type of VSM is the CVSM model [62], which is implemented in this thesis to test its performance under a voltage dip together with the Osaka model. The connection between the GFM VSM and the grid can be represented by the equivalent circuit in Fig. 3.3b. Here, L_f is the filter

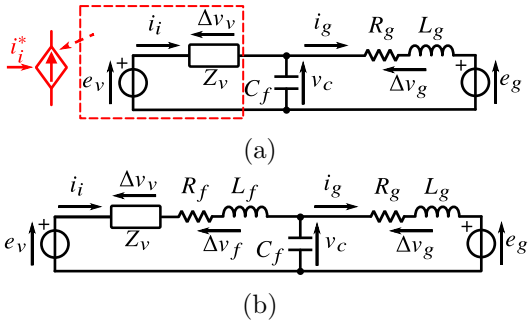

Fig. 3.3 Connection between the VSM and the grid. Equivalent circuit for: (a) GFL VSMs; (b) GFM VSMs [73].

inductance and R_f is the filter resistance. The other terms are the same of Fig. 3.3a.

As already stated in the previous chapter, there is a pervasive treatment of the grid-forming and VSM concepts as synonymous, although the VSM concept is independent on the grid-following or grid-forming mode. Indeed, the literature showcases VSMs functioning both as grid-forming (GFM VSM) and grid-following (GFL VSM) and providing grid support in a straightforward way [55, 70, 68, 49]. Notably, GFM converters exhibit the capability to operate in microgrid configuration, ensuring a higher level of resilience. However, in a system with a large penetration of grid-connected converters, not all of them can operate as GFM for stability issues [74]. Therefore, it is crucial that GFL converters play a key role in supporting the grid as well. For this purpose, GFL VSMs can guarantee the provision of ancillary services similarly to GFM VSMs, as it will be demonstrated in this chapter.

3.1.3 Common Tuning Procedure: Active Part

The tuning of VSMs parameters is performed starting from a common linearized model, in per unit (pu).

The circuit shown in Fig. 3.4 describes the interface between a voltage source (like the VSM equivalent stator) and the main grid, assuming a prevalent inductive system (e.g., Medium or High Voltage systems).

The equivalent circuit quantities, normalized in per unit, include:

- $V\angle 0$: grid voltage in polar notation (pu);

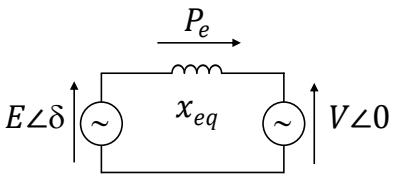

Fig. 3.4 Simplified circuit interfacing the VSM stator and the grid [65].

- $E\angle\Delta$: VSM electromotive force voltage (pu);
- x_{eq}: equivalent reactance between the two voltage sources (pu);
- P_e: active power transferred from one side to another, expressed in per unit (pu) as follows:

$$P_e = \frac{EV}{x_{eq}} \sin(\delta) = K_s \sin(\delta) \tag{3.9}$$

  where K_s represents the synchronizing power (pu), which corresponds to the theoretical maximum transferable power between the two voltage sources [7].

The equivalent reactance X_{eq} (Ω) is given by summing the following three contributions:

$$X_{eq} = \omega_b(L_s + L_{fg} + L_g) \tag{3.10}$$

where L_g is the grid inductance (H); L_{fg} is the grid-side filter inductance (H); L_s is the VSM inductance (H). For grid-forming VSMs L_s is the real filter inductance L_f, whereas, for grid-following VSMs, L_s corresponds to the virtual inductance L_v.

The equivalent reactance in pu is x_{eq}:

$$x_{eq} = \frac{X_{eq}}{Z_b} = \frac{\omega_b}{Z_b}(L_s + L_{fg} + L_g) = l_s + l_{fg} + l_g = x_s + x_{fg} + x_g \tag{3.11}$$

where l_g and x_g denote the grid inductance and reactance, respectively (pu); l_{fg} and x_{fg} denote the grid-side filter inductance and reactance, respectively (pu); l_s and x_s denote the VSM inductance and reactance, respectively (pu).

The system is linearized around its nominal working condition. Then, a small deviation (denoted by the prefix Δ) is applied. The linearized system consists of the swing equation with the droop-based damping shown in (3.4), the speed integration and (3.4) as follows:

$$\begin{cases} P_v^* - P_v = 2H\dfrac{d\omega_v}{dt} + k_d(\omega_v - \omega^*) & \text{(3.12a)} \\ \Delta\delta = \dfrac{\omega_b}{s}\Delta\omega & \text{(3.12b)} \\ \Delta P_e = K_s \sin(\Delta\Delta) \simeq K_s\Delta\delta & \text{(3.12c)} \end{cases}$$

By combining the three equations of (3.12), the linearized block scheme illustrated in Fig. 3.5 can be finally retrieved [65].

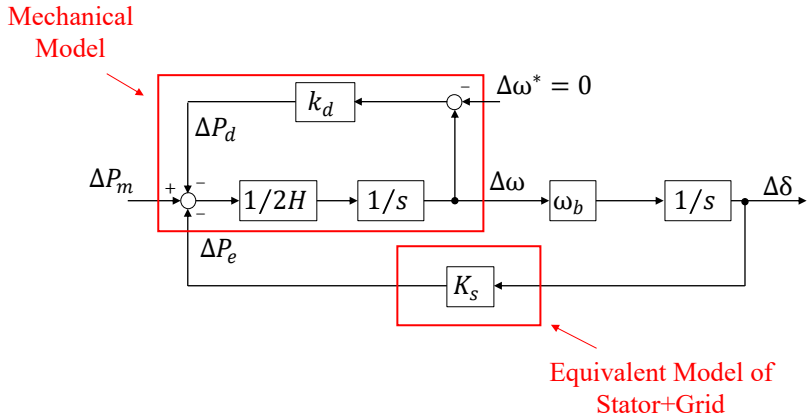

Fig. 3.5 Linearized model in per unit of VSM stator connected to the grid [65].

The characteristic equation of the scheme in the Fig. 3.5 (3.13a) can be compared with the general second order equation (3.13b) as follows:

$$\begin{cases} s^2 + \dfrac{k_d}{2H}s + \dfrac{\omega_b K_s}{2H} = 0 & \text{(3.13a)} \\ s^2 + 2\zeta\omega_N s + \omega_N^2 = 0 & \text{(3.13b)} \end{cases}$$

where ζ represents the desired damping factor and ω_N denotes the natural frequency (rad/s) of the system. The results, which are beneficial for certain VSM solutions, can be derived by comparing (3.13a) and (3.13b).

$$\begin{cases} k_d = 2\zeta\sqrt{2H\omega_b K_s} & \text{(3.14a)} \\ \omega_N = \sqrt{\dfrac{\omega_b K_s}{2H}} & \text{(3.14b)} \end{cases}$$

Some VSMs use the frequency ω_{PLL} tracked by the PLL in place of the reference ω^*. In this case, the linearized model changes and k_d must be modify of a factor k_c [75]:

$$\begin{cases} k_c = \dfrac{L_s + L_{fg} + L_g}{L_s} & \text{(3.15a)} \\ k'_d = k_d k_c & \text{(3.15b)} \end{cases}$$

The damping factor ζ and the inertia constant H are assigned typical values as per [7], while the synchronizing power K_s is contingent upon the equivalent reactance x_{eq}. Finally, the base values, tuning outcomes, and parameters for VSM models are detailed in Table 3.2, based on the experimental setup described in Section 3.4 [65].

Table 3.2 Parameters for VSM tuning.

Base Values		**Common Parameters**		**Current Source Parameters**		**Voltage Source Parameters**	
S_b	15 kVA	V	1 pu	l_v	0.1 pu	l_f	0.059 pu
V_b	$120\sqrt{2}$ V	E	1 pu	x_{eq}	0.146 pu	x_{eq}	0.105 pu
I_b	60 A	l_{fg}	0.013 pu	K_s	6.85 pu	K_s	9.5 pu
Z_b	2.88 Ω	l_g	0.033 pu	k_d	184 pu	k_d	216 pu
f_b	50 Hz	ζ	0.7	ω_N	16.40 rad/s	ω_N	19.31 rad/s
ω_b	314 rad/s	H	4 s	k_c	1.46 pu	k_c	1.77 pu
				k'_d	269 pu	k'_d	383 pu

To ensure a fair comparison among the VSM solutions, it has been chosen to employ identical design parameters such as inertia constant, virtual inductance, and damping factor for each model. This approach allows for an unbiased evaluation and comparison of the specific characteristics of each model. Optimizing each control algorithm individually is beyond the scope of this thesis, as it would minimally impact the performance of each solution, while preserving the fundamental behavior and features of the models [65].

3.1.4 Common Tuning Procedure: Excitation Control

The active parts of the VSMs solutions are very similar with each others. However, the same is not true for the reactive one.

Some models embed a PI regulator, others a pure integrator or a simple droop control. Nevertheless, a comprehensive tuning method for the excitation control can be performed according to the method proposed in [76]. The system on study is the same already

described for the active control in Fig.3.4. All quantities have been already described, expect for Q_e, the reactive power transferred from one side to another. It can be obtained from (3.16).

$$Q_e = \frac{V \cdot (E - V)}{X_{tot,pu}} \tag{3.16}$$

As for the active control, the system is linearized around the nominal working point. The Laplace block scheme is proposed in Fig. 3.6.

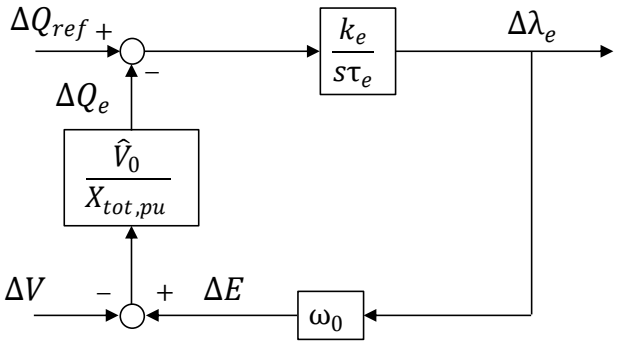

Fig. 3.6 Linearised model in pu of VSM's excitation control [76].

The quantities which take part into this model are:

- ΔQ_{ref}, the variation of the reactive power reference (pu);
- ΔQ_e, the variation of the reactive power transferred from the VSM's stator to the grid (pu);
- ΔV, the variation of the grid voltage (pu);
- ΔE, the variation of the VSM voltage (pu);
- ω_0, the nominal speed equal to 1 pu;
- $\hat{V}_0$, the nominal voltage equal to 1 pu;
- $X_{tot,pu}$, the equivalent reactance between the two voltages sources (pu);
- $\Delta\lambda_e$, the variation of the VSM excitation flux linkage (pu);
- τ_e, the time constant of the excitation control (s);

- k_e, the gain of the excitation control (pu).

The error between the reactive power reference and the VSM reactive power is provided to a pure integrator to obtain the excitation flux linkage amplitude. Then, this is used to retrieve the VSM voltage amplitude. The difference between it and the grid voltage leads to the exchange of reactive power.

The characteristic equation of the system can be retrieved as follows:

$$s\tau_e X_{tot,pu} + \omega_0 k_e = 0 \tag{3.17}$$

The system is characterized by a single pole, with the following time constant:

$$\tau = \frac{\tau_e X_{tot,pu}}{\omega_0 k_e} \tag{3.18}$$

where τ can be imposed by the user and set equal to τ_e. The excitation gain k_e becomes:

$$k_e = \frac{X_{tot,pu}}{\omega_0} \tag{3.19}$$

The inverse of k_e is chosen as reactive droop coefficient:

$$b_q = \frac{1}{k_e} \tag{3.20}$$

Finally, the constant K_{ecc} is defined as follows:

$$K_{ecc} = \frac{k_e}{\tau_e} \tag{3.21}$$

All values are listed in Table 3.3, referring to the experimental setup of section 3.4 [76].

Table 3.3 Parameters for Excitation Control.

Parameter	Value	Meas. Unit
Common Parameters		
V	1	pu
E	1	pu
$\hat{V}_0$	1	pu
ω_0	1	pu
l_{fg}	0.013	pu
$L_{g,pu}$	0.033	pu
Grid-Following Parameters		
l_v	0.1	pu
$X_{tot,pu}$	0.146	pu
τ_e	1	s
k_e	0.146	pu
b_q	6.85	pu
K_{ecc}	0.146	1/s
Grid-Forming Parameters		
l_f	0.059	pu
$X_{tot,pu}$	0.105	pu
τ_e	1	s
k_e	0.105	pu
b_q	9.52	pu
K_{ecc}	0.105	1/s

3.2 Grid Synchronization

To interface inverters with the grid, a process of synchronization has to be performed. Many synchronization method have been proposed in the literature. One of the most adopted one is the Phase Looked Loop (PLL) [77]. Another one is the Power Synchronization Loop (PSL) [78].

The synchronization procedure is independent of the control algorithm and so it is valid for both conventional techniques and VSM solutions.

3.2.1 Phase Locked Loop: PLL

The basic structure of the PLL is proposed in Fig.3.7 [77]. It is the normalized form, which is independent of the measured voltage amplitude. It is composed by three parts: Phase detector, Loop filter and Voltage Controller Oscillator (VOC).

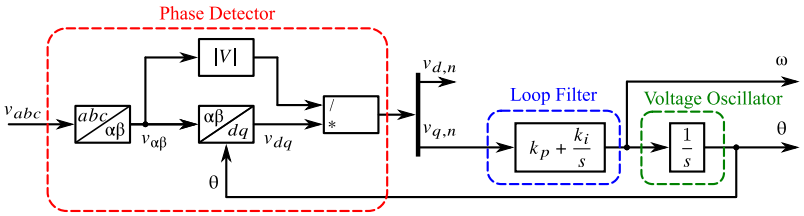

Fig. 3.7 Basic structure of the PLL.

- Phase Detector receives the three phase measured voltages v_{ga}, v_{gb}, v_{gc}. The first step is the transformation into the two phase voltages $v_{g\alpha}$, $v_{g\beta}$, applying the Clarke Transformation by means of the matrix $T_{\alpha\beta}$ as in (3.22).

$$\begin{bmatrix} v_{g\alpha} \\ v_{g\beta} \end{bmatrix} = T_{\alpha\beta} \cdot \begin{bmatrix} v_{ga} \\ v_{gb} \\ v_{gc} \end{bmatrix}$$

$$\begin{bmatrix} v_{g\alpha} \\ v_{g\beta} \end{bmatrix} = \begin{bmatrix} \frac{2}{3} & -\frac{1}{3} & -\frac{1}{3} \\ 0 & \frac{1}{\sqrt{3}} & -\frac{1}{\sqrt{3}} \end{bmatrix} \cdot \begin{bmatrix} v_{ga} \\ v_{gb} \\ v_{gc} \end{bmatrix} \tag{3.22}$$

  Then, the rotation transformation is performed to retrieve the two voltages v_{gd}, v_{gq}, by means of the matrix T_{dq}. It defines the frame (d, q), rotating the frame (α, β) with an angle equal to θ.

$$\begin{bmatrix} v_d \\ v_q \end{bmatrix} = T_{dq} \cdot \begin{bmatrix} v_\alpha \\ v_\beta \end{bmatrix}$$

$$\begin{bmatrix} v_d \\ v_q \end{bmatrix} = \begin{bmatrix} \cos(\theta) & \sin(\theta) \\ -\sin(\theta) & \cos(\theta) \end{bmatrix} \cdot \begin{bmatrix} v_\alpha \\ v_\beta \end{bmatrix} \tag{3.23}$$

  The Clarke and the rotation transformation define the Park Transformation.

- Loop Filter is a PI regulator which receives as input the normalised grid voltage component $v_{gq,norm}$. This can be written as follows:

$$v_{gq,norm} = \sin(\theta_g - \theta) \tag{3.24}$$

The working principle of the controller brings $v_{gq,norm}$ to zero. Therefore, in steady-state, θ will be equal to θ_g, the grid voltage will be aligned with the d-axis and $v_{gd,norm}$ will coincide with the amplitude $\widehat{V}_{norm}$. The output of the regulator is the frequency ω. For a small difference between the two angles, Equation (3.24) can be approximated:

$$v_{gq,norm} = \sin(\theta_g - \theta) \approx \theta_g - \theta \tag{3.25}$$

Next, the Laplace block scheme of Fig.3.8 can be retrieved.

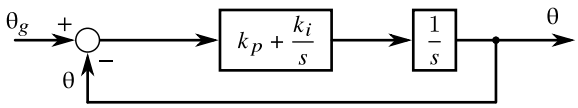

Fig. 3.8 PLL Laplace block scheme.

This scheme is useful to properly design the PI regulator. The open-loop and closed-loop transfer functions are expressed respectively in (3.26) and (3.27):

$$H_{OL,PLL} = \frac{k_{p,PLL}s + k_{i,PLL}}{s^2} \tag{3.26}$$

$$H_{CL,PLL} = \frac{k_{p,PLL}s + k_{i,PLL}}{s^2 + k_{p,PLL}s + k_{i,PLL}} \tag{3.27}$$

Next, the characteristic equation (3.28a) can be compared with the canonic formulation (3.28b), obtaining the expressions (3.29a) and (3.29b) for the PI regulator gains.

$$\begin{cases} s^2 + k_{p,PLL}s + k_{i,PLL} = 0 & \text{(3.28a)} \\ s^2 + 2\zeta\omega_{bw,PLL}s + \omega_{bw,PLL}^2 = 0 & \text{(3.28b)} \end{cases}$$

where:

- ζ_{PLL} is the desired damping factor;

- $\omega_{bw,PLL}$ is the bandwidth frequency, equal to $2\pi f_{bw,PLL}$ (rad/s).

$$\begin{cases} k_{p,PLL} = 2\zeta\omega_{bw,PLL} & (3.29a) \\ k_{i,PLL} = \omega_{bw,PLL}^2 & (3.29b) \end{cases}$$

where:

- $k_{p,PLL}$ is the proportional gain (1/s);
- $k_{i,PLL}$ is the integral gain ($1/s^2$).

$f_{bw,PLL}$ is imposed to 5 Hz and the damping factor ζ_{PLL} equal to $1/\sqrt{2}$. All PLL parameters are listed in Table 3.4.

Table 3.4 PLL Parameters.

Parameter	Value	Meas. Unit
$f_{bw,PLL}$	5	Hz
ζ_{PLL}	0.707	-
$k_{p,PLL}$	44.4	1/s
$k_{i,PLL}$	987	$1/s^2$

- Voltage Controlled Oscillator gives as output the phase angle θ integrating the frequency. Finally $\sin(\theta)$ and $\cos(\theta)$ are calculated and used as feedbacks to perform the rotation transformation.

This is the working principle of the standard PLL. Others and more complex structures exists in literature. The main disadvantage of this solution is the negative impact on the dynamic of the total system. Nevertheless, for many VSMs it is essential.

3.2.2 Power-based Synchronization

The Power-based synchronization is an alternative grid synchronization method based on the power-synchronization mechanisms of conventional SMs. [78] proposed for the first time in the literature a Power Synchronization Loop (PSL) method to overcome the limitation of a PLL.

The reference circuit is the one depicted in Fig. 3.4, assuming the two voltage sources as two synchronous machines, named in this subsection M1 (operating as generator) and M2 (operating as motor).

Starting from the steady-state operation, the transferred active power from M1 to M2 is described by (3.9). Imaging to increase the mechanical torque of M1 and going back to the previous value, the M1 will accelerate, by increasing the speed and so the rotor angle according to the swing equation (3.1). Therefore, the relative angle δ between $\overline{E}$ and $\overline{V}$ of Fig. 3.4 will increase, with a consequent increase of the active power delivered from M1 to M2. Looking at the swing equation for M2 (with the opposite signs because it operates as motor), this translates in an increase of the electric power, and so in the rotor angle and in the decrease of the relative angle δ. Therefore, after a transient, the two machines will rotate again at the same speed and will go back to the previous steady-state operation. This mechanism can be adopted as a synchronization method for grid-connected converters which emulate the mechanism of a synchronous machine connected to the main grid. However, not all the VSMs employ a power-based synchronization method. The method is described in the following and the following section will highlight which VSMs are PLL-based or power-based.

The power-based synchronization method of a grid-tied converter consists of activating the VSM algorithm before the PWM modulation enabling. Therefore, the virtual machine starts to synchronize to the grid in a similar way of a PLL. From the measured voltage, the electrical emulation block of the VSM creates the virtual currents. From the measured voltage and the virtual current, it is possible to retrieve the virtual power. This is used as feedback of the swing equation. The machine starts from a steady-state condition in which the speed is initialized to the nominal frequency value of the grid and an angle set to zero. As the starting angle position will be different from the angle of the measured voltage, the virtual current and so the virtual power will not be zero. However, the reference power of the swing equation is set to zero. Therefore, there will be a transient in which the swing equation will move the speed and so the angle to null the error between the virtual reference power and the virtual power as shown in Fig. 3.9. This transient happens while PWM modulation of the converter is disabled, as for a PLL. Therefore, this process is virtual and does not involve a real exchange of power with the grid. As soon as the virtual power error and the frequency derivative are equal to zero, the virtual machine and so the converter are synchronized to the grid (i.e., the VSM successfully tracked the grid frequency and angle). The PWM modulation can be enabled with no inrush currents similarly to the PLL-based synchronization. Fig. 3.9 shows the instance of PWM modulation enabling ($t = 1.7$ s) with a negligible current injection for a 15 kVA

inverter. This method is not adopted by all the VSMs because several VSMs available in the literature use the real measured power as feedback. Therefore, they need a PLL to synchronize to the grid, because they do not feature a virtual power feedback, which is essential for a power-based synchronization method.

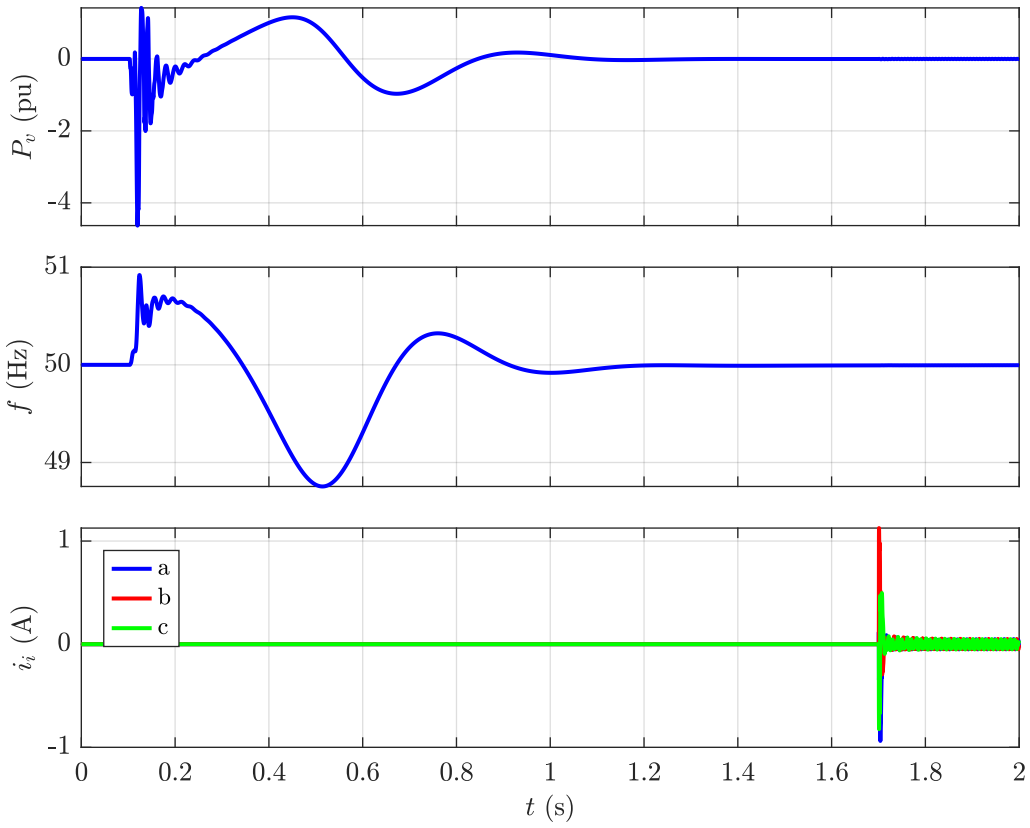

Fig. 3.9 Power-based synchronization example. From top to bottom: virtual power P_v (pu); virtual speed f (Hz); real inverter current (A).

3.3 Review of the VSM models

3.3.1 VISMA

VISMA is a model proposed for the first time in 2007 by Hans-Peter Beck and Ralf Hesse [52, 53, 65]. This solution fully emulates the behaviour of a synchronous generator (SG). It indeed implements the complete electromechanical model of a SG. The general structure is shown in Fig. 3.10.

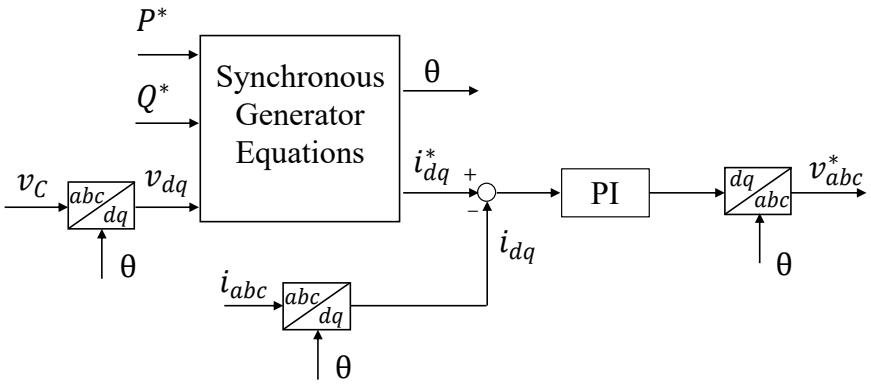

Fig. 3.10 Control scheme of the VISMA model in the Laplace domain [65].

It can be noted that this model belongs to the voltage-input current-output category. Starting from the external active and reactive power references (respectively P^* and Q^*) and the measured phase voltage $\overline{v}_C$, the VISMA model creates the current references on the (d,q) reference frame through the synchronous generators equations. Then, a conventional PI regulator is used to retrieve the voltage reference $\overline{v}^*_{dq}$. Finally, by means of the Park Transformation, the three phase voltage reference $\overline{v}^*_{abc}$ is obtained . The angle θ used for the Park Transformation is the angular position of VISMA.

All the following equations are expressed in pu, in the (d,q) reference frame and in the Laplace domain. The synchronization with the grid is actuated by means of PLL, as described in the subsection 3.2.1.

The first block on analysis is shown in Fig. 3.11. It is realized combining the electrical and the magnetic stator equations of a conventional synchronous generator, including the presence of damper windings.

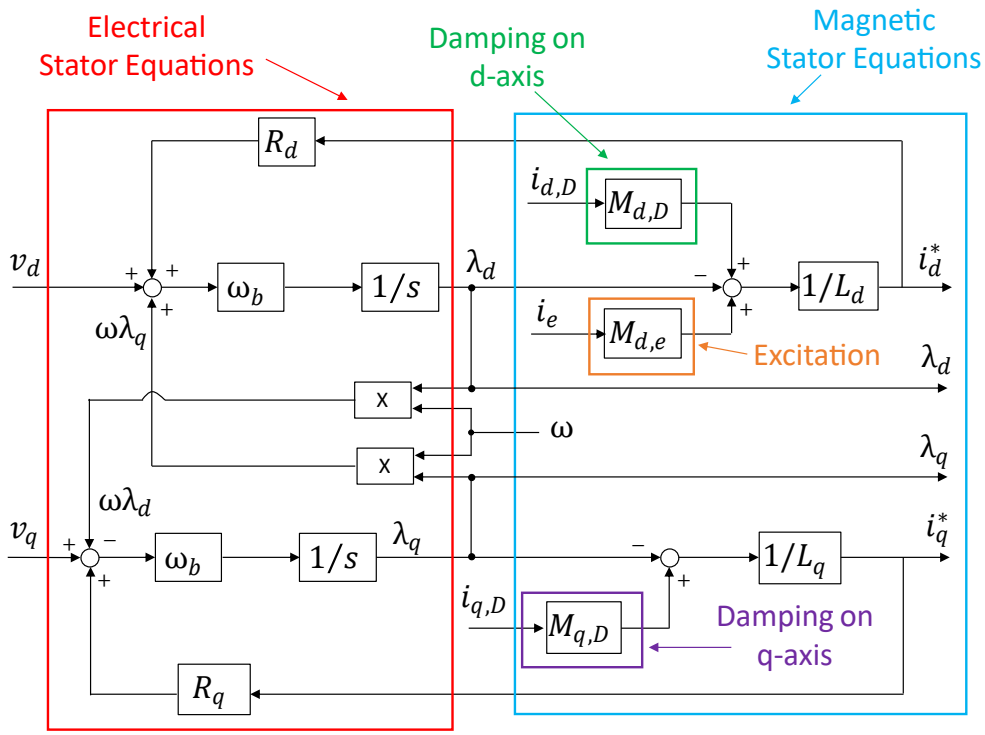

Fig. 3.11 VISMA control scheme in the Laplace domain: stator windings [65].

Next, the reference current can be retrieved through the magnetic equations:

$$\begin{cases} i_d^* = \dfrac{1}{L_d} \cdot (M_{d,D} i_{d,D} + M_{d,e} i_e - \lambda_d) & \text{(3.30a)} \\ i_q^* = \dfrac{1}{L_q} \cdot (M_{q,D} i_{q,D} - \lambda_q) & \text{(3.30b)} \end{cases}$$

where:

- i_d^* is the stator current reference on the d-axis (pu);
- i_q^* is the stator current reference on the q-axis (pu);
- λ_d is the stator flux linkage on the d-axis (pu);
- λ_q is the stator flux linkage on the q-axis (pu);
- L_d is the stator inductance on the d-axis (pu);
- L_q is the stator inductance on the q-axis (pu);
- i_e is the current of the excitation winding on the d-axis (pu);

- $i_{d,D}$ is the current of the damper winding on the d-axis (pu);
- $i_{q,D}$ is the current of the damper winding on the q-axis (pu);
- $M_{d,e}$ is the mutual inductance between the stator winding and the excitation winding on the d-axis (pu);
- $M_{d,D}$ is the mutual inductance between the stator winding and the damper winding on the d-axis (pu);
- $M_{q,D}$ is the mutual inductance between the stator winding and the damper winding on the q-axis (pu).

The virtual fluxes are calculated using the electrical equations:

$$\begin{cases} \lambda_d = \dfrac{1}{s} \cdot \omega_b \cdot (v_d + R_d i_d^* + \omega \lambda_q) & \text{(3.31a)} \\ \lambda_q = \dfrac{1}{s} \cdot \omega_b \cdot (v_q + R_q i_q^* - \omega \lambda_d) & \text{(3.31b)} \end{cases}$$

where:

- v_d is the measured voltage on the d-axis (pu);
- v_q is the measured voltage on the q-axis (pu);
- R_d is the stator resistance on the d-axis (pu);
- R_q is the stator resistance on the q-axis (pu);
- ω is the speed of VISMA (pu);
- ω_b is the base value of speed (rad/s).

The Laplace block schemes for the damper windings are proposed in Fig. 3.12.

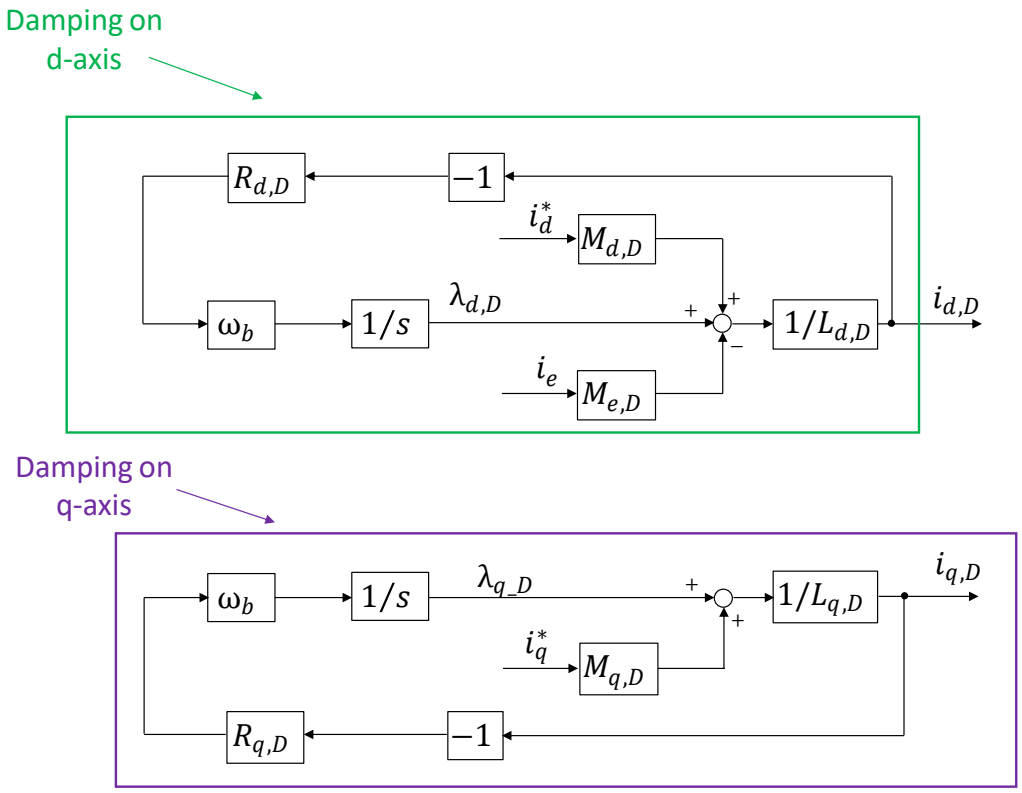

Fig. 3.12 VISMA control scheme in the Laplace domain: damper winding on the d-axis (top) and q-axis (bottom) [65].

The damping current on the d-axis $i_{d,D}$ is retrieved by combining the electrical equation and the magnetic equation of the damper winding on the d-axis, respectively written as (3.32a) and (3.32b):

$$\begin{cases} \lambda_{d,D} = \dfrac{1}{s} \cdot \omega_b \cdot (-R_{d,D} i_{d,D}) & \text{(3.32a)} \\ i_{d,D} = \dfrac{1}{L_{d,D}} \cdot (\lambda_{d,D} + M_{d,D} i_d^* - M_{e,D} i_e) & \text{(3.32b)} \end{cases}$$

where:

- $\lambda_{d,D}$ is the flux linkage of the damper winding on d-axis (pu);
- $R_{d,D}$ is the resistance of the damper winding on d-axis (pu);
- $L_{d,D}$ is the inductance of the damper winding on d-axis (pu);
- $M_{e,D}$ is the mutual inductance between the excitation winding and the damper winding on the d-axis (pu).

The same considerations are valid for the damping current on the q-axis $i_{q,D}$, where the electrical and the magnetic equations are respectively (3.33a) and (3.33b):

$$\begin{cases} \lambda_{q,D} = \dfrac{1}{s} \cdot \omega_b \cdot (-R_{q,D} i_{q,D}) & \text{(3.33a)} \\ i_{q,D} = \dfrac{1}{L_{q,D}} \cdot (\lambda_{q,D} + M_{q,D} i_q^*) & \text{(3.33b)} \end{cases}$$

where:

- $\lambda_{q,D}$ is the flux linkage of the damper winding on q-axis (pu);
- $R_{q,D}$ is the resistance of the damper winding on q-axis (pu);
- $L_{q,D}$ is the inductance of the damper winding on q-axis (pu).

The last variable of interest is the excitation current i_e. It is the output of the excitation block of Fig. 3.14. The VISMA model has an excitation part different from the other solutions, because it is the only model which aims to completely emulate the behaviour of a synchronous generator. It is proposed in Fig. 3.13.

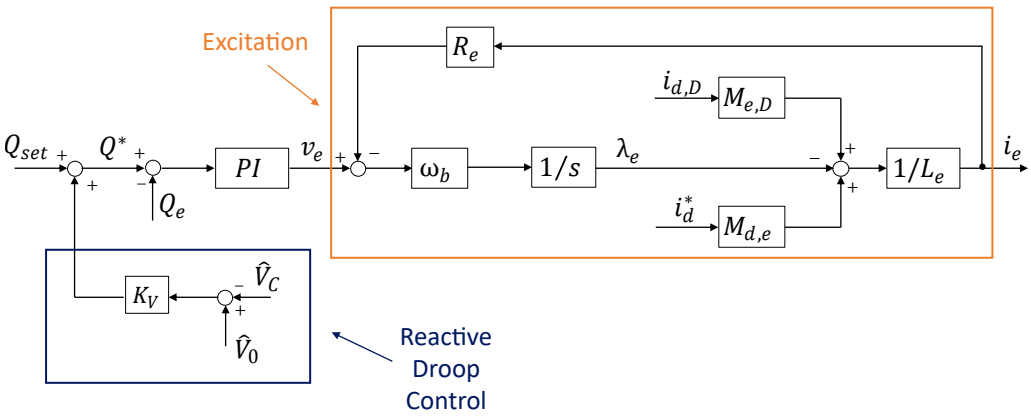

Fig. 3.13 VISMA control scheme in the Laplace domain: excitation winding [65].

The excitation system embeds a reactive power controller, which is based on a PI regulator. It uses the error between the reactive power reference Q^* and the virtual reactive power Q_e to retrieve the excitation voltage v_e.

Next, the virtual reactive power is computed as follows:

$$Q_e = v_q \cdot i_d^* - v_d \cdot i_q^* \tag{3.34}$$

The reactive power reference Q^* is obtained by the sum of two terms:

$$Q^* = Q_{set} + \Delta Q_d \tag{3.35}$$

where:

- Q_{set} is the external reactive power reference (pu);
- ΔQ_d is the reactive droop term in pu, obtained as follows:

$$\Delta Q_d = K_v(\widehat{V}_0 - \widehat{V}_C) \tag{3.36}$$

where:

- $\widehat{V}_0$ is the voltage reference amplitude (pu);
- K_v is the reactive droop coefficient (pu).

Then, the excitation current i_e is obtained by combining the electrical and the magnetic equations of the excitation winding. The two equations are respectively (3.37a) and (3.37b):

$$\begin{cases} \lambda_e = \dfrac{1}{s} \cdot \omega_b \cdot (-R_e i_e) & \text{(3.37a)} \\ i_e = \dfrac{1}{L_e} \cdot (M_{d,e} i_d^* + M_{e,D} i_{d,D} - \lambda_e) & \text{(3.37b)} \end{cases}$$

where:

- λ_e is the flux linkage of the excitation winding (pu);
- R_e is the resistance of the excitation winding (pu);
- L_e is the inductance of the excitation winding (pu).

This review completes the electromagnetic model of VISMA. The last part is the mechanical part, shown in Fig. 3.14.

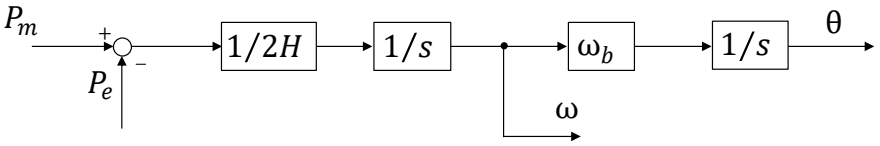

Fig. 3.14 VISMA control scheme in the Laplace domain: swing equation [65].

The mechanical part of the VISMA is characterized by the typical swing equation in per unit without the damping term as in (3.2):

$$P_m - P_e = 2Hs\omega \tag{3.38}$$

where P_e is the virtual active power obtained by equation (3.39) in pu:

$$P_e = v_d \cdot i_d^* + v_q \cdot i_q^* \tag{3.39}$$

The damping term of the swing equation is used to take the effect of damper windings into account. In this case it is not necessary, thanks to the presence of the damper windings [7]. The swing equation gives as output the VISMA speed ω and its angular position θ. The former is used to define the electromotive terms $\omega\lambda_d$ and $\omega\lambda_q$ of the previous equations. The latter allows to perform the Park Transformation [65].

3.3.2 VISMA I

VISMA I is a simplified version of VISMA, designed in 2011 [54, 65]. Its block scheme is depicted in Fig. 3.15.

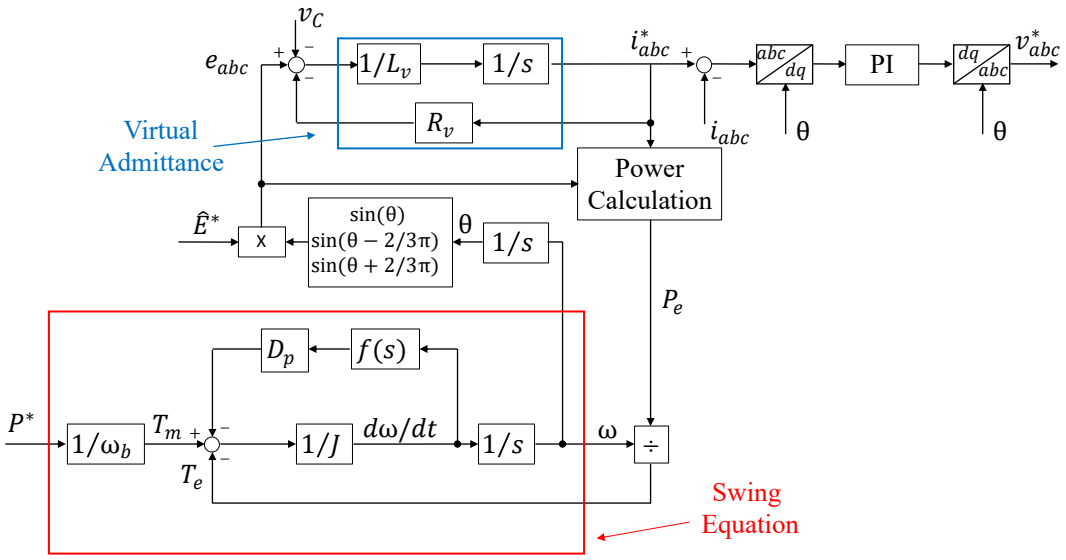

Fig. 3.15 Control scheme of the VISMA I model in the Laplace domain [65].

VISMA I is grid-following VSM. In the version proposed in the literature, a hysteresis regulator is used to retrieve the commands for the inverter. This kind of control introduces not negligible noise, therefore it has been decided to implement VISMA I using the conventional PI regulator designed for all grid-following converters. The synchronization with the grid is actuated through a PLL.

As stated before, this is a simplified version of the VISMA model. Therefore, it does not embed all the equations of a synchronous generator. Three main blocks can be distinguished: the active part, the reactive part and the virtual impedance block.

The active part consists of a slight different form of the swing equation described in (3.4) in terms of torque:

$$T_m - T_e = J\frac{d\omega}{dt} + k_d f(s)\frac{d\omega}{dt} \tag{3.40}$$

where:

- T_m represents the mechanical torque, simulating the mechanical torque of a primary motor used in conventional synchronous generators;
- T_e is the virtual torque;

- $f(s)$ is the phase compensation term, defined as follows:

$$f(s) = \frac{1}{1 + s\tau} \tag{3.41}$$

  where $f(s)$ represents a low pass filter with a time constant τ. In this case the feedback in the swing equation is not the speed but its derivative.

The speed of VISMA I ω is retrieved from the swing equation and the angular position θ is obtained by integrating the speed.

TO facilitate the comparison with the other solutions, this model has been implemented in terms of powers instead of torques:

$$\begin{cases} P_m = \dfrac{\omega T_m}{S_b} & \text{(3.42a)} \\ P_e = \dfrac{\omega T_e}{S_b} & \text{(3.42b)} \end{cases}$$

where the virtual active power in pu P_e can be computed as follows:

$$P_e = v_\alpha \cdot i_\alpha^* + v_\beta \cdot i_\beta^* \tag{3.43}$$

Next, the excitation block of VISMA I is shown in Fig. 3.16.

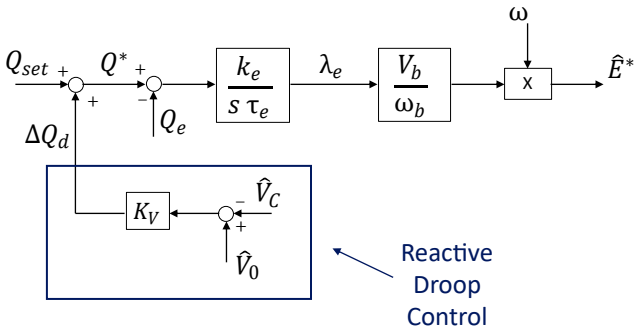

Fig. 3.16 VISMA I excitation block [65].

This block embeds a reactive power controller in per unit. It provides the error between Q^* (the reactive power reference) and Q_e (the virtual reactive power) to a pure integrator, in order to retrieve the amplitude of the electromotive force $\widehat{E}$ of VISMA I. The pure integrator is characterized by a gain k_e and an excitation time constant τ_e. The values are listed in Table 3.3.

A reactive droop control is also implemented. The reference Q^* is defined by the sum of the external reactive reference Q_{set} and the reactive droop term ΔQ_d as in (3.36).

With the electromotive force amplitude $\widehat{E}^*$ and the angular position θ, the three phase electromotive force $\overline{e}_{abc}$ can be retrieved. Finally, the current reference $\overline{i}^*_{abc}$ is retrieved as the voltage drop on the virtual admittance, calculated from the difference between the electromotive force $\overline{e}_{abc}$ and the phase voltage $\overline{v}_C$ over the virtual admittance:

$$\overline{i}^*_{abc} = \frac{\overline{e}_{abc} - \overline{v}_C}{R_v + sL_v} \tag{3.44}$$

3.3.3 VISMA II

VISMA II is the grid-forming version of the VISMA I, proposed in [56, 65]. The control scheme in the Laplace domain is proposed in Fig. 3.17.

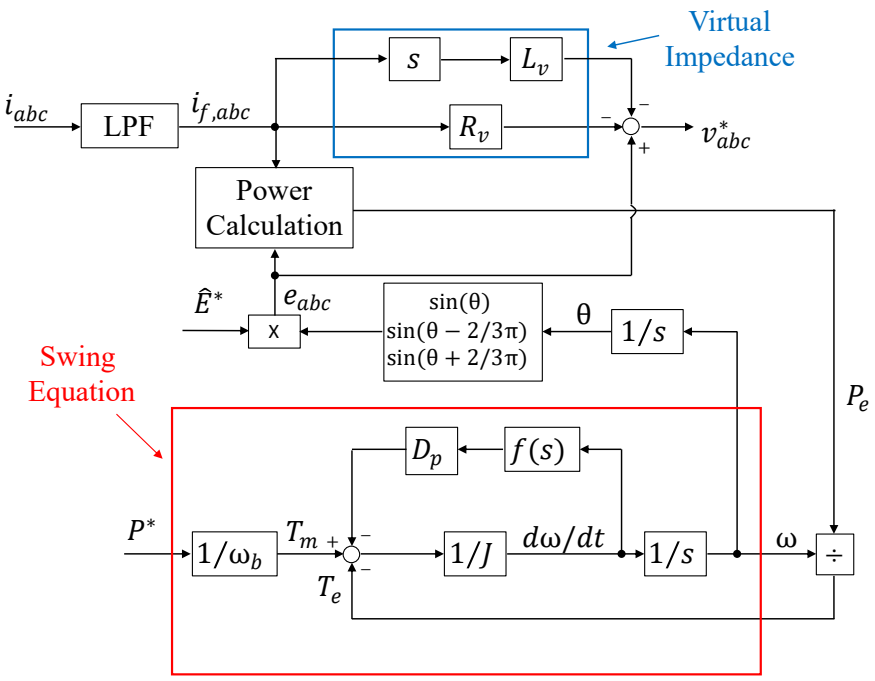

Fig. 3.17 Control scheme of the VISMA II model in the Laplace domain [65].

As a grid-forming VSM, VISMA II directly produces the voltage reference $\overline{v}^*_{abc}$ for the PWM modulator. VISMA I and VISMA II show several common elements. Also for VISMA II the synchronization with the grid is performed through a PLL.

VISMA II consists of by three blocks: active part, reactive part and virtual impedance block.

The active part implements the swing equation in terms of torque as the VISMA I model:

$$T_m - T_e = J\frac{d\omega}{dt} + k_d f(s)\frac{d\omega}{dt} \tag{3.45}$$

As VISMA I, even this model has been implemented in terms of powers in pu and no torques:

$$\begin{cases} P_m = \dfrac{\omega T_m}{S_b} & \text{(3.46a)} \\ P_e = \dfrac{\omega T_e}{S_b} & \text{(3.46b)} \end{cases}$$

where P_e in pu can be computed by means of the following equation:

$$P_e = i_\alpha \cdot v_\alpha^* + i_\beta \cdot v_\beta^* \tag{3.47}$$

Virtual active power P_e is computed using the voltage references $\overline{v}_{\alpha\beta}^*$ and the measured inverter current $\bar{i}_{\alpha\beta}$ in the (α, β) reference frame.

Also for the reactive part, all the concepts described for VISMA I are valid for VISMA II. The excitation block of VISMA II is proposed in Fig. 3.18.

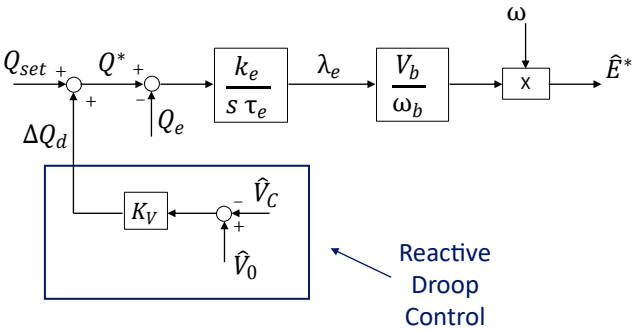

Fig. 3.18 VISMA II excitation block [65].

A reactive power controller is used to obtain the electromotive force amplitude $\widehat{E}^*$. To do this, the reactive power reference Q^* is compared with the virtual reactive power Q_e. The error goes through a pure integrator which gives $\widehat{E}$ as output. The values of the

gain k_e and the excitation time constant τ_e are listed in Table 3.3. Even in this case, the reactive droop control is embedded. Q^* is defined by summing the external reactive power Q_{set} and the reactive droop term ΔQ_d, defined as in (3.36).

With the amplitude $\widehat{E}^*$ and the angular position θ the three phase electromotive force $\overline{e}_{abc}$ can be retrieved.

As VISMA II is a grid-forming model, the connection between this kind of VSM and the PCC is performed as described in the subsection 3.1.2. But, differently from Synchronverter base form and Osaka, the electromotive force $\overline{e}_{abc}$ does not correspond to the voltage reference $\overline{v}^*_{abc}$. In fact, there is an additional stage constituted by the virtual stator impedance. In this case, the inverter current is measured and the virtual voltage drop on the virtual impedance can be computed. However, a derivation of the current must be performed. This operation strongly amplifies the noise of the measure. Therefore, it is necessary to filter the current before using it in the control. The filter is a lows pass filter with the following transfer function:

$$LPF(s) = \frac{1}{1 + s/\omega_f} \tag{3.48}$$

where ω_f is the cut-off frequency of the filter (rad/s).

Finally, the voltage reference $\overline{v}^*_{abc}$ can be obtained as follows:

$$\overline{v}^*_{abc} = \overline{e}_{abc} - (R_v + sL_v) \cdot \overline{i}_{abc} \tag{3.49}$$

Finally, the second main problem of VISMA II can be highlighted. As the voltage reference $\overline{v}^*_{abc}$ is directly provided to a PWM modulator, in open loop control, the currents are measured but not controlled. Therefore, there is no current limitation system. Additional blocks must be implemented to perform a safe and reliable saturation [65].

3.3.4 Synchronverter

Base version of Synchronverter

The Synchronverter is a solution proposed in 2009 by Qing-Chang Zhong and George Weiss [46, 47]. The control scheme is proposed in Fig. 3.19. The scheme is built in absolute values.

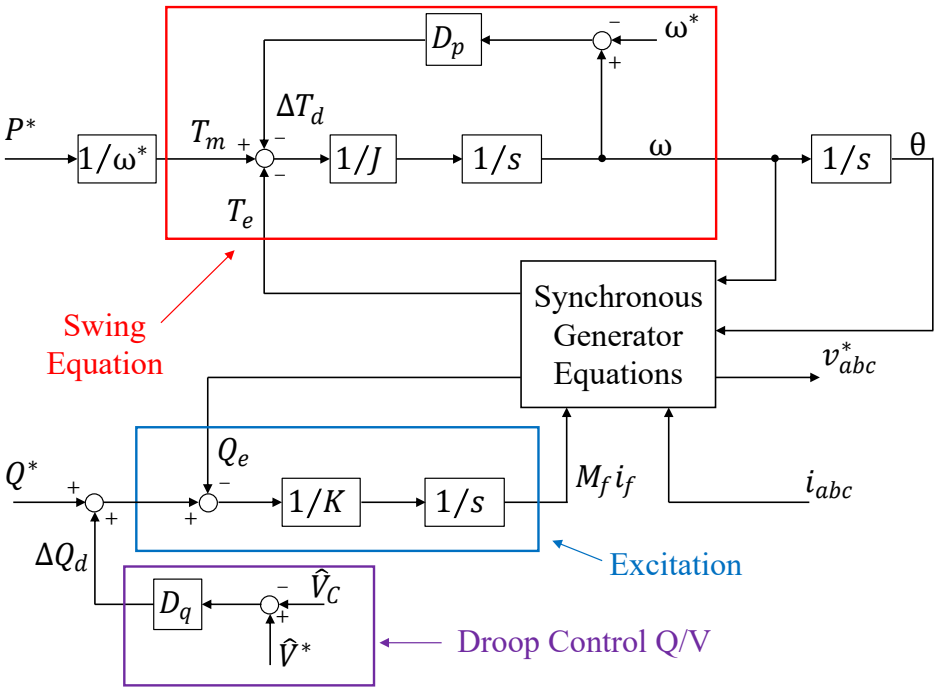

Fig. 3.19 Synchronverter control scheme for the base version in the Laplace domain.

The Synchronverter is a grid-forming VSM: starting from the measure of inverter currents, the voltage references are calculated and provided to the PWM modulator. There are neither closed-loop current control nor closed-loop voltage control. Therefore, there is no current saturation system and it is necessary to implement additional blocks to limit currents. A grid synchronization process is needed and the PLL is employed for this purpose.

The main part of this structure is the Synchronous Generator Equations block, which contains the electromechanical equations of the synchronous generator:

$$\begin{cases} T_e = M_f i_f \cdot \langle \bar{i}_{abc}, \widetilde{\sin(\theta)} \rangle & \text{(3.50a)} \\ Q_e = -\omega \cdot M_f i_f \cdot \langle \bar{i}_{abc}, \widetilde{\cos(\theta)} \rangle & \text{(3.50b)} \\ \bar{v}^*_{abc} = \omega \cdot M_f i_f \cdot \widetilde{\sin(\theta)} & \text{(3.50c)} \end{cases}$$

where:

- $\bar{i}_{abc}$ is the three phase inverter current (A);
- $\widetilde{\sin\theta}$ and $\widetilde{\cos\theta}$ are the vectors:

$$\widetilde{\sin\theta} = \begin{bmatrix} \sin(\theta) \\ \sin\left(\theta - \frac{2\pi}{3}\right) \\ \sin\left(\theta + \frac{2\pi}{3}\right) \end{bmatrix} \quad , \quad \widetilde{\cos\theta} = \begin{bmatrix} \cos(\theta) \\ \cos\left(\theta - \frac{2\pi}{3}\right) \\ \cos\left(\theta + \frac{2\pi}{3}\right) \end{bmatrix} \tag{3.51}$$

where $\langle \cdot, \cdot \rangle$ denotes the conventional inner product in $\mathbb{R}^3$;

- $M_f i_f$ is the excitation flux linkage (Vs);
- T_e is the virtual torque (Nm);
- ω is the virtual speed (rad/s);
- Q_e is the virtual reactive power (var);
- $\overline{v}^*_{abc}$ is the three phase reference voltage (V).

The mechanical part of Synchronverter is based on the complete swing equation written in terms of torque and not power. In the Laplace domain it is written as follows:

$$T_m - T_e = Js\omega + D_p \cdot (\omega - \omega_r) \tag{3.52}$$

where T_m is the virtual mechanical torque, expressed in Nm. It is calculated as the real power setpoint P_{set} coming from the source and the speed, assumed equal to the reference speed ω_r. Next, D_p is the damping factor, expressed in $\text{kg} \cdot \frac{\text{m}^2}{\text{s}}$. The damping torque is defined as follows:

$$\Delta T_d = D_p \cdot (\omega - \omega_r) = D_p \cdot \Delta\omega \tag{3.53}$$

Its main role is to provide damping to the electromechanical part. Moreover, it actually behaves as a frequency droop coefficient. It means that Synchronverter solution inherently embeds frequency droop control, but the coefficient is strictly dependent on the damping effect and the vice versa is also true: there is a coupling between the droop control and the damping factor. The relationship between the damping factor D_p and the damping coefficient in per unit k_d is:

$$D_p = \frac{k_d S_b}{\omega_b^2} \tag{3.54}$$

Then, the speed of the Synchronverter is retrieved from the swing equation and it is integrated to retrieve the angular position θ.

The last portion of the scheme regards the reactive one. It consists of two parts: Droop Control Q/V and Excitation. The first one embeds the voltage droop control as in (3.55):

$$\Delta Q_d = D_q \cdot (\widehat{V}^* - \widehat{V}_{PLL}) \tag{3.55}$$

where:

- D_q is the reactive droop coefficient (var/V);
- $\widehat{V}^*$ is the voltage reference amplitude;
- $\widehat{V}_C$ is the measured voltage amplitude (V).

The reactive power reference is defined by the sum of ΔQ_d and the external power Q_{set}:

$$Q^* = Q_{set} + \Delta Q_d \tag{3.56}$$

The second part is based on a pure integrator and it is used to retrieve the excitation virtual flux, starting from the difference between the reference Q^* and Q_e:

$$M_f i_f = \frac{1}{s} \cdot \frac{1}{K} (Q^* - Q_e) \tag{3.57}$$

Here, K is the inverse of K_{ecc} of Equation (3.21), expressed in the absolute form [65].

Enhanced version of Synchronverter

An enhanced version of Synchronverter is proposed [49, 65]. Its control scheme is shown in Fig. 3.20.

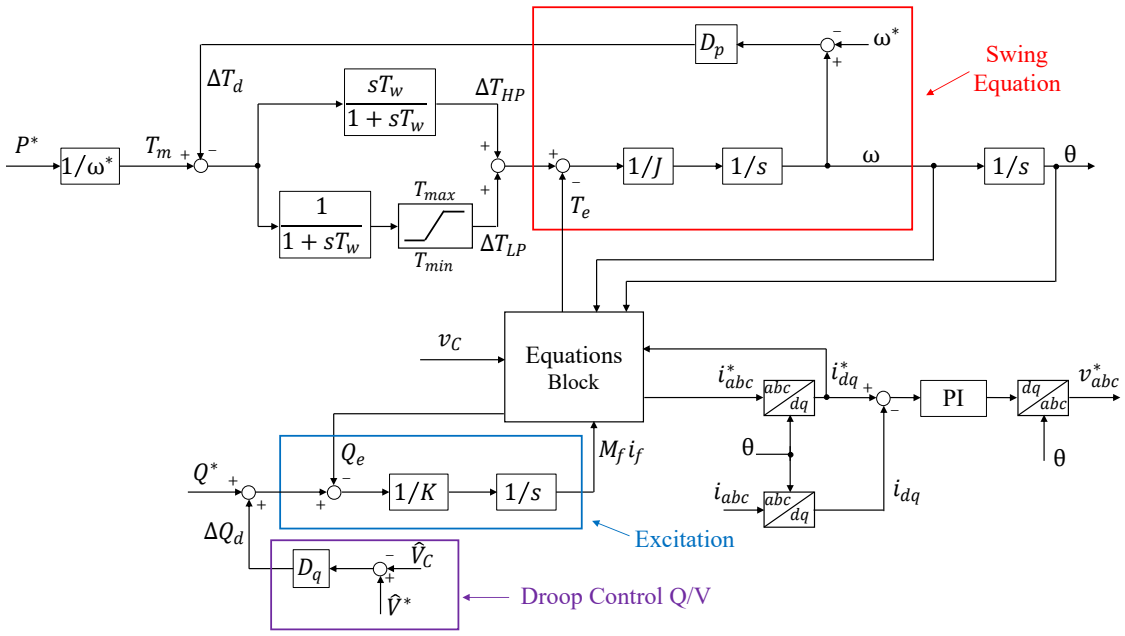

Fig. 3.20 Synchronverter control scheme for the enhanced version in the Laplace domain [65].

Differently from the base version, this model operates as a grid-following converter. Therefore its output is the current reference $\bar{i}^*_{abc}$. Then, a current regulator is used to control the inverter current. The other difference lies in the synchronization process with the grid. This model can synchronize with the grid on its own, avoiding the employment of the PLL. This is the version used for experimental tests and comparison.

There are some analogies and differences with respect to the base version. The reactive portion of the model (Excitation and Droop Control Q/V) are exactly the same. The active one is, instead, different.

As it can be observed from Fig. 3.20, the difference between the mechanical torque T_m and the damping torque ΔT_d divides into two paths: in the first one the error goes through a high pass filter, whereas in the second one there is a low pass filter. Then, the sum between these two contributions is compared to the virtual torque T_e and the conventional swing equation block can be completed. The other difference lies in the Equations Block, which substitutes the Synchronous Generator Equations block. It includes:

- the Park Transformation used to transform the phase voltage $\bar{v}_C$ in the $\bar{v}_{dq}$ on the rotating reference frame (d, q);

- the computation of the virtual torque T_e, the virtual reactive power Q_e and electromotive force $\overline{e}_{abc}$:

$$\begin{cases} T_e = -M_f i_f \cdot i_q^* & \text{(3.58a)} \\ Q_e = \dfrac{3}{2}(v_q i_d^* - v_d i_q^*) & \text{(3.58b)} \\ \overline{e}_{abc} = \omega \cdot M_f i_f \cdot \widetilde{\sin(\theta)} & \text{(3.58c)} \end{cases}$$

- the virtual impedance implementation to calculate the reference current $\overline{i}_{abc}^*$. The difference between the electromotive force $\overline{e}_{abc}$ and the measured phase voltage $\overline{v}_C$ is the voltage drop on the virtual impedance. The reference is therefore equal to:

$$\overline{i}_{abc}^* = \frac{1}{R_v + sL_v} \cdot (\overline{e}_{abc} - \overline{v}_{C,abc}) \tag{3.59}$$

To facilitate the comparison with the other solutions, the results will be provided in terms of powers in per unit and no torque using the following relationships:

$$\begin{cases} P_m = \dfrac{\omega T_m}{S_b} & \text{(3.60a)} \\ P_e = \dfrac{\omega T_e}{S_b} & \text{(3.60b)} \end{cases}$$

3.3.5 Osaka

The Osaka model is a VSM realized in 2011 [50, 51, 65]. Fig. 3.21 shows its control block scheme.

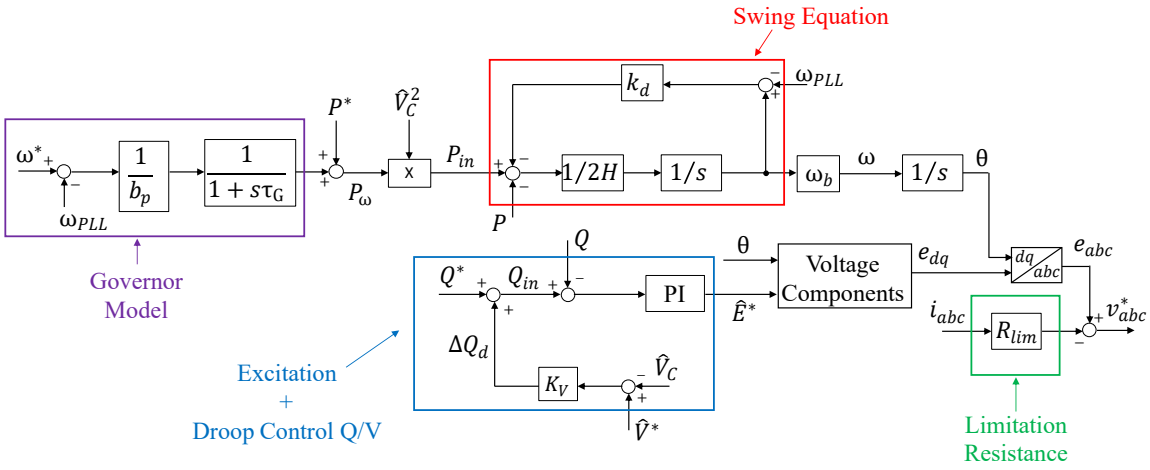

Fig. 3.21 Osaka's control scheme in Laplace domain [65].

The Osaka model is a grid-forming VSM as it imposes its virtual electromotive as voltage reference. The main blocks are: Governor Model, Swing Equation and Excitation + Droop Control Q/V. They are expressed in pu.

The first block on analysis is the Governor Model. This block performs the primary frequency regulation. It compares the reference frequency ω^* with the PLL frequency ω_{PLL}. The error is divided by the droop coefficient Δ and then it goes through a low pass filter, obtaining the droop active power reference P_ω:

$$P_\omega = \frac{K_d}{1 + sT_d} \cdot \frac{1}{\Delta} \cdot (\omega^* - \omega_{PLL}) \tag{3.61}$$

where:

- K_d is the gain of the low pass filter (pu);
- T_d is the time constant of the low pass filter (pu).

Then, the active power reference P_{in} can be computed taking also in account the dependence on the measured voltage, as shown in (3.62) [50]:

$$P_{in} = \widehat{V}_{PLL}^2 \cdot (P_\omega + P_L) \tag{3.62}$$

where:

- P_L is the external active power reference (pu);

- $\widehat{V}_C$ is the measured voltage amplitude (pu).

The successive block consists of the swing equation in pu already seen in (3.4) and written in the Laplace domain.

$$P_{in} - P_{out} = 2Hs \cdot \omega_m + k_d \cdot \Delta\omega \tag{3.63}$$

Here, P_{out} is the real measured active power (pu). The damping term $k_d \cdot \Delta\omega$ is obtained as follows:

$$k_d \cdot \Delta\omega = k_d(\omega_m - \omega_{PLL}) \tag{3.64}$$

where ω_{PLL} is the PLL frequency in pu. The Osaka model features indeed a PLL-based damping.

The swing equation gives as output the Osaka's speed ω_m which is integrated to retrieve the position θ_m. This is the first piece of the model needed to create the voltage references. The other one is the electromotive force amplitude $\widehat{E}^*$. It its obtained by the Excitation+Droop Control Q/V block.

The reactive power reference Q_{in} is obtained as the combination of two terms:

$$Q_{in} = Q_L + \Delta Q_d \tag{3.65}$$

where:

- Q_L is the external reactive power reference (pu);
- ΔQ_d is the reactive droop term in pu as calculated for the previous VSMs:

$$\Delta Q_d = K_v(\widehat{V}_0 - \widehat{V}_C) \tag{3.66}$$

The Excitation block is built using a PI regulator, which receives the error between the reactive power reference Q_{in} and the measured power Q_{out}. Its output is $\widehat{E}^*$. The integral gain is equal to K_{ecc} of Table 3.3, whereas the proportion gain is experimentally tuned.

With the electromotive force amplitude $\widehat{E}^*$ and the angular position θ_m, the electromotive force vector $\overline{e}_{dq}$ can be created. Using Park Transformation, it is converted in

the three phase vector $\overline{e}_{abc}$.
Finally, the three phase reference voltage $\overline{v}^*_{abc}$ is calculated as follows:

$$\overline{v}^*_{abc} = \overline{e}_{abc} - R_{lim}\overline{i}_{abc} \tag{3.67}$$

where:

- $\overline{i}_{abc}$ is three phase measured current (A);
- R_{lim} is a virtual resistance which can be tune to reduce the inrush currents (Ω) [65].

3.3.6 SPC

The SPC is a grid-following VSM proposed by Abengoa Research in 2011 [57, 79, 65]. The block scheme is shown in Fig.3.22.

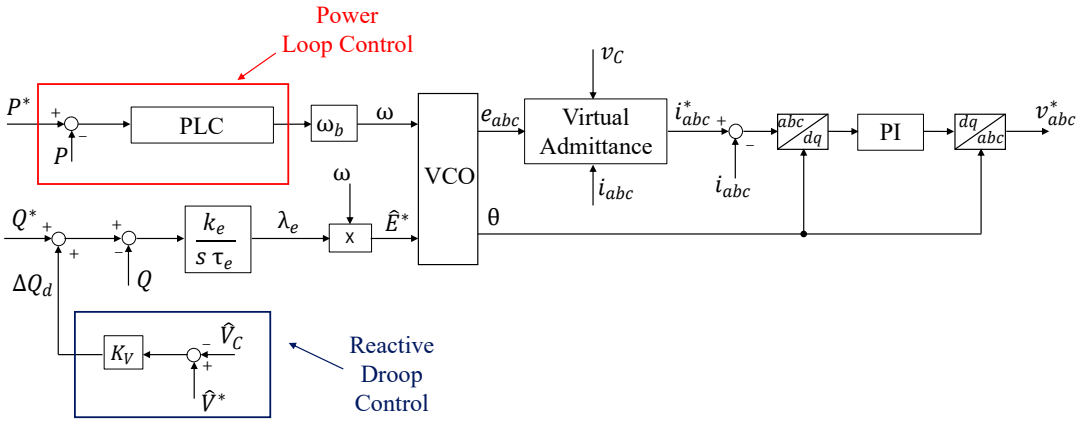

Fig. 3.22 Control scheme of the SPC model in the Laplace domain [65].

The SPC model adopts a power-based method to synchronize with the grid, avoiding the employment of a PLL. The main blocks are: Power Loop Controller (PLC), reactive block, Voltage Controller Oscillator (VCO) and virtual admittance block. All of them are expressed in per unit.

The PLC will be accurately described in the following Section. It provides the virtual speed ω in pu, starting from the difference between the active power reference P^* and the measured active power P in pu. It is computed as follows in the (α, β) reference frame:

$$P = v_\alpha \cdot i_\alpha + v_\beta \cdot i_\beta \tag{3.68}$$

As regards the reactive part, the error between the reactive power reference Q^* and the real reactive power Q feeds a pure integrator. The values for the gain k_e and the excitation time constant τ_e are proposed in Table 3.3. The output of the integrator is the electromotive force amplitude $\widehat{E}^*$. The reactive droop control is also implemented. In fact, the reactive power reference Q^* is obtained by the sum between the external reference Q_{set} and the reactive droop term ΔQ_d. It is obtained as for the other models:

$$\Delta Q_d = K_v(\widehat{V}_0 - \widehat{V}_C) \tag{3.69}$$

The VCO provides two output. The former is the angular position θ of SPC, obtained from the integration of the speed ω. Then, θ and $\widehat{E}^*$ combine to calculate virtual electromotive force $\overline{e}_{abc}$. Next, the current reference $\overline{i}^*_{abc}$ are calculated by multiplying the virtual admittance per the difference between the electromotive force and the measured voltage:

$$\overline{i}^*_{abc} = \frac{1}{R_v + sL_v} \cdot (\overline{e}_{abc} - \overline{v}_C) \tag{3.70}$$

Three different types of Power Loop Controller (PLC) have been studied: Synchronous Generator Emulation, PI Regulator and Lead-Lag [65].

Synchronous Generator Emulation

The first type of PLC on analysis is the Synchronous Generator (SG). Its transfer function is the following:

$$PLC_{SG}(s) = \frac{S_b}{\omega_b} \frac{k\omega_c}{s + \omega_c} \tag{3.71}$$

It is based on the conventional swing equation, already described in (3.4):

$$P^* - P = 2H\frac{d\omega}{dt} + k_d \cdot \Delta\omega \tag{3.72}$$

The block scheme related to (3.72) is shown in Fig. 3.23.

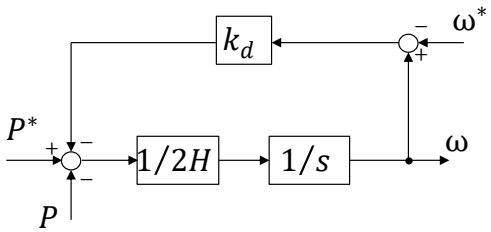

Fig. 3.23 SPC SG: Block scheme of swing equation.

In Fig. 3.23 ω^* is the reference speed (pu).

The transfer function retrievable from the scheme in Fig. 3.23 is:

$$PLC_{SG}(s) = \frac{1}{2Hs + k_d} \tag{3.73}$$

Comparing (3.71) with (3.73), the two coefficients of PLC_{SG} can be calculated:

$$\begin{cases} k = \dfrac{\omega_b}{S_b \cdot k_d} & \text{(3.74a)} \\ \omega_c = \dfrac{k_d}{2H} & \text{(3.74b)} \end{cases}$$

With this kind of PLC, SPC emulates the behaviour of the conventional synchronous generators. There is no dedicated part for the frequency droop control. Therefore, there is a strict coupling between the damping factor k_d and the frequency droop coefficient: the former is one over of the latter. Therefore, when a grid frequency occurs, the SPC SG will inject active power according to the tuning of the damping factor k_d. Next, P^* corresponds to the external reference P_{set}.

PI Regulator

The second type of PLC is a conventional PI regulator. Its transfer function is the following:

$$PLC_{PI}(s) = \frac{S_b}{\omega_b} \frac{k_p s + ki}{s} \tag{3.75}$$

A PI regulator guarantees a reliable active power control, with no steady state error. On the opposite, in case of grid frequency variations, the droop control cannot be actuated. Therefore, an additional dedicated governor model can be added. It is shown in Fig. 3.24.

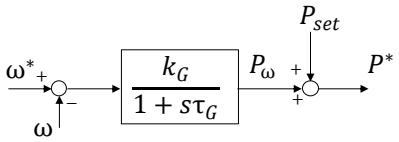

Fig. 3.24 SPC PI's governor.

The governor model performs the active power primary control. It compares the reference frequency ω^* with the SPC frequency ω. The error is multiplied by k_G, which is the inverse of the droop coefficient. It can be arbitrarily tuned. Then, the product goes through a low pass filter obtaining the active droop term P_ω. The filter has a time constant τ_G and it is used to avoid abrupt variations of active power when grid frequency changes.

In this case, P^* is the sum between the external active power reference P_{set} and the active droop term P_ω.

Lead-Lag

The third type of PLC is a Lead-Lag. Its transfer function is the following:

$$PLC_{LL}(s) = \frac{S_b}{\omega_b}\frac{k_p s + ki}{s + k_g} \tag{3.76}$$

This structure guarantees no steady state error as happens for SPC PI. Moreover, it has an additional freedom degree given by k_g. A properly tuning of this parameter leads to the damping-droop decoupling. Therefore, SPC LL can actuate an active droop control, which will depend only on the tuning of k_g. No additional blocks are needed. In this final case, P^* is equal to the external active power reference P_{set}.

3.3.7 VSYNC

The VSYNC model is proposed by M.P.N van Wesenbeeck, S.W.H. de Haan, P. Varela and K. Visscher in 2009 [60, 65]. Fig. 3.25 shows the block control scheme in the Laplace domain.

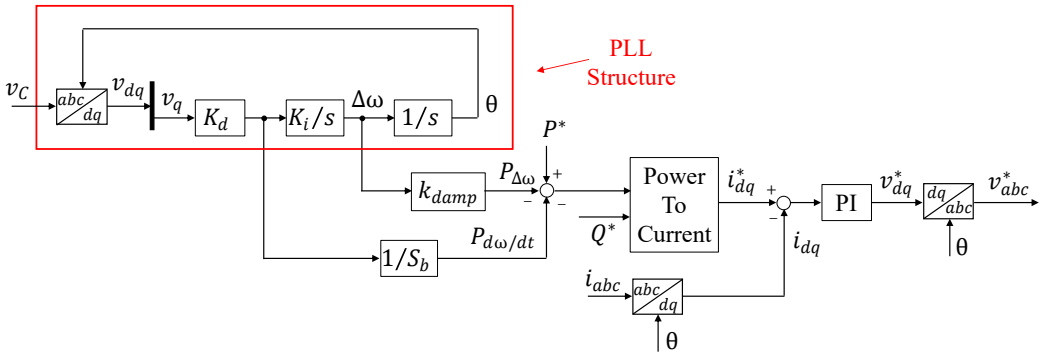

Fig. 3.25 VSYNC control scheme in Laplace domain.

As it can be observed from the control scheme, it is grid-following model. It provides as output the current reference $\bar{i}^*_{dq}$ in the (d, q) reference frame.

VSYNC is a peculiar model because, differently from many other solutions, its core is constituted by a PLL structure, highlighted in red in Fig. 3.25. It can be noticed that there are many elements in common with the conventional structure of PLL, described in Subsection 3.2.1 and shown in Fig. 3.7. Since it is structured based on a PLL architecture, the VSYNC model can synchronize with the grid on its own, without the use of external elements.

Differently from the conventional PLL of Fig. 3.7, this model is built in absolute value and the PI regulator is substituted by a pure integrator, but the working principle is the same. Even here in fact, a synchronization process with the grid is performed. The phase voltage $\bar{v}_C$ is measured and transformed in the vector $\bar{v}_{dq}$ by means of the Park Transformation. The angle used to actuate the rotation and define the (d, q) reference frame is the VSYNC angular position θ_r. The angle δ is defined as the difference between the grid phase voltage θ_g and θ_r. The q-axis component of $\bar{v}_{dq}$ will be:

$$v_q = V_b \sin(\theta_g - \theta) = V_b \sin(\delta) \tag{3.77}$$

where V_b is the base value of voltage.

The component v_q is provided to a pure integrator to retrieve the speed variation $\Delta\omega_r$. Integrating $\Delta\omega_r$, the angular position θ_r is obtained. In steady state, the integrator zeroes the q-axis component v_q and consequently even the difference between the VSYNC angle θ_r and the grid phase θ_g. The synchronization is completed.

VSYNC is based on the PLL structure because a strict analogy between it and the swing equation can be retrieved. The active power reference P^* in per unit can be written as follows:

$$P^* = P_{set} - P_{\Delta\omega} - P_{d\omega/dt} \tag{3.78}$$

where:

- P_{set} is the external reference of active power (pu);
- $P_{\Delta\omega}$ is the inertial term (pu);
- $P_{d\omega/dt}$ is the derivative term (pu).

The two terms $P_{\Delta\omega}$ and $P_{d\omega/dt}$ can be retrieved thanks to the analogy between the swing equation and the PLL structure. The starting point is the conventional swing equation described in (3.2):

$$P^* - P_e = \frac{2HS_b}{\omega_b^2} \cdot \omega \cdot \frac{d\omega}{dt} \tag{3.79}$$

where P_e is the active power flowing from the inverter to the grid.

As in Subsection 3.1.3, a linearized model can be built to define the needed parameters. In the Laplace domain, and assuming $\omega \simeq \omega_b$, (3.79) becomes:

$$\Delta P_e = \frac{2HS_b}{\omega_b} \cdot s\Delta\omega \tag{3.80}$$

Note that ΔP_e in absolute value is obtainable as seen in (3.9), applying the base value S_b:

$$\Delta P_e = \frac{3}{2}\frac{V_b^2}{X_{tot}} \sin(\Delta\delta) \tag{3.81}$$

Substituting (3.77) in (3.81), an alternative form for the active power P_e can be retrieved:

$$\Delta P_e = \frac{3}{2}\frac{V_b}{X_{tot}} \cdot V_b \sin(\Delta\delta) = \frac{3}{2}\frac{V_b}{X_{tot}}\Delta v_q = K_d \Delta v_q \tag{3.82}$$

This first comparison leads to the definition of the gain K_d:

$$K_d = \frac{3}{2}\frac{V_b}{X_{tot}} \tag{3.83}$$

K_d the first gain on the direct chain in Fig. 3.25 expressed in V/Ω. Finally, the derivative term $P_{d\omega/dt}$ in pu is retrieved:

$$P_{d\omega/dt} = \frac{K_d}{S_b} v_q \tag{3.84}$$

From the Fig. 3.25 it can be noticed that:

$$s\Delta\omega = K_i K_d \Delta v_q = K_i \Delta P_e \tag{3.85}$$

Comparing (3.85) with (3.80) the integral gain K_i can be defined:

$$K_i = \frac{\omega_b}{2HS_b} \tag{3.86}$$

Finally the damping term $P_{\Delta\omega}$ can be retrieved as follows:

$$P_{\Delta\omega} = k_{damp}\Delta\omega_r \tag{3.87}$$

where k_{damp} corresponds to k_d of Table 3.2.

As regards the reactive power reference Q^*, no excitation part is implemented. Q^* consists of two contributions: the external reactive power reference Q_{set} and the reactive droop term ΔQ_d. The reactive droop control is used to balance the voltage variation by means of reactive droop term ΔQ_d, as for the other models. The two power references in per unit are used to computed the current reference $\bar{i}^*_{dq}$ in per unit. No active or reactive power loop control is used. The phase voltage $\bar{v}_C$ is measured and transform in $\bar{v}_{dq}$ by

means of Park Transformation, using the VSYNC angular position θ_r. The two current reference components in per unit can be finally computed:

$$\begin{cases} i_d^* = \dfrac{P^* v_d + Q^* v_q}{\sqrt{v_d^2 + v_q^2}} & \text{(3.88a)} \\ i_q^* = \dfrac{P^* v_q - Q^* v_d}{\sqrt{v_d^2 + v_q^2}} & \text{(3.88b)} \end{cases}$$

Then, a conventional PI regulator is used to retrieve the voltage reference $\overline{v}_{dq}^*$. Successively, the three phase voltage reference $\overline{v}_{abc}^*$ is retrieved by means of the Park Transformation [65].

3.3.8 KHI

The Kawasaki Heavy Industries (KHI) is VSM model proposed in 2012 [61, 65]. The block control scheme in the Laplace domain is proposed in Fig. 3.26.

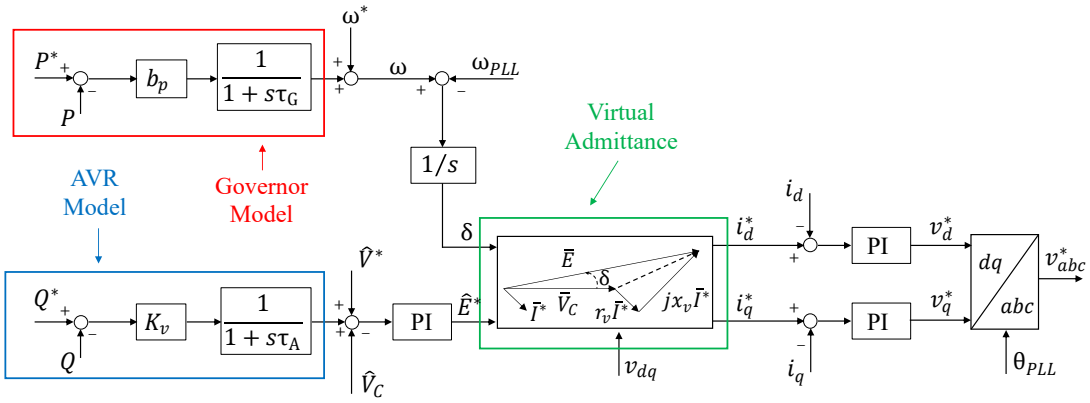

Fig. 3.26 KHI control scheme in Laplace domain [65].

The KHI model is a grid-following VSM, which provides the current reference $\overline{i}_{dq}^*$ in the (d, q) reference frame. The synchronization with the grid is performed by means of PLL, as described in Subsection 3.2.1.

It consists of three main blocks: Governor Model, AVR Model and Virtual Impedance Block. Each of them is implemented in per unit.

The Governor Model compares the reference P^* with the virtual power P_v, computed as follows:

$$P_v = v_d i_d^* + v_q i_q^* \tag{3.89}$$

where v_d and v_q are the components of the measured phase voltage $\overline{v}_C$ transformed in $\overline{v}_{dq}$ by means of Park Transformation. It is performed using the PLL phase angle θ_{PLL}.

The active power error is multiplied by the active droop coefficient K_{gd} and then it goes through a low pass filter characterized by an unitary gain and a time constant T_{gd}. The output is the frequency variation $\Delta\omega_{gd}$ related to the active power error. When a grid frequency variation occurs, the KHI model can inject active power according to the tuning of K_{gd}. Then, the sum between the frequency variation $\Delta\omega_{gd}$ and the reference frequency ω^* defines the KHI frequency ω_R.

The electromotive force $\overline{e}_{abc}$ and the measured phase voltage $\overline{v}_{C,abc}$ can be respectively expressed as the rotating vectors $\overline{E}$ and $\overline{V}_C$. Moreover, the angle between them is denoted as δ. By integrating the difference between the virtual frequency ω_R and the PLL frequency ω_{PLL}, δ can be retrieved. This is the phase angle of the electromotive force vector $\overline{E}$.

Next, the amplitude of $\overline{E}$ can be obtained by the AVR model. It shares the same structure with the governor model: the error between Q^* (reactive power reference) and Q_v (virtual reactive power) is multiplied by the gain K_a and the result goes through a low pass filter characterised by the time constant T_a. The outcome is the voltage variation $\Delta\widehat{V}$. Q_v is calculated as follows:

$$Q_v = v_q i_d^* - v_d i_q^* \tag{3.90}$$

Then, the voltage error ϵ_v is retrieved as follows:

$$\epsilon_v = \Delta\widehat{V} + \widehat{V}^* - \widehat{V}_C \tag{3.91}$$

where:

- $\widehat{V}_C$ is the amplitude of the phase voltage in pu;
- $\widehat{V}^*$ is the reference voltage in pu.

This error feeds a PI regulator which provides the electromotive force amplitude $\widehat{E}_f$. The integral gain of the regulator is equal to K_{ecc} of Table 3.3, whereas k_p is experimentally tuned.

By means of the amplitude $\widehat{E}$ and the phase angle δ, the components of the vector $\overline{E}$ on the (d, q) reference frame can be retrieved:

$$\begin{cases} e_d = \widehat{E}\cos(\delta) & \text{(3.92a)} \\ e_q = \widehat{E}\sin(\delta) & \text{(3.92b)} \end{cases}$$

The KHI model is based on the concept of virtual admittance as other VSM solutions. The current reference vector $\overline{I}^*_{dq}$ is retrieved from the difference between $\overline{E}$ and $\overline{V}_C$ multiplied by the virtual admittance. However, differently from the SPC, for instance, the KHI virtual impedance is algebraically implemented. Therefore, no integration is performed and the two components of $\overline{I}^*_{dq}$ in pu can be computed as follows:

$$\begin{bmatrix} i^*_d \\ i^*_q \end{bmatrix} = Y \cdot \left(\begin{bmatrix} e_d \\ e_q \end{bmatrix} - \begin{bmatrix} v_d \\ v_q \end{bmatrix} \right) \tag{3.93}$$

where Y is the virtual admittance matrix defined in (3.94):

$$Y = \frac{1}{r_v^2 + l_v^2} \begin{bmatrix} r_v & l_v \\ -l_v & r_v \end{bmatrix} \tag{3.94}$$

Finally, the reference current $\overline{i}^*_{dq}$ is compared with the measured current i_{dq} and the error feeds a PI regulator, which produces the reference voltage for the PWM modulator [65].

3.3.9 CVSM

The Cascaded Virtual Synchronous Machine (CVSM) is a VSM model proposed in 2013 [62]. Fig. 3.27 shows the general block control scheme. It shows the main blocks of this control algorithm. The CVSM can synchronize with the grid with no need of a PLL. The model is built on the (d, q) reference frame, defined by the CVSM angular position θ.

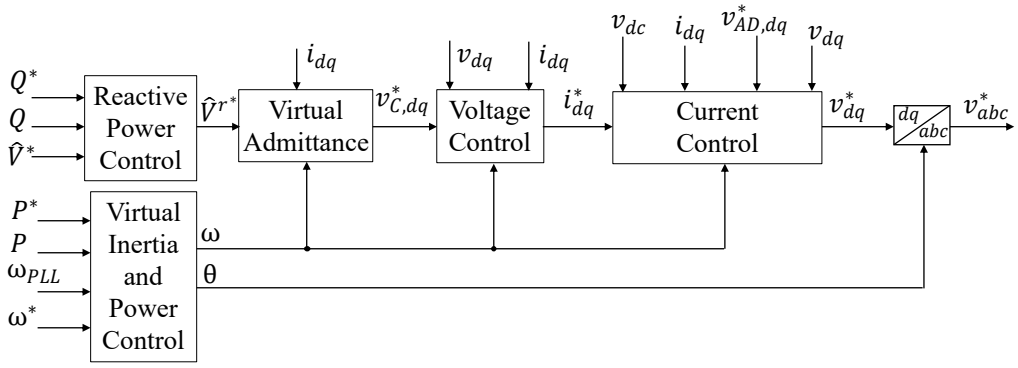

Fig. 3.27 CVSM control scheme in Laplace domain [65].

The first step is the measurement processing. As shown in Fig. 3.28, the phase voltage $\overline{v}_C$ and the inverter current $\bar{i}_{abc}$ are measured to obtain:

- inverter current $\bar{i}_{dq}$ in pu;
- phase voltage $\overline{v}_{C,dq}$ in pu;
- active power P and reactive power Q in pu:

$$\begin{cases} P = v_{C,d} i_d + v_{C,q} i_q & \text{(3.95a)} \\ Q = v_{C,q} i_d - v_{C,d} i_q & \text{(3.95b)} \end{cases}$$

Moreover, the active damping algorithm in pu is implemented to reduce the oscillations caused by the filter between the inverter and the grid. The block scheme is proposed on the bottom of Fig. 3.28. A low pass filter is used to eliminate all the oscillations on the measured phase voltage $\overline{v}_{C,dq}$, obtaining ϕ_{dq}. The cut-off frequency ω_{AD} is set to 5 Hz. Then, the difference between $\overline{v}_{C,dq}$ and ϕ_{dq} contains only the undesired components of $\overline{v}_{C,dq}$. The active damping voltage $\overline{v}^*_{AD,dq}$ can be finally defined, setting the gain K_{AD} to 1 pu.

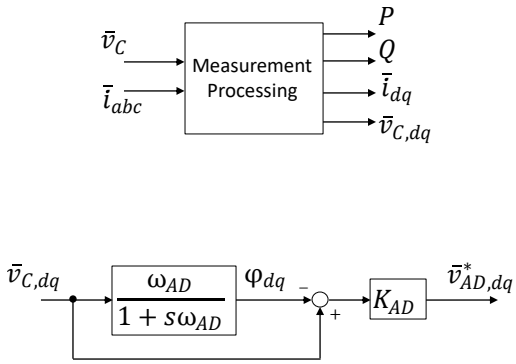

Fig. 3.28 CVSM control scheme: Measuring Processing (top) and Active Damping (bottom) [65].

In Fig. 3.29 the two external power control loops in pu are shown. On the top there is the Reactive Power Droop Controller. It is used to retrieve the amplitude of the electromotive force amplitude $\widehat{v}^{r^*}$. The gain k_q is the reactive droop coefficient. It multiplies the difference between the reactive power reference Q^* and the filtered reactive power Q_m. The result of the reactive droop control is the voltage variation Δv. Finally, the electromotive force amplitude $\widehat{v}^{r^*}$ is:

$$\widehat{v}^{r^*} = \widehat{v}^* + \Delta v \tag{3.96}$$

On the bottom of the Fig. 3.29 the active part of the model is also proposed. It consists of two parts: Frequency Droop and Swing Equation.

The Frequency Droop block performs the active droop control. The active power reference P^{r^*} consists of two contributions: the external active power reference P^r and the active droop term P_ω defined as follows:

$$P_\omega = k_\omega(\omega^* - \omega) \tag{3.97}$$

where k_ω is the active droop coefficient in pu.

Then, the swing equation is implemented, as already seen in (3.2):

$$P^{r^*} - P = T_a \frac{d\omega}{dt} + k_d \cdot (\omega - \omega_{PLL}) \tag{3.98}$$

where $T_a = 2H$. Here the PLL is only used to perform the damping as it can be seen from (3.98). Through of the swing equation, the CVSM speed ω and the CVSM angular position θ can be retrieved.

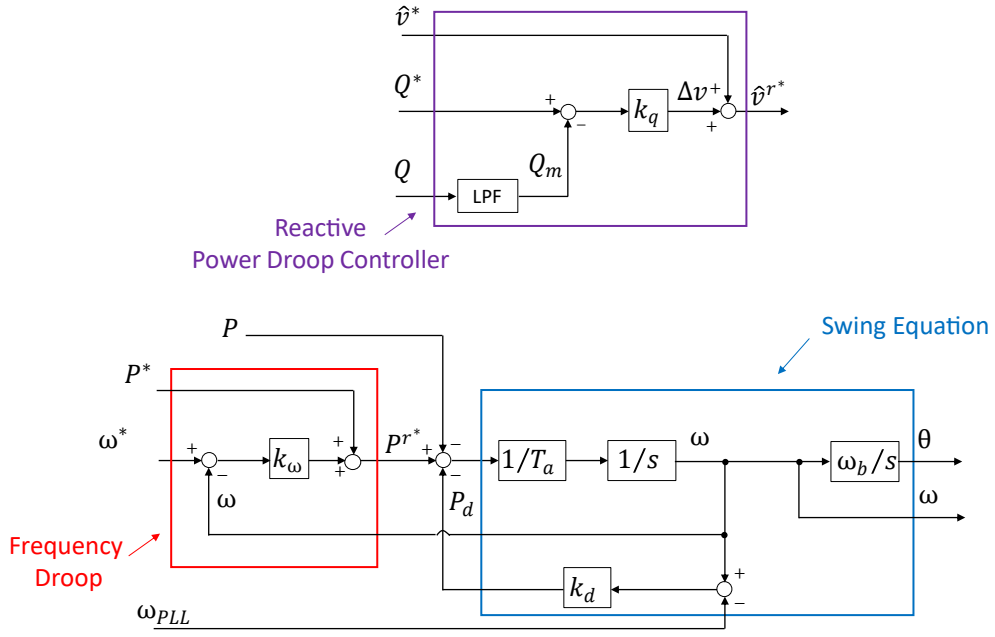

Fig. 3.29 CVSM control scheme: Reactive Power Droop Controller (top); Virtual Inertia and Power Control (bottom) [65].

The CVSM is an examble of grid-forming VSM with a two cascaded voltage and current closed loop controls. The electromotive force on the (d, q) reference frame consists of two components: v^{r^*} and 0. The parameters of virtual impedance are the same of the other VSMs. The difference between the electromotive force and the virtual impedance voltage drop defines the capacitor reference voltage $\overline{v}^*_{C,dq}$, as shown in Fig. 3.30.

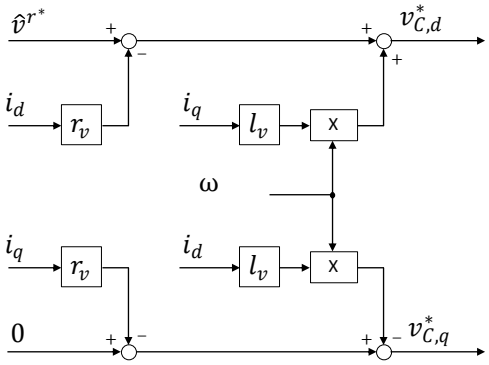

Fig. 3.30 CVSM control scheme: virtual impedance [65].

As it can be observed, the virtual impedance is algebraically implemented as for the KHI model.

Next, the closed loop voltage control can be performed. Fig. 3.31 shows the block scheme. It is a conventional control actuated in the (d, q) reference frame using PI regulators. The result is the current reference $\bar{i}^*_{dq}$.

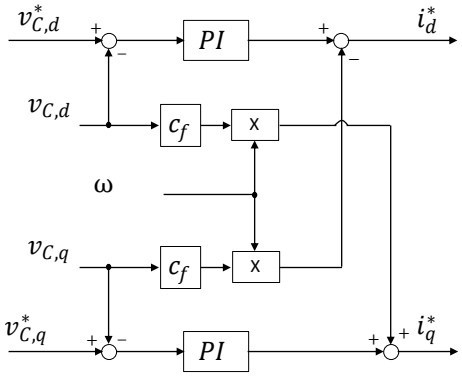

Fig. 3.31 CVSM control scheme: voltage control [65].

Finally, the closed loop current control can be actuated, as shown in Fig. 3.32. Even here conventional PI regulators are used. They guarantees a reliable current limitation. The output of the PI regulator is compensated by the damping voltage as well as the cross electromotive force term. The result is the voltage reference $\bar{v}^*_{dq}$. Park Transformation is used to obtain the three phase voltage reference $\bar{v}^*_{abc}$ for the PWM modulator.

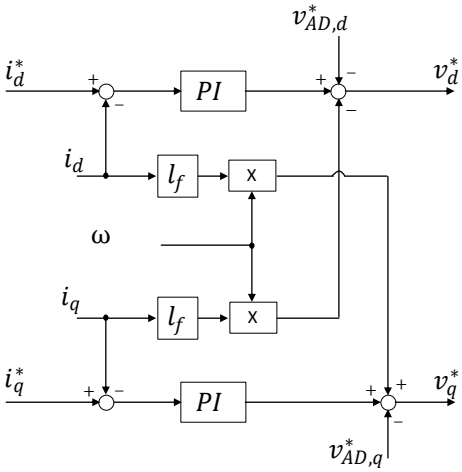

Fig. 3.32 CVSM control scheme: current control [65].

3.3.10 Simplified Virtual Synchronous Compensator

The S-VSC (Simplified Virtual Synchronous Compensator) is grid-following VSM implemented at the Politecnico di Torino [80, 68]. Fig. 3.33 shows the block scheme.

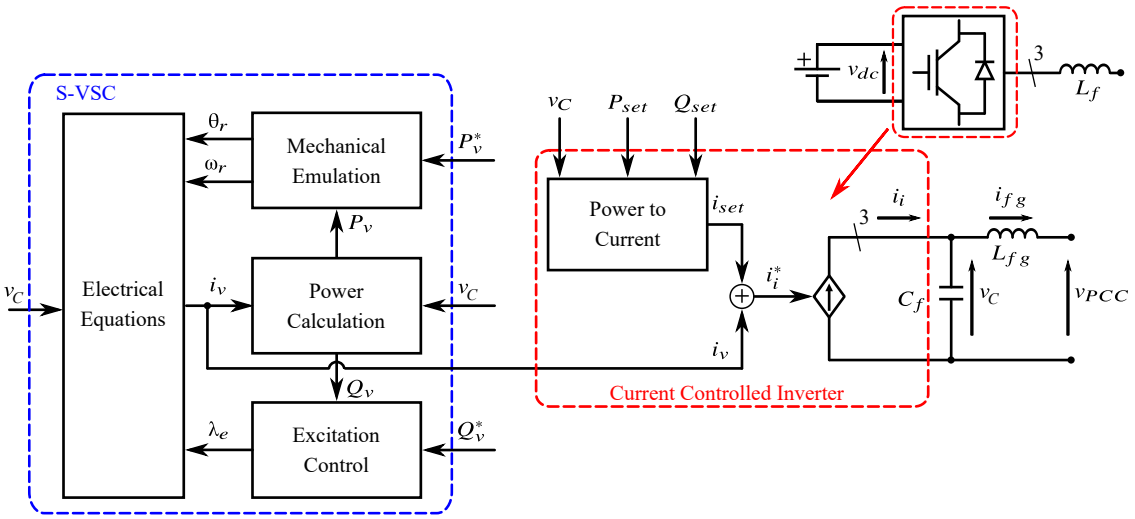

Fig. 3.33 S-VSC block control scheme [64].

The S-VSC consists of four main blocks:

- *Electrical Equations*: this block contains the five virtual stator equations of the virtual machine. They are written in the (d, q) reference frame which rotates at the virtual rotor speed ω_r. The block receives as input the measured voltage v_g, the virtual rotor angle θ_r, the virtual speed ω_r and the virtual excitation flux λ_e. The virtual current i_v is the output. The equations are as follows:

$$v_{Cd} = -R_v i_{vd} - \omega_r \lambda_q + \frac{1}{\omega_b}\frac{d\lambda_d}{dt} \tag{3.99}$$

$$v_{Cq} = -R_v i_{vq} + \omega_r \lambda_d + \frac{1}{\omega_b}\frac{d\lambda_q}{dt} \tag{3.100}$$

$$\frac{L_{rq}}{\omega_b R_{rq}}\frac{d\lambda_{rq}}{dt} = -\lambda_{rq} - L_{rq} i_{vq} \tag{3.101}$$

$$i_{vd} = \frac{\lambda_e - \lambda_d}{L_d''} \tag{3.102}$$

$$i_{vq} = \frac{\lambda_{rq} - \lambda_q}{L_q''} \tag{3.103}$$

where R_v denotes the virtual resistance, λ_d and λ_q represent the d-axis and q-axis components of the virtual stator flux linkages, $L_d^{''}$ and $L_q^{''}$ denote the machine subtransient inductances, which are equal to the virtual inductance L_v (indicating a subtransient isotropic machine), λ_{rq} is the flux linkage of the damper winding, and R_{rq} and L_{rq} are the parameters of the q-axis virtual damper winding [81].

- *Mechanical Emulation*: it implements the swing equation [7], generating outputs for both ω_r and θ_r using the virtual active power P_v and the virtual active power reference P_v^*. The swing equation is represented as (3.2):

$$P_v^* - P_v = 2H\frac{d\omega_r}{dt} \tag{3.104}$$

- *Excitation Control*: this block regulates the excitation flux λ_e and the reactive power exchange with the grid [82] by receiving as inputs the virtual reactive power reference Q_v^* and the virtual reactive power Q_v as the majority of the other VSMs:

$$\lambda_e = \int k_e \frac{Q_v^* - Q_v}{V_g} dt \tag{3.105}$$

$$k_e = \frac{L_v + L_{fg} + L_g}{\tau_e} \tag{3.106}$$

- *Power Calculation*: this block calculates P_v and Q_v using i_v and v_C.

The grid synchronization is power-based, i.e., there is no need of an additional PLL.

All the previous VSMs described operate as Virtual Synchronous Generators, i.e., the virtual power references correspond to the setpoint of power exchange to the grid. In other words, when a VSM operates a VSG, it is responsible for processing the total power exchange. In this way, the dynamic of the control is strictly dependent on the slow dynamic of the VSM. However, VSMs can operate as a Virtual Synchronous Compensator as well, such as the S-VSC. The following paragraph aims at describing the differences of the two mode operations [68].

Distinction between VSG and VSC

The S-VSC is a peculiar VSM model which can operate either as VSG or VSC. To clearly describe the difference the model is reshaped according to the Fig. 3.34 and consists of two main parts: a VSM algorithm (highlighted in green) and a current control block

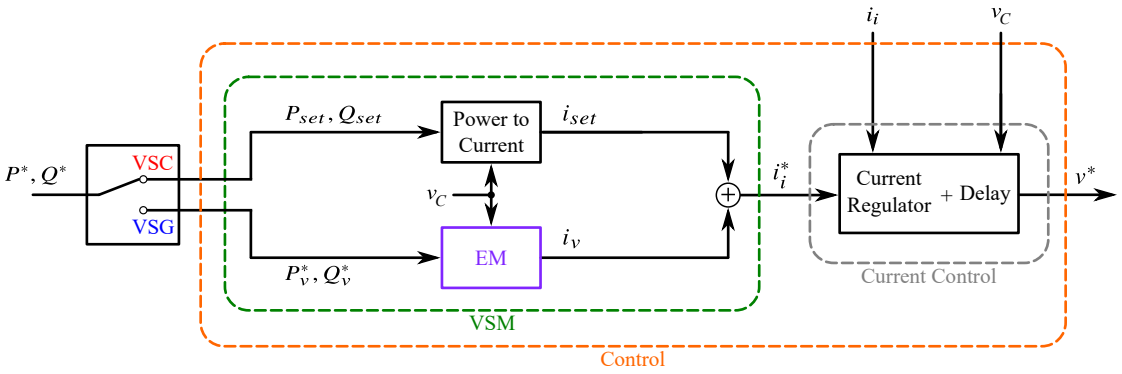

Fig. 3.34 Scheme of the S-VSC to distinguish the two mode operations (i.e., VSG and VSC).

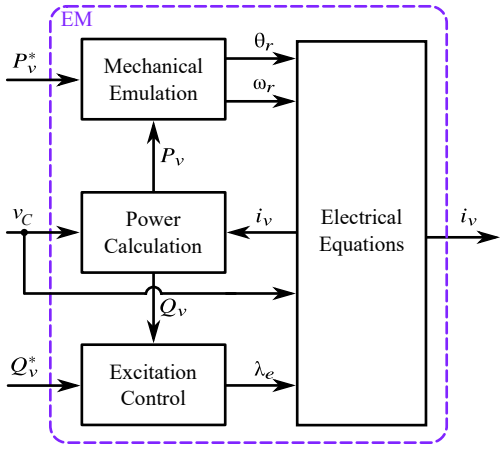

Fig. 3.35 Scheme of the Electromechanical block (EM).

(highlighted in grey). The VSM provides the reference current i_i^* which is tracked by a current regulator. The current control block provides the voltage reference v^* needed to retrieve the inverter commands q. The converter operates as a grid-following.

The VSM block contains the Simplified Virtual Synchronous Compensator [25], whose model is detailed in Fig. 3.34 and Fig. 3.35.

As shown in Fig. 3.34, the Control (highlighted in orange) receives as input four quantities: reference active power P^*, reference reactive power Q^*, measured inverter current i_i and measured voltage v_C. The active and reactive power references come from a higher level control (e.g., Maximum Power Point Tracking algorithm, dc-link voltage control, droop control) and represent the desired amount of power to exchange with the grid. The VSM (highlighted in green) consists of two main blocks: Electromechanical Emulation (EM) block and Power to Current block. According to the selector position in Fig. 3.34, the reference power P^*, Q^* can be applied either to the EM block (VSG operation) or to the Power to Current block (VSC operation). The Electromechanical

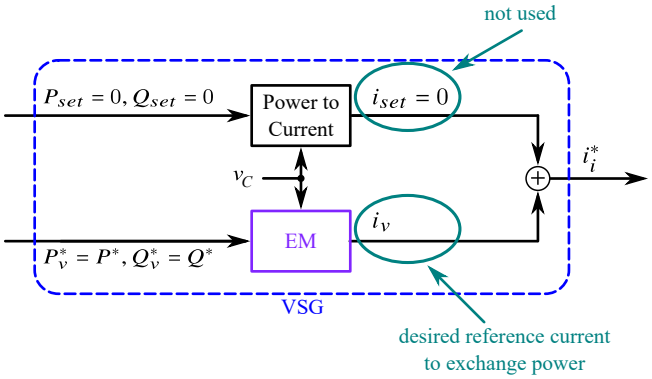

Fig. 3.36 Scheme of the S-VSC in VSG mode.

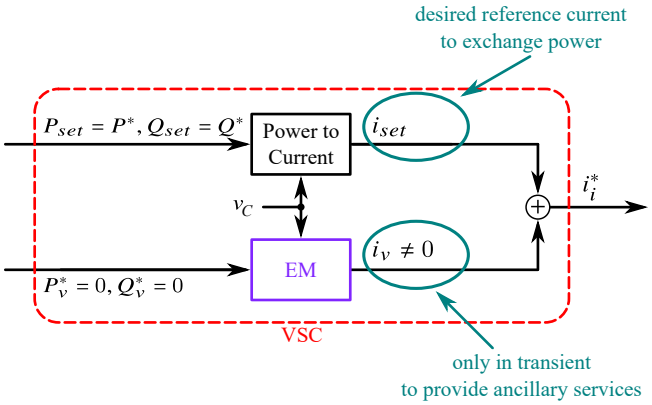

Fig. 3.37 Scheme of the S-VSC in VSC mode.

Emulation block is the block already described above. The Power to Current block calculates the setpoint current i_{set} from the active and reactive setpoints P_{set} and Q_{set} and the measured voltage v_g.

When the VSM operates as VSG, the selector of Fig. 3.34 is low (blue position). The virtual references P_v^* and Q_v^* are respectively equal to P^* and Q^*, whereas $P_{set} = 0$ and $Q_{set} = 0$, as highlighted in Fig. 3.36. Consequently, i_{set} is equal to zero and the reference current i_i^* is equal to the virtual current i_v. Therefore, the EM block is responsible of managing the total power exchange, i.e., the VSM is operating a VSG.

If the VSM is configured as a compensator (VSC mode), the selector in Fig. 3.34 is set to a high position (indicated in red). The virtual power references P_v^* and Q_v^* are consistently maintained at zero. This setup ensures that the virtual component of the control algorithm focuses solely on providing grid services, while the power generation setpoints P^* and Q^* are managed by the conventional inverter structure (i.e., $P_{set} = P^*$, $Q_{set} = Q^*$) [25]. Fig. 3.37 illustrates the control scheme of the VSM operating as a virtual compensator. Here, the reference current i_i^* is the sum of two components: i_v for dynamic

support and i^*_{set} for high-level control law. The virtual current is active only during transient conditions to guarantee the provision of grid services such as inertial support, and it remains zero during steady-state operations. Consequently, power exchange is closely tied to the rapid dynamics of the current control regulator (hundreds of Hz). This advantage suggests that operating in VSC mode can enhance the robust stability of a grid-connected converter compared to VSM mode operation [68].

3.4 Experimental Comparison

In this section, the results of the experimental tests are presented along with comments on the key aspects of the experimental implementation [65].

3.4.1 Experimental Setup and Tests

A picture of the experimental setup is shown in Fig. 3.38a. The setup consists of a three phase inverter interfaced to a grid emulator through an LCL filter. The grid emulator creates an ideal grid voltage to emulate the grid and test grid frequency and voltage variations. The inverter is supplied by an ideal dc-source and controlled by a dSPACE platform according to the VSM algorithms. The scheme of the experimental setup is illustrated in Fig. 3.38b, while Table 3.5 collects the main data.

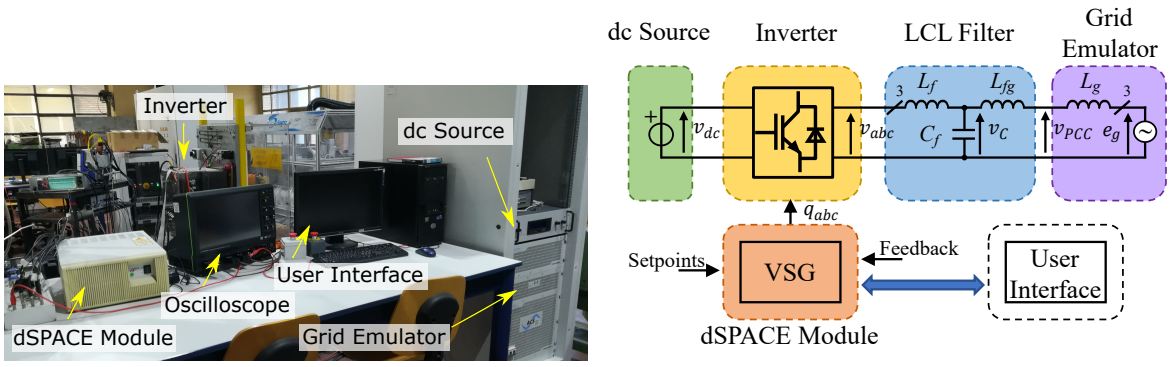

(a) (b)

Fig. 3.38 From left to right: (a) experimental setup; (b) scheme of the experimental setup [65].

This thesis presents an experimental comparison of the ten VSM solutions discussed. Three tests were conducted. Two for the active part (i.e., inertial behavior and frequency regulation) and one for the reactive part (i.e., grid support during faults) [65, 66].

Table 3.5 Experimental setup main data.

dc Source		**Inverter**		**LCL Filter**		**Grid Emulator**	
V_{dc}	380 V	S_N	15 kVA	L_f	545 µH	$\widehat{E}_g$	$120\sqrt{2}$ V
		I_N	60 A	C_f	22 µF	f_g	50 Hz
		f_{sw}	10 kHz	L_{fg}	120 µH	L_g	300 µH

Test 1: Active power reference step from 0.3 pu to 0.4 pu. This test demonstrates the dynamic behavior of the VSM models when their power setpoint changes, such as when the power generated by a renewable energy source on the dc side of the converters varies. This test was designed to evaluate the dynamic performance of the control algorithm.

Test 2: Large power imbalance emulation. The grid frequency follows a profile similar to the one qualitatively shown in Fig. 1.6 and stabilizes at 49.58 Hz, a typical trend when a generation source is lost. Test 2 examines three aspects:

1. *Inertial behavior*: As described in Chapter 1, when a power imbalance occurs, SGs provide part of their kinetic energy to compensate. This test evaluates the VSMs capability to emulate this feature [65];
2. *Active droop control*: represented by the second step of the profile in Fig. 1.6. Some models include this as an additional feature, while others have it inherently. This test evaluates their performance in primary frequency control [65];
3. *Damping-droop coupling*: this test evaluates the presence of coupling between the damping and droop coefficients in various models [66].

Test 3: Symmetrical voltage dip. The grid voltage decreases at 0.5 pu for 300 ms to observe the grid support behavior of the VSMs. The test shows the Fault Ride Through capability and the different behaviors of the various VSM topologies under analysis. Their response is also compared to the behavior of a conventional GFL control [66].

3.4.2 Test 1: Active Power Reference Step

Fig. 3.39 displays the results of Test 1 for each model. The active power reference changes from 0.3 pu to 0.4 pu. The models are grouped based on the time required to reach the steady-state condition [65].

Each VSM model tracks the reference without steady-state error.

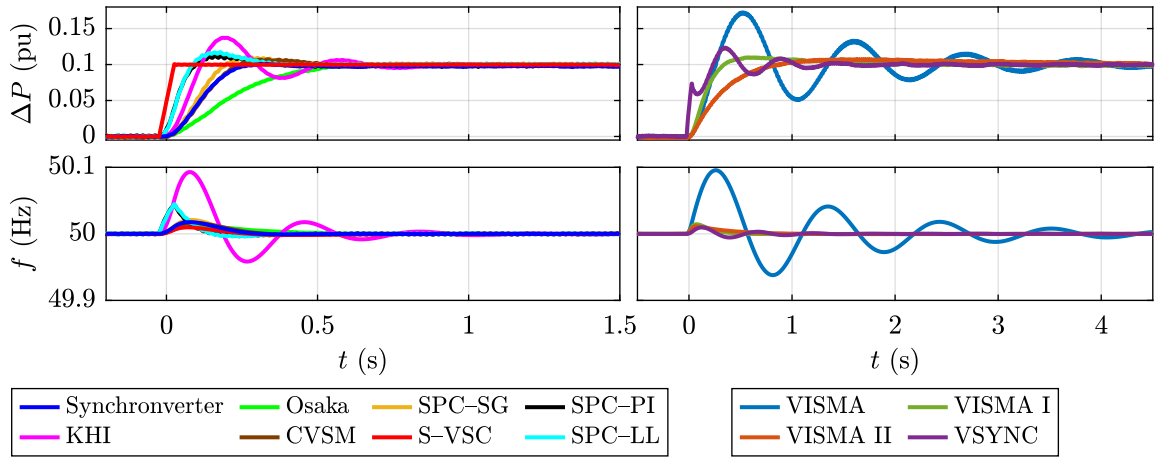

Fig. 3.39 Test 1 results: (top) moving average of the active power ΔP injected by the inverter (pu); (bottom) virtual frequency f (Hz) [65].

The S-VSC model has the fastest response among the solutions, with no overshoot. Since the virtual active power P_v of the S-VSC is minimally modified, the response is solely dependent on the current loop dynamics, with no virtual mechanical transient or load angle variation. Consequently, the frequency profile shows the smallest variation among the models.

The profiles for the Osaka and VISMA II solutions are well-damped, while the responses for Synchronverter, VISMA I, the three SPC versions, and CVSM are underdamped or show limited overshoot. In all these cases, the setpoint is matched within 1 second. Regarding frequency variation, it remains below 20 mHz in almost all cases. Exceptions are SPC-PI and SPC-LL, which have a maximum variation of about 60 mHz due to the presence of a proportional gain.

The VISMA, VSYNC, and KHI models exhibit a consistently underdamped profile. VISMA, in particular, shows the highest overshoot and longest settling time because it fully emulates conventional synchronous generators, which are characterized by low damping.

Finally, both the VSYNC and KHI solutions show an underdamped response with the transient ending after approximately 1.5 seconds. The frequency variation of the VSYNC is about 10 mHz, whereas the KHI shows a 100 mHz variation, which is the highest frequency variation among the solutions.

3.4.3 Test 2: Large Power Imbalance Emulation

The results of Test 2 are shown in Fig.3.40. The grid frequency changes with an initial ROCOF of about -0.89 Hz/s, reaches a Nadir around 48.65 Hz, and stabilizes at 49.58 Hz. As discussed in Section 3.3, the VSM models are compared without altering their original control algorithms. They can be categorized into three groups:

- Models showing a coupling between droop and damping: VISMA I, VISMA II, Synchronverter, and SPC–SG. See Fig.3.40 on the right;
- Models with embedded droop control where droop and damping control are decoupled: Osaka, SPC–PI, SPC–LL, KHI, and CVSM. See Fig.3.40 on the left.
- Models without embedded droop control but can easily add it externally if needed: VISMA, VSYNC, and S–VSC. See Fig.3.40 on the left.

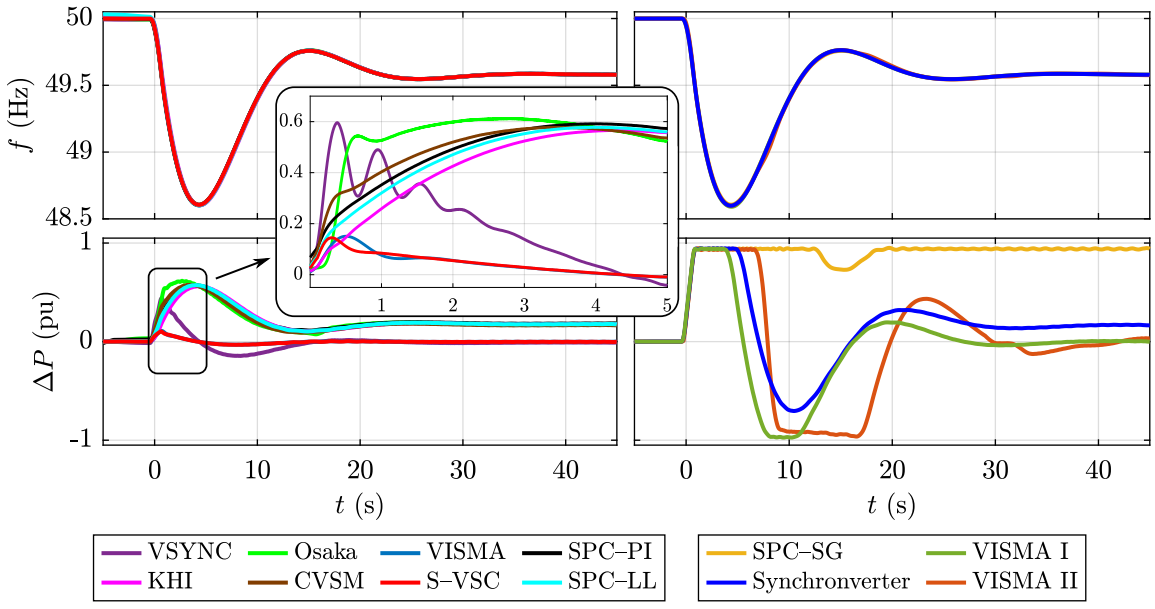

Fig. 3.40 Test 2 results: (top) VSM frequency f; (bottom) moving average of the active power ΔP (pu).

Almost all models employ an active power loop control where the feedback signal is the active power (or torque). This feedback can either be directly measured (real active power, denoted as P) or calculated (virtual active power, denoted as P_v), depending on the model. These two values coincide when the injected active power is not constrained. However, if saturation occurs, the virtual power must be recalculated without limitations to ensure control stability, and the algorithm adjusts the current accordingly.

In the left group of Fig. 3.40, the virtual active power does not exceed 1 pu due to the decoupling of damping and droop coefficients. Here, the damping term manages oscillations (if present), while the droop coefficient determines the injected active power in steady state (if applicable). Conversely, in the right group, the virtual active power of VSM models exceeds the nominal value because of the coupling between damping and droop. In these models, the droop coefficient influences the damping coefficient.

In all scenarios, the real active power injected by the inverter must be capped to adhere to the inverter's operational limits. Fig. 3.41 illustrates the active power before and after saturation.

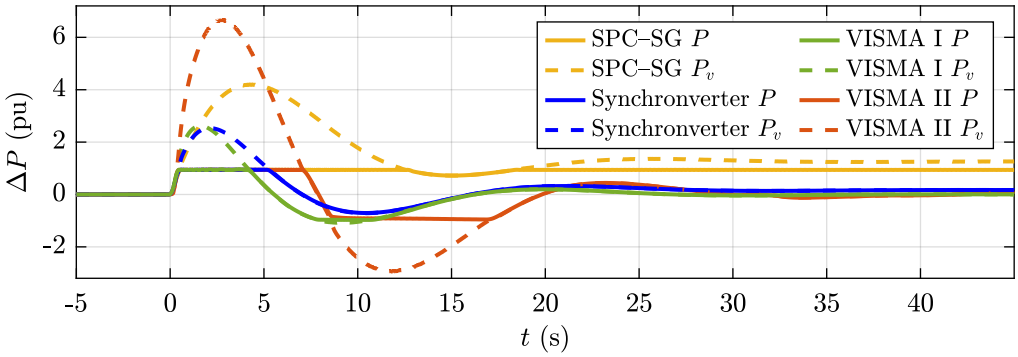

Fig. 3.41 Results of Test 2: Comparison between the real active power P injected by VISMA I, VISMA II, Synchronverter, and SPC-SG and the corresponding virtual active power P_v [65].

Each model, regardless of using a PLL, accurately tracks the grid frequency. Initially, the VSM models exhibit the typical inertial behavior of conventional SGs, injecting inertial active power proportional to the inverse of the frequency derivative. In the following seconds, the responses depend heavily on the implementation of active droop control.

Osaka, SPC-PI, KHI, and CVSM models use a governor model to regulate frequency. In steady state, with a droop coefficient of 5%, these VSMs provide the same active power, equal to 0.168 pu. During the transient, SPC-PI and KHI show similar responses.

For the Osaka model, the active power trend shows a steeper slope compared to the other three models due to its higher damping coefficient, as indicated in Table 3.2. Initially, the damping coefficient amplifies the frequency difference, contributing alongside the governor. A higher damping coefficient results in a higher active power peak, which is about 0.6 pu in this case.

The CVSM solution exhibits a faster dynamic compared to SPC-PI and KHI, lacking a low pass filter in the frequency controller, relying solely on a droop coefficient of 5%. The active power peak is around 0.6 pu.

The Synchronverter and SPC-LL models operate without a governor but can exchange active power following changes in grid frequency. Initially, the Synchronverter exhibits a peak in virtual active power up to 2.5 pu because its high-pass term ΔT_{HP} remains unsaturated. In steady state, this term reduces to zero, and the only active power contribution comes from ΔT_{LP}, which is limited to 0.168 pu, i.e., the maximum transferable active power considering a 5% droop coefficient.

The SPC-LL model behaves similarly to SPC-PI and KHI, despite lacking a dedicated governor model, due to the lead-lag PLC structure providing an additional degree of freedom to decouple damping and droop control.

VISMA, VISMA I, VISMA II, SPC-SG, VSYNC, and S-VSC models do not implement a governor and therefore do not perform primary frequency control. However, an external droop controller can be added.

VISMA fully emulates a synchronous generator's behavior, with a much lower active power trend than the others, peaking at 0.1 pu. At steady state, the active power is zero due to the absence of a governor. S-VSC, with a similar control scheme to VISMA, shows a similar response.

For VISMA I, VISMA II, and SPC-SG models, P_v surpasses 1 pu during the initial frequency variation. Upon reaching steady state, the active power for VISMA I and VISMA II decreases to zero because these models do not feature a frequency regulator. Conversely, SPC-SG continuously injects maximum active power due to the coupling of droop and damping coefficients. The droop coefficient, constrained by the damping one, is about ten times lower than in other models, leading to higher active power injection compared to SPC-PI and SPC-LL.

Lastly, the VSYNC model operates without an active loop control, relying solely on the measured active power. During the frequency contingency, the active power increases and exhibits oscillations, settling to zero in steady state due to the absence of a governor [65].

3.4.4 Test 3: Voltage Dip

Three different VSMs (Osaka, SPC and CVSM) are experimentally tested against a symmetric voltage dip of 50% depth and 300 ms duration. They have been chosen as representative of the following three categories: GFM open loop VSM, GFL VSM, GFM close loop VSM. Moreover, the test is repeated for the VISMA model as a reference of a real synchronous machine [52, 7] and for a conventional GFL (CGFL) control responseas a benchmark for comparing with other control algorithms [38].

The experimental results are illustrated in Fig. 3.42 and Fig. 3.43. The results of the different models are proposed in Fig. 3.42 on different time scales to highlight the peculiarity of each solution. Instead, the comparison among the solutions in terms of response speed is performed in Fig. 3.43 using the same time scale.

Before the fault, the inverter current is almost zero. Indeed, in this test it is assumed zero active power injection for simplicity. Next, at $t = 0$ s the voltage dip occurs and lasts for 300 ms. Then, the grid voltage immediately goes back to the normal operating conditions. All the control algorithms provide reactive current as soon as the the fault occurs for the entire duration of the faults, as shown in Fig. 3.42. To demonstrate the current limitation capability, during the fault the current is limited to 0.6 pu (i.e., 36 A) of the nominal current. Next, at the end of the voltage dip, the current decreases up to the pre-fault condition. Fig. 3.43 shows the inverter current acquired by the dSPACE platform.

In all cases the inverter immediately starts to inject reactive current as soon as the dip occurs. The Osaka model (i.e., GFM VSM) shows the fastest response as it operates as a grid-forming converter in voltage open loop. Consequently, it does not feature a current limitation algorithm. The results are shown in Fig. 3.43a. To avoid the overcurrent protection trip, if a current threshold of 0.6 pu is reached, the inverter moves to a current control mode to safety saturate the current. For this reason the current increases above the current limit and then it goes back to 36 A. Then, the original control algorithm is restored as soon as a safe condition is reached. Next, the SPC model (i.e., GFL VSM) immediately starts to inject reactive current as depicted in Fig. 3.43b. It keeps the inverter current within the limit of 36 A with no overshoot as it operates as a grid-following converter with a current regulator. The results of these two models are proposed on the same time scale in Fig. 3.42 to highlight that the Osaka model needs circa 2 seconds to go back to the steady-state GFM operation, whereas on the same time scale the SPC settles in the steady-state condition with no need of operating modes

switches. Fig. 3.42c and Fig. 3.43c show the response of the CVSM model (i.e., dual loop VSM). In Fig. 3.42c the time scale is shorter to better appreciate the current behavior at the beginning and at the end of the fault. The entire behavior is quite similar to the SPC one, as the CVSM embeds a current regulator. Next, the response of the VISMA model represents the equivalent response of a conventional synchronous machine as illustrated in Fig. 3.43d. The current shows a unidirectional component that decreases during the fault as it can be also observed in Fig. 3.42d. Finally, the conventional grid-following control (CGFL) shows the slowest response among the five algorithms due to the dynamic of the PLL, as it can be noted in Fig. 3.43e. After about 8 ms the current reaches the limit value of 36 A. After the fault clearance, the current shows a short transient to go back to the previous operating condition, as highlighted in Fig. 3.42e. It can be concluded that all the three VSMs typologies (i.e., GFM VSM, GFL VSM, dual loop VSM) satisfy the GC0137 requirement of providing reactive current within 5 ms when the voltage falls below 90% of its nominal value with negligible differences among them. However, the GFM VSM needs a backup strategy to avoid the overcurrent fault [66].

3.4.5 Experimental implementation aspects

The VSM algorithms and their tuning were initially verified through PLECS simulations and subsequently implemented on the experimental setup. Several challenging issues were encountered during this phase:

- *Synchronization procedure*: the converter must synchronize to the grid without causing inrush currents. Typically, this is achieved with a PLL algorithm or other techniques, which are unsuitable for the SPC and KHI models because they use measured powers as feedback in their active power loops. To synchronize these models to the grid, power must first be calculated using current references. Once synchronization is complete, the control is reverted to the original configuration, using the measured power;

- *Current Limitation*: the grid-forming VSMs (e.g., VISMA II and Osaka) lack a built-in current limitation algorithm. Therefore, a backup strategy was implemented to ensure the inverter's safe operation. If a current threshold is exceeded, the inverter switches to GFL operation to limit the current. Once a safe condition is restored, the original control algorithm is reinstated. This transition can be observed for VISMA II in Fig. 3.40 at 32 seconds.

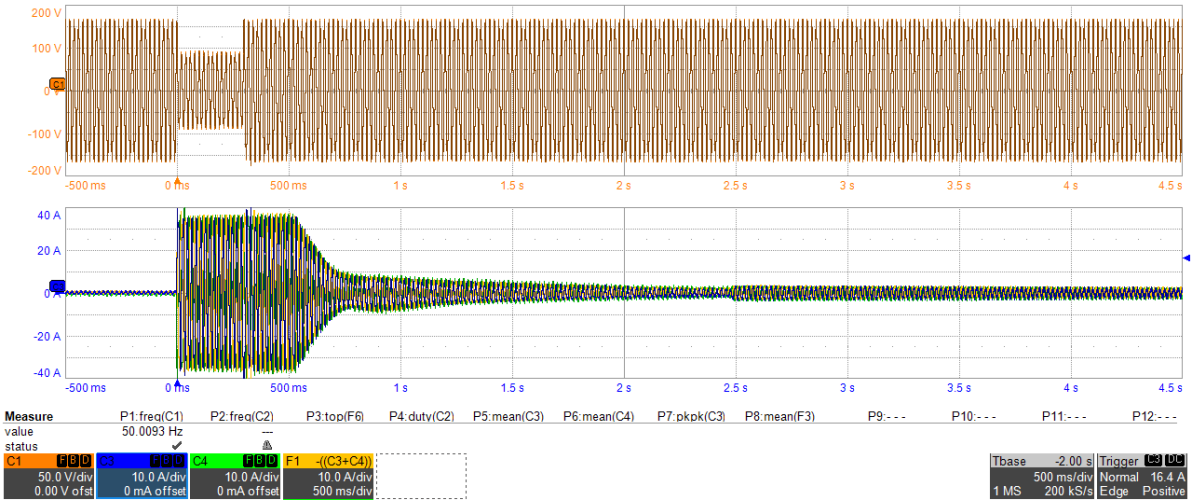

(a)

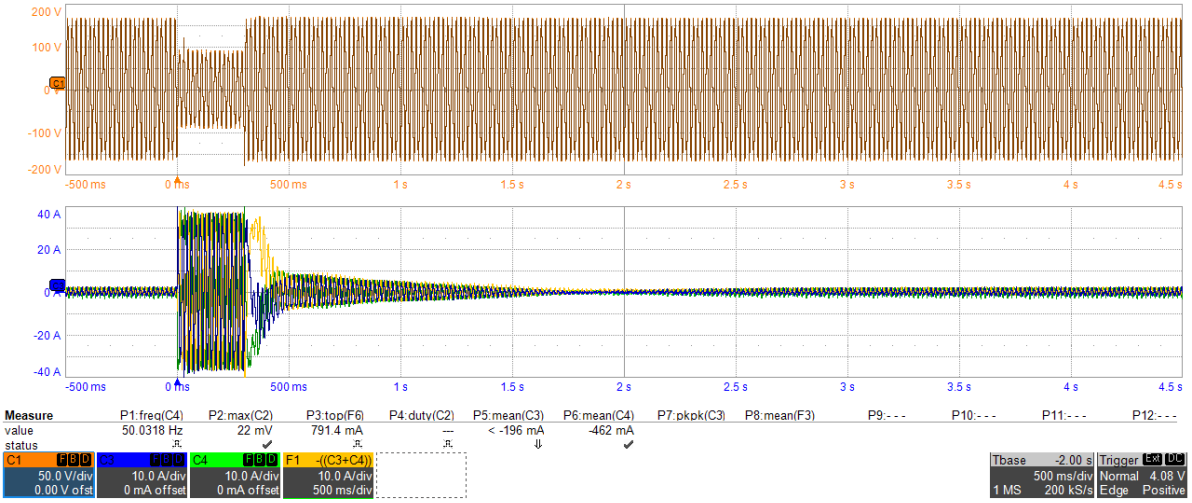

(b)

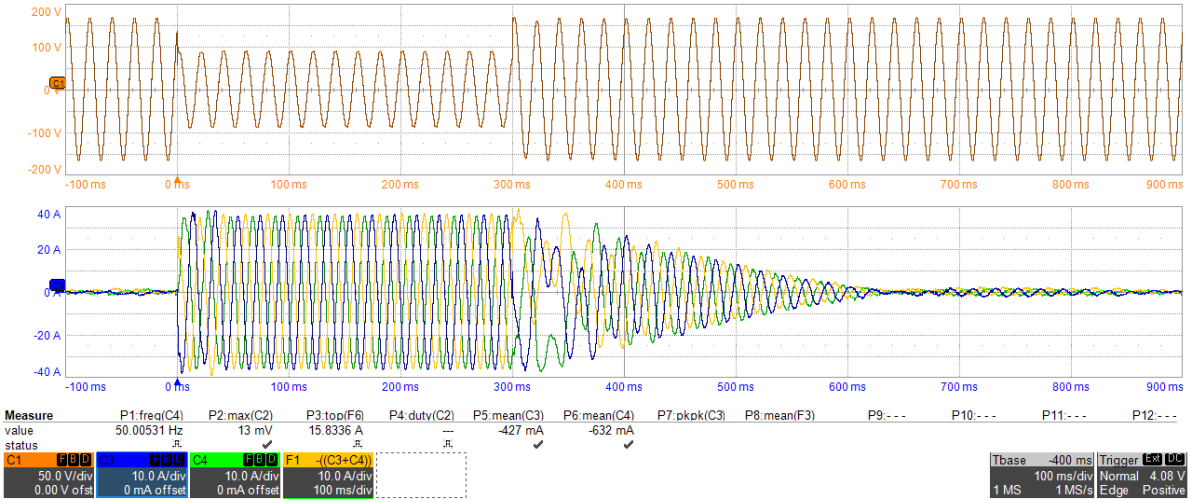

(c)

Fig. 3.42 Capacitor measured phase voltage $v_{c,a}$ (C1), grid measured current i_g (C3, C4, F1) under a 0.5 pu voltage dip for 300 ms: (a) Osaka; (b) SPC; (c) CVSM; (d) VISMA; (e) CGFL [66] (1/2).

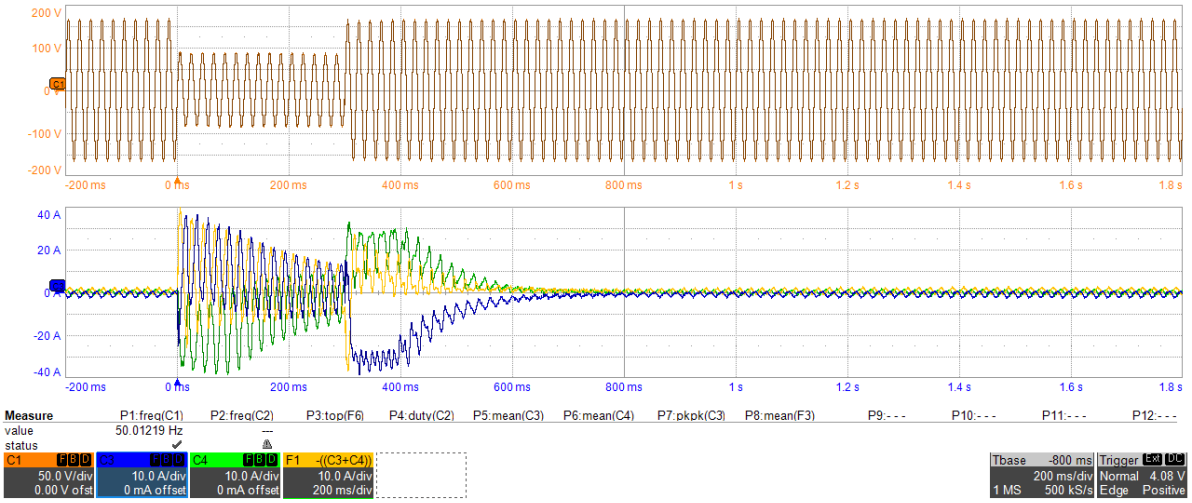

(d)

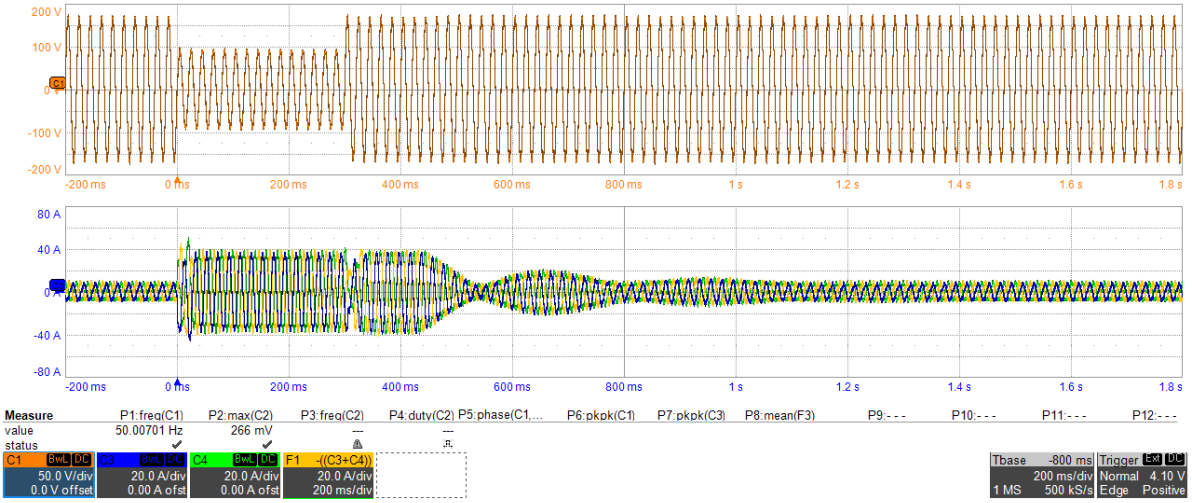

(e)

Fig. 3.42 Capacitor measured phase voltage $v_{c,a}$ (C1), grid measured current i_g (C3, C4, F1) under a 0.5 pu voltage dip for 300 ms: (a) Osaka; (b) SPC; (c) CVSM; (d) VISMA; (e) CGFL [66] (2/2).

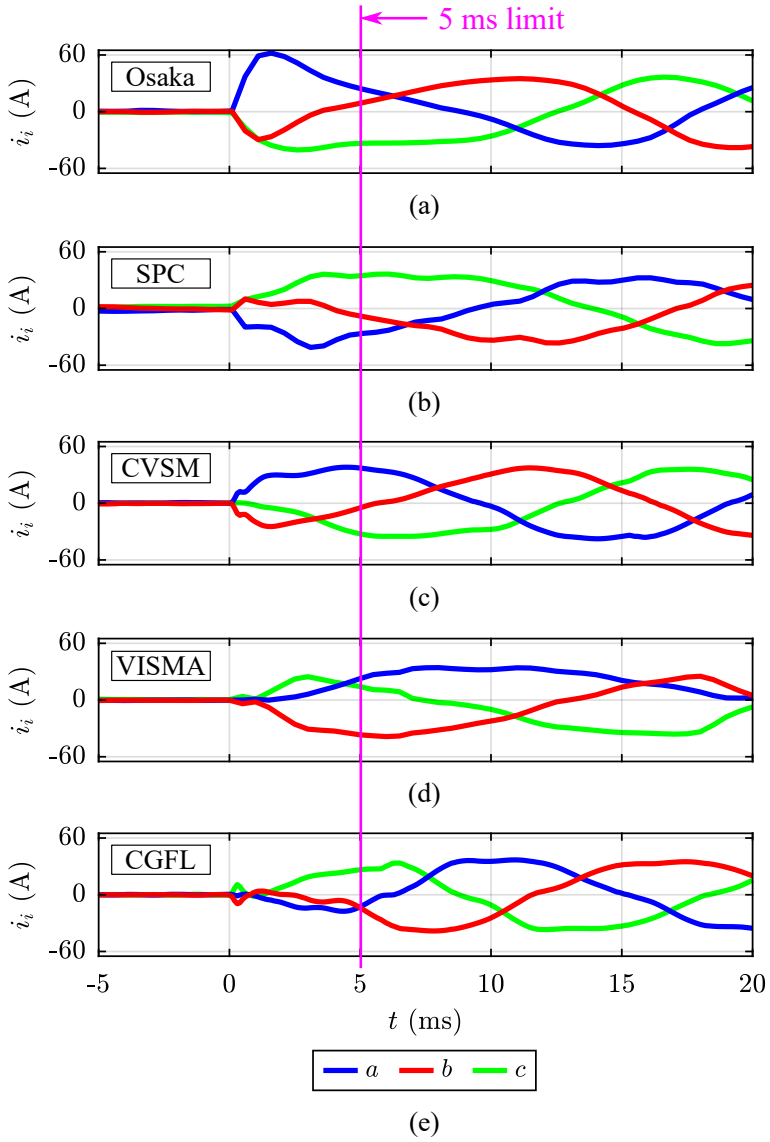

Fig. 3.43 Zoom of the three-phase measured inverter current i_i at the beginning of the fault: (a) Synchronverter (Synch in the figure); (b) SPC; (c) CVSM; (d) VISMA; (e) CGFL [66].

Another current limitation issue pertains to the SPC and KHI models, which use measured power as feedback. When the current reference is saturated to prevent faults, they must switch to calculated power feedback without the saturated current reference; otherwise, the control diverges [65].

3.5 Experimental validation of the dynamic grid

All the experimental tests proposed in the previous section demonstrated the capability of VSMs to provide inertial support. However, the tests are performed on VSMs connected to a static grid emulator, whose voltage (amplitude, frequency and phase) is imposed as an ideal voltage source. Therefore, the VSMs cannot affect the the grid voltage. To experimentally validate the beneficial effects of VSMs on the grid stability, the converter must be able to influence the grid voltage. For this purpose, the experimental setup is improved by making the grid emulator able to behave as a "dynamic grid", i.e., a voltage source whose grid voltage changes according to the inverter current. By adding this feature, this section proposes the experimental validation of the beneficial inertial support of VSMs on the grid stability, as demonstrated in [67].

3.5.1 Dynamic grid model

The grid emulator operates as a signal amplifier, i.e., it receives an analog three phase voltage signal with an amplitude of 10 V and it amplifies the signal to the desired value (e.g., $120\sqrt{2}$ V as base value) e_g. The analogue signals come from the PLEXIM RTBox, a microcontroller capable of performing a real-time PLECS simulation and to send the analog signals to the emulator.

The real-time PLECS simulation implements a grid model depicted in Fig. 3.44. It consists of a swing equation, a primary frequency regulation using a statism of 5% and a secondary frequency regulation with a time constant of 50 s. The output frequency is the imposed grid frequency f_g to the emulator. The PLECS simulation receives as input the grid-side current i_g and calculates the grid interface power P_g from i_g and e_g. The frequency is then integrated to obtain the angle of the voltage phasor. The power step ΔP_L is used to emulate grid contingencies and it is expressed in pu of the grid base power.

3.5.2 Experimental setup

The scheme of the experimental setup is proposed in Fig. 3.45. The setup consists of three converters, named G1, G2 and R1. G1 and G2 are supplied by the same dc-source. Each converter has its own LCL filter. The converters are connected through the line impedances Z_1, Z_2, Z_3 to the grid. Moreover, G1 and G2 operate at base voltage of $208\sqrt{2}$

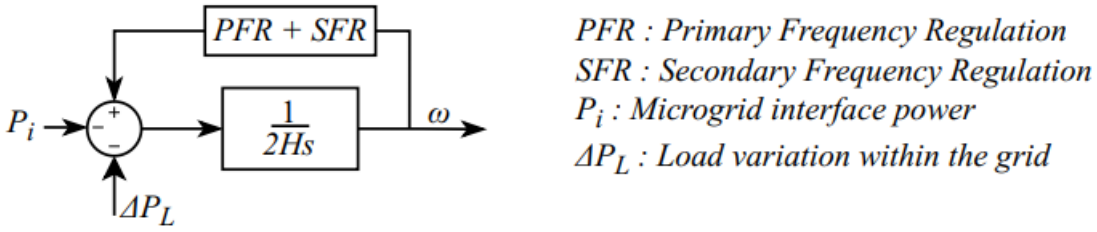

Fig. 3.44 Swing equation using the grid interface feedback power [67].

V, whereas R1 operates at $120\sqrt{2}$ V. The grid voltage is $120\sqrt{2}$ V. The transformer T1 connects the two subsystems. The system can also operate in a microgrid configuration by disconnecting the grid emulator. The island operation will be investigated in Chapter 6.

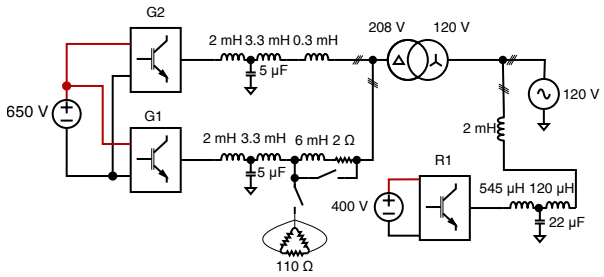

Fig. 3.45 Scheme of the microgrid consisting of 3 converters [67].

From this setup three different tests are performed:

- Test 1: Single Inverter connected to the grid. The system described in Fig. 3.45 is reduced to a single converter (G1) connected to the grid operating at $208\sqrt{2}$ V. The converter and the grid have the same size (15 kVA). This is a representative case of a relevant-size power plant able to strongly influence the grid voltage.
- Test 2: Two Inverters connected to the grid. G1 and G2 are connected to the grid operating at $208\sqrt{2}$ V.The two converters and the grid have the same size (15 kVA) as Test 1.
- Test 3: Three Inverters connected to the grid. G1, G2 and R1 are connected to the grid as described in Fig. 3.45. G1, G2 and R1 have the same size (15 kVA). The rated grid power is 100 kVA. This is a more general and realistic scenario where the grid shows a higher size with respect to the generation units.

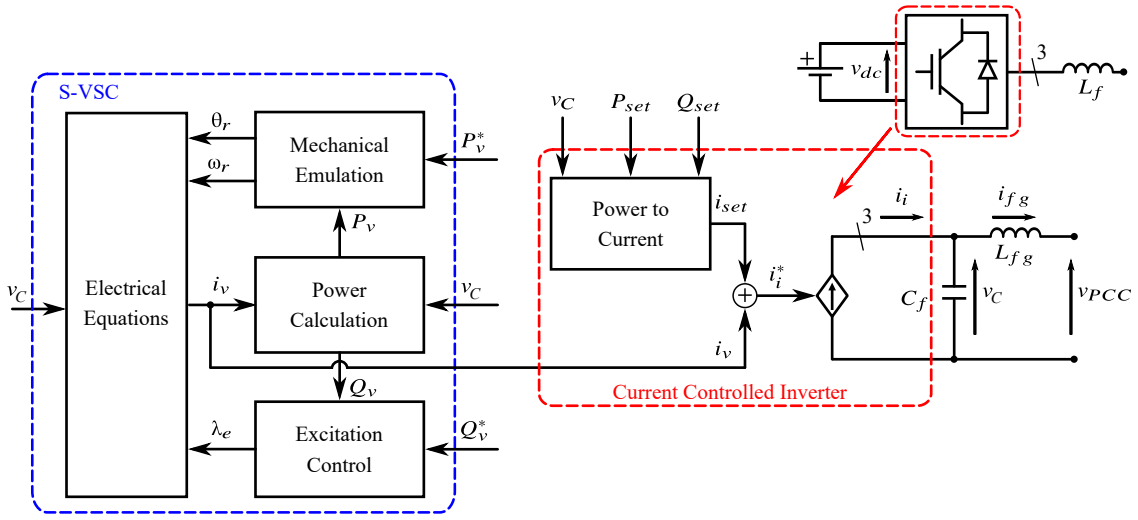

Fig. 3.46 Scheme of the S-VSC model.

In all tests, a grid contingency induces a frequency reduction, as described in the previous section. All the converters are controlled with the S-VSC model. The three tests empirically illustrate how the S-VSC can offer inertial support, effectively enhancing grid stability by lowering the Rate of Change of Frequency (RoCoF) and increasing the Nadir.

3.5.3 Single Inverter connected to the grid

In this test only G1 is connected to the grid. The converter and the grid have the same base value (i.e., same size). The experimental results are proposed in Fig. 3.47. At t = 0 s, the frequency starts to drop following the same behavior of the previous section. Two cases are compared: S-VSC disabled (i.e., OFF) in blue and S-VSC enabled (i.e., ON) in red. For simplicity, the S-VSC control block scheme is reported again here in Fig. 3.46. When the S-VSC is disabled, the virtual current is not added the setpoint current, i.e., the converter operates as a conventional grid-following converter employing the VSM algorithm only to synchronize to the grid (equivalently to a PLL). In this case, the converter does not react to the grid contingency and the grid frequency shows a Nadir of 49.34 Hz at t= 2.63 s (point c of 3.47b) and a RoCoF of:

$$\text{RoCoF}_{OFF} \approx \frac{49.6 - 50}{0.83} = 0.4819 \text{ Hz/s} \tag{3.107}$$

The RoCoF is calculated as a first approximation as the difference between the last steady-state point (t = 0 s, f_g = 50 Hz) and the point point a of 3.47b. Next, the test is repeated by enabling the S-VSC (i.e., i_v is summed to i_{set}). It can be observed that the

converter injects inertial power, and the inertial power contribution positively affects the grid frequency, by decreasing the RoCoF and shifting the Nadir upward and rightward. Indeed, the new Nadir is equal to 49.43 Hz and it is reached at t= 3.89 s (point d of 3.47b). The new RoCoF, calculated with respect to the point b of 3.47b is:

$$\text{RoCoF}_{OFF} \approx \frac{49.6 - 50}{1.58} = 0.2532 \text{ Hz/s} \tag{3.108}$$

These experimental results demonstrate the beneficial effect of the VSM to support the grid by increasing the Nadir and reducing the RoCoF [67].

3.5.4 Two Inverters connected to the grid

The G1 and G2 inverters are connected to the grid. They feature the same base power S_b and inertia time constant H of the grid. Therefore, it is expected that each element of the system will contribute with 1/3 of the total power, as the sharing of the inertial power is proportional to the aforementioned parameters. The test is executed four times and the outcomes are proposed in Fig. 3.48. First, the grid contingency is applied while both G1 and G2 are controlled in a traditional (trad.) way. The traditional way refers again to the case of S-VSC control disabled, i.e., i_v not added to the setpoint current i_{set}. Therefore, the converter operates as a conventional grid-following converter synchronized to the grid through a VSM algorithm. The two converters do not provide active power ad demonstrated in the previous test and the grid frequency trend is illustrated in Fig. 3.48c. Next, G1 is controlled as VSM and G2 not (case blue of Fig. 3.48) and viceversa, i.e., G2 is controlled as VSM and G1 not (case red of Fig. 3.48). In both cases the converter controlled as VSM provides inertial support while the other one does not react. Moreover, they contribute in a almost equal to reduce the grid frequency RoCoF and increase the Nadir in amplitude and time occurrence. Finally, both converters operate as VSM (case green of Fig. 3.48), further enhancing the grid frequency trend [67].

3.5.5 Three Inverters connected to the grid

Finally, the tests are performed with the three inverters G1, G2 and R1 connected to the grid emulator. The results are reported in Fig. 3.49. To portray a more realistic scenario, the base power of the grid emulator is increased to 100 kVA. It is still a relatively low value, but it is chosen to be able to still see the inertial contributions of the different VSMs. The three converters have the same size S_b = 15 kVA. However, it has been chosen

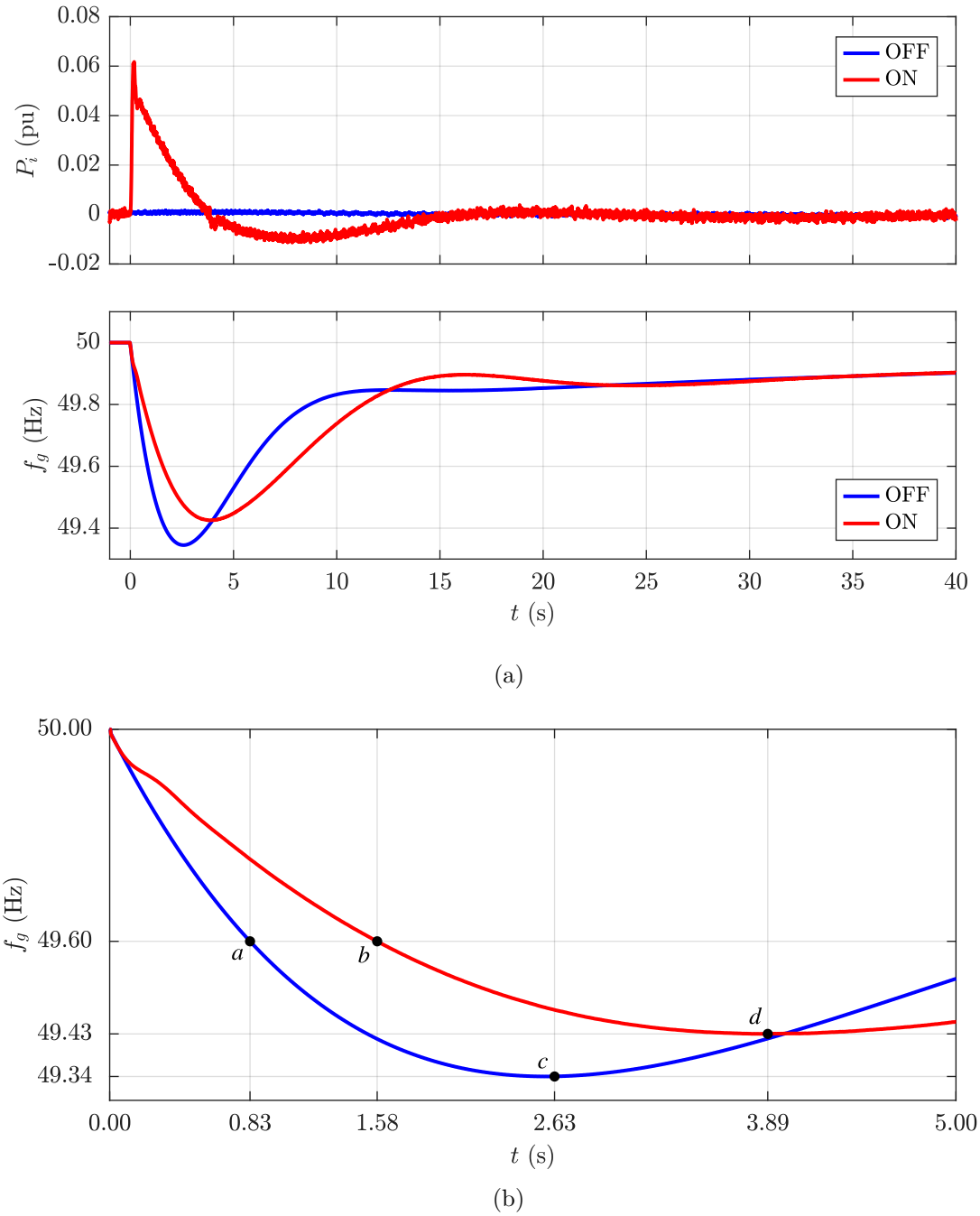

Fig. 3.47 (a) Test 1. From top to bottom: inverter power P_i (pu) with the S-VSC disabled (blue) and enabled (red); grid frequency f_g (Hz) with the S-VSC disabled (blue) and enabled (red); (b) zoom of the grid frequency [67].

to set different values of inertia constant to show the different inertial contributions. They are equal to 4 s, 8 s and 2 s, respectively for G1, G2 and G3. Fig. 3.49 shows how

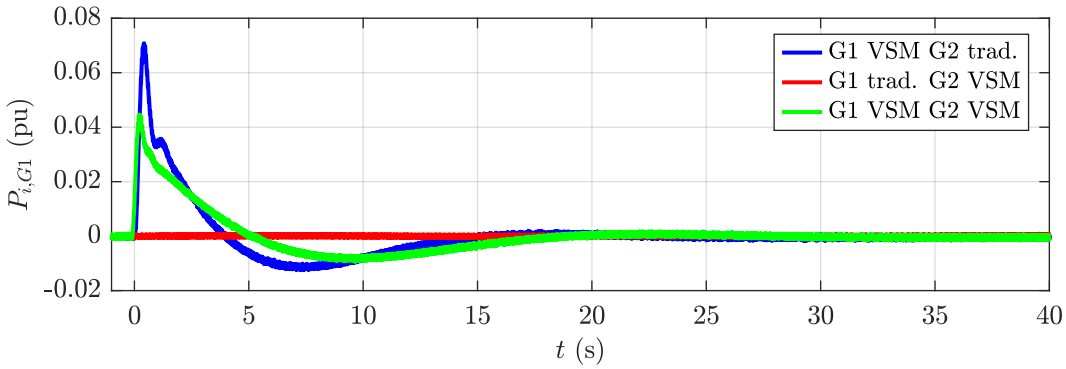

(a)

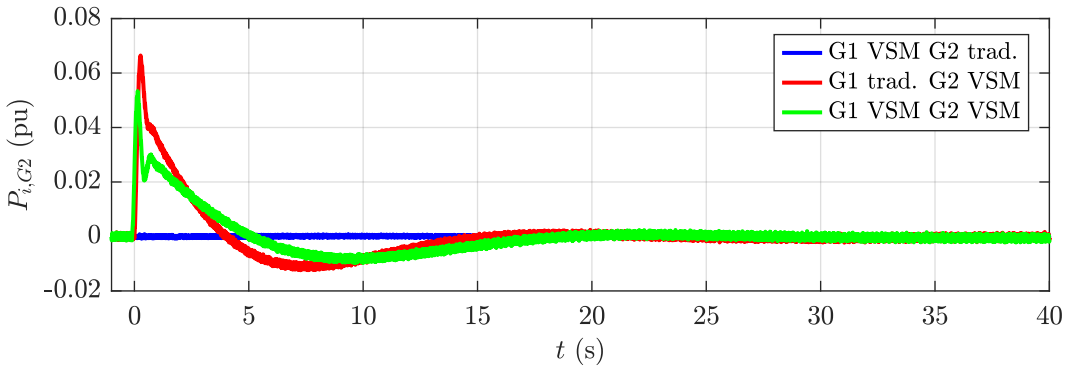

(b)

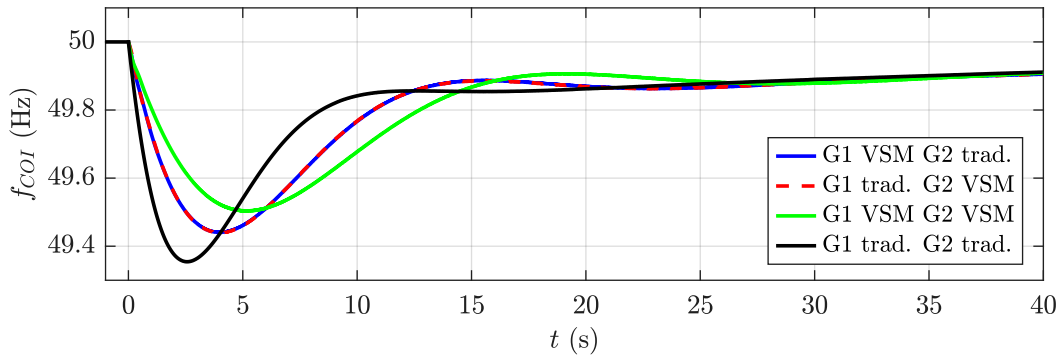

(c)

Fig. 3.48 Results of Test 2: (a) G1 measured power $P_{i,G1}$ (pu); (b) G2 measured power $P_{i,G2}$ (pu); (c) grid frequency f_g (Hz) [67].

the three converters share the inertial active power (referred in per unit to the base value of the grid) proportionally to the inertia constant. Moreover, Fig. 3.49a and 3.49b show the four frequencies of the converters and the grid, which slightly oscillate between each others [67]. This additional result highlights how the S-VSC control algorithm guarantees

a robust control of a multi converters microgrid connected to the grid against the low frequency oscillation issues raised by numerous papers available in the literature [83].

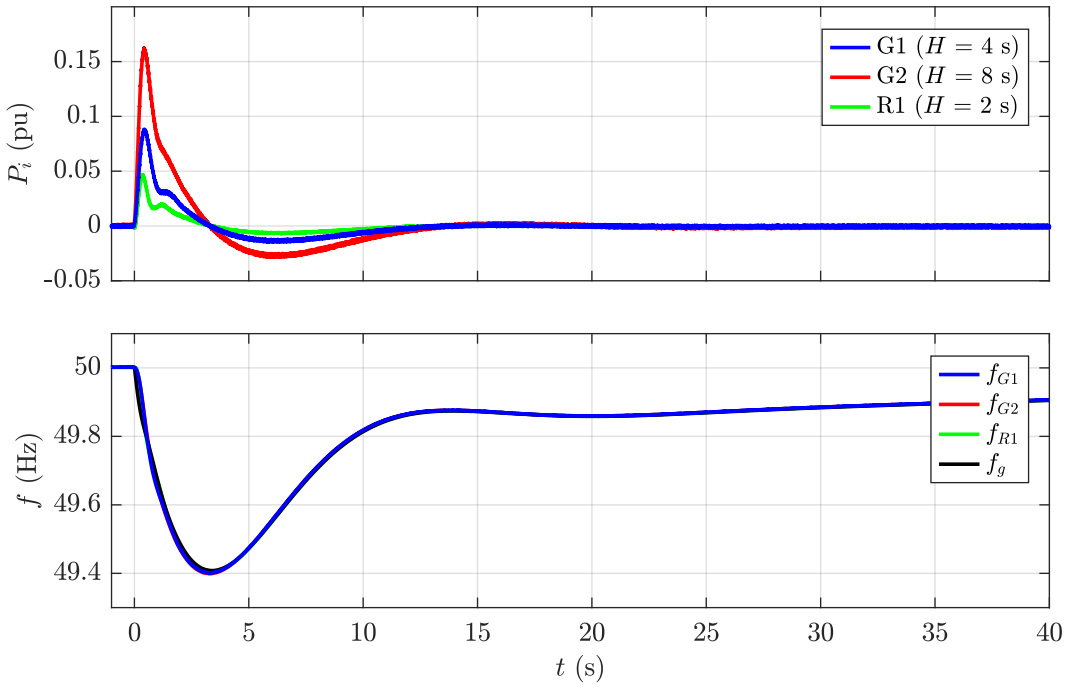

(a)

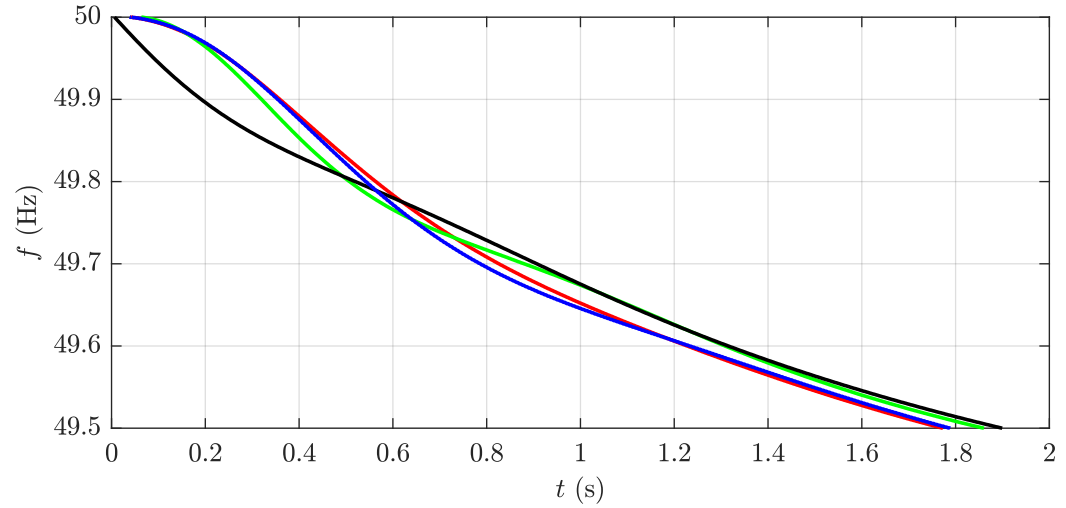

(b)

Fig. 3.49 (a) Result of Test 3: (a) from top to bottom: G1, G2 and R1 inverter power P_i (pu); G1, G2, R1 and grid frequency f (Hz); (b) zoom of the four frequencies [67].

3.6 Conclusions & Main Contributions

As grid codes now mandate active participation from renewable energy sources (RESs), the concept of Virtual Synchronous Machine (VSM) has emerged as a promising solution. VSMs emulate the behavior of synchronous machines, providing a way for RESs to contribute to grid stability.

In this chapter, ten representative VSM models available in the technical literature have been reviewed and evaluated by adopting the proposed tuning procedure. Three types of tests were conducted to experimentllay demonstrate how VSMs perform under two different grid contingencies: a frequency drop, simulating the loss of a generating unit in the grid (Tests 1 and 2), and a symmetrical voltage dip (Test 3).

Test 1 examines the dynamic properties of the active parts through a power reference step variation. Only the VISMA and KHI models exhibited unsatisfactory behavior due to significant overshoots;

Test 2 evaluates the inertial behavior and the capability to perform frequency control, both crucial for proper grid operation. Models such as Synchronverter, Osaka, SPC-SG, SPC-PI, SPC-LL, KHI, and CVSM can perform primary frequency regulation. However, in the SPC-SG model, the droop coefficient depends on the damping term. For the other models, droop control can be added as a feature with tunable parameters.

The experimental results of the ten VSM solutions are summarized in Table 3.6, with the three versions of the SPC displayed separately [65].

Test 3 shows the Fault Ride Through capability of different typologies of VSMs demonstrating that all VSM typologies met the GC0137 requirements of National Grid ESO, providing reactive current within the stipulated 5 ms timeframe when the voltage falls below 90% of its nominal value. The performance of these VSMs was compared against an emulated synchronous generator (VISMA) and a conventional grid-following control (CGFL), highlighting the superiority of VSMs in responding quickly to faults.

Notably, the three experimental tests conducted on various VSM typologies, including GFL VSMs, GFM VSMs, and dual-loop VSMs, validate their ability to both provide inertial contribution and support the grid during faults with no particular differences between GFL VSMs and GFM VSMs. Moreover, the thesis emphasizes the need for clarity in distinguishing between GFL, GFM, and VSM, urging for standardized definitions in the technical literature [65, 66].

Finally, by substituting the "static" grid with the "dynamic" one, it is possible to quantify and validate the real effectiveness of the grid frequency stability improvement given by the inertial contributions of VSMs. The tests are performed for different case studies: single converter connected to the grid (converter and grid of the same size), two parallel converters connected to the grid (converters and grid of the same size), three different converters distributed in a microgrid connected to the main grid [66].

Table 3.6 Results of the comparison [65].

Model	**Active Power Reference Step**		**Frequency Variation**		**Imp. Aspects**
	Damping	**Frequency Peak**	**Damping-Droop Decoupling**	**Tunable Droop**	
VISMA	✘	✘	✔	✔	✔
VISMA I	✔	✔	✘	✔	✔
VISMA II	✔	✔	✘	✔	✘
Synchronverter	✔	✔	✘	✔	✔
Osaka	✔	✔	✔	✔	✘
SPC-SG	✔	✔	✘	✘	✔
SPC-PI	✔	✘	✔	✔	✔
SPC-LL	✔	✘	✔	✔	✔
VSYNC	✘	✔	–	✔	✔
KHI	✘	✘	–	✔	✘
CVSM	✔	✔	✔	✔	✘
S-VSC	✔	✔	✔	✔	✔

Chapter 4

VSMs under non-ideal grid conditions

4.1 Introduction

According to the Virtual Synchronous Machine (VSM) approach, power electronic converters can emulate conventional synchronous machines (SMs) by providing ancillary grid services. Furthermore, they can exhibit superior performance compared to SMs, particularly under non-ideal grid voltage conditions [84]. The literature documents several VSM-based methods aimed at enhancing voltage quality at the grid connection point through harmonic current absorption, effectively acting as sinks for harmonics and mitigating unbalances [85–89].

For instance, [85] proposes a strategy employing multiple virtual admittances operating in parallel and tuned at the desired harmonic to compensate. Another example is [89], where various control strategies combining VSM functionalities with active filter capabilities are compared, identifying their respective advantages and limitations.

Generally, existing literature on the VSM behavior under non-ideal grid voltage conditions tends to focus on individual VSM implementations. Consequently, a unified method for predicting the response of a generic VSM configuration under these conditions, together with a well-defined set of criteria to enable VSMs to function effectively as sinks for harmonics and unbalances, is lacking in current research. Therefore, this thesis proposes a highly general methodology capable of anticipating the response of VSM

models in terms of power quality, specifically their performance under distorted and unbalanced grid voltage conditions.

This chapter aims to introduce a straightforward and comprehensive approach for predicting the behavior of various VSM typologies under non-ideal grid voltage conditions prior to experimental implementation. Furthermore, it evaluates the essential features necessary for VSMs to effectively mitigate harmonics and unbalances, identifying which configurations have the potential to improve voltage quality at the Point of Common Coupling (PCC).

The proposed methodology has been applied to seven models: S-VSC, VISMA II, Osaka, a modified version of the Osaka model (referred to as Osaka II) [90], KHI, VISMA, and VSYNC. Each model represents a distinct VSM configuration, detailed in the following section.

These VSM models are implemented using a grid-connected converter connected to the grid via an LC filter. Consequently, the PCC voltage aligns with the measured capacitor voltage, as depicted in Fig.4.1. The main system parameters are summarized in Table 4.1. The VSM Model block encompasses the analyzed VSM algorithms, all of which have been tuned according to Chapter 3. The models are expressed in per unit. The experimental validation was conducted under the following testing conditions related to the grid voltage e_g:

- Test 1: 5% fifth harmonic, the predominant non-fundamental component in real three-phase systems;
- Test 2: 5% inverse sequence distortion, occurring during asymmetrical faults.

The selected testing conditions are designed to simulate common non-idealities in grid voltage, crucial for emphasizing distinctions among the implemented VSM configurations.

Under these conditions, the anticipated beneficial outcomes of VSMs include a decrease in the 5^{th} harmonic distortion and a reduction in the Voltage Unbalance Factor (VUF) on the PCC voltage v_c. These criteria are essential for determining whether a VSM effectively mitigates harmonics and balances voltage unbalances, respectively, establishing its capability to function as a harmonic and unbalance sink.

As a second contribution of this chapter, this thesis demonstrates that grid-forming VSMs with no current loop control suffer the effect of the switching dead-time. The result is the reduction of the harmonic and unbalance sink capability of GFM VSMs. To solve this limitation, a dead-time compensation is mandatory. Experimental tests on two

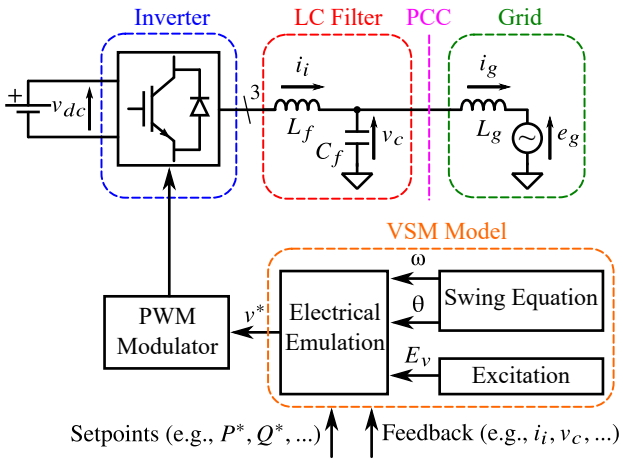

Fig. 4.1 Considered hardware of the system under study [73].

Table 4.1 System parameters [73].

Inverter		**Base Values**			
S_N	15 kVA	S_b	15 kVA	f_b	50 Hz
I_N	30 A	V_b	$230\sqrt{2}$ V	ω_b	314 rad/s
f_{sw}	10 kHz	I_b	30 A	L_b	33.7 mH
V_{dc}	650 V	Z_b	10.6 Ω	C_b	0.3 mF
Virtual Impedance		**LC Filter**		**Grid**	
R_v	0.02 pu	R_f	0.024 pu	$\widehat{E}_g$	$230\sqrt{2}$ V
L_v	0.15 pu	L_f	0.059 pu	R_g	0.007 pu
		C_f	0.017 pu	L_g	0.009 pu

representative VSM models demonstrate these findings under the same cases of non-ideal voltage conditions described above.

The findings of this chapter have been published on [73, 91, 92].

4.2 VSM Models

The virtual stator of the VSM can be modeled using an equivalent Thévenin circuit, which includes a virtual electromotive force generator e_v and a virtual impedance Z_v. This impedance consists of a virtual resistance R_v and a virtual inductance L_v [73].

As already described in Chapter 3, the VSMs can be gathered in two main categories: GFL VSMs and GFM VSMs. For simplicity, the two equivalent circuit shown in Fig. 3.3a and Fig. 3.3b are illustrated again here, in Fig. 4.2a and Fig. 4.2b, respectively [73].

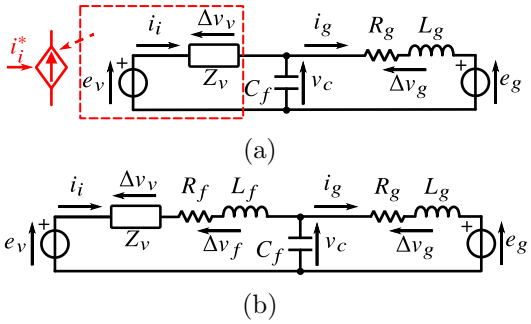

Fig. 4.2 Equivalent circuits of VSMs connected to the grid, for: (a) GFL VSMs; (b) GFM VSMs [73].

In Fig. 4.2a L_g is the grid inductance, R_g is the grid resistance and C_f is the LC filter capacitance. In Fig. 4.2b, L_f is the filter inductance and R_f is the filter resistance. The other elements are the same of Fig. 4.2a.

4.3 Theoretical Analysis

A generic quantity $\overline{x}$ in the (d,q) rotating reference frame at ω, can be represented as:

$$\overline{x} = x_d + jx_q \tag{4.1}$$

where j is the imaginary unit, wherease x_d and x_q are the components of $\overline{x}$ along the d-axis and the q-axis, respectively.

Given the equivalent circuits depicted in Fig. 4.2, it is possible to neglect the current through the capacitor for the scope of this thesis, as it is significantly lower than the current through the inverter. Consequently, we assume that the grid current i_g equals the inverter current i_i. Under this assumption, the voltage law for the circuit in Fig. 4.2a can be expressed as follows:

$$\begin{aligned}
\overline{e}_v &= R_v\overline{i}_i + L_v\frac{d\overline{i}_i}{dt} + j\omega L_v\overline{i}_i + \overline{v}_c \\
\overline{e}_v &= \Delta\overline{v}_v + \overline{v}_c \\
&= \Delta\overline{v}_v + R_g\overline{i}_i + L_g\frac{d\overline{i}_i}{dt} + j\omega L_g\overline{i}_i + \overline{e}_g \\
&= \Delta\overline{v}_v + \Delta\overline{v}_g + \overline{e}_g
\end{aligned} \tag{4.2}$$

Considering the generic harmonic order h, the steady-state derivative term is:

$$\frac{d}{dt} \rightarrow jh\omega \tag{4.3}$$

Then, (4.2) for the h-th order becomes:

$$\begin{aligned} \overline{e}_v^h &= \Delta\overline{v}_v^h + \overline{v}_c^h \\ &= \Delta\overline{v}_v^h + R_g\overline{i}_i^h + j(h+1)\omega L_g\overline{i}_i^h + \overline{e}_g^h \\ &= \Delta\overline{v}_v^h + \Delta\overline{v}_g^h + \overline{e}_g^h \end{aligned} \tag{4.4}$$

The equivalent circuit depicted in Fig. 4.2b follows the same principle:

$$\overline{e}_v = \Delta\overline{v}_v + \Delta\overline{v}_f + \Delta\overline{v}_g + \overline{e}_g \tag{4.5}$$

$$\overline{e}_v^h = \Delta\overline{v}_v^h + \Delta\overline{v}_f^h + \Delta\overline{v}_g^h + \overline{e}_g^h \tag{4.6}$$

The virtual impedance Z_v can be considered as [73]:

- Complete virtual impedance (CVI). The Kirchhoff's voltage law (4.2) remains unchanged, as the virtual impedance mimics a physical impedance;
- Simplified virtual impedance (SVI). In this case, the derivative term in (4.2) is disregarded, and the virtual reactance is consistent for each harmonic order. Consequently, in this scenario, the virtual impedance deviates from behaving like a physical impedance;
- Not implemented (NI).

Six VSM typologies have been implemented as representative cases. They are gathered into groups according to their category (GFL or GFM) and the method of virtual impedance implementation. The 6 typologies are detailed as follows [73]:

A. *GFL with CVI.* The implemented and representative VSM is the S-VSC model, but all the outcomes are valid for any other GFL VSM available in the literature, such as VISMA I, GFL Synchronverter and SPC. Moreover, the same analysis can be applied to most recent GFL VSMs [93–95, 71, 73].

B. *GFM with CVI.* The representative VSM model is the VISMA II [73].

C. GFL with SVI. The KHI model is the representative VSM implemented to analyze this kind of typology. The modeling and the finding are also valid for the CVSM [62, 63]. The same methodology can be applied to other VSMs found in the literature, including those discussed in [96, 97, 73].

D. GFM with NI. The representative VSM model is Osaka. Moverover, the results are also valid for other grid-forming VSMs with no virtual impedance, such as the original version of the Synchronverter or [98, 72].

E. GFM with SVI. The representative VSM solution selected for the analysis validation is the Osaka II model [90, 73].

F. GFL with NI. This final configuration includes two GFL models, VISMA and VSYNC, which do not incorporate a virtual impedance. Although no simplified models are available for them, they have been implemented and tested as benchmarks for the configurations mentioned earlier [73].

4.3.1 GFL with CVI

The equivalent circuit of the first category is retrieved from (4.2) and it is proposed in Fig. 4.3a. For the generic h-th harmonic order, (4.2) becomes:

$$\begin{aligned}\overline{e}_v^h &= R_v\overline{i}_i^h + jh\omega L_v\overline{i}_i^h + j\omega L_v\overline{i}_i^h + \overline{v}_c^h \\ &= \underbrace{(R_v + R_g)}_{R_{eq}}\overline{i}_i^h + j\underbrace{(h+1)\omega(L_v + L_g)}_{X_{eq}^h}\overline{i}_i^h + \overline{e}_g^h \\ &= (R_{eq} + jX_{eq}^h)\overline{i}_i^h + \overline{e}_g^h\end{aligned} \tag{4.7}$$

The method is applicable to other VSM configurations as well. For instance, in the VSM proposed in [93], the virtual impedance exhibits a virtual capacitor that can be integrated into X_{eq}^h. Furthermore, Equation (4.7) remains valid for VSMs employing a comprehensive and adaptive virtual impedance, whose magnitude can vary based on the selected algorithm [94, 95]. Additionally, [71] utilizes a complete virtual impedance with a low-pass filter, where the harmonic and unbalance absorption capabilities hinge on the filter cut-off frequency. Eq. (4.7) can accommodate this by incorporating the low-pass filter into the virtual impedance [73].

4.3.2 GFM with CVI

This configuration refers to the equivalent circuit of Fig. 4.2b. Eqs. (4.5) and (4.6) become (4.8) and (4.9), respectively:

$$\bar{e}_v = (R_v + R_f)\bar{i}_i + (L_v + L_f)\frac{d\bar{i}_i}{dt} + j\omega(L_v + L_f)\bar{i}_i + \bar{v}_c \tag{4.8}$$

$$\begin{aligned}
\bar{e}_v^h =& (R_v + R_f)\bar{i}_i^h + j(h+1)\omega(L_v + L_f)\bar{i}_i^h + \bar{v}_c^h \\
=& \underbrace{(R_v + R_f + R_g)}_{R_{eq}}\bar{i}_i^h + \\
&+ j\underbrace{(h+1)\omega(L_v + L_f + L_g)}_{X_{eq}^h}\bar{i}_i^h + \bar{e}_g^h \\
=& (R_{eq} + jX_{eq}^h)\bar{i}_i^h + \bar{e}_g^h
\end{aligned} \tag{4.9}$$

The equivalent circuit is illustrated in Fig. 4.3b.

In conclusion, for VSM configurations with a CVI (i.e., configurations A and B), the virtual reactance performs similarly to real reactances such as the filter impedance and the grid impedance. Indeed, the reactance is directly proportional to the harmonic order h. Therefore, the voltage drop across the virtual impedance Δv_v^h shows the same polarity of the grid impedance voltage drop Δv_g^h. Finally, configuration B introduces the contribution of the filter impedance Z_f, resulting in a bigger equivalent impedance under the same conditions [73].

4.3.3 GFL with SVI

This third configuration features a simplified implementation of the virtual impedance, as the derivative term is null. (4.2) becomes:

$$\begin{aligned}
\bar{e}_v &= R_v\bar{i}_i + L_v\cancel{\frac{d\bar{i}_i}{dt}} + j\omega L_v\bar{i}_i + \bar{v}_c \\
&= R_v\bar{i}_i + j\omega L_v\bar{i}_i + \bar{v}_c
\end{aligned} \tag{4.10}$$

The equivalent circuit is shown in Fig. 4.3c. For the generic harmonic order h, (4.10) becomes:

$$\begin{aligned}\bar{e}_v^h &= R_v\bar{i}_i^h + j\omega L_v\bar{i}_i^h + \bar{v}_c^h \\ &= \underbrace{(R_v + R_g)}_{R_{eq}}\bar{i}_i^h + j\underbrace{\omega\left[L_v + (h+1)L_g\right]}_{X_{eq}^h}\bar{i}_i^h + \bar{e}_g^h \\ &= (R_{eq} + jX_{eq}^h)\bar{i}_i^h + \bar{e}_g^h\end{aligned} \tag{4.11}$$

From (4.11), it is evident that the virtual impedance does not depend on the harmonic order h. It exhibits characteristics resembling a real impedance only at the fundamental frequency (i.e., $h = 0$). Conversely, for $h \neq 0$, the equivalent reactance behaves as non physical one. It can be observed that it will be lower than the X_{eq}^h in configurations A and B. This suggests increased current exchange under identical conditions. In particular, for $h < 0$ (e.g., inverse sequence, 5^{th} harmonic, 11^{th} harmonic, etc.), $|X_{eq}^h|$ is:

$$|X_{eq}^h| = |\omega L_v - (|h| - 1)\omega L_g| \tag{4.12}$$

Notably, the virtual and grid reactances contribute with opposite signs if $h < 0$. Moreover, in the particular case of $\omega L_v = (|h|-1)\omega L_g$, the total reactance is canceled and the harmonic current would be limited only by the equivalent resistance, introducing the risk of overcurrent faults. Therefore, during the tuning procedure, L_v must be properly tuned also according to the estimated L_g value.

The same methodology can also be extended to the VSM introduced in [97]. Similar to [71], a low-pass filter is employed in conjunction with the virtual impedance. As previously mentioned, the harmonic and unbalance mitigation capabilities are affected by the cut-off frequency of this filter. Furthermore, the magnitudes of the virtual resistance and reactance adapt dynamically based on operational conditions. Nonetheless, (4.11) remains applicable in this context [73].

4.3.4 GFM with NI

The configuration D can be represented using the circuit shown in Fig. 4.2b, where a zero virtual impedance is assumed due to the direct use of the electromotive force as the voltage reference for the inverter connected to the grid. Thus, the voltage law for the circuit in Fig. 4.2b can be expressed as:

$$\bar{e}_v = R_f \bar{i}_i + L_f \frac{d\bar{i}_i}{dt} + j\omega L_f \bar{i}_i + \bar{v}_c \tag{4.13}$$

The equivalent circuit is shown in Fig. 4.3d. For the generic h-th, (4.13) is:

$$\begin{aligned} \bar{e}_v^h &= R_f \bar{i}_i^h + jh\omega L_f \bar{i}_i^h + j\omega L_f \bar{i}_i^h + \bar{v}_c^h \\ &= \underbrace{(R_f + R_g)}_{R_{eq}} \bar{i}_i^h + j \underbrace{(h+1)\omega(L_f + L_g)}_{X_{eq}^h} \bar{i}_i^h + \bar{e}_g^h \\ &= (R_{eq} + jX_{eq}^h)\bar{i}_i^h + \bar{e}_g^h \end{aligned} \tag{4.14}$$

It is important to note that for this typology, the response under non-ideal grid voltage conditions is solely determined by the physical parameters, without any ability to adjust the equivalent impedance, as is possible with the first three configurations (A, B, and C) [73].

4.3.5 GFM with SVI

The same approach used in 4.3.3 can be adopted for GFM VSMs with SVI. Considering the equivalent circuit in Fig. 4.2b, (4.8) and (4.9) become respectively (4.15) and (4.16):

$$\bar{e}_v = (R_v + R_f)\bar{i}_i + L_f \frac{d\bar{i}_i}{dt} + j\omega(L_v + L_f)\bar{i}_i + \bar{v}_c \tag{4.15}$$

$$\begin{aligned} \bar{e}_v^h =& (R_v + R_f)\bar{i}_i^h + j\omega\left[L_v + (h+1)L_f\right]\bar{i}_i^h + \bar{v}_c^h \\ =& \underbrace{(R_v + R_f + R_g)}_{R_{eq}} \bar{i}_i^h + \\ &+ j \underbrace{\omega\left[L_v + (h+1)(L_f + L_g)\right]}_{X_{eq}^h} \bar{i}_i^h + \bar{e}_g^h \\ =& (R_{eq} + jX_{eq}^h)\bar{i}_i^h + \bar{e}_g^h \end{aligned} \tag{4.16}$$

The equivalent circuit is shown in Fig. 4.3e.

Assuming $h < 0$ (e.g., inverse sequence, 5^{th} harmonic, 11^{th} harmonic, etc.), $|X_{eq}^h|$ is:

$$|X_{eq}^h| = |\omega L_v - (|h| - 1)\omega(L_f + L_g)| \tag{4.17}$$

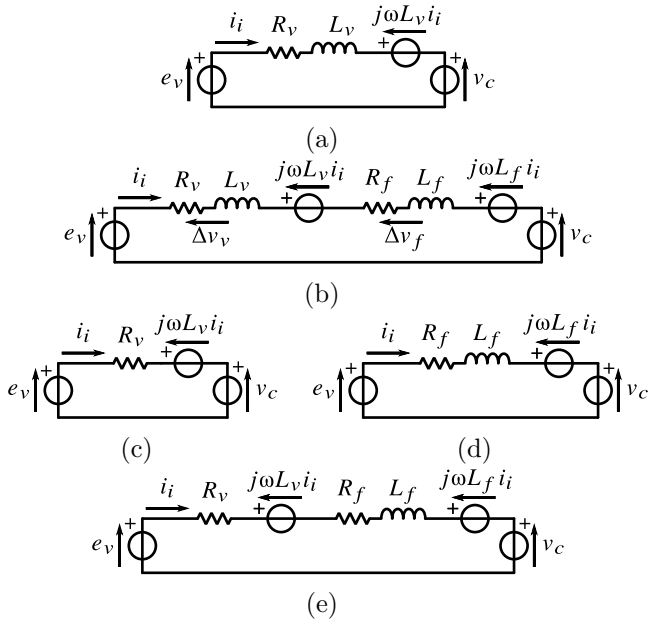

Fig. 4.3 Equivalent circuits in the (d, q) rotating reference frame for first five configurations under study: (a) A; (b) B; (c) C; (d) D; (e) E [73].

Similar to GFL VSMs with SVI, in this configuration, both the virtual and physical reactances contribute with opposite signs when $h < 0$. Specifically, when $\omega L_v = (|h| - 1)\omega(L_f + L_g)$, the equivalent reactance becomes zero. Therefore, even in this case, the harmonic current is solely constrained by the resistances, posing an overcurrent fault risk. Even in such scenarios, it remains crucial to appropriately adjust the virtual inductance [73].

4.3.6 GFL with NI

The last category is dedicated to two GFL models which do not feature a virtual impedance [73].

VISMA is a VSM model based on the 7^{th} order electromagnetic model of conventional synchronous generators whose parameters are selected according to Chapter 3 [99, 100].

The last model is the VSYNC, which does not incorporate a virtual stator. Instead, it generates active power reference using a PLL-based method, whereas the reactive power reference comes from an external control law. From the power references the model generates the reference current. Consequently, its response to distorted grid voltage conditions is directly influenced by the performance of the PLL [101].

Table 4.2 Results of the theoretical analysis [73].

Conf.	R_{eq}	X^h_{eq}		
		Harmonic h	**5^{th} Harmonic ($h = -6$)**	**Inverse Sequence ($h = -2$)**
A	$R_v + R_g$	$(h+1)\omega(L_v + L_g)$	$-5\omega(L_v + L_g)$	$-\omega(L_v + L_g)$
B	$R_v + R_f + R_g$	$(h+1)\omega(L_v + L_f + L_g)$	$-5\omega(L_v + L_f + L_g)$	$-\omega(L_v + L_f + L_g)$
C	$R_v + R_g$	$\omega L_v + (h+1)\omega L_g$	$\omega(L_v - 5L_g)$	$\omega(L_v - L_g)$
D	$R_f + R_g$	$(h+1)\omega(L_f + L_g)$	$-5\omega(L_f + L_g)$	$-\omega(L_f + L_g)$
E	$R_v + R_f + R_g$	$\omega L_v + (h+1)\omega(L_f + L_g)$	$\omega[L_v - 5(L_f + L_g)]$	$\omega[L_v - (L_f + L_g)]$

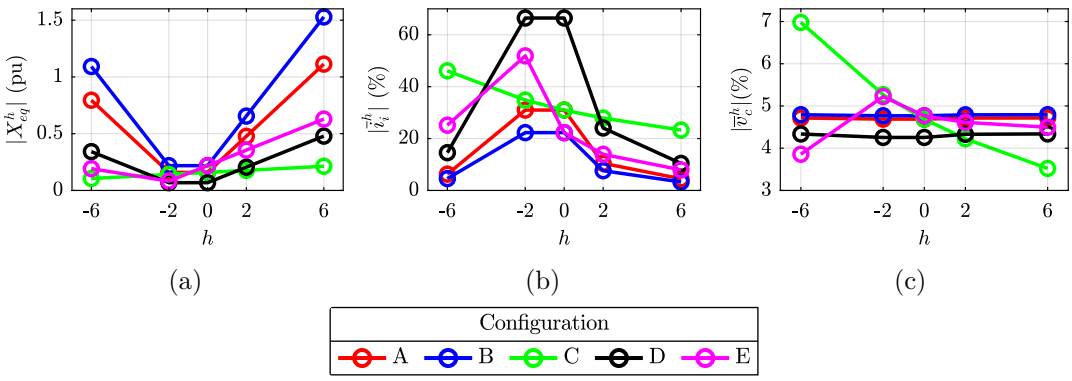

Fig. 4.4 Theoretical values of: (a) equivalent reactance $|X^h_{eq}|$; (b) current amplitude $|\bar{i}^h_i|$; (c) PCC voltage amplitude $|\bar{v}^h_c|$, where h is the harmonic order in the (d, q) rotating reference frame [73].

4.3.7 Theoretical Conclusions

In the (d, q) reference frame synchronized with the fundamental frequency of 50 Hz ($h = 0$), the 5$^{\text{th}}$ harmonic corresponds to 300 Hz ($h = -6$), and the inverse sequence corresponds to 100 Hz ($h = -2$). e_v, generated by the VSM, is zero if $h \neq 0$. Therefore, the current amplitude $|\bar{i}_i^h|$ can be determined in a straightforward way:

$$|\bar{i}_i^h| \approx |\bar{i}_g^h| = \frac{|\bar{e}_g^h|}{\sqrt{R_{eq}^2 + X_{eq}^{h,2}}} \tag{4.18}$$

where the grid voltage amplitude $|\bar{e}_g^h|$ is set to 5%.

Next, the amplitude $|\bar{v}_c^h|$ can be calculated using the voltage divider equation:

$$|\bar{v}_c^h| = \sqrt{\frac{R_i^2 + X_i^{h,2}}{R_{eq}^2 + X_{eq}^{h,2}}} |\bar{e}_g^h| \tag{4.19}$$

where R_i and X_i^h represent the equivalent resistance and reactance on the inverter side between e_v and v_c for the harmonic h.

From (4.19), a VSM improves the voltage quality at the PCC if and only if [73]:

$$\sqrt{\frac{R_i^2 + X_i^{h,2}}{R_{eq}^2 + X_{eq}^{h,2}}} < 1 \Longleftrightarrow (R_i R_g + X_i^h X_g^h) > -\frac{R_g^2 + X_g^{h,2}}{2} \tag{4.20}$$

Assuming positive values for R_v and L_v, configurations A, B and D always satisfies (4.20) because the term $(R_i R_g + X_i^h X_g^h)$ is always positive. Therefore, these configurations are expected to reduce both the fifth harmonic distortion and the unbalance of the PCC voltage regardless of the virtual impedance parameters. Conversely, configurations C and E may have a negative term $(R_i R_g + X_i^h X_g^h)$ because their virtual and physical reactances show opposite signs.

For the configurations C and E, (4.20) becomes respectively as (4.21) and (4.22):

$$(R_v R_g + \omega L_v X_g^h) > -\frac{R_g^2 + X_g^{h,2}}{2} \tag{4.21}$$

$$[(R_v + R_f) R_g + (\omega L_v + X_f^h) X_g^h] > -\frac{R_g^2 + X_g^{h,2}}{2} \tag{4.22}$$

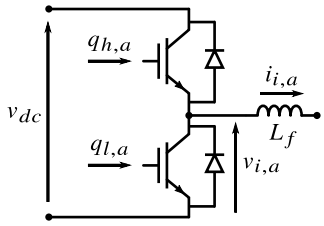

Fig. 4.5 Phase a leg of the IGBT inverter [92].

Based on the values listed in Table 4.1, configuration C increases the voltage distortions in both cases as (4.21) is never satisfied. Conversely, configuration E reduces the 5^{th} harmonic distortion. However, it amplifies the unbalance of the PCC voltage since (4.22) is true only for the fifth harmonic distortion.

More in general, using (4.20) represents an easy and straightforward method to quantify the beneficial or detrimental effects of the VSM under study. The theoretical analysis results are summarized in Table 4.2 and illustrated in Fig. 4.4.

Additionally, this method can be applied separately to the d-axis and q-axis, especially in cases of asymmetric impedances between the two axes [73].

4.4 Dead Time Effect

Considering a two-level converter, a dead-time t_d is necessary between the switching commands of switches within the same leg to prevent shoot-through conditions during switching operations. An example pciture for phase a is illustrated in Fig. 4.5, where $q_{h,a}$ and $q_{l,a}$ denote the commands for the high-side switch and low-side switch. The dead-time generation is depicted in Fig. 4.6, where T_{sw} represents the switching period, v_{tr} is the triangular carrier signal, and v_{mod} is the modulation control voltage. The presence of the dead-time creates a non-linear phase voltage error v_d, as follows [102]:

$$v_d = \frac{4}{3} t_d f_{sw} v_{dc} \text{sign}(i_i) \tag{4.23}$$

where f_{sw} denotes the switching frequency, and $\text{sign}(i_i)$ represents the sign function of the three-phase converter current space vector i_i in a stationary reference frame [102].

The effect of the dead-time affects the output inverter voltage v_i waveform. Fig. 4.7 shows the difference between the phase voltage reference $v^*_{i,a}$ and the moving average of the output inverter voltage $v_{i,a}$ for phase a.

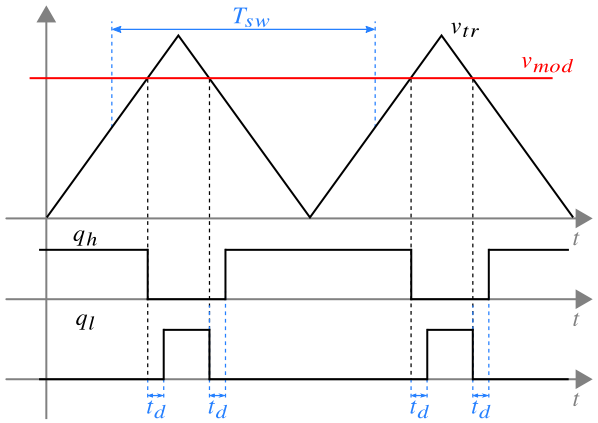

Fig. 4.6 Dead-time generation on the converter control signals [92].

Due to the presence of the dead-time, the waveform of the inverter voltage becomes distorted. The zero crossings of the current determine the deviation of the voltage with respect to its ideal value [103]. To further understand the impact of this voltage error, the sign function is represented in both the stationary reference frame (α, β) and the rotating one (d, q) (rotating at the fundamental frequency ω) [102]. The waveforms are depicted in Fig. 4.8. In the d and q axes, a voltage error with a frequency six times that of the fundamental frequency is superimposed on the mean value. These errors minimally affect the behavior of VSMs at the fundamental frequency. Nevertheless, under non-ideal grid voltage conditions (i.e., in case of voltage unbalance and fifth harmonic), the inverter current sequence also exhibits negative components, as also seen in the previous section. This behavior is illustrated by the waveforms of the sign functions shown in Fig. 4.8 and Fig. 4.8 for voltage unbalance and fifth harmonic distortion, respectively.

In both cases, significant voltage errors are evident on both axes. For voltage unbalance, an error appears on both axes with a frequency twice that of the fundamental frequency, and the d-axis error exhibits a non-zero mean value. Similarly, in the case of fifth harmonic distortion, the error frequency is six times that of the fundamental frequency.

As discussed previously, grid-forming VSMs with open-loop voltage control cannot mitigate these errors due to the absence of closed-loop current control. Therefore, compensating for dead-time is essential to ensure their ability to manage harmonic and unbalance distortions. Various techniques proposing solutions to compensate for the dead-time have been discussed in the literature [103, 104, 102, 105, 106]. In this thesis, the chosen method is based on [103], as it represents one of the simpler solutions available

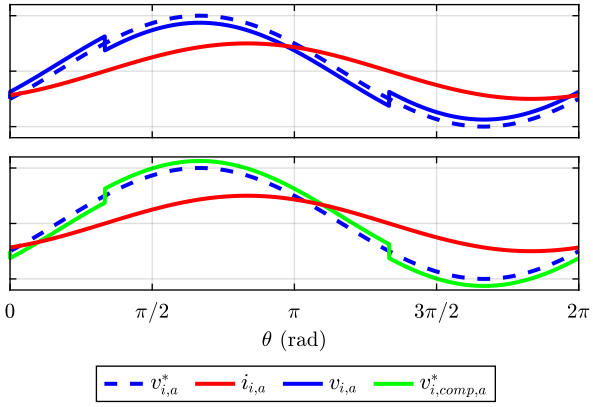

Fig. 4.7 From left to right in the legend: voltage reference v_i^*, the actual inverter current i_i, the inverter voltage moving average v_i and compensated voltage reference $v^*_{i,comp}$ for phase a [92].

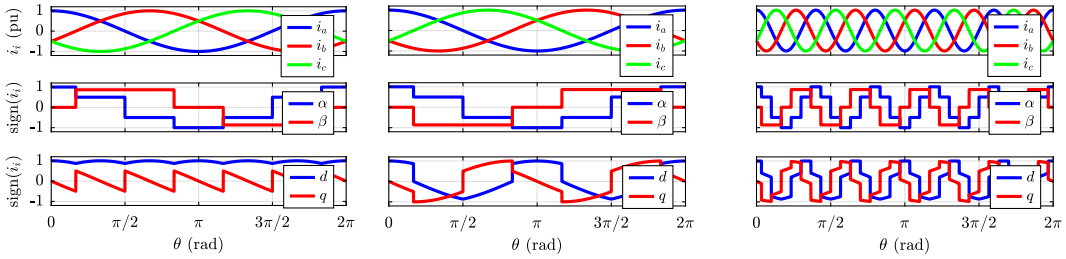

(a) (b) (c)

Fig. 4.8 From top to bottom: three phase current i_i; sign(i_i) in the (α, β) reference frame; sign(i_i) in the (d, q) reference frame. For: (a) direct sequence; (b) negative sequence; (c) fifth harmonic distortion [92].

in the literature. Nevertheless, any technique described in the literature can be applied, as the analysis conducted has broad applicability.

According to [103], the average voltage deviation ΔV, resulting from the accumulation of dead-time pulses, is computed as follows:

$$\Delta V = t_d f_{sw} v_{dc} \tag{4.24}$$

The deviation ΔV serves to compensate for the dead-time by adjusting the three-phase voltage reference v_i^*. Finally, the compensated three-phase voltage reference $v^*_{i,comp}$ can be determined as follows:

$$v^*_{i,comp,k} = \begin{cases} v^*_{i,k} + \Delta V, & \text{if } \text{sign}(i_{i,k}) > 0^- \\ v^*_{i,k} - \Delta V, & \text{if } \text{sign}(i_{i,k}) < 0^+ \end{cases} \tag{4.25}$$

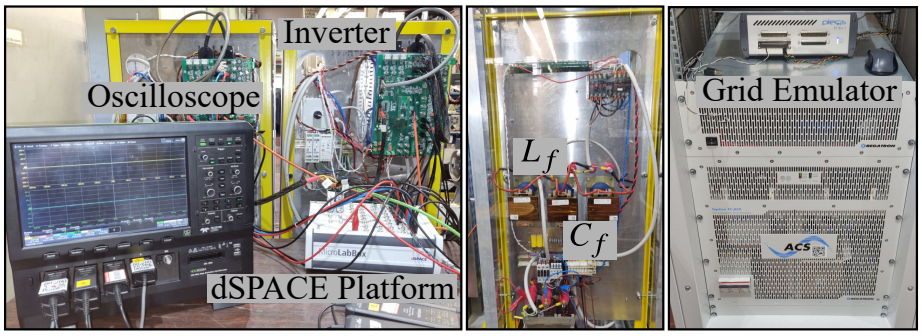

Fig. 4.9 Experimental setup [73].

where k indicates the phase (i.e., a, b or c). The compensated voltage reference waveform is shown in Fig. 4.7 for phase a [92].

4.5 Experimental Tests

This section is divided into two subsection. The first subsection focuses on the experimental validation of the model. In this case, the inverter dead-time of GFM VSMs is already compensated to focus of the match to the theoretical model and to compare the results with the other models [73]. Next, the following subsection focuses on the experimental validation of the inverter dead-time effect of GFM VSMs, showing the behavior of GFM VSMs with and without dead-time compensation under both normal operating conditions and non-ideal grid voltage conditions [92].

The experimental setup used for validation is illustrated in Fig. 4.9. It consists of a two-level three-phase inverter controlled by a dSPACE platform, connected to a grid emulator via an LC filter. The grid emulator imposes the three-phase voltage e_g. Key parameters of the setup are summarized in Table 4.1. R_f represents the combined resistance of the measured LC filter and the ON resistance of the converter IGBTs.

For GFL models, a conventional PI regulator is employed. Additionally, two resonant current controllers are tuned for the second and sixth harmonics (100 Hz and 300 Hz respectively) to enable the inverter to control these harmonic components. Initially, two experimental tests were conducted to validate the proposed simplified method.

The chosen test values are arbitrary but sufficient to highlight differences among the various configurations. Furthermore, the active and reactive power references are set to 0 pu to specifically evaluate the harmonic and unbalance mitigation capabilities [73, 92].

4.5.1 Experimental Model Validation

The two tests to the validate the model are the following [73]:

- Test 1: The grid voltage e_g exhibits 5% fifth harmonic distortion. If the VSM is deactivated, the Discrete Fourier Transform (DFT) applied on the PCC line-to-line voltage $v_{c,ll}$ registers approximately 28 V at the fifth harmonic;
- Test 2: The grid voltage e_g exhibits 5% inverse sequence components. In grid systems, inverse sequence components can occur, especially during asymmetrical faults. The VUF, defined in standard EN 50160, is calculated for the PCC line-to-line voltage $v_{c,ll}$ to quantify the contribution of inverse sequence components. When the VSM control is inactive, the PCC line-to-line voltage shows a VUF of 5%.

4.5.2 Test 1: Fifth Harmonic

The Test 1 results are analyzed using the DFT on the PCC line-to-line voltage $v_{c,ll}$ and the grid current i_g, depicted in Fig. 4.10 and Fig. 4.11.

Configurations with complete virtual impedance (S-VSC and VISMA II) effectively compensate for harmonics. Models corresponding to configurations A and B enhance the voltage quality at the PCC by acting as active filters. Specifically, the fifth harmonic decreases from 28 V to 26 V and 27 V respectively for S-VSC (Fig. 4.10a) and VISMA II (Fig. 4.10b). Similarly, the Osaka model operates as an harmonic sink despite not utilizing a virtual impedance (Fig. 4.10d). Its effectiveness depends on the physical parameters of the grid connection. In these cases (categories A, B, and D), the inverter current induces a voltage drop across the grid impedance, thereby reducing the voltage harmonic distortion. The corresponding current waveforms and their DFTs are illustrated in Fig. 4.11a, Fig. 4.11b, and Fig. 4.11d respectively.

Conversely, the KHI model exacerbates distortion, increasing the 5^{th} harmonic to 39.7 V (Fig. 4.10c). This is attributed to the simplified structure of its virtual reactance, where the voltage drops on the virtual and grid reactances feature opposite signs for $h < 0$, as discussed in sections 4.3.3 and 4.3.7. Since (4.20) is not matched, the voltage distortion increases. Finally, the current waveform and its DFT are illustrated in Fig. 4.11c.

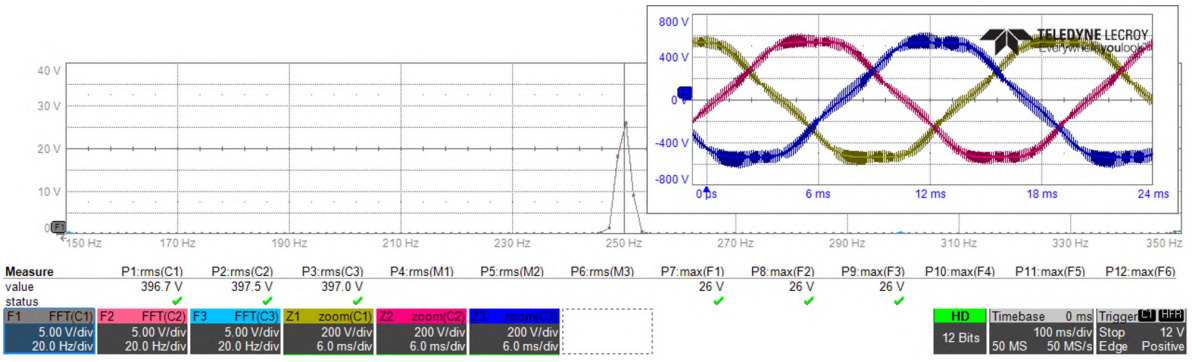

(a)

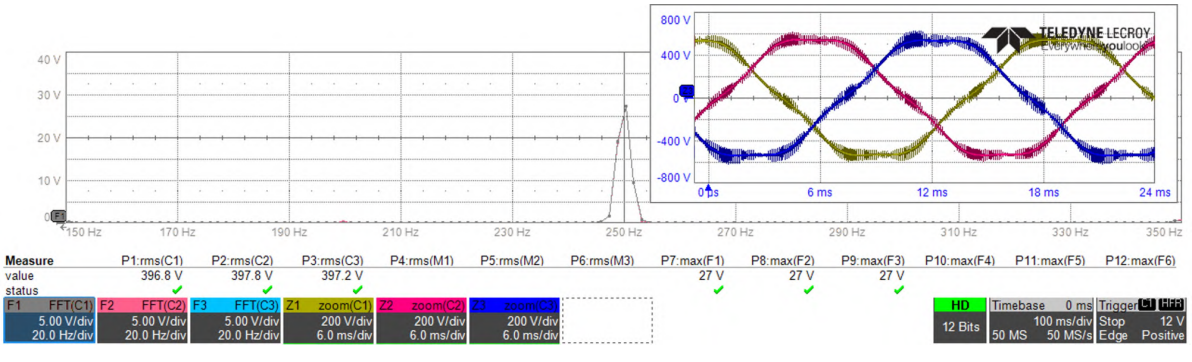

(b)

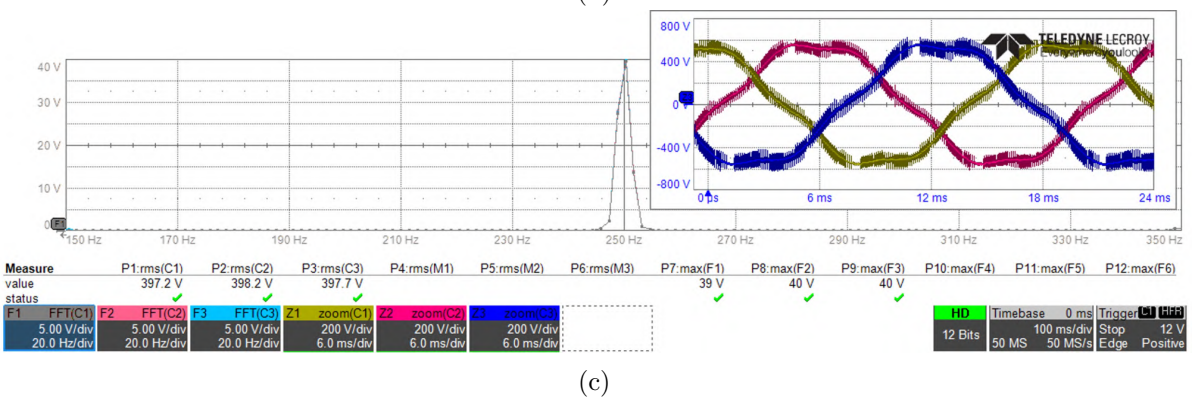

(c)

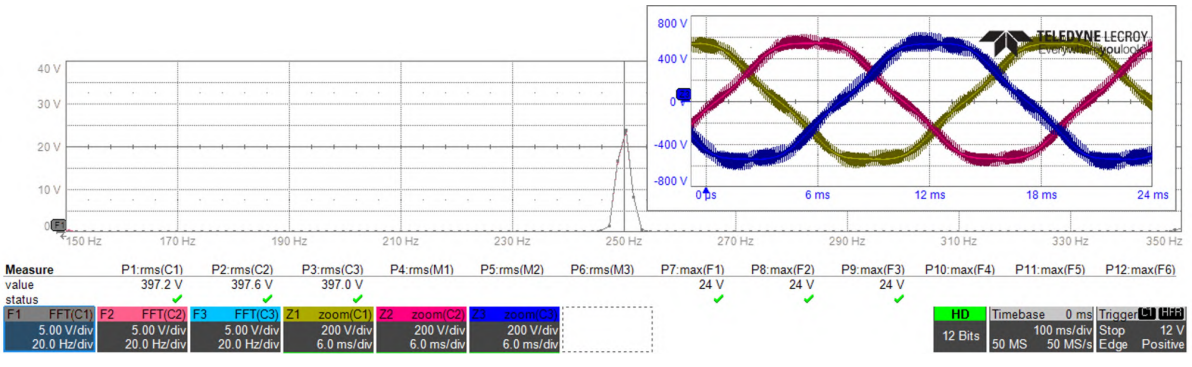

(d)

Fig. 4.10 Test 1 results. DFT of the PCC line to line voltage $v_{c,ll}$, respectively for: (a) S-VSC; (b) VISMA II; (c) KHI; (d) Osaka; (e) Osaka II; (f) VISMA; (g) VSYNC [73] (1/2).

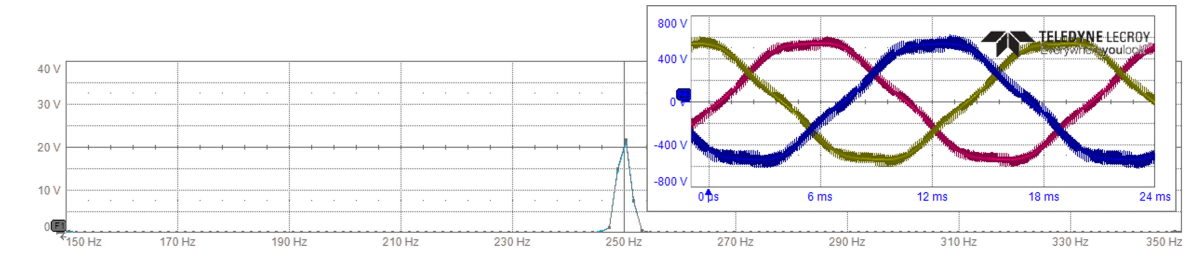

(e)

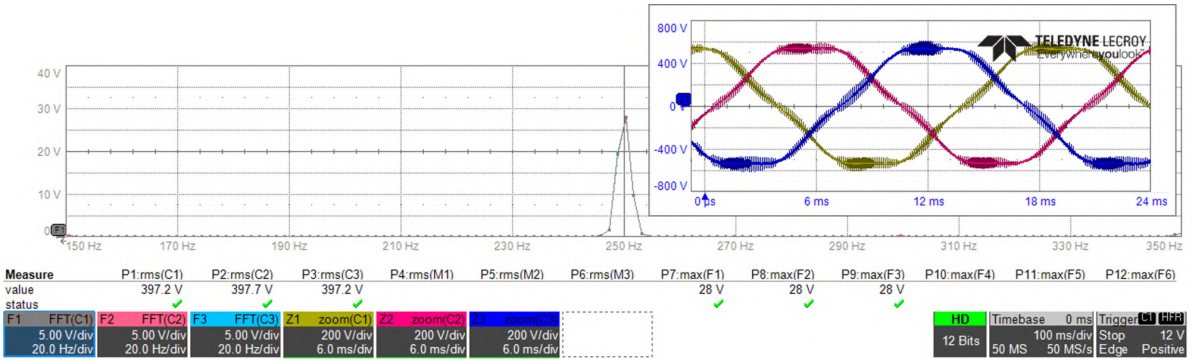

(f)

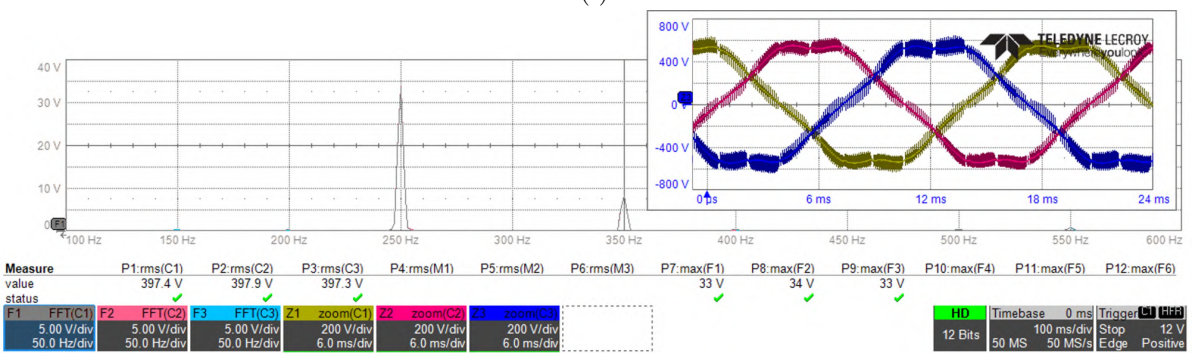

(g)

Fig. 4.10 Test 1 results. DFT of the PCC line to line voltage $v_{c,ll}$, respectively for: (a) S-VSC; (b) VISMA II; (c) KHI; (d) Osaka; (e) Osaka II; (f) VISMA; (g) VSYNC [73] (2/2).

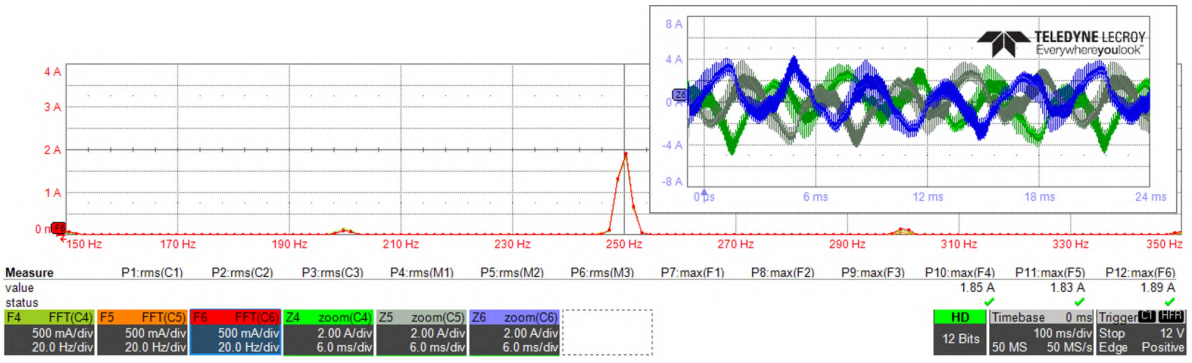

(a)

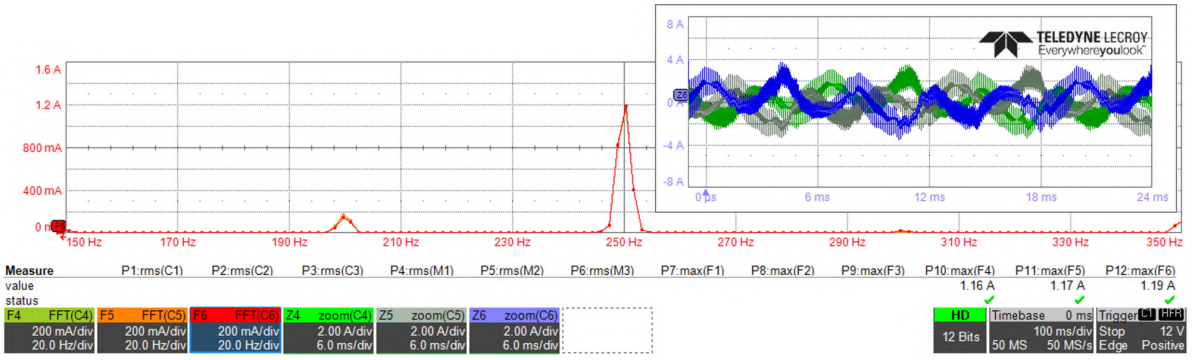

(b)

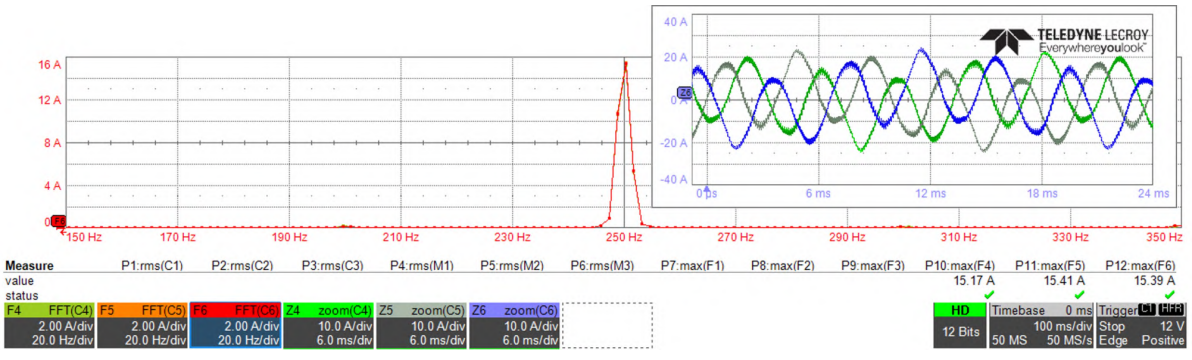

(c)

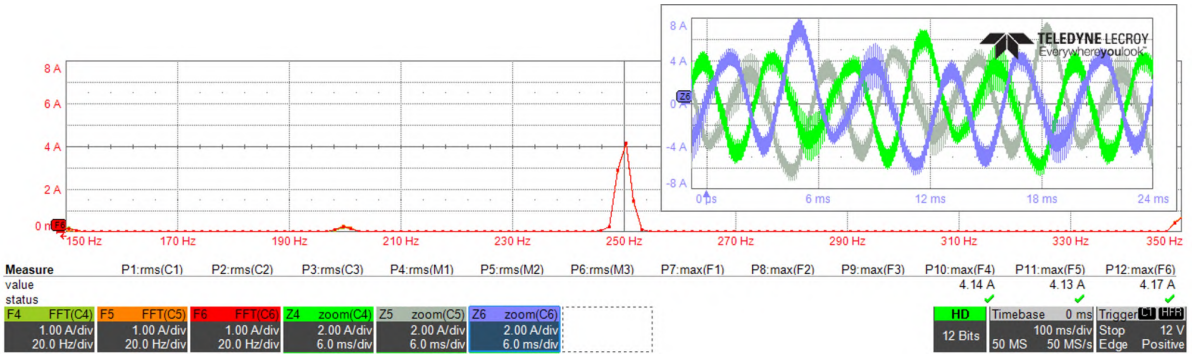

(d)

Fig. 4.11 Test 1 results. DFT of the grid current i_g, respectively for: (a) S-VSC; (b) VISMA II; (c) KHI; (d) Osaka; (e) Osaka II; (f) VISMA; (g) VSYNC [73] (1/2).

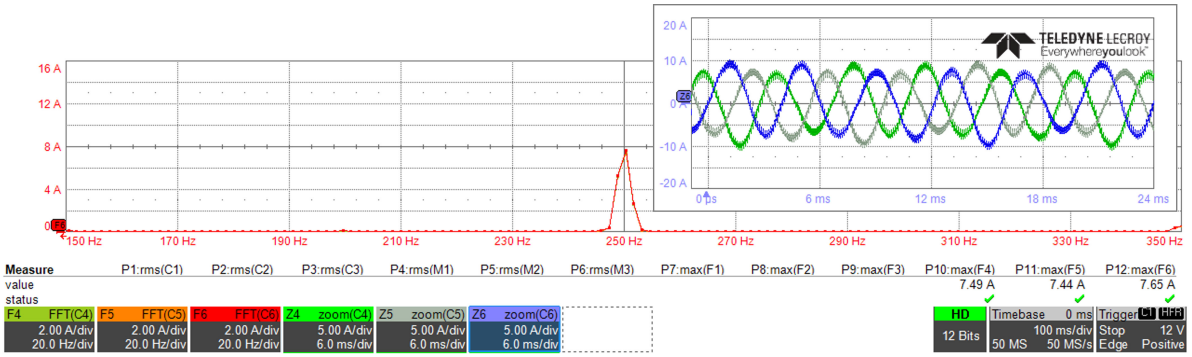

(e)

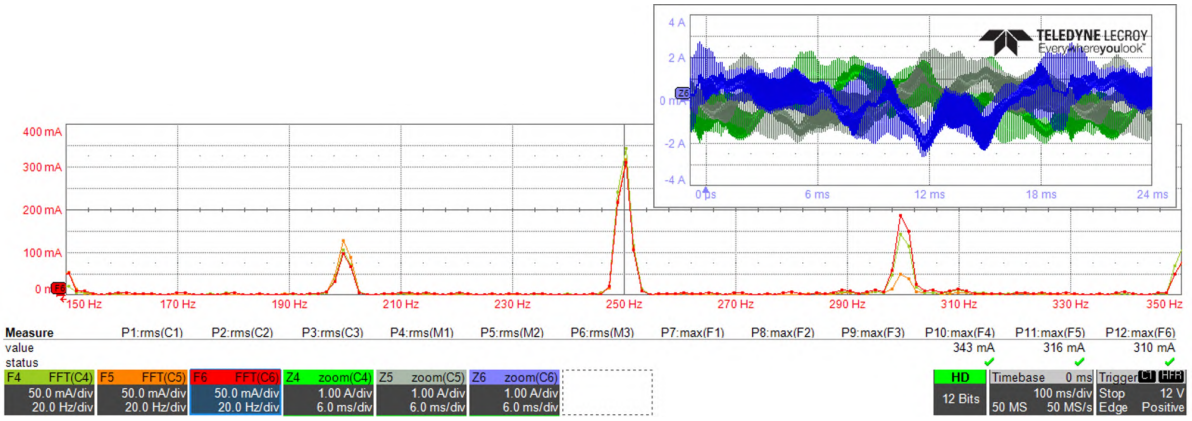

(f)

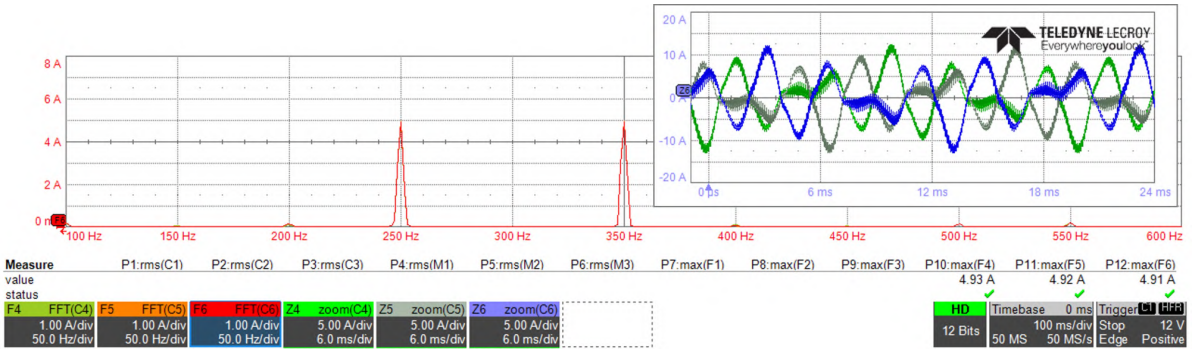

(g)

Fig. 4.11 Test 1 results. DFT of the grid current i_g, respectively for: (a) S-VSC; (b) VISMA II; (c) KHI; (d) Osaka; (e) Osaka II; (f) VISMA; (g) VSYNC [73] (2/2).

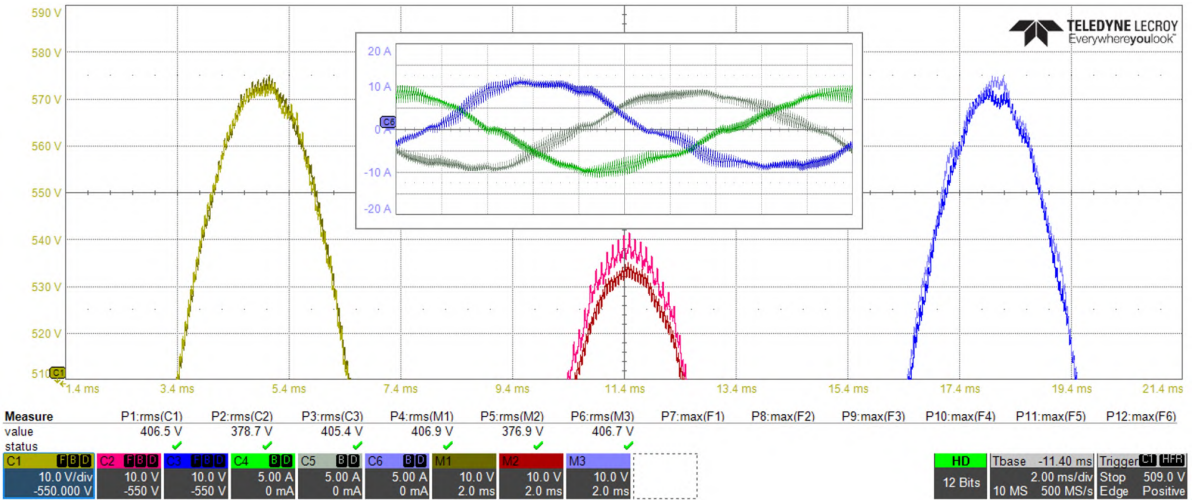

(a)

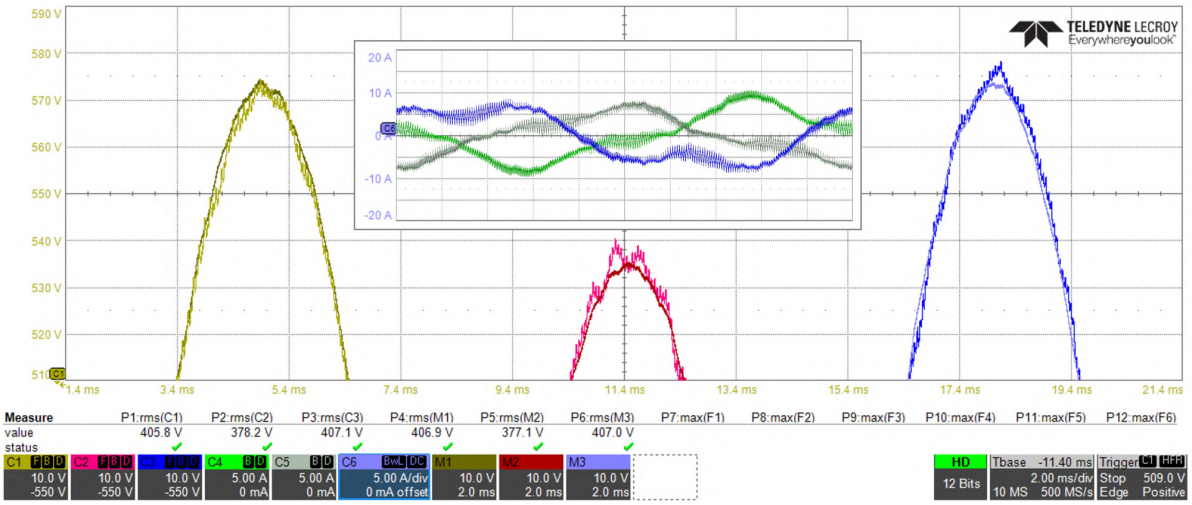

(b)

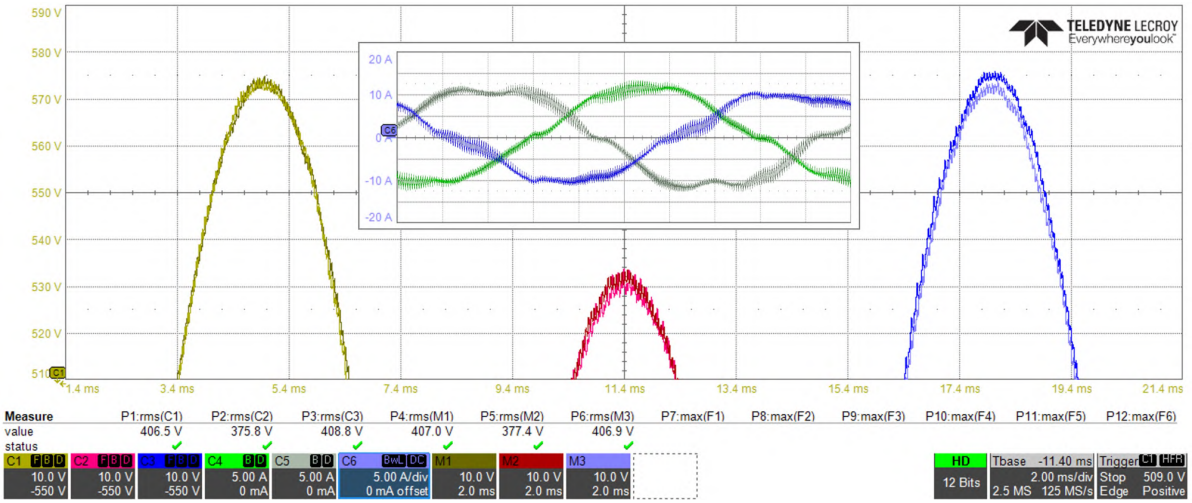

(c)

Fig. 4.12 Test 2 results. The waveforms C1, C2, C3: PCC line to line voltage $v_{c,ll}$ with VSM control; the waveforms C4, C5, C6: grid current i_g with VSM control (time base: 2.0 ms/div); the waveforms M1, M2, M3: unbalanced PCC line to line voltage $v_{c,ll}$ without VSM control. Models: (a) S-VSC; (b) VISMA II; (c) KHI; (d) Osaka; (e) Osaka II; (f) VISMA; (g) VSYNC [73] (1/3).

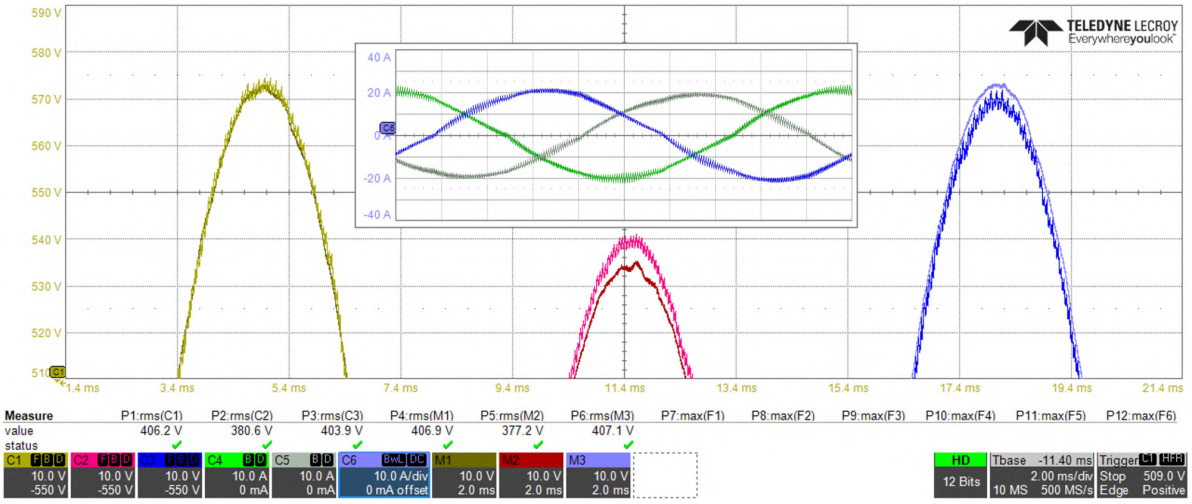

(d)

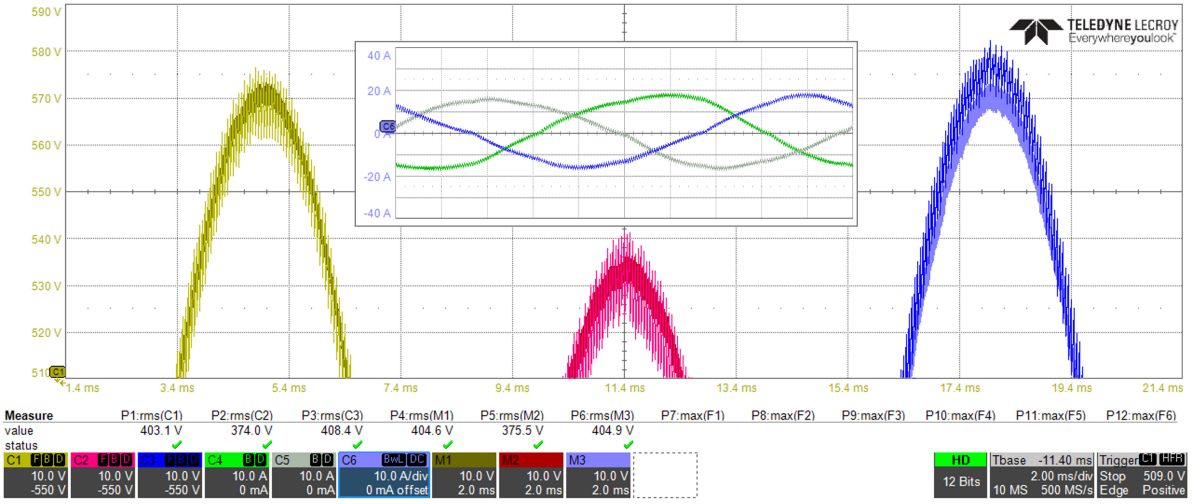

(e)

Fig. 4.12 Test 2 results. The waveforms C1, C2, C3: PCC line to line voltage $v_{c,ll}$ with VSM control; the waveforms C4, C5, C6: grid current i_g with VSM control (time base: 2.0 ms/div); the waveforms M1, M2, M3: unbalanced PCC line to line voltage $v_{c,ll}$ without VSM control. Models: (a) S-VSC; (b) VISMA II; (c) KHI; (d) Osaka; (e) Osaka II; (f) VISMA; (g) VSYNC [73] (2/3).

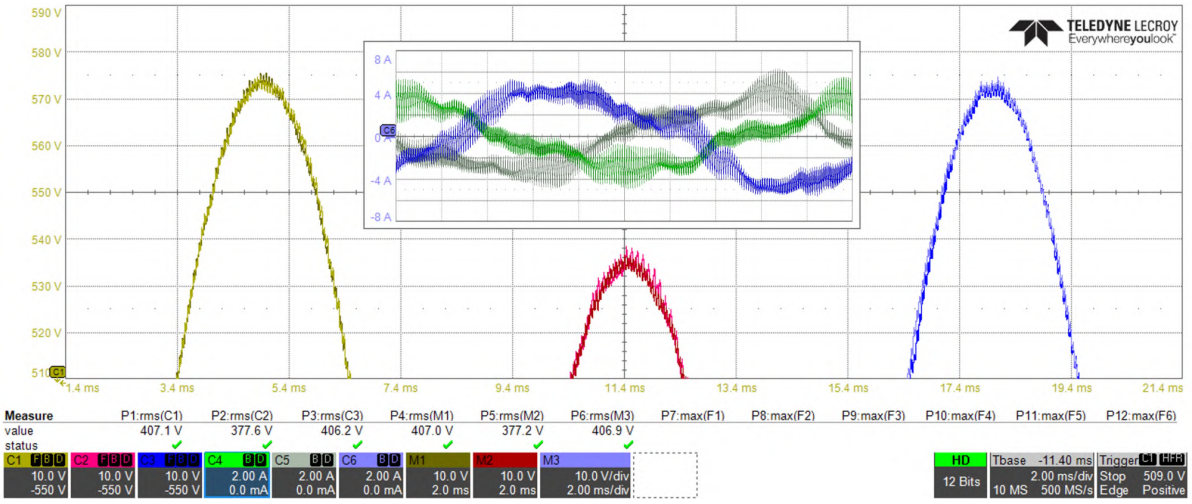

(f)

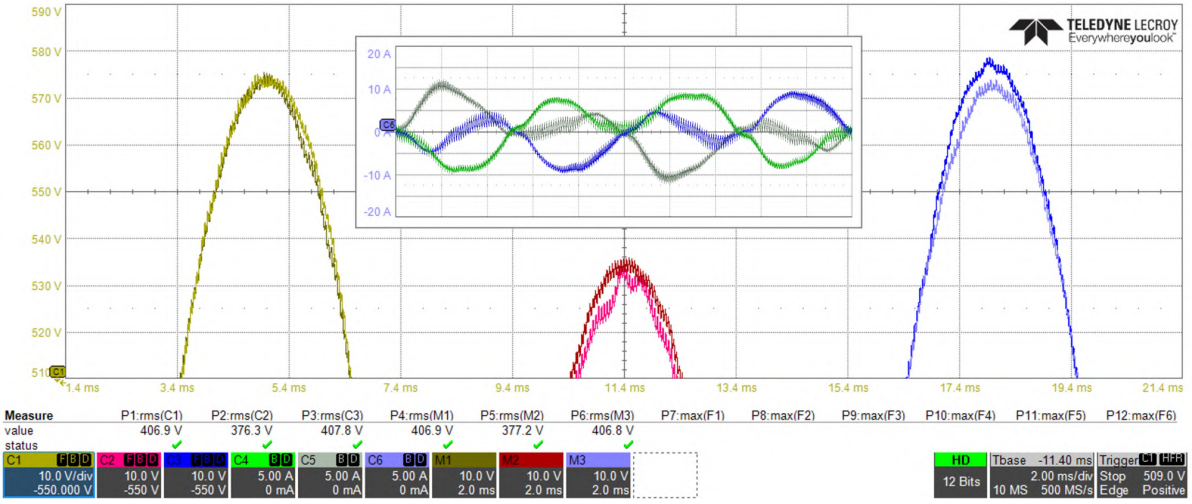

(g)

Fig. 4.12 Test 2 results. The waveforms C1, C2, C3: PCC line to line voltage $v_{c,ll}$ with VSM control; the waveforms C4, C5, C6: grid current i_g with VSM control (time base: 2.0 ms/div); the waveforms M1, M2, M3: unbalanced PCC line to line voltage $v_{c,ll}$ without VSM control. Models: (a) S-VSC; (b) VISMA II; (c) KHI; (d) Osaka; (e) Osaka II; (f) VISMA; (g) VSYNC [73] (3/3).

Table 4.3 Results of Test 1: Fifth Harmonic [73].

Model	$\lvert\bar{i}_g^h\rvert$ (A)		$\lvert\bar{v}_{c,II}^h\rvert$ (V)	
	Theory	**Experimental**	**Theory**	**Experimental**
S-VSC	1.93	1.86	26.57	26
VISMA II	1.4	1.17	27	27
KHI	14.18	15.32	39.3	39.7
Osaka	4.48	4.15	24.43	24
Osaka II	7.74	7.53	21.75	21.3
VISMA	0.49	0.32	27.95	28
VSYNC	4.85	4.92	32.23	33.3

Table 4.4 Results of Test 2: Inverse Sequence [73].

Model	$\lvert\bar{i}_g^h\rvert$ (A)		VUF (%)	
	Theory	**Experimental**	**Theory**	**Experimental**
S-VSC	9.53	9.22	4.69	4.51
VISMA II	6.85	6.58	4.77	4.61
KHI	10.7	10.99	5.27	5.42
Osaka	20.44	20.09	4.25	4.2
Osaka II	15.95	16.05	5.22	5.36
VISMA	3.59	3.58	4.91	4.9
VSYNC	5.04	5.11	5.13	5.22

Configuration E (Osaka II model), like configuration C, features a simplified virtual reactance structure but satisfies (4.20), thereby reducing the voltage distortion as shown in Fig. 4.10e. Fig. 4.11e illustrates the corresponding current waveform and its DFT.

Furthermore, VSYNC degrades the quality of the voltage by increasing the 5^{th} harmonic and introducing a significant 7^{th} harmonic component (Fig. 4.10g and Fig. 4.11g). Lastly, VISMA draws a negligible current that has no impact on the PCC voltage (Fig. 4.11f), maintaining the fifth harmonic at 28 V (Fig. 4.10f).

All the findings are collected in Table 4.3, where the theoretical part for VISMA and VSYNC are derived from PLECS simulations due to the absence of simplified models for these VSMs [73].

4.5.3 Test 2: Inverse Sequence

The Test 2 results are depicted in Fig. 4.12 and listed in Table 4.4. Similar to Table 4.3, the theoretical benchmarks for VISMA and VSYNC are obtained from PLECS simulations. Many observations from Test 1 remain applicable here as well.

The S-VSC, VISMA II, and Osaka models demonstrate positive effects by reducing voltage unbalance, as evident in Fig. 4.12a, Fig. 4.12b, and Fig. 4.12d, respectively. Specifically, the RMS voltage of the smallest phase (C2) increases compared to the previous condition (M2), while the other two phases decrease, resulting in an overall reduction of the VUF.

Conversely, the KHI (Fig. 4.12c), Osaka II (Fig. 4.12e), and VSYNC (Fig. 4.12g) configurations led to the unbalance amplification: phase b becomes significantly smaller (C2 compared to M2), and phase c increases (C3 compared to M3), leading to a VUF higher than 5%. In these cases, configurations C and E do not satisfy (4.20).

Finally, the VISMA model marginally reduces the PCC voltage unbalance, as illustrated in Fig. 4.12f [73].

4.5.4 Experimental Dead-time Effect Validation

Two GFM VSMs, namely the Osaka model and the VISMA II model, are selected for experimental validation to assess the negative effect of dead-time and the beneficial effects of its compensation on harmonic and unbalance sink capabilities. These models share identical design parameters such as virtual inertia, damping coefficient, etc., which were tuned as per the methodology outlined in Chapter 3 [92].

Initially, a preliminary test is conducted to demonstrate that the switching dead-time has negligible effects on the normal operating conditions of VSMs. Subsequently, two experimental tests are carried out to evaluate the negative influence of dead-time and the beneficial effect of dead-time compensation. The three tests are the following [92]:

- Test 3: active power reference step from 0.3 pu to 0.4 pu. This test is designed to observe the dynamic response of the VSM models when they are required to adjust their power setpoint. Such scenarios mimic real-world situations where there are variations in power output from renewable energy sources connected to the DC side of the converter;
- Test 4: grid voltage e_g with 5% of negative sequence;

- Test 5: grid voltage e_g with 10% of fifth harmonic distortion.

For Test 4 and Test 5, the expected sink capabilities of the VSMs are respectively translated in the reduction of the voltage unbalance factor (VUF) and the fifth harmonic distortion on the PCC voltage $v_{c,ll}$ as for the previous subsection [92].

4.5.5 Test 3: Active power reference step

Test 3 illustrates that the switching dead-time has no impact on the VSM performance at the fundamental frequency due to compensation by the power loop control. In this initial test, a dead-time of 3 µs and a switching frequency of 10 kHz are employed. The results of this test are presented in Fig. 4.13. It is evident that even without dead-time compensation, both the Osaka model and VISMA II model track the power reference accurately without any steady-state error.

Subsequently, the test is repeated with the activation of dead-time compensation. Fig. 4.13a shows that the compensation does not affect the steady-state operation of the VSMs, confirming expected behavior. Therefore, dead-time compensation can be enabled to ensure the VSM capability to mitigate harmonics and unbalance, while maintaining performance during normal operational conditions.

Finally, the test is conducted with a dead-time of 1.1 µs, which is the minimum recommended by the inverter manufacturer, both with and without compensation. The results are shown in Fig. 4.13b. Even in this scenario, the VSMs maintain their performance during normal operating conditions [92].

4.5.6 Test 4: 5% of voltage unbalance

Considering (4.18), the theoretical peak current values for Osaka and VISMA II are 20.12 A and 6.82 A, respectively. The results of the test are presented in Fig. 4.14 and summarized in Table 4.5. During the initial 100 ms interval, dead-time compensation is disabled. It is evident that the current amplitudes are significantly lower than the expected values (1.77 A observed against the expected 20.12 A for Osaka and 1.62 A observed against the expected 6.82 A for VISMA II).

Subsequently, dead-time compensation is enabled. After a transient period, the Osaka current amplitudes converge to 19.88 A, whereas the the VISMA II current amplitudes settles at 6.62 A (close to the theoretical values 20.12 A and 6.82 A, respectively).

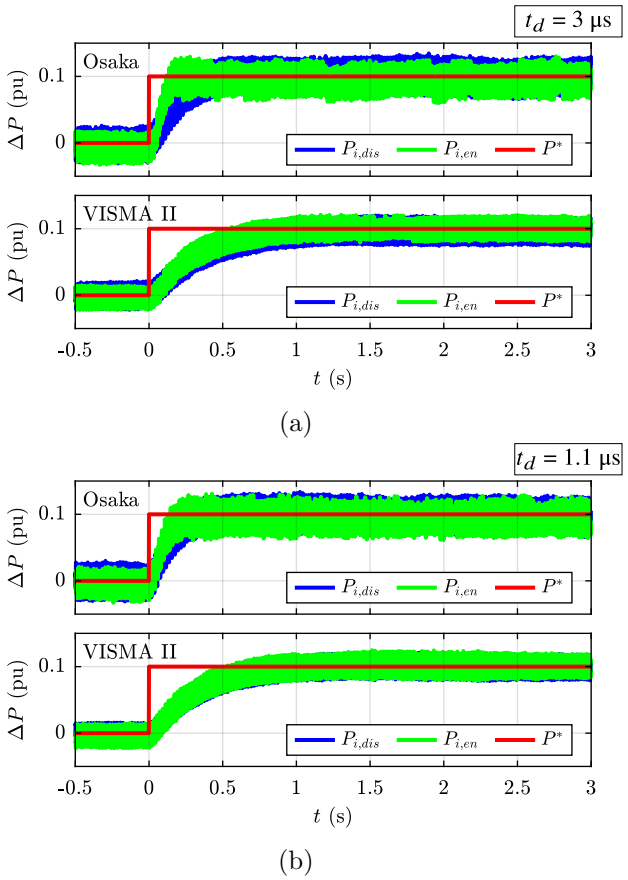

Fig. 4.13 Results of Test 3: Active power variation injected by the inverter after a reference step of 0.1 pu when the dead-time compensation is disabled ($P_{i,dis}$) and enabled ($P_{i,en}$): (a) t_d = 3 µs; (b) t_d = 1.1 µs [92].

This demonstrates the validity of both the modeling approach and the effectiveness of dead-time compensation.

Next, the dead-time value is reduced from 3 µs to 1.1 µs, and the updated results are shown in Fig. 4.15 and Table 4.5. As anticipated, the adverse effects of dead-time are reduced compared to the previous case due to the lower dead-time duration. However, dead-time compensation remains essential to achieve the theoretical current values accurately.

Finally, Test 4 is repeated with switching frequencies of 15 kHz and 20 kHz, while maintaining a dead-time of 1.1 µs. The 20 kHz frequency is the maximum allowable for safe steady-state operation of the converter at nominal power. The results are shown in Fig. 4.16 and Fig. 4.17, and summarized in Table 4.5. Increasing the switching frequency results in a decrease of the injected current without dead-time compensation, as the voltage error is directly proportional to the switching frequency. However, in each test

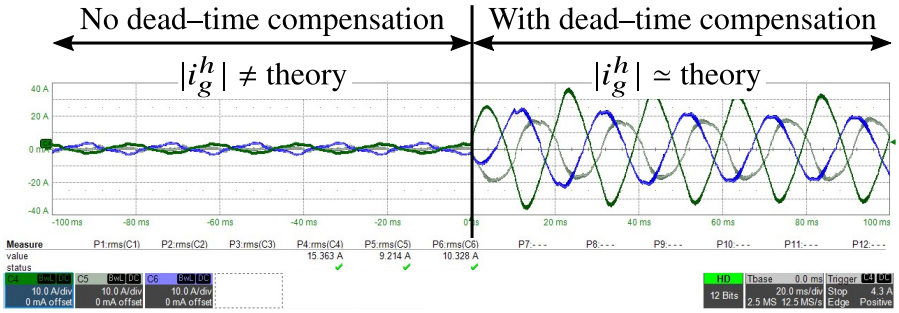

(a)

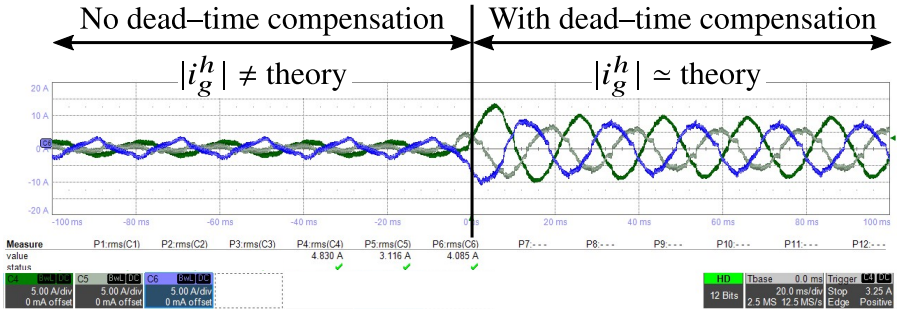

(b)

Fig. 4.14 Results of Test 4, $t_d = 3$ µs, $f_{sw} = 10$ kHz. Grid measured current i_g for Osaka (a) and VISMA II (b) [92].

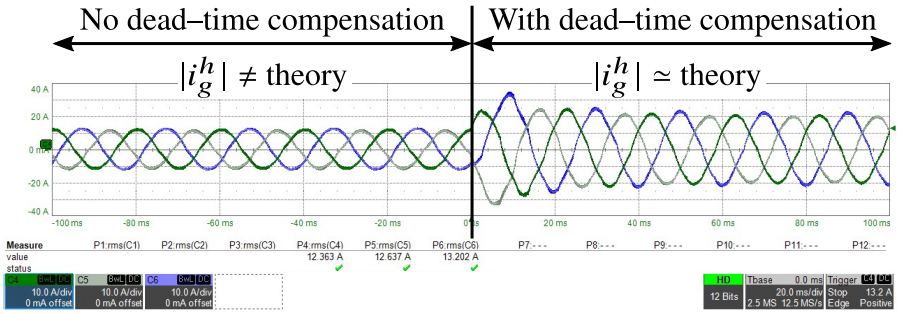

(a)

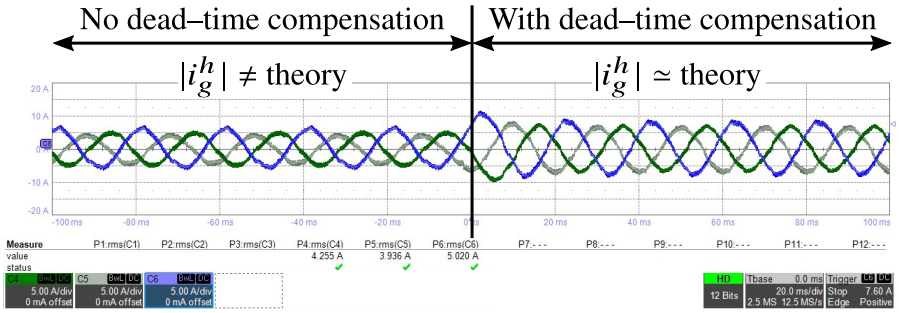

(b)

Fig. 4.15 Results of Test 4, $t_d = 1.1$ µs, $f_{sw} = 10$ kHz. Grid measured current i_g for Osaka (a) and VISMA II (b) [92].

Table 4.5 Results of Test 4: current amplitudes in case of 5% of grid voltage unbalance [92].

VSM	t_d **(µs)**	f_{sw} **(kHz)**	$t_d f_{sw}$ (%)	$\lvert\bar{i}_i^h\rvert$ **(A)** **No Comp.**	**With Comp.**	**Theoretical**
Osaka	3	10	3	1.77	19.88	20.12
	1.1	10	1.1	10.56	19.98	
	1.1	15	1.65	7.70	20.09	
	1.1	20	2.2	5.02	20.15	
VISMA II	3	10	3	1.62	6.62	6.82
	1.1	10	1.1	4.79	6.72	
	1.1	15	1.65	3.90	6.80	
	1.1	20	2.2	3.10	6.89	

Table 4.6 Results of Test 4: VUF in case of 5% of grid voltage unbalance [92].

VSM	t_d **(µs)**	f_{sw} **(kHz)**	$t_d f_{sw}$ (%)	**VUF** (%) **No Comp.**	**With Comp.**
Osaka	3	10	3	4.84	4.13
	1.1	10	1.1	4.23	4.15
	1.1	15	1.65	4.37	4.10
	1.1	20	2.2	4.66	4.19
VISMA II	3	10	3	4.74	4.59
	1.1	10	1.1	4.69	4.67
	1.1	15	1.65	4.73	4.65
	1.1	20	2.2	4.82	4.58

scenario, enabling dead-time compensation brings the injected current closer to the theoretical values, underscoring the necessity of dead-time compensation to mitigate these effects.

Furthermore, the VUF, defined in standard EN 50160, is calculated for the PCC line-to-line voltage $v_{c,ll}$ to quantify the presence of negative sequence components. When VSM control is disabled, the VUF is measured at 5%. Table 4.6 compiles the VUF results for all tests. It shows that compensating for dead-time and reducing the injected current leads to a decrease in VUF, thereby enhancing the unbalance sink capability of VSMs.

These results emphasize the critical role of dead-time compensation in maintaining VSM performance and improving grid stability under varying operating conditions [92].

Table 4.7 Results of Test 5: current amplitude in case of 10% of grid voltage fifth harmonic distortion [92].

VSM	t_d (µs)	f_{sw} (kHz)	$t_d f_{sw}$ (%)	$\lvert\bar{i}_i^h\rvert$ (A) No Comp.	With Comp.	Theoretical
Osaka	3	10	3	4.61	8.48	8.86
	1.1	10	1.1	7.30	8.61	
	1.1	15	1.65	6.83	8.60	
	1.1	20	2.2	6.39	8.68	
VISMA II	3	10	3	1.73	2.66	2.80
	1.1	10	1.1	2.66	3.02	
	1.1	15	1.65	2.55	2.98	
	1.1	20	2.2	2.46	3.01	

Table 4.8 Results of Test 5: voltage amplitude in case of 10% of grid voltage fifth harmonic distortion [92].

VSM	t_d (µs)	f_{sw} (kHz)	$t_d f_{sw}$ (%)	$\lvert\bar{v}_{c,ll}^h\rvert$ (V) No Comp.	With Comp.
Osaka	3	10	3	51.71	48.16
	1.1	10	1.1	48.12	47.70
	1.1	15	1.65	47.87	47.10
	1.1	20	2.2	48.35	47.00
VISMA II	3	10	3	55.63	53.74
	1.1	10	1.1	53.84	53.70
	1.1	15	1.65	53.33	52.86
	1.1	20	2.2	53.10	52.62

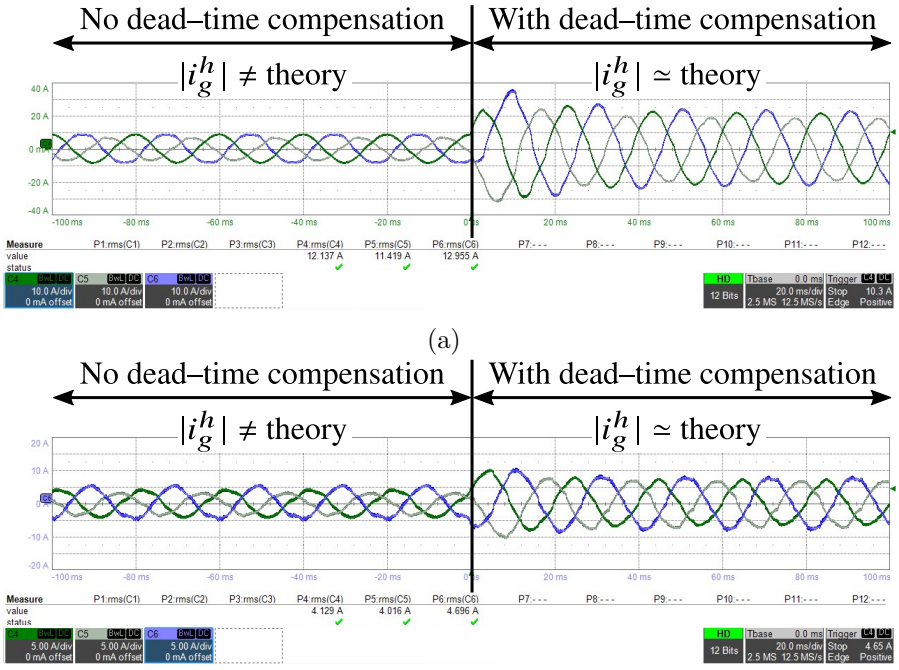

Fig. 4.16 Results of Test 4, $t_d = 1.1$ µs, $f_{sw} = 15$ kHz. Grid measured current i_g for Osaka (a) and VISMA II (b) [92].

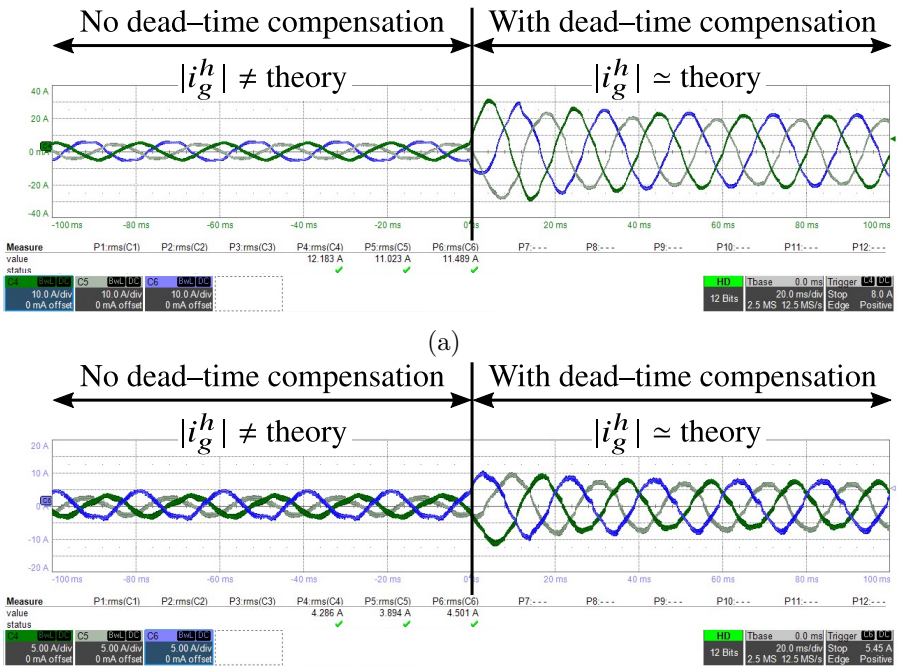

Fig. 4.17 Results of Test 4, $t_d = 1.1$ µs, $f_{sw} = 20$ kHz. Grid measured current i_g for Osaka (a) and VISMA II (b) [92].

4.5.7 Test 5: 10% of fifth harmonic distortion

The Test 5 results are presented in Fig. 4.18 and Table 4.7. Similar to the previous tests, during the initial 100 ms interval, the dead-time is not compensated. In this period, the current amplitudes show a lower value compared to the theoretical ones calculated by (4.18): 4.61 A instead of 8.86 A for Osaka and 1.73 A instead of 2.80 A for VISMA II. Subsequently, when the dead-time is compensated, the current peak values almost align with the theoretical ones (Osaka 8.48 A and VISMA II 2.66 A, against 8.86 A and 2.80 A respectively).

Next, Test 5 is repeated with different dead-time values and switching frequencies, as shown in Figs. 4.19, 4.20, and 4.21, and summarized in Table 4.7. As anticipated, a decrease in the switching dead-time results in less reduction of current amplitude from the ideal case. Conversely, without dead-time compensation, increasing the switching frequency leads to a decrease in current amplitude. When the VSM control is disabled, the DFT of the PCC line-to-line voltage $v_{c,ll}$ indicates a fifth harmonic voltage amplitude of approximately 56 V. The calculated fifth harmonic voltage amplitudes $|\overline{v}^{h}_{c,ll}|$ for all testing conditions are detailed in Table 4.8. It is evident that compensating for dead-time increases the harmonic current flow, thereby reducing fifth harmonic voltage distortion. Thus, Test 5 underscores the effectiveness of dead-time compensation in enhancing the harmonic sink capability of VSMs, demonstrating its critical role in maintaining performance under varying operational conditions [92].

4.6 Conclusion & Main Contributions

Virtual Synchronous Machines (VSMs) represent a promising solution for enabling renewable energy plants to provide grid services, particularly in terms of harmonic and unbalance compensation. This chapter has introduced a method to foresee the response of different VSM configurations, which was experimentally validated using five distinct VSM models across various configurations. The theoretical analysis confirmed the effectiveness and reliability of the simplified modeling approach in identifying which VSM configurations can effectively compensate for harmonic and unbalance distortions, thereby improving voltage quality at the Point of Common Coupling (PCC).

According to the analysis summarized in Table 4.9, VSM models that fully implement virtual impedance (such as S-VSC and VISMA II) act as effective harmonic and unbalance sinks, consistent with the theoretical predictions. These models operate akin to active

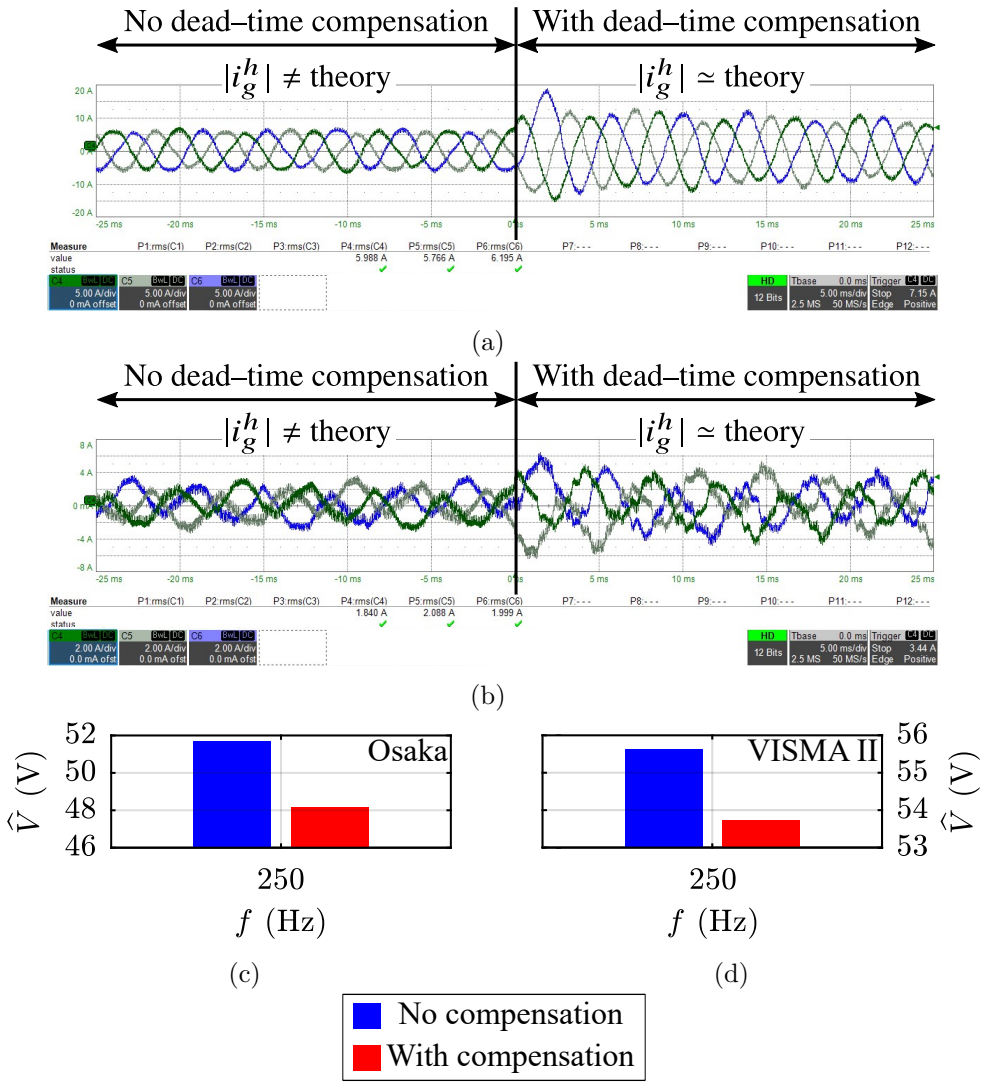

Fig. 4.18 Results of Test 5, $t_d = 3$ µs, $f_{sw} = 10$ kHz. Grid measured current i_g for Osaka (a) and VISMA II (b). Mean DFT of the PCC measured line to line voltage for Osaka (c) and VISMA II (d) [92].

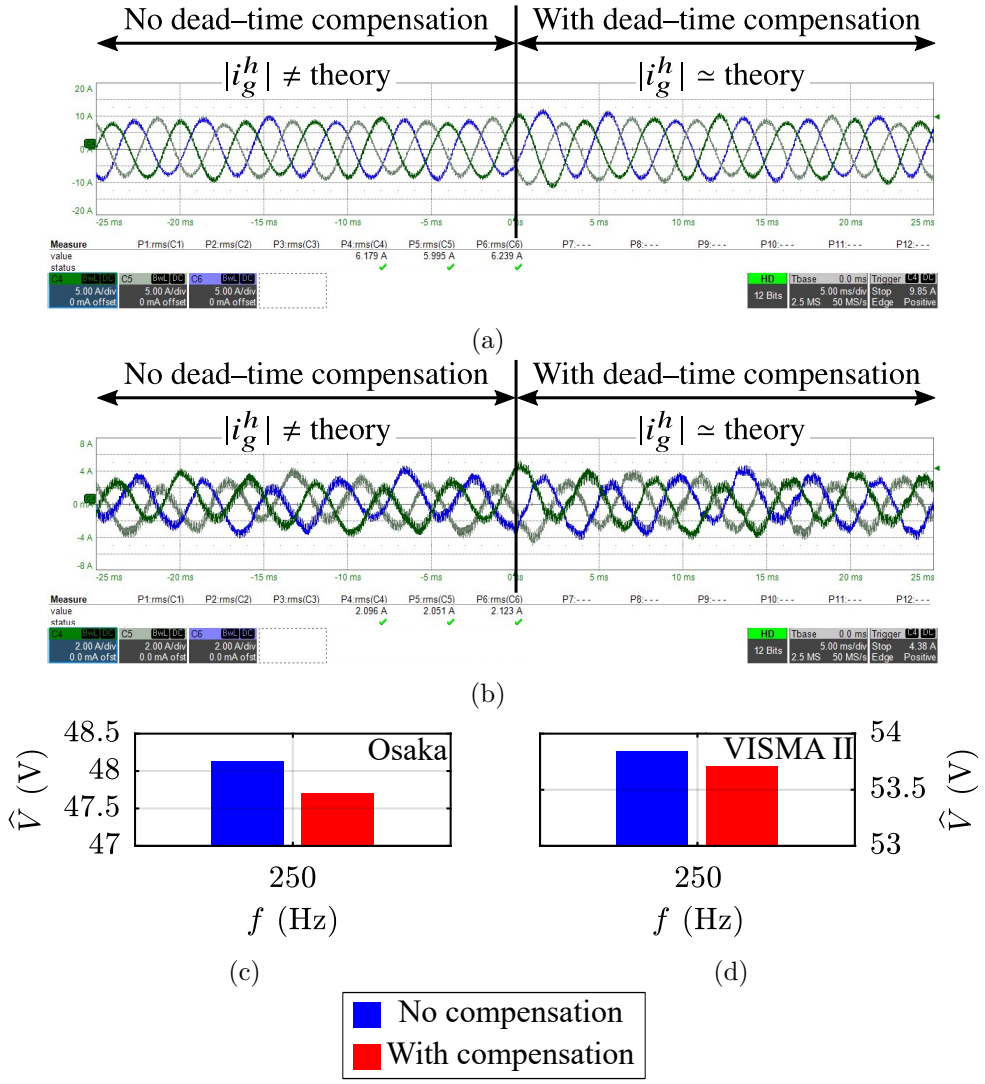

Fig. 4.19 Results of Test 5, $t_d = 1.1$ µs, $f_{sw} = 10$ kHz. Grid measured current i_g for Osaka (a) and VISMA II (b). Mean DFT of the PCC measured line to line voltage for Osaka (c) and VISMA II (d) [92].

filters, significantly enhancing PCC voltage quality. Even grid-forming VSMs without virtual impedance (e.g., Osaka) demonstrate a positive impact on PCC voltage, although their effectiveness depends on system-specific physical parameters (such as filter and grid impedances).

The configurations with a complete impedance (i.e, A, B, and D) incorporate the necessary features to ensure VSMs operate effectively as harmonic/unbalance sinks, without constraints related to virtual parameter selection. In contrast, VSMs with simplified implementation of the virtual impedance (e.g., KHI and Osaka II) may either reduce or amplify the voltage harmonic content depending on parameter choices.

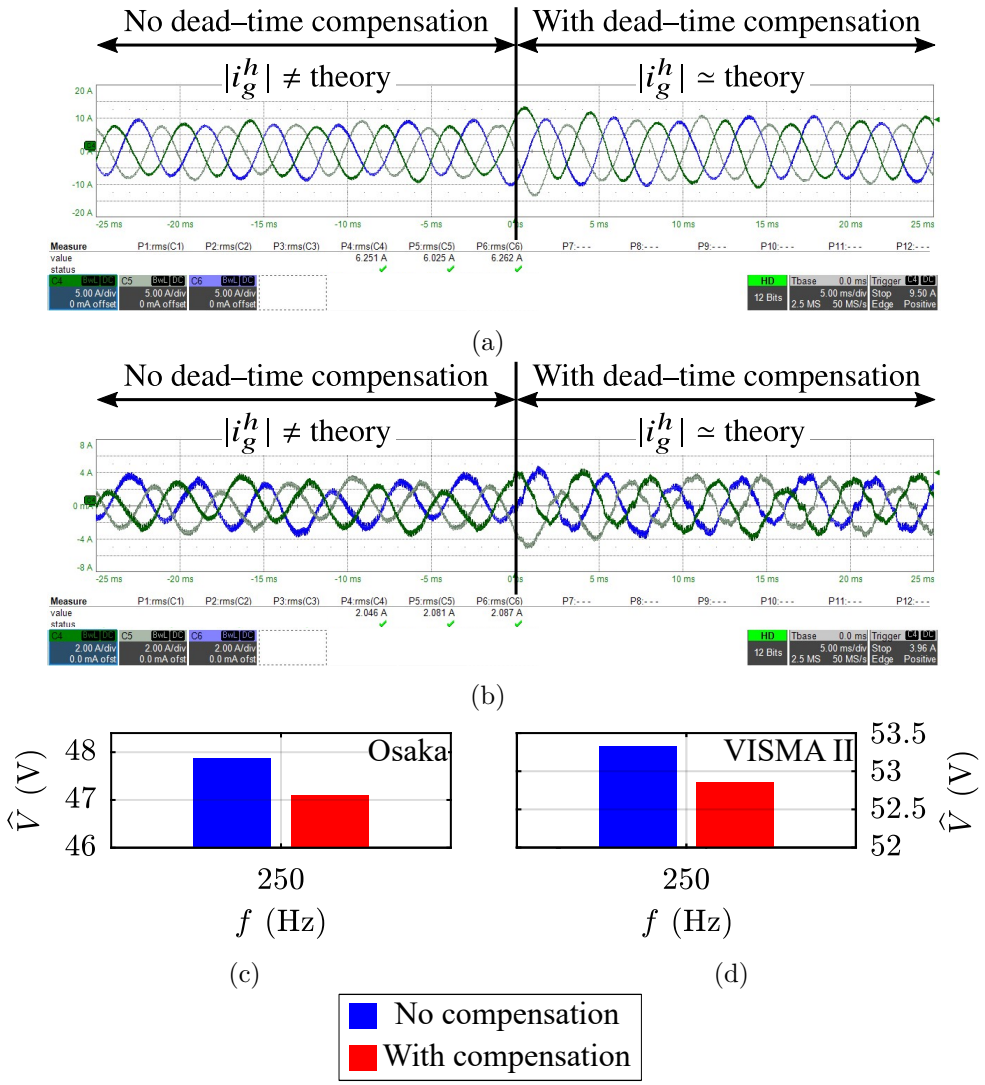

Fig. 4.20 Results of Test 5, $t_d = 1.1$ µs, $f_{sw} = 15$ kHz. Grid measured current i_g for Osaka (a) and VISMA II (b). Mean DFT of the PCC measured line to line voltage for Osaka (c) and VISMA II (d) [92].

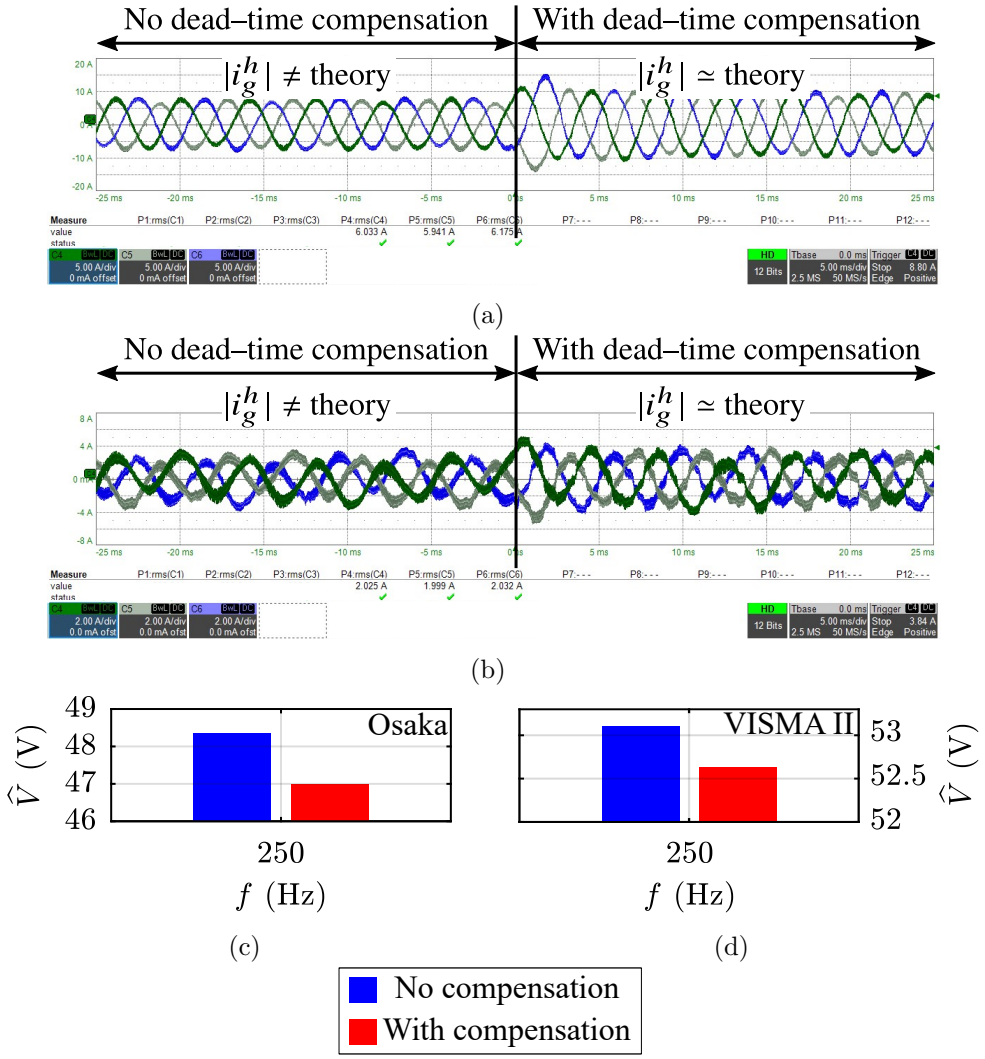

Fig. 4.21 Results of Test 5, $t_d = 1.1$ µs, $f_{sw} = 20$ kHz. Grid measured current i_g for Osaka (a) and VISMA II (b). Mean DFT of the PCC measured line to line voltage for Osaka (c) and VISMA II (d) [92].

Configuration C amplifies distortions as it fails to satisfy (4.20), whereas configuration E decreases the fifth harmonic distortion, but increases PCC voltage unbalance due to partial satisfaction of (4.20) only for fifth harmonic [73].

Furthermore, considering the effect of dead-time, experiments with Osaka and VISMA II models demonstrated significant discrepancies in current injection when dead-time compensation was not applied. This limitation worsens the harmonic and unbalance sink capabilities of VSMs. However, upon enabling dead-time compensation, experimental results closely matched theoretical expectations, validating the effectiveness of the proposed compensation method. Moreover, dead-time compensation reduced the VUF and

Table 4.9 Harmonic and unbalance sink capability of the VSMs under study [73].

Group	**Model**	**Harmonic and Unbalance Sink Capability**			
		Tunable	**Harmonic**	**Inverse Sequence**	**Z_v Constrain**
A	S-VSC	✔	✔	✔	✔
B	VISMA II	✔	✔	✔	✔
C	KHI	✔	✘	✘	✘
D	Osaka	✘	✔	✔	-
E	Osaka II	✔	✔	✘	✘
F	VISMA	✘	✔	✔	-
	VSYNC	✘	✘	✘	-

fifth harmonic voltage amplitude compared to non-compensated scenarios, underscoring its role in enhancing VSM capabilities.

Notably, the experiments confirmed that dead-time and its compensation did not compromise VSM performance during normal grid operations (e.g., active power injection and setpoint changes). This study conclusively demonstrates that dead-time compensation is indispensable for ensuring robust harmonic and unbalance sink capabilities in grid-forming VSMs while maintaining performance under varying operational conditions [92].

Chapter 5

Grid-Forming S-VSC

5.1 Introduction

Previous papers demonstrated that the S-VSC model can provide inertial behavior, grid support during faults and harmonic compensation in grid-following operation [81, 107]. However, it has never been examined whether the S-VSC can operate even in island-mode. Therefore, this chapter proposes an extension of the S-VSC for the control of a microgrid both in grid-connected and island-mode. The proposed S-VSC model is able to provide all the aforementioned grid services, including the island capability, in a microgrid whose block scheme is depicted in Fig. 5.1. The system under study consists of a three phase inverter connected to the grid through an LCL filter. Moreover, three loads are connected at the point of common coupling (PCC): a resistive load (R load), an induction machine (IM) and a non-linear load (NL load). Then, a circuit breaker is located at the PCC to the interface the microgrid to the main grid. If the circuit breaker is opened, the microgrid is isolated from the rest of the power system. The inverter is supplied by an ideal dc-source (representing, e.g., a storage system) and it is controlled according to the S-VSC control algorithm [64].

This chapter begins with a small-signal stability analysis of the control using eigenvalue-based methods. Following this, experimental tests demonstrate that the S-VSC can function both as a grid-following and as a grid-forming converter. The tests reveal that the S-VSC can seamlessly transition from grid-connected to island operation if the circuit breaker suddenly opens (Fig. 5.1) with no communication about the grid connection. Moreover, the experimental tests show that the S-VSC can continue to operate in island

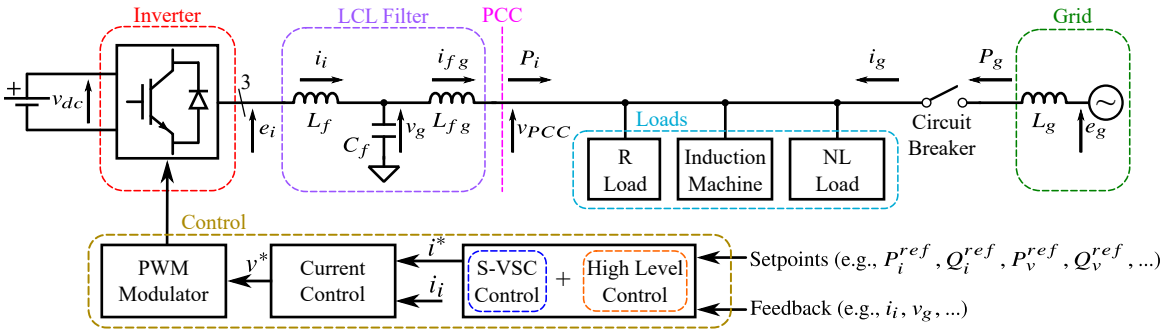

Fig. 5.1 Block scheme of the microgrid under study [64].

mode even during a fault. During the fault, the current is saturated, and once the fault is cleared, the system returns to normal operation.

Finally, the microgrid is modified by adding a second converter. One converter is controlled as grid-following S-VSC and the second one as grid-forming. Experiments show the smooth transition of the microgrid from the grid-connected to the island operation. As soon as the system is islanded, the grid-forming S-VSC takes in charge of the power required by the connected resistive load. The grid-following converter provides its inertial contribution and then tracks the frequency of the grid-forming converter providing zero power.

The findings of this chapter led to the publications of [108, 64]. The results of the microgrid consisting of two converters are instead obtained as part of the co-supervised Master's Thesis [67].

5.2 High Level Control

The grid-forming capability of the S-VSC model is achieved by incorporating the High Level control block, depicted in Fig. 5.2, into the original structure shown in Fig. 3.33.

Fig. 5.2 illustrates that the High Level control comprises two external control loops: the former consists in the active droop control law, the latter consists in the reactive droop control law [64].

The active droop control law proportionally regulates the frequency during both grid-connected and island operation:

$$P_d^* = \frac{\omega_r^* - \omega_r}{b_p} \tag{5.1}$$

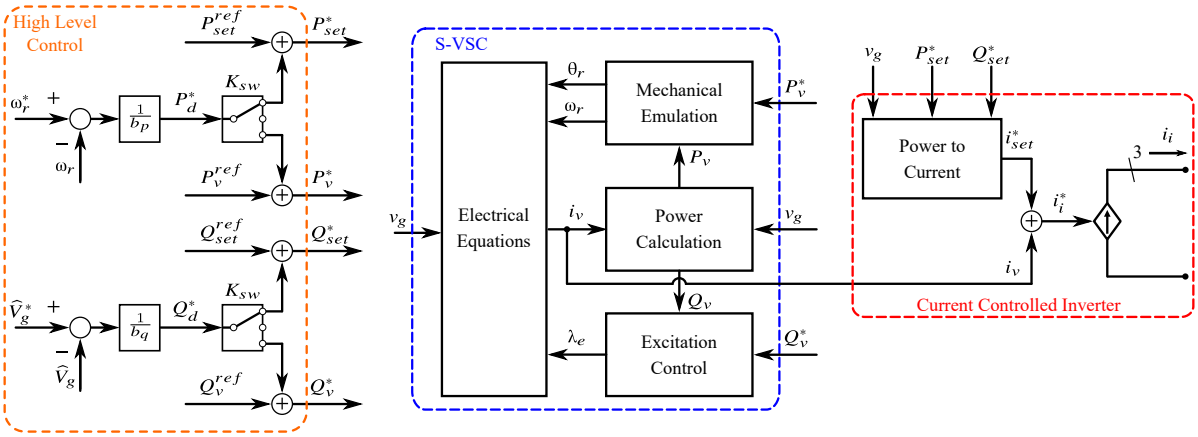

Fig. 5.2 Block scheme of the inverter controlled according to the S-VSC model with the High Level control [64].

where P_d^*, ω_r^* and b_p are, respectively, the active power droop reference, the speed reference and the active droop coefficient. b_p is set by the user. In this case, it is set to the conventional value of 2% [7, 64].

The second external controller employs a reactive droop control law for proportional regulation of the voltage amplitude $\widehat{V}_g$ in both grid-mode and island operation:

$$Q_d^* = \frac{\widehat{V}_g^* - \widehat{V}_g}{b_q} \tag{5.2}$$

where Q_d^*, $\widehat{V}_g^*$ and b_q are, respectively, the reactive power droop reference, the voltage reference and the reactive droop coefficient. b_q is set by the user. In this case it is equal to the conventional value of 50% [7, 64].

These two external loops have a dual purpose: 1) in grid-connected operation, the S-VSC can execute the primary frequency and voltage regulation; 2) the High Level Control enables the S-VSC model to operate as a grid-forming while maintaining superior performance compared to conventional virtual synchronous generators [81]. According to the switch K_{sw} in Fig. 5.2, the two references P_d^* and Q_d^* can be [64]:

- added to P_{set}^{ref} and Q_{set}^{ref} to retrieve P_{set} and Q_{set}. In this case, $P_v^* = P_v^{ref}$ and $Q_v^* = Q_v^{ref}$;
- not used (i.e., the High Level control is disabled);
- added to P_v^{ref} and Q_v^{ref} to retrieve P_v^* and Q_v^*. In this case, $P_{set} = P_{set}^{ref}$ and $Q_{set} = Q_{set}^{ref}$.

If the references P_d^* and Q_d^* are added to the inverter external references, the compensator operation is preserved. In this thesis they are always applied to the inverter external side. In grid-connected mode, the S-VSC functions as a grid-following converter, exchanging power with the grid based to the references P_{set} and Q_{set}, while also providing various grid services. Conversely, in island mode, the S-VSC works as a grid-forming converter, supplying power as required by the loads [64].

5.3 State-space Modeling

First, the thesis investigates the small-signal stability of the control algorithm under both grid-connected and islanded operation modes using an eigenvalue-based stability analysis, similar to the approach found in references [109, 110]. The initial step involves constructing the complete state-space model of the system illustrated in Figure 5.1. A commonly adopted approach in the literature involves obtaining the state-space model for each component of the system and subsequently applying the Component Connection Method (CCM) [109–111]. This method involves integrating the state-space models of individual subsystems to form the complete state-space representation of the total system in a modular way. Each subsystem indexed by k is formulated in the state-space format defined by equation (5.3):

$$\begin{cases} \dfrac{d\mathbf{x_k}}{dt} &= \mathbf{A_k x_k} + \mathbf{B_k u_k} \\ \mathbf{y_k} &= \mathbf{C_k x_k} + \mathbf{D_k u_k} \end{cases} \qquad k = 1 \ldots \mathrm{n} \tag{5.3}$$

where the vectors $\mathbf{x_k}$, $\mathbf{u_k}$, and $\mathbf{y_k}$ represent the state variables, inputs, and outputs of the k-th subsystem, respectively. The matrices $\mathbf{A_k}$, $\mathbf{B_k}$, $\mathbf{C_k}$, and $\mathbf{D_k}$ are the state-space matrices for the subsystem. The system is composed of a total of n subsystems.

Next, the aggregated model is obtained by combining the subsystem matrices as follows:

$$\begin{cases} \dfrac{d\mathbf{x_s}}{dt} &= \mathbf{A x_s} + \mathbf{B u} \\ \mathbf{y} &= \mathbf{C x_s} + \mathbf{D u} \end{cases} \tag{5.4}$$

$$\begin{cases} \mathbf{x_s} &= \left[\mathbf{x_1} \ldots \mathbf{x_n}\right]^{\mathrm{T}} \\ \mathbf{u} &= \left[\mathbf{u_1} \ldots \mathbf{u_{n+m}}\right]^{\mathrm{T}} \\ \mathbf{y} &= \left[\mathbf{y_1} \ldots \mathbf{y_{n+m}}\right]^{\mathrm{T}} \end{cases} \tag{5.5}$$

$$\mathbf{A} = \begin{bmatrix} \mathbf{A_1} & 0 & \cdots & 0 \\ 0 & \mathbf{A_2} & \cdots & 0 \\ \vdots & \vdots & \ddots & \vdots \\ 0 & 0 & \cdots & \mathbf{A_n} \end{bmatrix} \tag{5.6}$$

$$\mathbf{B} = \begin{bmatrix} \mathbf{B_1} & 0 & \cdots & 0 & \overbrace{0 & \cdots & 0}^{\text{number of algebraic blocks inputs}} \\ 0 & \mathbf{B_2} & \cdots & 0 & 0 & \cdots & 0 \\ \vdots & \vdots & \ddots & \vdots & \vdots & \ddots & \vdots \\ 0 & 0 & \cdots & \mathbf{B_n} & 0 & \cdots & 0 \end{bmatrix} \tag{5.7}$$

$$\mathbf{C} = \begin{bmatrix} \mathbf{C_1} & 0 & \cdots & 0 \\ 0 & \mathbf{C_2} & \cdots & 0 \\ \vdots & \vdots & \ddots & \vdots \\ 0 & 0 & \cdots & \mathbf{C_n} \\ 0 & \cdots & \cdots & 0 \\ \vdots & \vdots & \ddots & \vdots \\ 0 & \cdots & \cdots & 0 \end{bmatrix} \Bigg\} \text{number of algebraic blocks outputs} \tag{5.8}$$

$$\mathbf{D} = \begin{bmatrix} \mathbf{D_1} & 0 & \cdots & 0 \\ 0 & \mathbf{D_2} & \cdots & 0 \\ \vdots & \vdots & \ddots & \vdots \\ 0 & 0 & \cdots & \mathbf{D_{n+m}} \end{bmatrix} \tag{5.9}$$

where $\mathbf{x_s}$, $\mathbf{u}$ and $\mathbf{y}$ are, respectively, the aggregated state variables, inputs and outputs of the system; the matrices $\mathbf{A}$, $\mathbf{B}$, $\mathbf{C}$ and $\mathbf{D}$ are the aggregated state-space matrices; m is the number of algebraic blocks [110].

Next, the CCM can be applied. The aggregated matrices are connected through the so-called interconnection matrices $\mathbf{L_{uy}}$, $\mathbf{L_{us}}$, $\mathbf{L_{sy}}$ and $\mathbf{L_{ss}}$, as follows:

$$\begin{cases} \mathbf{u} = \mathbf{L_{uy}y} + \mathbf{L_{us}u_s} \\ \mathbf{y_s} = \mathbf{L_{sy}y} + \mathbf{L_{ss}u_s} \end{cases} \tag{5.10}$$

where $\mathbf{u_s}$ and $\mathbf{y_s}$ are, respectively, the inputs and the outputs of the overall system, while $\mathbf{x_s}$ is the state variables vector of the system.

Finally, the state-space representation of the entire system is the following:

$$\begin{cases} \dfrac{d\mathbf{x_s}}{dt} &= \mathbf{A_s x_s} + \mathbf{B_s u_s} \\ \mathbf{y_s} &= \mathbf{C_s x_s} + \mathbf{D_s u_s} \end{cases} \tag{5.11}$$

where:

$$\begin{cases} \mathbf{A_s} &= \mathbf{A} + \mathbf{BL_{uy}WC} \\ \mathbf{B_s} &= \mathbf{BL_{uy}WDL_{us}BL_{us}} \\ \mathbf{C_s} &= \mathbf{L_{sy}WC} \\ \mathbf{D_s} &= \mathbf{L_{sy}WDL_{us}} + \mathbf{L_{ss}} \\ \mathbf{W} &= \left(\mathbf{I} - \mathbf{DL_{uy}}\right)^{-1} \end{cases} \tag{5.12}$$

The components comprising the system under investigation include: High-Level Control, S-VSC Control, Reference Calculation (comprising Power to Current block and current reference calculation), Inverter, LCL Filter, Loads Block, and Grid. The S-VSC control block is subdivided into two sub-blocks: Electrical Equations and Power Loops (Mechanical Emulation and Excitation Control). The inverter block consists of the PI current controller and the control delay [110].

All state-space models are linearized around an equilibrium point defined by the desired power setpoint and initial conditions of the system to derive small-signal models. These models are formulated in the (d, q) reference frame, rotating at the virtual speed ω_r. The symbol "Δ" denotes the variation of a variable around its equilibrium point, whereas the subscript "0" indicates the value of the quantity at the equilibrium point. The grid voltage vector is aligned with the q-axis. The model is expressed in per unit, with the base values listed in Table 5.1.

Detailed state-space models are provided in Appendix A.1, Component Connection Method (CCM) for the three loads in Appendix A.2, CCM for grid-connected mode in Appendix A.3, and CCM for island configuration in Appendix A.4 [64].

The validation of these state-space models is conducted through PLECS simulations and experimental tests. Results from validation are presented in Fig. 5.3 for grid-connected mode, where a 0.1 pu IM load step change is applied with the resistive load connected and the NL load disconnected. Similarly, Fig. 5.4 shows results for island operation, where the same load step change is applied with both resistive load and NL

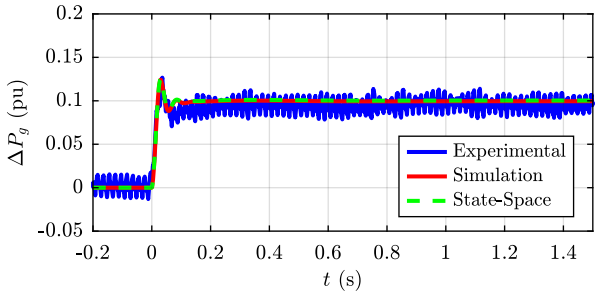

Fig. 5.3 Grid power variation to an IM load change in grid-connected operation [64].

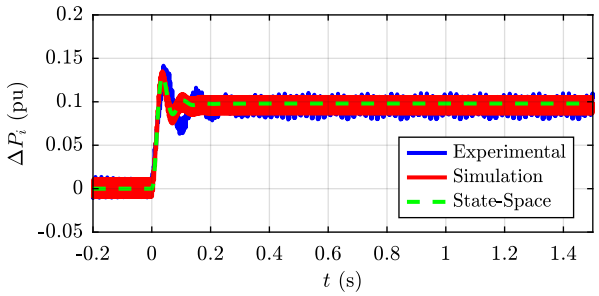

Fig. 5.4 Inverter power variation to an IM load change in island operation [64].

load connected. In both scenarios, the state-space models closely align with both the simulation and experimental outcomes [64].

5.4 Eigenvalue-Based Stability Analysis

This section provides an eigenvalue-based stability analysis for both the grid-connected and the island operations [64].

5.4.1 Grid-Connected Operation

The system in grid-connected operation has 25 eigenvalues, plotted on the complex plane shown in Fig. 5.5. The system is linearized around the converter nominal power. A modal analysis provides the relationship between the state variables and the eigenvalues, by calculating the participation factors [7, 110]. The results of the modal analysis are listed below:

- Eigenvalues 1 to 6: dynamic of the LCL filter. The loads are assumed ideal current sources connected at the PCC. Consequently, a high-value shunt resistor R_s is

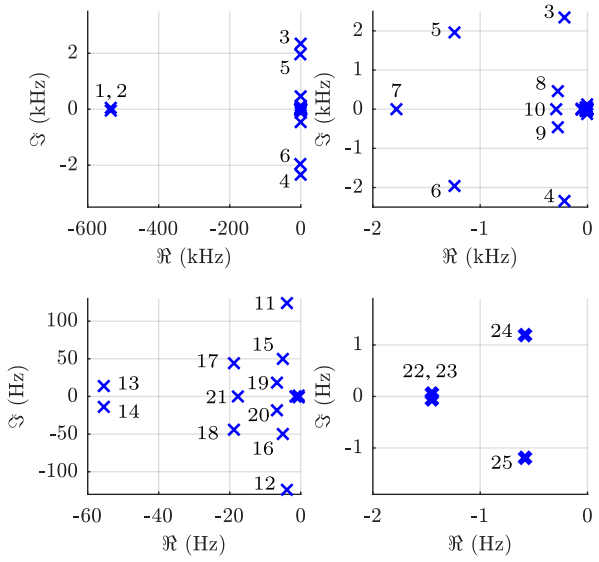

Fig. 5.5 Eigenvalues map of the system in grid-connected mode [64].

located at the PCC for the electrotechnical compatibility [109, 112]. The eigenvalues 1 and 2 depend on R_s. However, it does not influence the stability of the stability, as demonstrated in the literature, for instance in [109];

- Eigenvalues 7 to 10, 13 and 14: digital current control. Specifically, eigenvalues 7 and 8 are associated with the delay due to the digital control (i.e., sampling time), while eigenvalues 9, 10, 13, and 14 are related to the integrators of the PI current control;
- Eigenvalues 11 and 12: NL load;
- Eigenvalues 17 to 21: IM load;
- Eigenvalues 15, 16 and from 22 to 25: electromechanical part of the S-VSC (i.e., electrical equations, swing equation and excitation control).

Finally, the Short Circuit Ratio (SCR) is changed to study how different grid conditions affect the control stability. As shown in Fig. 5.6, the eigenvalues move from left to right on the half right complex plan by decreasing the SCR from the nominal value of 100 (stiff grid condition) to 1 (very weak grid condition). It can be noted that all the eigenvalues related to the grid inductance (i.e., LCL filter, electrical equation block, excitation control) move from left to right. The conclusion is that the system tends to become

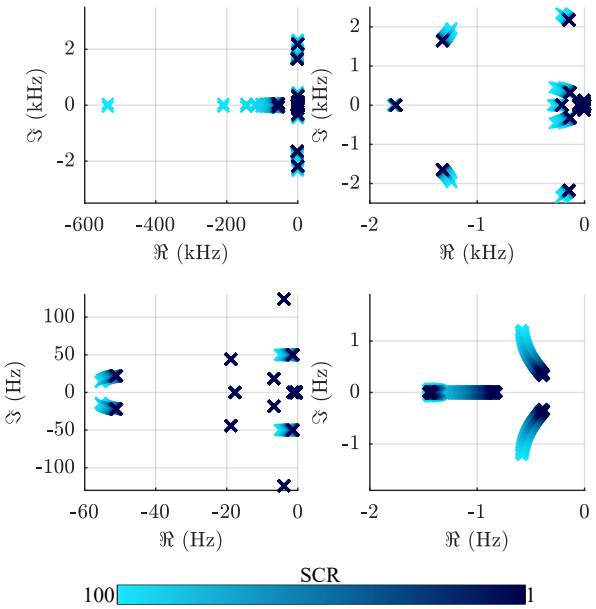

Fig. 5.6 Eigenvalues map of the system in grid-connected mode varying the SCR from 100 to 1 [64].

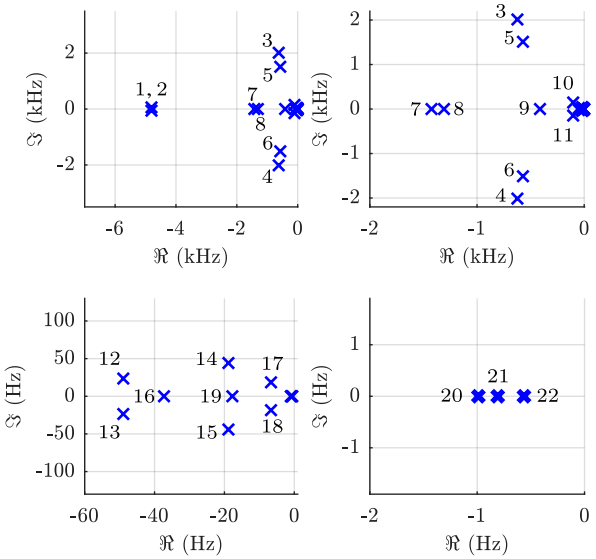

Fig. 5.7 Eigenvalues map of the system in island mode [64].

unstable as the SCR decreases. However, the system remains stable even under very weak grid conditions [64].

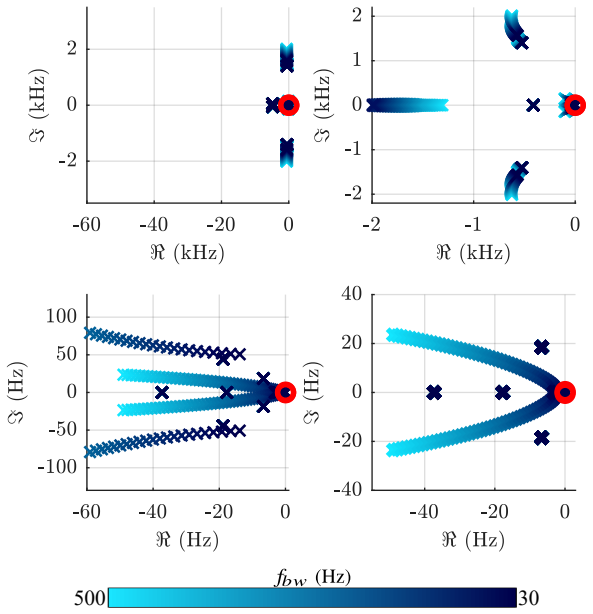

Fig. 5.8 Eigenvalues map of the system in island mode varying the current control bandwidth f_{bw} from 500 Hz to 30 Hz. The red circle indicate the eigenvalues with positive real part [64].

5.4.2 Island Operation

The same procedure described in Section 5.4.1 is performed for the island operation. In this example, the eigenvalues map is obtained with the R load inserted while the other two loads are disconnected. The eigenvalue map is illustrated in Fig. 5.7. There is a total of 22 eigenvalues, due to the absence of the grid. According to the modal analysis:

- Eigenvalues 1 to 6: LCL filter;
- Eigenvalues 7, 8, 12 and 13: digital current control. In particular, eigenvalues 7 and 8 are linked to the delay due to the digital control, while 12 and 13 relate to the integrators of the PI current regulator;
- Eigenvalues 9 and 16: NL load;
- Eigenvalues 14, 15, 17-19: IM load;
- Eigenvalues 10, 11, 20-22: S-VSC electromechanical part.

To validate the accuracy of modeling procedure, the bandwidth f_{bw} of the PI current regulator is systematically reduced from its nominal value of 500 Hz until a condition

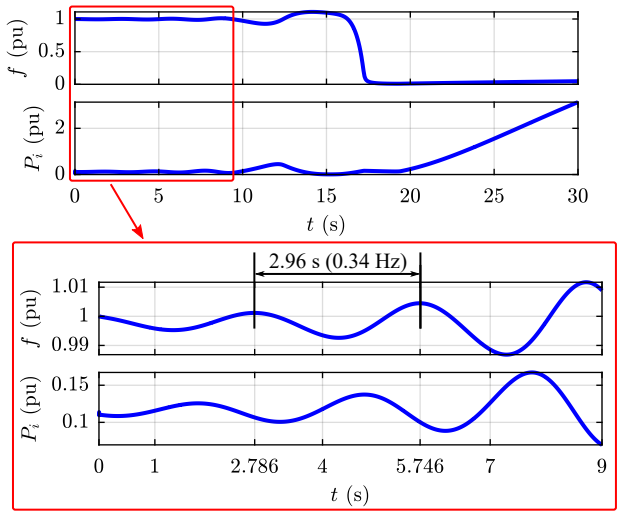

Fig. 5.9 Instability test to validate the state-space modeling and the eigenvalue analysis. The oscillation frequency is in compliance with the theoretical analysis [64].

of instability is observed. As previously noted, the eigenvalues associated with the integrators of the PI current regulator are at 12 and 13. Figure 5.8 demonstrates that instability occurs when the bandwidth is reduced to 30 Hz, causing eigenvalues 12 and 13 to transition into the right half-plane. Modal analysis indicates that at this point, the frequency of eigenvalues 12 and 13 is 0.34 Hz, suggesting an expected divergence frequency of 0.34 Hz for the system.

This prediction is corroborated by a PLECS simulation, depicted in Figure 5.9, where oscillations occur with a period of 2.96 s, closely matching the calculated 0.34 Hz frequency. This successful validation supports the reliability of the state-space modeling approach and the eigenvalue-based stability analysis [64].

5.5 Experimental Validation

Five experimental tests are proposed in this section to validate the grid-forming capability of the S-VSC under different cases. The experimental setup is depicted in Fig. 5.10. The main data are collected in Table 5.1. The scheme of the system is the one shown in Fig. 5.1 [64].

The inverter, powered by a 15 kW dc-source, is controlled via a dSPACE platform. It is linked to the Point of Common Coupling (PCC) through its LCL filter. A circuit breaker is located at the PCC to the connect the converter with the grid, as illustrated in

Table 5.1 Main data of the experimental setup [64].

Base Values		**Inverter**		**LCL Filter & Grid**	
S_b	15 kVA	S_N	15 kVA	L_f	0.060 pu
V_b	230 $\sqrt{2}$ V	I_N	30 A	R_f	0.006 pu
I_b	30 A	f_{sw}	10 kHz	C_f	0.017 pu
Z_b	10.67 Ω	V_{dc}	650 V	L_{fg}	0.065 pu
f_b	50 Hz			R_{fg}	0.01 pu
ω_b	$2\pi f_b$			L_g	0.001 pu
				R_g	0.00001 pu
Resistive Load		**Induction Machine**		**Non-linear Load**	
P_N	0.1 pu	S_N	0.27 pu	P_N	0.1 pu
S-VSC Parameters					
R_v	0.02 pu	L_v	0.2 pu	H	4 s
L_{rq}	0.71 pu	R_{rq}	0.01 pu	τ_e	0.1 s

Figures 5.1 and 5.10b. Importantly, there is no communication interface to connect the breaker and the converter, meaning the converter operates independently of the status of the breaker.

Three distinct loads are installed at the PCC to accommodate various load types: a resistive load (R load), an induction motor (IM) load, and a non-linear load (NL load). These loads can be connected or disconnected manually using breakers. To manage inrush current during IM startup, a starter limits the maximum slew rate of the supply voltage. Additionally, the IM is coupled with a programmable load.

The NL load consists of a three-phase diode rectifier interfaced to the grid through a 0.09 pu inductive filter ($L_{f,NL}$), as depicted in Figure 5.11. On the dc-side, the rectifier is linked to a 3.3 mF capacitor bank ($C_{dc,NL}$) in parallel with a constant current load $I_{load} = 0.1$ pu (ITECH IT 8332 dc electronic load). Capacitor pre-charging is facilitated by a soft-start resistor $R_{p,NL}$.

Five experimental tests have been performed, as follows [64]:

- Test 1: effect of the High Level control. The system is in grid-mode operation. Then, the circuit breaker is opened while only the R load is connected. The test is conducted twice under the following conditions:
  - The High-Level control is disabled, resulting in system collapse due to the lack of frequency and voltage control;

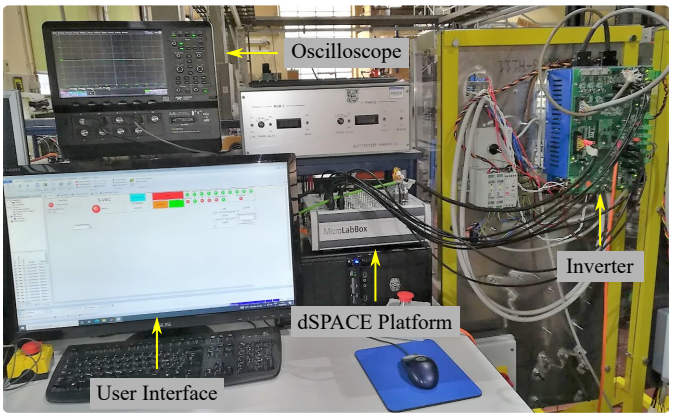

(a)

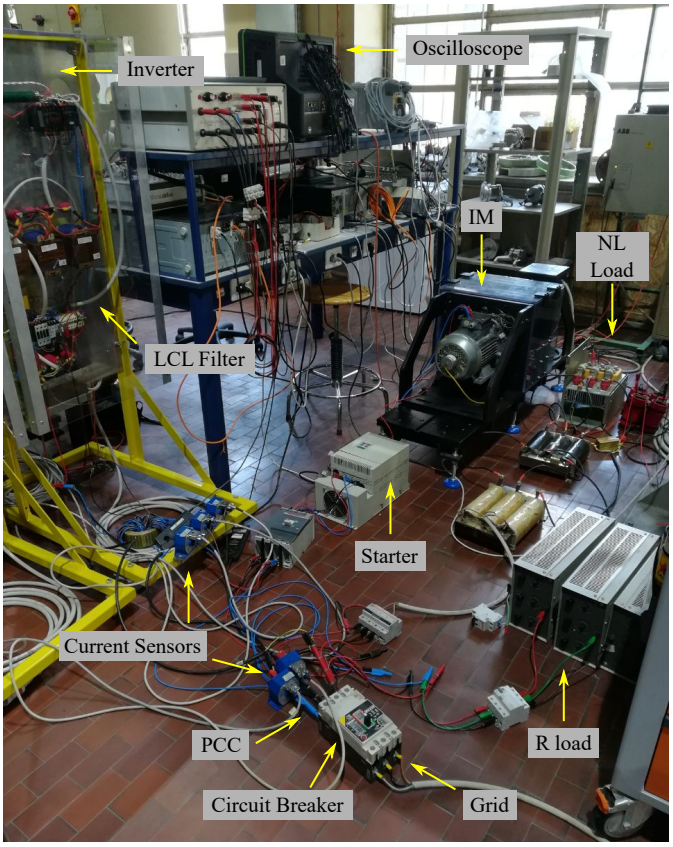

(b)

Fig. 5.10 Experimental setup pictures [64].

– The High-Level control is enabled, allowing the S-VSC to provide the power requested by the load and control the microgrid frequency and voltage.

This test demonstrates the necessity of the High-Level control for enabling the S-VSC to function in a grid-forming configuration.

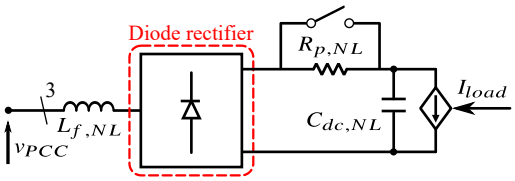

Fig. 5.11 Scheme of the NL load [64].

- Test 2: inverter external power references set to 0 pu. While connected to the grid, the inverter's role is limited to providing ancillary services, with the grid supplying power to the loads. Upon islanding the microgrid (i.e., opening the circuit breaker), the inverter promptly takes over to supply power to the loads and adjusts to changes in load demand without requiring island detection;

- Test 3: non-zero inverter external references (e.g., emulating renewable plant generation). Test 2 is conducted again with a non constant active power reference P_{set}^{ref}, which varies over time to simulate the fluctuating production of a PV or wind source. Similar to the previous test scenario, when the microgrid transitions to islanded mode by opening the circuit breaker, the inverter must promptly supply the power demanded by the loads and adapt to changes in load requirements seamlessly, without relying on islanding detection mechanisms;

- Test 4: fault occurrence during island-mode. The inverter operates in grid-forming mode, providing power to the R load, the IM load, and a programmable load set to an apparent power of 0.2 pu. Subsequently, the programmable load is set to a low impedance to simulate a symmetric three-phase fault. Approximately 1.6 s later, the fault is cleared by disconnecting the programmable load, restoring the normal operation of the system;

- Test 5: a microgrid consisting of two converters connected to the grid is suddenly islanded. In this case, there is only the resistive load. The scheme of the system is illustrated in Fig. 5.23. One converter is controlled according to the proposed grid-forming S-VSC, while the other one operates as a grid-following. Even in this multi-converters microgrid, the proposed solution seamlessly moves from the grid-connected to the island mode supplying the connected loads.

In all tests, the speed reference ω_r^* is set to the S-VSC frequency value (pu) following the inverter synchronization procedure, which corresponds to the grid frequency value at that moment. Similarly, the voltage reference $\widehat{V}_g^*$ is adjusted to match the measured voltage amplitude $\widehat{V}_g$ obtained at the conclusion of the synchronization process [64].

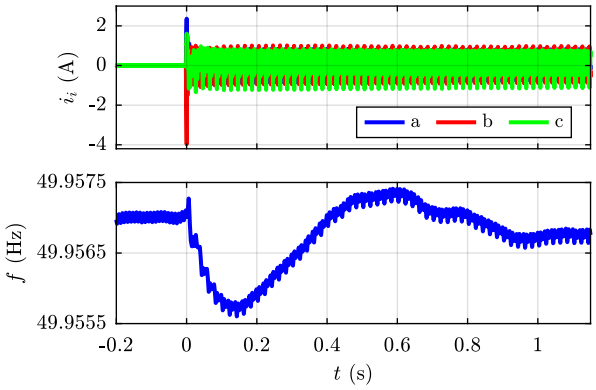

Fig. 5.12 Grid synchronization and current control enable. From top to bottom: three phase inverter current i_i (A); S-VSC frequency f (Hz) [64].

5.5.1 Test 1: Effect of the High Level control

Test 1 begins in grid-connected mode with the R load connected. Figure 5.12 illustrates the synchronization phase of the S-VSC from -0.2 s to 0 s. Once the S-VSC achieves synchronization with the real grid frequency, PWM modulation and current control are activated at $t = 0$ s. This synchronization phase operates independently of the High-Level control.

Subsequently, Test 1 is initiated, and the outcomes are depicted in Figure 5.13. At $t = 0$ s, the circuit breaker is opened to assess the impact of the High-Level control. Without the High-Level control engaged, the S-VSC begins supplying power to meet the demands of the R load. However, the absence of frequency and voltage control loops results in a deterioration of both frequency and voltage levels, as shown in Figure 5.13. The test is conducted using two different values of the inertia constant H to emphasize the influence of virtual inertia on the rate of frequency decline. It is observed that higher inertia leads to a slower frequency decline, akin to behavior seen in traditional synchronous machines.

Conversely, when the High-Level control is activated, the S-VSC operates as a grid-forming converter by actively controlling frequency and voltage while fulfilling the power requirements of the R load, as demonstrated under identical test conditions in Figure 5.13 [64].

5.5.2 Test 2: Zero inverter external references

The results from Test 2 are depicted in Fig. 5.14, with a summary of key events shown in Fig. 5.16. Test 2 is structured into two phases: grid-mode and island operation. Initially,

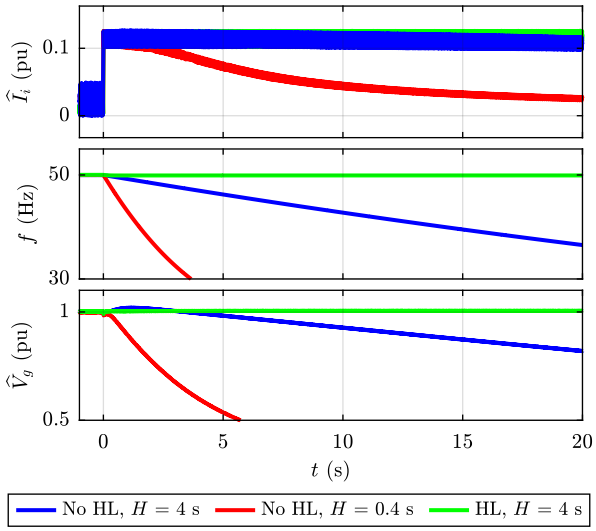

Fig. 5.13 Island operation with and without the High Level control (HL) for different values of H (s). From top to bottom: inverter current amplitude $\widehat{I}_i$ (pu); S-VSC frequency f (Hz); measured voltage amplitude $\widehat{V}_g$ (pu) [64].

in the grid-mode phase, the circuit breaker closes and the three loads are sequentially connected, each satisfying their demand from the grid. The introduction of the IM load at $t = 23.3$ s mirrors the step change illustrated in Fig. 5.3. Moving to the second phase at $t = 42.53$ s, the circuit breaker suddenly opens without prior notification to the control system. Despite this, the S-VSC smoothly delivers the required power to the loads without necessitating any communication, as evidenced in Fig. 5.15. As the capacitor voltage decreases during the transition from grid-mode to island operation, the total load power also diminishes accordingly. Subsequently, the converter accurately tracks the load variations over time. The insertion of the IM load at $t = 110.6$ s aligns with the step change depicted in Fig. 5.4.

Additionally, Fig. 5.17 displays the measured line-to-line voltage $v_{g,ab}$ and current $i_{fg,a}$ during island operation under two distinct conditions: with all loads connected (Fig. 5.17a) and with the non-linear load (NL) disconnected (Fig. 5.17b). Notably, the NL load, which includes a diode rectifier, introduces significant harmonic distortion evident in the first case (Fig. 5.17a), where the Total Harmonic Distortion (THD) of the current is 7.70% and the THD of the voltage is 3.53%. The primary contributors to distortion are observed at the 5th, 7th, 11th, and 13th harmonic orders. Conversely, in the second case (Fig. 5.17b), THDs decrease to 2.80% for current and 1.44% for voltage. Finally, Fig. 5.17 underscores a significant feature of the S-VSC model: it regulates current rather than voltage, particularly noticeable in island operation where load current heavily influences voltage distortion [64].

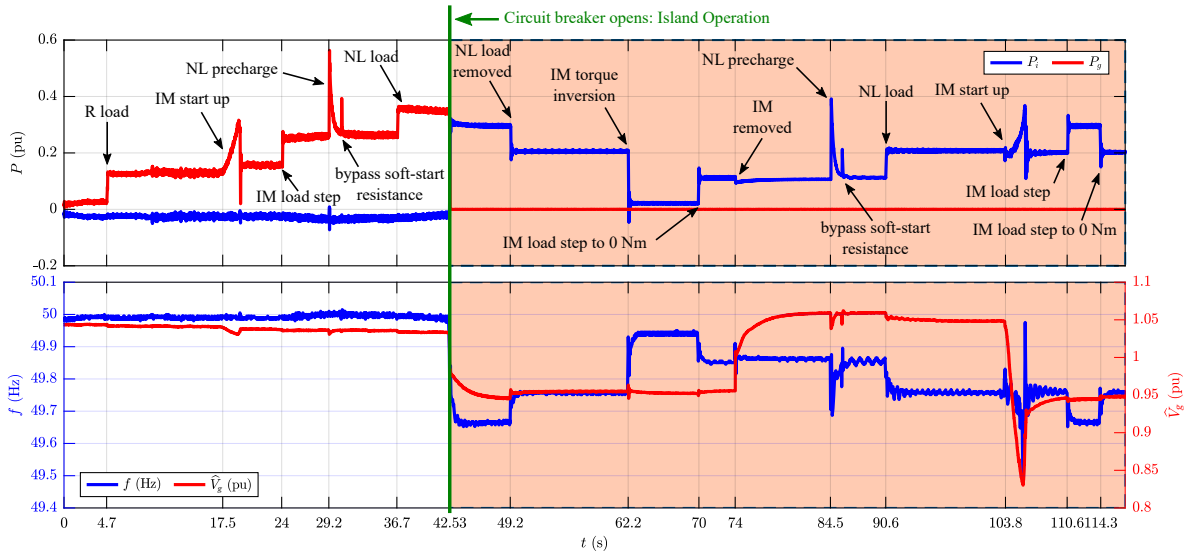

Fig. 5.14 Results of Test 2: (top) inverter power P_i (pu) and grid power P_g (pu) moving average trends; (bottom) S-VSC frequency f (Hz) and voltage amplitude $\widehat{V}_g$ (pu) trends [64].

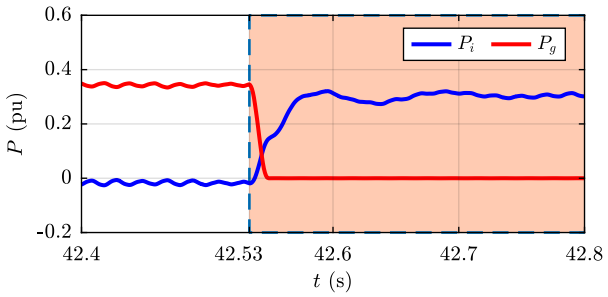

Fig. 5.15 Test 2: transition from grid-connected to island mode. Inverter power P_i (pu) and grid power P_g (pu) moving average trends [64].

5.5.3 Test 3: Non-zero inverter external references

The findings from Test 3 are compiled in Fig. 5.18, with detailed annotations of key events provided in Fig. 5.20. Similar to Test 2, Test 3 is structured into two distinct phases: grid-connected and island operation.

In the grid-connected phase, the external reference P_{set}^{ref} for the inverter varies over time. Loads are sequentially connected, and their power demands are met either by the grid alone or jointly by the grid and the inverter, depending on availability. For example, at t = 33.7 s, the inverter supplies a portion of the load power while the remainder is sourced from the grid. Conversely, by t = 49 s, the entire load demand is satisfied by the inverter alone. At t = 58.44 s, the circuit breaker opens, prompting the inverter

Time (s)	Comment
0	$f \neq 50$ Hz $\Rightarrow P_d^* \neq 0 \Rightarrow P_i \neq 0$.
4.7	R Load insertion $\Rightarrow \Delta P_g = 0.1$ pu.
17.5	IM start up. The starter limits the inrush current.
24	10 Nm IM load insertion $\Rightarrow \Delta P_g = 0.1$ pu.
29.2	NL load precharge.
30.6	Bypass of the soft–start NL load resistance.
36.7	NL load insertion $\Rightarrow \Delta P_g = 0.1$ pu.
42.53	The circuit breaker is opened: Islanding $\Rightarrow$ $\Rightarrow P_g = 0$ pu , $\Delta P_i = 0.3$ pu: the inverter immediately supplies the loads.
49.2	NL load disconnection $\Rightarrow \Delta P_i = -0.1$ pu.
62.2	IM torque reversal from 10 Nm to -10 Nm $\Rightarrow$ $\Rightarrow \Delta P_i = -0.2$ pu: the IM works as a generator and provides almost all the R load power.
70	IM torque load = 0 Nm $\Rightarrow \Delta P_i = 0.1$ pu: the inverter provides the power requested by the loads.
74	IM disconnection.
84.5	NL load precharge.
85.8	Bypass of the soft–start NL load resistance.
90.6	NL load insertion $\Rightarrow \Delta P_i = 0.1$ pu.
103.8	IM start up. The starter limits the inrush current.
110.6	10 Nm IM load insertion $\Rightarrow \Delta P_i = 0.1$ pu.
114.3	IM torque load = 0 Nm $\Rightarrow \Delta P_i = -0.1$ pu.

Fig. 5.16 Events list of Test 2 [64].

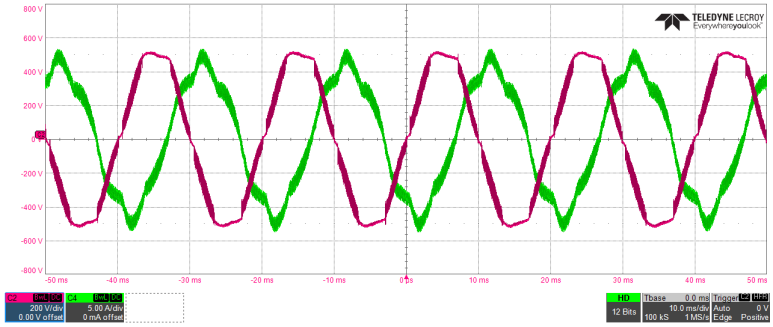

(a)

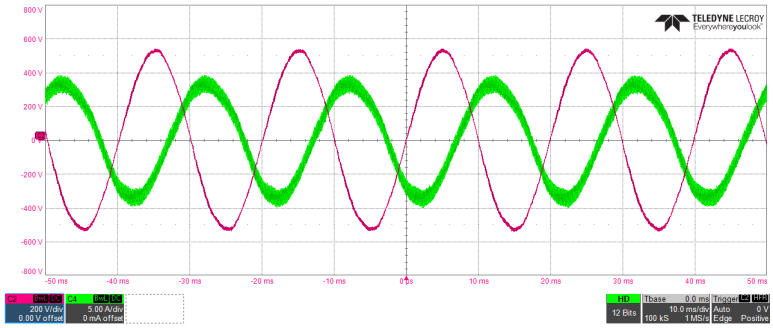

(b)

Fig. 5.17 Line to line voltage $v_{g,ab}$ and current $i_{fg,a}$ waveforms in island mode: (a) with all loads connected; (b) without the NL load [64].

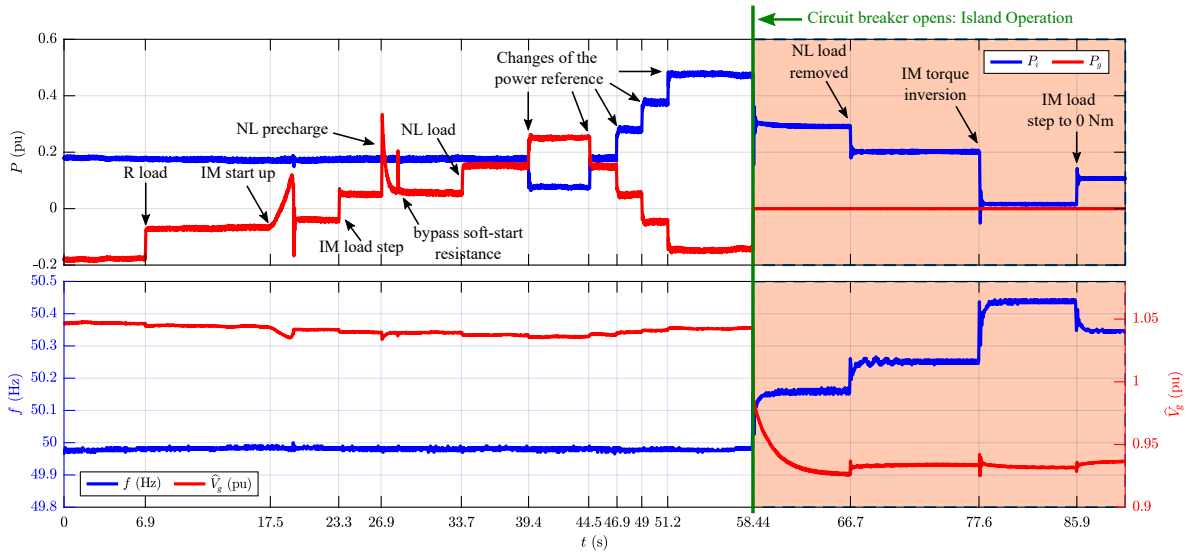

Fig. 5.18 Results of Test 3: (top) inverter power P_i (pu) and grid power P_g (pu) moving average trends; (bottom) S-VSC frequency f (Hz) and voltage amplitude $\widehat{V}_g$ (pu) trends [64].

to autonomously reduce its injected power, like curtailment operations, even without an external reference change. Under such circumstances, the converter only injects the

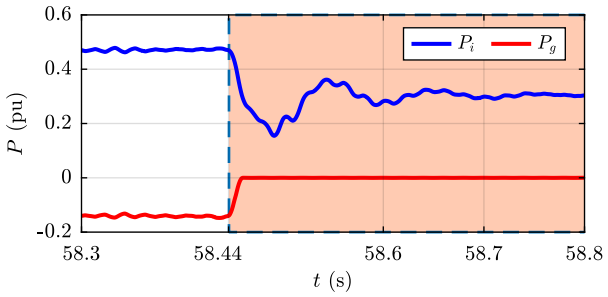

Fig. 5.19 Test 3: transition from the grid-connected to the island operation. Inverter power P_i (pu) and grid power P_g (pu) moving average trends [64].

Time (s)	Comment
0	$P_i^{ref} = 0.2$ pu. The inverter injects power into the grid. $f \neq 50$ Hz $\Rightarrow P_d^* \neq 0 \Rightarrow P_i^* = P_d^* + P_i^{ref}$.
6.9	R Load insertion $\Rightarrow \Delta P_g = 0.1$ pu. The inverter satisfies the R load request and the remaing power is injected into the grid.
17.5	IM start up. The starter limits the inrush current.
23.3	10 Nm IM load insertion $\Rightarrow \Delta P_g = 0.1$ pu. The inverter provides part of the loads power. The remaing contribution is guaranteed by the grid.
26.9	NL load precharge.
28.3	Bypass of the soft–start NL load resistance.
33.7	NL load insertion $\Rightarrow \Delta P_g = 0.1$ pu. The inverter and the grid almost equally provide the loads power.
39.4	Inverter reference step $\Delta P_i^{ref} = -0.1$ pu $\Rightarrow$ $\Rightarrow \Delta P_g = 0.1$ pu.
44.5	Inverter reference step $\Delta P_i^{ref} = 0.1$ pu $\Rightarrow$ $\Rightarrow \Delta P_g = -0.1$ pu.
46.9	Inverter reference step $\Delta P_i^{ref} = 0.1$ pu $\Rightarrow$ $\Rightarrow \Delta P_g = -0.1$ pu.
49	Inverter reference step $\Delta P_i^{ref} = 0.1$ pu $\Rightarrow$ $\Rightarrow \Delta P_g = -0.1$ pu. The inverter provides all the power requested by the loads and the remaining term is injected into the grid.
51.2	Inverter reference step $\Delta P_i^{ref} = 0.1$ pu $\Rightarrow$ $\Rightarrow \Delta P_g = -0.1$ pu.
58.44	The circuit breaker is opened: Islanding $\Rightarrow P_g = 0$ pu. The inverter immediately provides only the loads power.
66.7	NL load disconnection $\Rightarrow \Delta P_i = -0.1$ pu.
77.6	IM torque reversal from 10 Nm to -10 Nm $\Rightarrow$ $\Rightarrow \Delta P_i = -0.2$ pu: the IM works as a generator and provides almost all the R load power.
85.9	IM torque load = 0 Nm $\Rightarrow \Delta P_i = 0.1$ pu: The inverter provides the power requested by the loads.

Fig. 5.20 Events list of Test 3 [64].

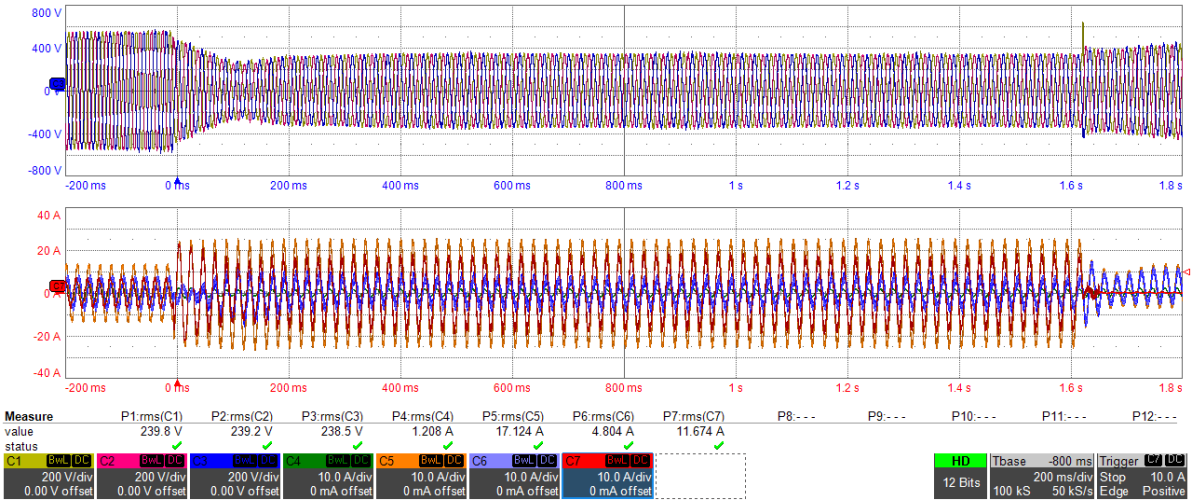

(a)

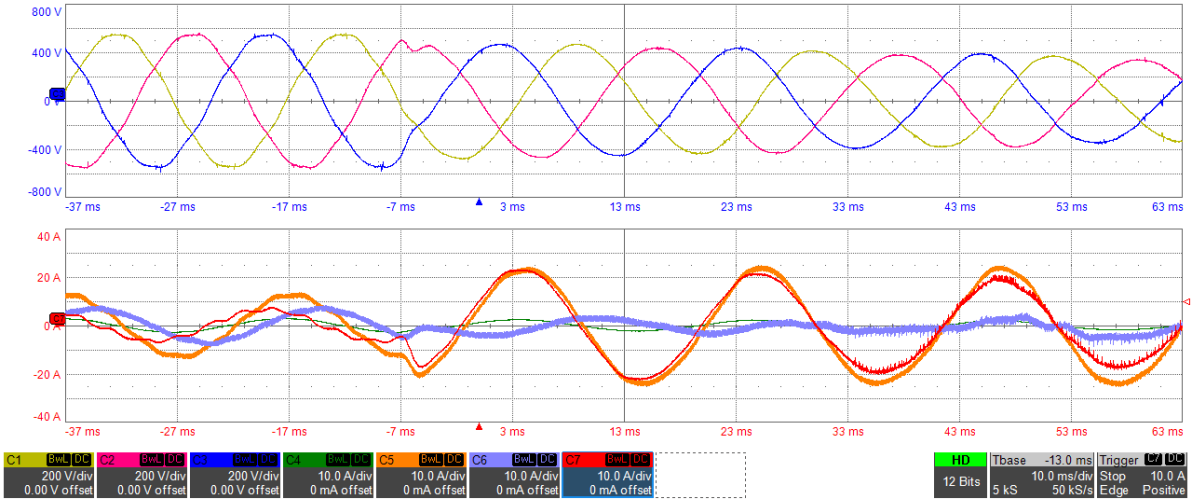

(b)

Fig. 5.21 Results of Test 4. C1, C2 and C3 are the line-to-line three phase voltages $v_{g,ll}$. C4 is the R load current $i_{R,a}$, C5 is the inverter current $i_{i,a}$, C6 is the IM current $i_{IM,a}$ and C7 is the fault current $i_{F,a}$. The RMS values are calculated in the time range from 200 ms to 1.6 s. From top to bottom: (a) entire fault; (b) zoom at the beginning of the fault [64].

power required by the loads. If a storage system were integrated, any surplus power could potentially be used for charging. Importantly, there is no communication between the converter and the grid in these scenarios, yet the converter seamlessly meets the load power requirements, as depicted in Fig. 5.19. Lastly, as for Test 2, the converter adapts to changes in load demands throughout the test period [64].

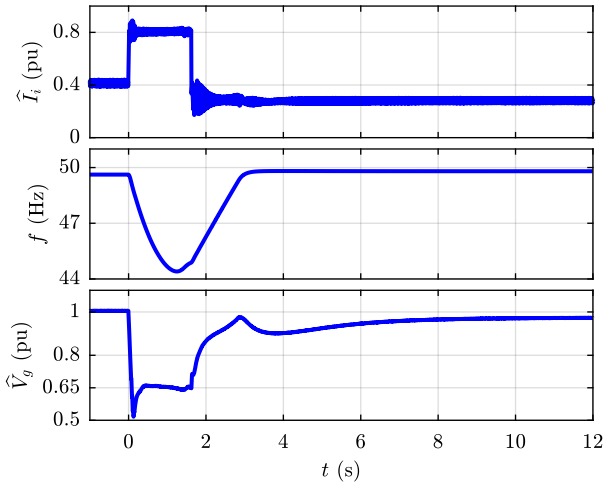

Fig. 5.22 Results of Test 4. From top to bottom: inverter current amplitude $\widehat{I}_i$ (pu); S-VSC frequency f (Hz); measured voltage amplitude $\widehat{V}_g$ (pu) [64].

5.5.4 Test 4: Fault occurrence in island operation

The findings from Test 4 are depicted in Figures 5.21 and 5.22. At $t = 0$ s, a fault occurs, resulting in a voltage dip of approximately 0.35 pu. Throughout the fault duration, the inverter remains operational without tripping, continuing to supply power to the loads. The frequency decreases, whereas the inverter current saturates at the user-defined limit of 0.8 pu. Upon clearing of the fault, both the frequency and voltage return to their normal operating conditions, and the inverter resumes supplying power to the loads. This test serves to validate the robustness of the proposed solution against faults, demonstrating that the microgrid remains stable throughout the fault event. Once the fault is resolved, the S-VSC promptly restores the microgrid to its pre-fault operational state [64].

5.5.5 Test 5: Parallel Operation of two VSMs

As a final test, the grid-forming S-VSC control algorithm is tested in the microgrid schematized in Fig. 5.23. The microgrid consists of two converters (named G1 and G2), supplied by the same dc-source and connected in parallel to the grid at the PCC through their own LCL filter. At the PCC there is also a resistive load. A transformer is also interposed between the PCC and the grid. The test consists of controlling the converter G1 with the proposed grid-forming S-VSC control algorithm, while the converter G2 is controlled according to the original S-VSC control (i.e., grid-following). The results of the tests are illustrated in Fig. 5.24. At the beginning of the test, the two converters are

connected to the grid and the resistive load is supplied by the grid. Next, at $t = 0$ s, the system is islanded as in the previous tests. As for Test 2 and Test 3, the G1 converter operates as a grid-forming providing the power required by the resistive load. On the opposite, G2 is a grid-following that instantly provides inertial power and in steady-state operates at zero power. This test demonstrates the S-VSC is valid solution also for the control of multi converters systems both connected to the grid and islanded [67].

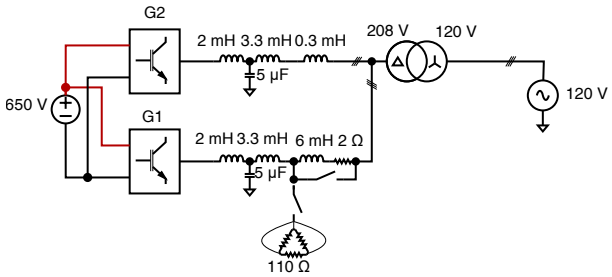

Fig. 5.23 Scheme of the microgrid for Test 5 [67].

5.6 Conclusion & Main Contributions

This chapter introduces the extended version of the S-VSC model, capable of operating in both grid-following and grid-forming modes, maintaining the performance of the compensator as described in prior studies. The eigenvalues stability analysis theoretically confirms the stability of this solution in both grid-connected and islanded configurations. Experimental validation on a microgrid, encompassing various load types (including passive linear, non-linear, and active loads such as line-fed motors), corroborates these findings. Upon islanding, the S-VSC seamlessly supplies the required load power, underscoring its efficacy in controlling inverter-based microgrids [64].

Furthermore, the results demonstrate the S-VSC's ability to transition from grid-connected to islanded operation without requiring communication between the grid and the converter. Experimental tests also illustrate the S-VSC capability to operate in island mode even during fault conditions, showing the robustness of the microgrid under the proposed control scheme [64].

Additionally, the control algorithm is validated in a microgrid comprising two VSMs—one acting as grid-forming and the other as grid-following—further validating the effectiveness of the proposed approach. Future work will focus on incorporating grid connection status feedback into the inverter control, enabling: 1) re-synchronization

with the grid post-islanding, and 2) integration of secondary frequency and voltage control during islanded operation [67].

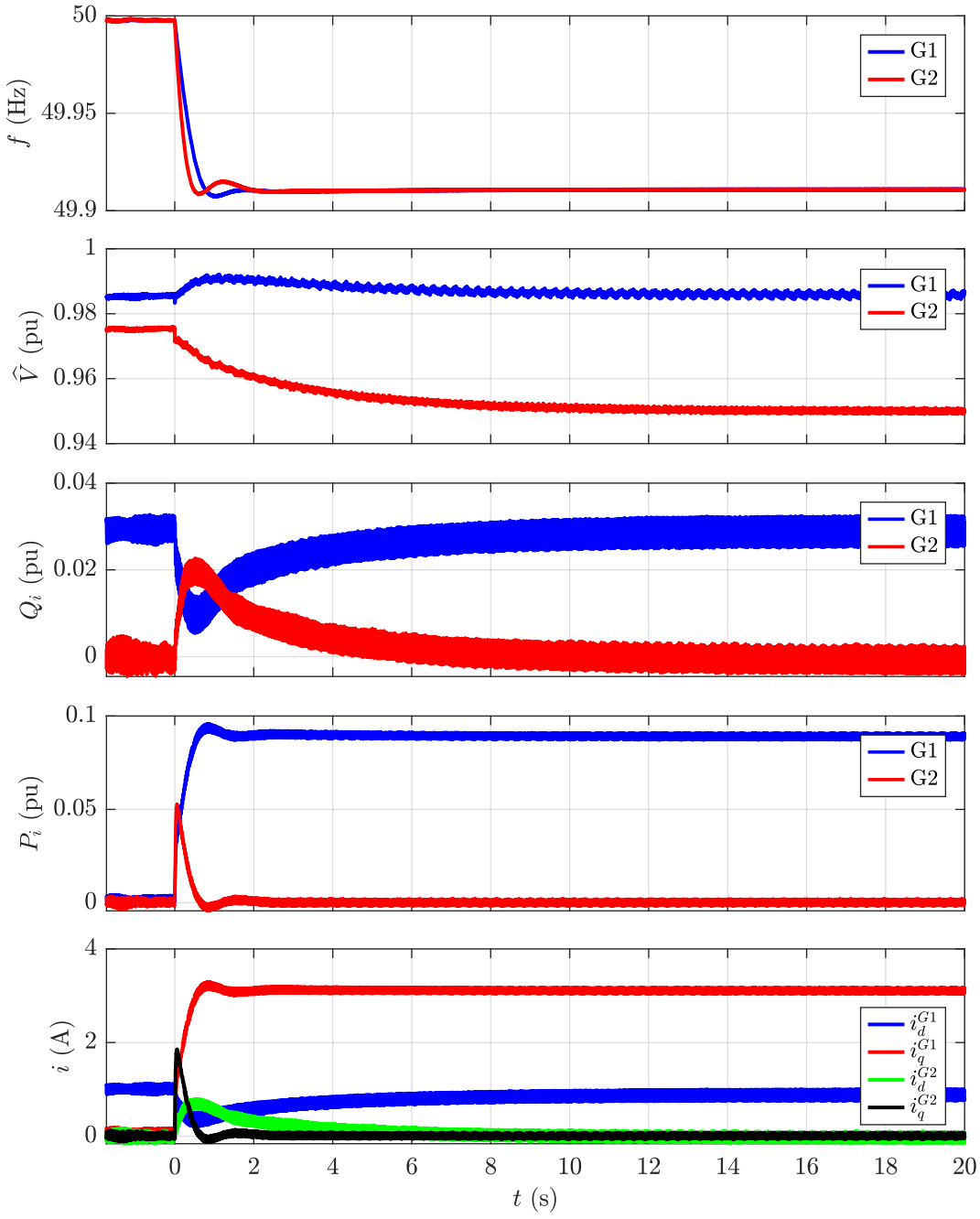

Fig. 5.24 Results of Test 5. From top to bottom: G1 and G2 frequency (Hz); G1 and G2 peak voltage measured at the filter capacitors (pu); G1 and G2 measured reactive power (pu); G1 and G2 measured active power (pu); G1 and G2 inverter currents in the (d, q) rotating reference frame [67].

Chapter 6

Robust Stability Analysis of the S-VSC

6.1 Introduction

Plant uncertainties (e.g. inaccurate estimation of grid impedance), grid reconfigurations and interactions with converters from neighbouring power plants can affect the grid-connected converters stability. To address these challenges, recent studies have focused on the robust stability analysis of grid-tied converters under specified uncertainties using μ-analysis [41, 74]. In existing literature, the μ-analysis has predominantly been performed to VSMs operating as VSGs. However, a VSM can operate as a Virtual Synchronous Compensator (VSC) as well, as described in Chapter 3. The VSC operates at a minimal load angle, demonstrating superior performance in transient stability and damping compared to VSGs, as demonstrated in [25]. Nevertheless, the robustness differences between VSCs and VSGs have not been thoroughly explored in literature.

As a primary contribution, this chapter proposes the robust stability analysis of the S-VSC [25], which is able to operate both as VSC and VSG. Nevertheless the findings are applicable to any VSM operating in both VSG and VSC modes. The theoretical findings from the μ-analysis indicate that a VSM operating as a virtual compensator exhibits greater robustness compared to when operating in VSG mode. Specifically, in the identical nominal conditions, a converter operating as a VSC remains stable over a wider range of uncertainties. This advantage holds true for both stiff and weak grid conditions, thereby enhancing the robust stability of grid-tied converters over the conventional VSG approach.

Table 6.1 Experimental setup 1 parameters.

Inverter		**Base Values**			
S_N	4 kVA	S_b	4 kVA	ω_b	314 rad/s
I_N	10 A	V_b	$120\sqrt{2}$ V	L_b	34.4 mH
f_{sw}	10 kHz	Z_b	10.8 Ω	C_b	0.3 mF
VSM		**LCL Filter**		**Grid**	
R_v	0.02 pu	L_f	5 mH	$\widehat{E}_g$	$120\sqrt{2}$ V
L_v	0.2 pu	C_f	1.5 µF	L_g	2.5 mH
H	4 s	L_{fg}	0.5 mH	R_g	0.5 Ω

Table 6.2 Simulation parameters.

Inverter		**Base Values**			
S_N	100 kVA	S_b	100 kVA	ω_b	314 rad/s
I_N	205 A	V_b	$230\sqrt{2}$ V	L_b	5.1 mH
f_{sw}	10 kHz	Z_b	1.6 Ω	C_b	2 mF
VSM		**LCL Filter**		**Grid**	
R_v	0.02 pu	L_f	0.05 pu	$\widehat{E}_g$	$230\sqrt{2}$ V
L_v	0.2 pu	C_f	0.03 pu	L_g	0.05 pu
H	4 s	L_{fg}	0.02 pu	R_g	0.005 pu

As a secondary contribution, this thesis introduces a novel experimental validation method for the outcomes derived from µ-analysis, a novelty in the literature. This experimental approach aims to empirically confirm the theoretical robustness advantages of operating as a VSC rather than a VSG.

As a third contribution, the same analysis is repeated for a grid-tied converter operating in parallel to a grid-forming converter. The grid-forming converter is controlled according to the Synchronverter algorithm [46]. The grid-tied converter can operate as both VSG and VSC. Even in this case, the theoretical and experimental results demonstrate that the VSC enhances the robustness of the system under the same operating conditions. Therefore, the VSC approach represents a more robust solution for controlling grid-tied converters, whether operating alone or in parallel with other converters.

Some of the findings and the results collected in this chapter led to the publication of [113].

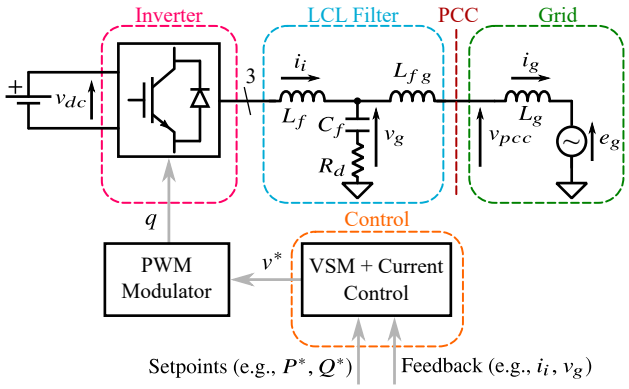

Fig. 6.1 Scheme of the system under study [114].

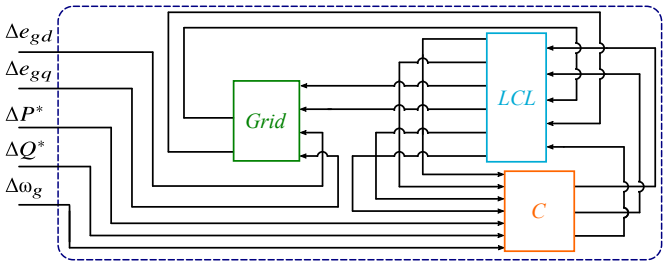

Fig. 6.2 Block scheme of the nominal system under study [114].

6.2 Robust Stability Analysis

6.2.1 System under analysis

The goal of robust stability analysis is to assess the stability of a set of systems that deviate from a designated reference system due to specified uncertainties. The initial step in conducting this analysis involves constructing a system model depicted in Fig. 6.1. In this thesis, the model of the system is built in the Laplace domain and linearized around a desired equilibrium point (such as the nominal working condition), and expressed in per unit (pu) values. Moreover, it is formulated in the (d, q) reference frame rotating at ω_r. The schematic diagram of the system, as shown in Fig. 6.2, includes the subsystems listed below [114]:

- *Controller C* represents the state-space model of the converter controlled using the VSM algorithm. The model is created by incorporating all the blocks shown in Fig. 3.34 and Fig. 3.35 (pay attention to the control block highlighted in orange). The block C features the following inputs and outputs:

$$\mathbf{u_C} = \left[\Delta i_{id}, \Delta i_{iq}, \Delta v_{gd}, \Delta v_{gq}, \Delta P^*, \Delta Q^*, \Delta \omega_g\right]^{\mathrm{T}} \tag{6.1}$$

$$\mathbf{y_C} = \left[\Delta e_{id}, \Delta e_{iq}, \Delta \omega_r\right]^{\mathrm{T}} \tag{6.2}$$

where e_i is the inverter output voltage (assumed equal to the voltage reference v^* for the modeling), i_i is the inverter current and ω_g is the frequency of the grid.

The state-space matrices are collected in Appendix A. [64];

- *LCL* represents the state-space model of the LCL filter. It receives the following inputs and generates the following outputs:

$$\mathbf{u_{LCL}} = \left[\Delta e_{id}, \Delta e_{iq}, \Delta i_{gd}, \Delta i_{gq}, \Delta \omega_r\right]^{\mathrm{T}} \tag{6.3}$$

$$\mathbf{y_{LCL}} = \left[\Delta i_{id}, \Delta i_{iq}, \Delta v_{gd}, \Delta v_{gq}, \Delta v_{pccd}, \Delta v_{pccq}\right]^{\mathrm{T}} \tag{6.4}$$

where i_g is the grid current and v_{pcc} is the PCC voltage.

The LCL filter features an auxiliary shunt resistance R_{aux} connected at the PCC [115, 64]. Such resistance is necessary to make the *LCL* block able to provide the PCC voltage v_{pcc} as output and to receive the grid current i_g as input. This is the needed structure to properly connect the *LCL* block to the *Grid* block described in the following. Note that R_{aux} does not alter the dynamic response of the overall system and it is set to 10^4 pu [64, 115]. The detailed state-space model of the *LCL* block can be retrieved from [64]. The PCC voltage v_{pcc} is computed as the voltage drop on R_{aux} as follows:

$$v_{pcc} = R_{aux}(i_{fg} - i_g) \tag{6.5}$$

- *Grid* represents the state-space model of the grid, which is modeled as a grid admittance. All the matrices of this subsystem are provided here:

$$\begin{cases} \dfrac{d\mathbf{x_{Grid}}}{dt} &= \mathbf{A_{Grid}}\mathbf{x_{Grid}} + \mathbf{B_{Grid}}\mathbf{u_{Grid}} \\ \mathbf{y_{Grid}} &= \mathbf{C_{Grid}}\mathbf{x_{Grid}} + \mathbf{D_{Grid}}\mathbf{u_{Grid}} \end{cases} \tag{6.6}$$

$$\mathbf{x_{Grid}} = \left[\Delta i_{gd}, \Delta i_{gq}\right]^{\mathrm{T}} \tag{6.7}$$

$$\mathbf{u_{Grid}} = \left[\Delta v_{pccd}, \Delta v_{pccq}, \Delta e_{gd}, \Delta e_{gq}\right]^{\mathrm{T}} \tag{6.8}$$

$$\mathbf{y_{Grid}} = \left[\Delta i_{gd}, \Delta i_{gq}\right]^{\mathrm{T}} \tag{6.9}$$

$$\mathbf{A_{Grid}} = \omega_b \begin{bmatrix} -\dfrac{R_g}{L_g} & \omega_{ro} \\ -\omega_{ro} & -\dfrac{R_g}{L_g} \end{bmatrix} \; ; \; \mathbf{C_{Grid}} = \mathbf{I}^{2x2} \tag{6.10}$$

$$\mathbf{B_{Grid}} = \frac{\omega_b}{L_g}\begin{bmatrix} 1 & 0 & -1 & 0 \\ 0 & 1 & 0 & -1 \end{bmatrix} \; ; \; \mathbf{D_{Grid}} = [\mathbf{0}]^{2x4} \tag{6.11}$$

where e_g, L_g and R_g are the grid voltage, the grid inductance and the grid resistance, respectively. ω_{ro} is the virtual speed at the linearized equilibrium point.

The comprehensive state-space model of the system under investigation can be derived using the Component Connection Method (CCM) [109–111]. This approach, widely used in the literature, involves integrating the individual state-space models of each subsystem into a unified representation of the overall system in a modular form [114].

6.2.2 Nominal Plant and Uncertainty Function

The second step involves identifying a nominal plant, $\mathbf{P_n}$, and a set of uncertain plants, $\mathbf{\Pi_u}$. System uncertainty can be modeled in various ways, such as parametric, additive, or multiplicative [116, 117]. In this thesis, the uncertainty is modeled multiplicatively as described in [41, 114]:

$$\mathbf{\Pi_u} = (\mathbf{I} + \mathbf{W})\mathbf{P_n} \tag{6.12}$$

where $\mathbf{I}$ is the identity matrix, $\mathbf{W}$ is a frequency-dependent uncertainty matrix, and $\mathbf{\Pi_u}$ is a set of plants that deviate from the nominal plant due to the given uncertainty $\mathbf{W}$.

The chosen nominal plant $\mathbf{P_n}$ corresponds to the grid model of (6.6). Thus, in the context of the schematic shown in Fig. 6.2, the *Grid* block introduces a certain level of uncertainty. Conversely, both the Controller (C) and the LCL filter (LCL) are considered known and are unaffected by any uncertainties. In the case of grid-connected converters, uncertainties typically arise from factors like grid impedance estimation errors, system reconfigurations, and interactions with other converters connected to the grid [74].

To account for these uncertainties, the uncertainty function W_u is constructed by incorporating the following specific uncertainties: a 20% variation in the Short Circuit Ratio (SCR), a 33% variation of the X/R ratio (i.e., the ratio between the grid reactance and the grid resistance), and resonant high-frequency effects as discussed in [74].

As stated in the previous subsection, the system is modeled in the (d, q) rotating reference frame. The Bode diagram of the nominal plant P_n either on the d-axis or q-axis is depicted in blue in Fig. 6.3. It represents an ideal resistive-inductive admittance. The same figure proposes the Bode diagrams by adding the sources of uncertainty: different SCR in red ($P_{u,SCR}$), different X/R ratio in green ($P_{u,XR}$), high frequency effects in magenta ($P_{u,HF}$) [74]. Next, for the i-th element of uncertainty, the i-th uncertainty

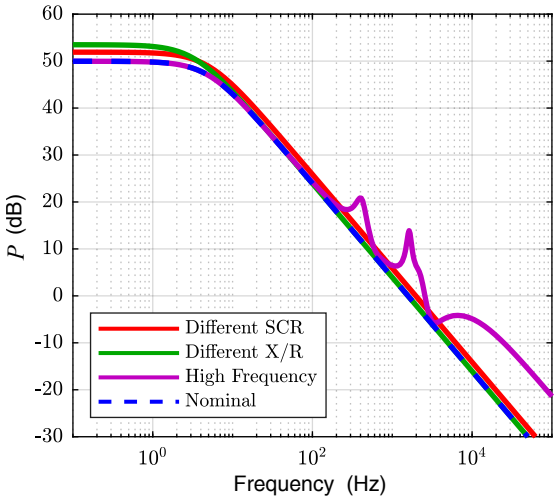

Fig. 6.3 Bode diagram of the nominal plant P_n and the uncertain plants.

function $W_{u,i}$ can be computed as follows [74]:

$$W_{u,i} = \left| \frac{P_{u,i} - P_n}{P_n} \right| \tag{6.13}$$

where $P_{u,i}$ is the i-th uncertain plant.

The Bode diagrams of the i-th uncertainty functions $W_{u,i}$ are depicted in Fig. 6.4 in red, green and magenta, respectively for the different SCR, the different X/R ration and the high frequency effects. Finally, the overall function W_u is built as an envelope of all of the i-th terms as demonstrated in [74]. Its Bode diagram is illustrated in Fig. 6.4 as well. The uncertainty matrix $\mathbf{W}$ can ultimately be constructed as follows:

$$\mathbf{W} = \begin{bmatrix} W_d & 0 \\ 0 & W_q \end{bmatrix} \tag{6.14}$$

where W_d and W_q are respectively the uncertainty function on the d-axis and the uncertainty function on the q-axis. Additionally, $W_d = W_q = W_u$. The uncertain plants contained in the set $\mathbf{\Pi}_p$ are derived from all the uncertainties encompassed by W_u [114].

6.2.3 Perturbation Matrix and $M\Delta$ structure

The third step of the μ-analysis involves defining a set of perturbed uncertain plants, $\mathbf{\Pi_p}$, as follows:

$$\mathbf{\Pi_p} = (\mathbf{I} + \mathbf{W\Delta})\mathbf{P_n} \tag{6.15}$$

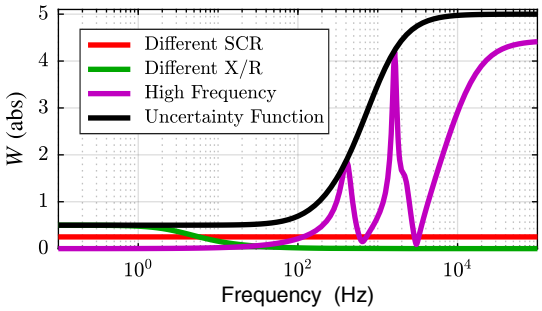

Fig. 6.4 Bode diagram of the uncertainty function W_u with its single terms [114].

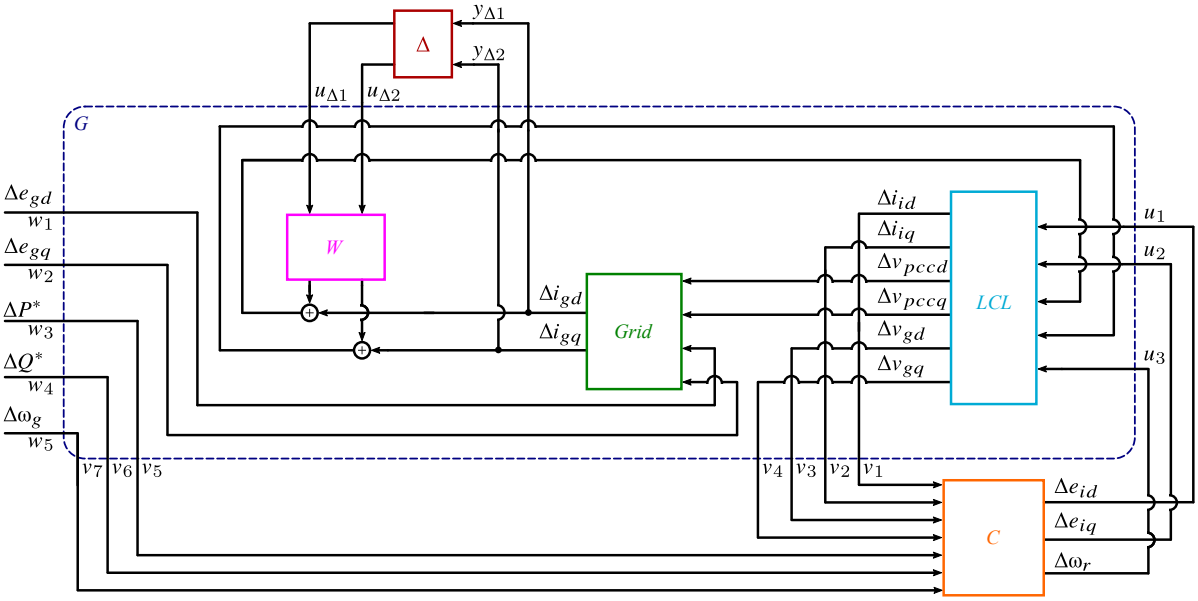

Fig. 6.5 Overall block scheme of the system needed to execute the μ-analysis [114].

where $\mathbf{\Delta}$ is the perturbation matrix.

The perturbation matrix $\mathbf{\Delta}$ is the unknown variable that is affected by the minimization problem on which the μ-analysis is based. With no constraints, it is a generic matrix, i.e., it can be real or complex, diagonal or full, structured or unstructured [116, 117]. It is possible to impose constraints on the perturbation matrix through the variable *BlkStruct*. This variable defines the constraints of the μ-analysis solutions. For example, the matrix can be forced to be real and diagonal. This way, the analysis will provide a solution withing the imposed constraints. Note that the perturbed uncertain plants $\mathbf{\Pi_p}$ of (6.15) are retrieved by perturbing the nominal plant $\mathbf{P_n}$ with a perturbation $\mathbf{\Delta}$, weighted through the uncertainty matrix $\mathbf{W}$. In other words, the uncertainty matrix $\mathbf{W}$ behaves as a weight of the perturbation at each frequency.

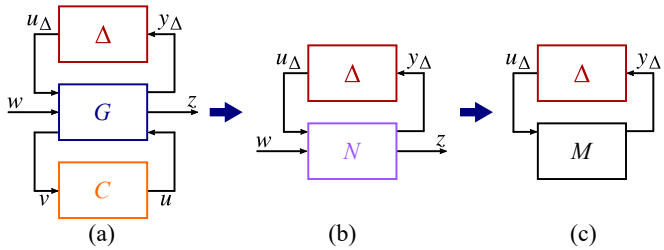

Fig. 6.6 Structure steps for the μ-analysis: (a) $CG\Delta$; (b) $N\Delta$; (c) $M\Delta$ [114].

Subsequently, to construct the final state-space model, the uncertainty block denoted as W and the perturbation block represented by $\mathbf{\Delta}$ are inserted into the schematic shown in Fig. 6.2. This results in the revised schematic shown in Fig. 6.5, where the uncertainty block incorporates the uncertainty matrix $\mathbf{W}$, and the perturbation block contains the perturbation matrix $\mathbf{\Delta}$. The CCM enables a more compact representation of the scheme, which consists of three blocks: the generalized plant $\boldsymbol{G}$, the controller $\boldsymbol{C}$ and the perturbation block Δ. As highlighted in dark blue in Fig. 6.5, the generalized plant $\boldsymbol{G}$ is the portion of the system which gathers the known part of the system (i.e., LCL block), the nominal plant (i.e., $Grid$) and the uncertainty block $\boldsymbol{W}$. Therefore, it merges each block of the system which is not related to the control and the perturbation matrix.

A simpler representation is illustrated in Fig. 6.6a with the name of $CG\Delta$ structure. This is the first milestone of the procedure to perform the μ-analysis. Next, the $CG\Delta$ structure is simplified to the $N\Delta$ structure, as illustrated in Fig. 6.6b, using the linear fractional transformation (LFT) [116, 117]. Through this operation, the generalized plant $\boldsymbol{G}$ and the controller $\boldsymbol{C}$ are merged into the N block. Finally, the M block is retrieved by taking into account only the inputs and outputs of the N block related to Δ. The $M\Delta$ structure of Fig. 6.6c is thus obtained. The $M\Delta$ structure is the system on which apply the μ-analysis. The M block contains the state-space model of the entire system, only considering the inputs coming from the perturbation block Δ and the outputs which are perturbed by $\mathbf{\Delta}$ [114].

6.2.4 Theory of the μ-analysis

The structured singular value (commonly denoted as SSV or μ) is a mathematical concept established to derive necessary and sufficient conditions for robust stability [117]. The definition of μ is closely linked to the theorem detailed below [117, 114]:

Theorem 1 (Determinant stability condition) *Assume that the nominal system* $\mathbf{M}(s)$ *and the perturbations* $\mathbf{\Delta}(s)$ *are stable. [...] Then, the M*Δ *structure of Fig. 6.6c is stable for all allowed perturbations (we have robust stability) if and only if*

$$\det[\mathbf{I} - \mathbf{M\Delta}(j\omega)] \neq 0 \, , \forall \omega, \forall \mathbf{\Delta} \text{ such that } ||\mathbf{\Delta}||_\infty \leq 1 \tag{6.16}$$

The comprehensive theorem and its proof are detailed in [117]. In (6.16), $||\mathbf{\Delta}||_\infty$ denotes the H_∞ norm of $\mathbf{\Delta}$. Starting from (6.16), μ-analysis involves determining, at each frequency ω, the smallest matrix $\mathbf{\Delta_{min}}$ (i.e., $\mathbf{\Delta}$ with the smallest maximum singular value $\overline{\sigma}$) that renders the matrix $\mathbf{I} - \mathbf{M\Delta}(j\omega)$ singular (i.e., makes its determinant zero). The maximum singular value $\overline{\sigma}$ is equal to $||\mathbf{\Delta}||_\infty$. Consequently, μ is defined as the reciprocal of $\overline{\sigma}$. Mathematically, this can be expressed as:

$$\mu(\mathbf{M}) \triangleq \frac{1}{\min\limits_{\mathbf{\Delta}} \{\overline{\sigma}(\mathbf{\Delta}) \mid \det(\mathbf{I} - \mathbf{M\Delta}) = 0\}} \tag{6.17}$$

where μ is defined as $\mu = 1/\overline{\sigma}(\mathbf{\Delta})$ at each frequency.

Eq. (6.17) is strictly applicable for structured $\mathbf{\Delta}$ (not full matrices). However, (6.17) can be generalized to the unstructured case (full matrix) as demonstrated in [117]. Finally, the perturbation matrix $\mathbf{\Delta}$ can be normalized such that $\overline{\sigma}(\mathbf{\Delta}) \leq 1$. Applying the μ-analysis yields the following result [114]:

- For each frequency, the determinant of (6.17) may become zero for various values of $\mathbf{\Delta}$. Among these potential solutions, ensuring robust stability involves selecting the smallest matrix $\mathbf{\Delta_{min}}$. This matrix determines, at each frequency, the minimal condition that induces system instability, quantified by the magnitude of its maximum singular value $\overline{\sigma}$. Thus, the μ-analysis functions as a minimization problem, aiming to identify the smallest $\mathbf{\Delta_{min}}$ at each analyzed frequency;
- As (6.17) is evaluated at every frequency within the specified range, $\mathbf{\Delta_{min}}$ varies with frequency. Among all the $\mathbf{\Delta_{min}}$ matrices computed at each frequency ω_h, there exists a frequency ω_k such that:

$$\begin{cases} ||\mathbf{\Delta_{min}}(j\omega_k)||_\infty < ||\mathbf{\Delta_{min}}(j\omega_h)||_\infty \;\; , \;\; \forall \; h \neq k \\ \mathbf{\Delta_{min}}(j\omega_k) = \mathbf{\Delta_{Min}} \\ \mu_{max} = \mu(\omega_k) = 1/\overline{\sigma}(\mathbf{\Delta_{Min}}) \end{cases} \tag{6.18}$$

According to (6.18), $\mathbf{\Delta_{Min}}$ is the smallest perturbation matrix across the entire frequency range, and μ_{max} is the peak value of μ over this range, both evaluated at frequency ω_k. Therefore, $\mathbf{\Delta_{Min}}$ represents the minimal perturbation required to render the system unstable. Indeed, based on (6.17), there is no smaller matrix $\mathbf{\Delta}$ that can nullify the determinant (i.e., induce instability in the system). Moreover, the system will diverge at frequency ω_k. Consequently, μ_{max} serves as an index of robustness because it allows to identify [114]:

- The smallest perturbation matrix $\mathbf{\Delta_{Min}}$ that induces instability in the system at the specific frequency ω_k;
- The frequency ω_k at which the smallest unstable system oscillates;
- The collection of perturbed stable plants within the specified uncertainty set.

- The set of stable perturbed plants $\mathbf{\Pi_{p,s}}$ is defined by all matrices $\mathbf{\Delta}$ satisfying $\overline{\sigma}(\mathbf{\Delta}) < 1/\mu_{max}$;
- The set of unstable perturbed plants $\mathbf{\Pi_{p,u}}$ consists of all matrices $\mathbf{\Delta}$ where $\overline{\sigma}(\mathbf{\Delta}) > 1/\mu_{max}$ and $\det(\mathbf{I} - \mathbf{M\Delta}) = 0$.

In summary, depending on the value of μ_{max}, the following conditions apply [114]:

- If $\mu_{max} = 1$, all the plants in the set of uncertainty $\mathbf{\Pi_u}$ are stable;
- If $\mu_{max} > 1$, not all plants in the uncertainty set $\mathbf{\Pi_u}$ are stable; only plants in the set $\mathbf{\Pi_{p,s}}$ are stable. Thus, a higher μ_{max} results in a smaller set of stable plants given the uncertainties;
- If $\mu_{max} < 1$, all plants in the uncertainty set $\mathbf{\Pi_u}$ are stable. Furthermore, even perturbed plants where $1 \leq \overline{\sigma}(\mathbf{\Delta}) \leq 1/\mu_{max}$ remain stable.

Therefore, μ_{max} indicates the size of the set of stable plants under the given uncertainty. Specifically, a lower μ_{max} corresponds to a larger set of stable plants. In essence, μ_{max} quantifies the system robustness as a larger set of stable plants indicates greater robustness [114].

6.2.5 Physical meaning of the μ-analysis

Initially, the μ-analysis is conducted in a simplified scenario to elucidate its physical significance. This and all the following results of the μ-analysis are retrieved through a

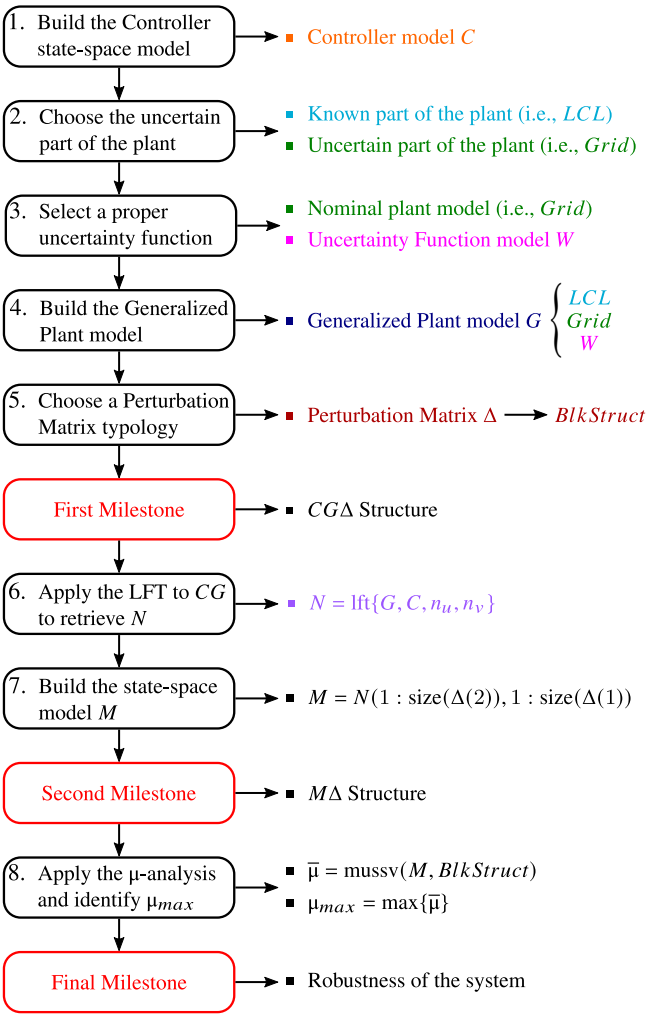

Fig. 6.7 Step-by-step flow chart to perform the μ-analysis.

MATLAB script. All the steps needed to perform the analysis are summarized in the flow chart of Fig. 6.7. To simplify, the sole source of uncertainty is the Short Circuit Ratio (SCR). Assuming a 20% uncertainty in the SCR, the uncertainty matrix $\mathbf{W_{SCR}}$ can be expressed as:

$$\mathbf{W_{SCR}} = w_{SCR} \begin{bmatrix} 1 & 0 \\ 0 & 1 \end{bmatrix} = w_{SCR} \mathbf{I}^{2x2} \tag{6.19}$$

where $w_{SCR} = 0.25$ across the entire frequency range, as depicted in Fig. 6.4 [114]. Therefore, a set of uncertain plants can be defined as follows:

$$\mathbf{\Pi_{u,SCR}} = (\mathbf{I} + \mathbf{W_{SCR}})\mathbf{P_n} = (1 + w_{SCR})\mathbf{P_n} \tag{6.20}$$

Then, the set of perturbed uncertain plants is established as follows:

$$\mathbf{\Pi_{p,SCR}} = (\mathbf{I} + \mathbf{W_{SCR}}\mathbf{\Delta})\mathbf{P_n} \tag{6.21}$$

As the uncertainty is applied only on the SCR, it means that all the reasonable pertubed plants differ from the nominal one for a real multiplicative coefficient of the grid admittance. Therefore, the perturbation matrix can be forced to be real and diagonal (i.e., perturbations are not cross-coupled). Moreover, the elements of Δ are forced to be equal, as there is no reason to consider solutions with different perturbations for the d and q axes. All these constraints are forced on MATLAB through the variable *BlkStruct*. The μ-analysis is conducted using the parameters detailed in Table 6.1 and with an inverter active power injection of $P_i = 0.2$ pu. These parameters correspond to those utilized in the experimental setup. As soon as the system is arranged in the $M\Delta$ structure, the μ-analysis is performed through the command `mussv` of MATLAB. It provides a vector $\overline{\mu}$ which contains the value of μ for each frequency of the considered range. The range and step size can be chosen by the user [114].

The results for the VSM operating as both VSC and VSG are presented in Fig. 6.8. This figure displays the μ value across the analyzed frequency range. In this case, μ is zero among all the frequency range expect for one point as, for the considered condition (i.e., operating point, control and setup parameters), the instability is triggered only by that non null condition. In the following section μ will be non zero among all the frequency range, as, for each frequency, there exist a perturbation which makes the system unstable. The μ-analysis determines which plants are stable within the set of uncertain plants $\mathbf{\Pi_{u,SCR}}$. The least perturbed unstable plant $\mathbf{P_{p,u,min}}$ is found using the smallest perturbation matrix $\mathbf{\Delta_{Min}}$ that satisfies (6.17), as follows:

$$\mathbf{P_{p,u,min}} = (\mathbf{I} + \mathbf{W_{SCR}}\mathbf{\Delta_{Min}})\mathbf{P_n} = \frac{1}{k_{SCR}}\mathbf{I}^{2x2}\mathbf{P_n} \tag{6.22}$$

where:

$$\begin{cases} \mathbf{\Delta_{Min}} = k_\Delta \mathbf{I}^{2x2} \\ |k_\Delta| = ||\mathbf{\Delta_{Min}}||_\infty = 1/\mu_{max} \\ k_{SCR} = 1/(1 + w_{SCR}k_\Delta) \end{cases} \tag{6.23}$$

Based on (6.22), the minimal condition to induce system instability corresponds to a grid impedance k_{SCR} times the nominal value. The collection of stable perturbed plants

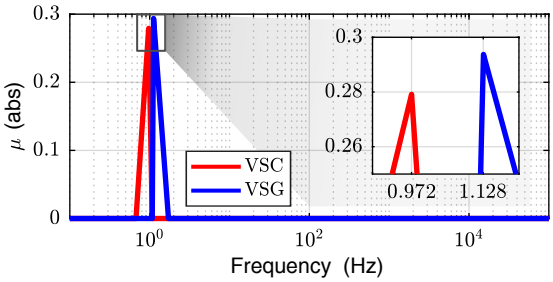

Fig. 6.8 μ-analysis results assuming the SCR as a sole source of uncertainty: VSC in red, VSG in blue [114].

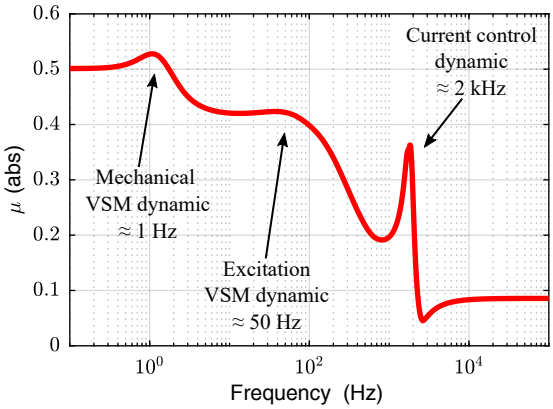

Fig. 6.9 μ-analysis result of the VSC with the uncertainty **W**.

can be expressed as follows:

$$\mathbf{\Pi_{p,s,SCR}} = (\mathbf{I} + \mathbf{W_{SCR}}\mathbf{\Delta_s})\mathbf{P_n} = \frac{1}{k_{SCR,s}}\mathbf{I}^{2x2}\mathbf{P_n} \tag{6.24}$$

where:

$$\begin{cases} \mathbf{\Delta_s} = k_{\Delta,s}\mathbf{I}^{2x2} \\ |k_{\Delta,s}| = ||\mathbf{\Delta_s}||_\infty < ||\mathbf{\Delta_{Min}}||_\infty = |k_\Delta| \\ k_{SCR,s} = 1/(1 + w_{SCR}k_{\Delta,s}) < k_{SCR} \end{cases} \tag{6.25}$$

According to equations (6.24) and (6.25), systems where the grid impedance is less than k_{SCR} times the nominal value are stable. In the VSC mode, μ_{max} is 0.278 at a frequency of 0.972 Hz, and $\mathbf{\Delta_{Min}}$ is $-3.6 \cdot \mathbf{I}^{2x2}$. Hence, k_{SCR} equals 9.93 (approximately 10). This indicates that the system becomes unstable if the grid impedance increases by a factor of 10. Under these conditions, the system will oscillate with a frequency of 0.972 Hz.

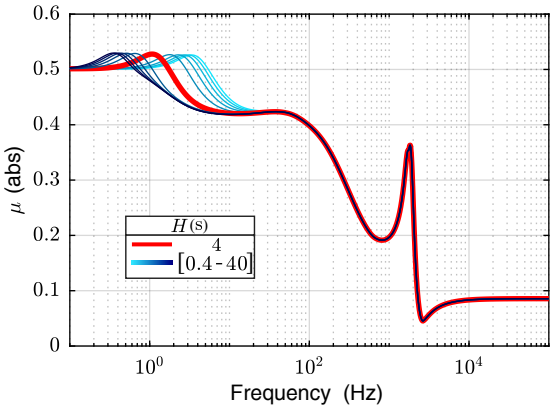

Fig. 6.10 μ-analysis result of the VSC with the uncertainty **W** varying the inertia constant H.

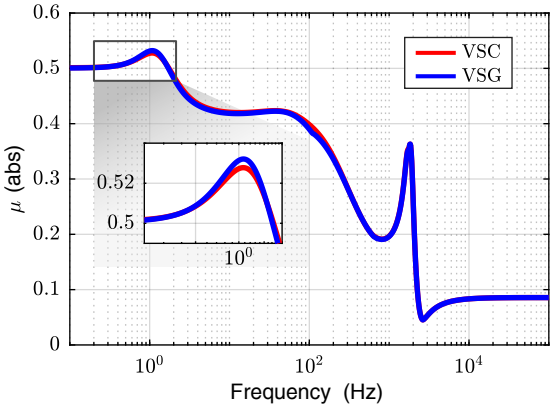

Fig. 6.11 μ-analysis results with the uncertainty **W** for VSC (red) and VSG (blue).

Similarly, in VSG mode, μ_{max} is 0.292 with an oscillation frequency of 1.128 Hz, and $\mathbf{\Delta_{Min}}$ is $-3.43 \cdot \mathbf{I}^{2x2}$. Here, k_{SCR} is 6.95 (approximately 7). Therefore, the system becomes unstable for a smaller increase in grid impedance compared to VSC mode. This theoretical analysis highlights the enhanced robustness of VSC compared to VSG. Under identical nominal conditions, the VSM operating in VSC mode maintains stability across a broader spectrum of perturbed plants, spanning grid impedance values from 7 to 10 times the nominal value. This finding is corroborated by experimental validation in Section 6.5 [114].

6.3 Robust Stability Analysis of the single converter

This section conducts a robust stability analysis of the VSM using the uncertainty function depicted in Fig. 6.4. The parameters employed for this analysis are outlined in Table 6.2, selected to reflect a typical scenario of a power plant connected to the grid

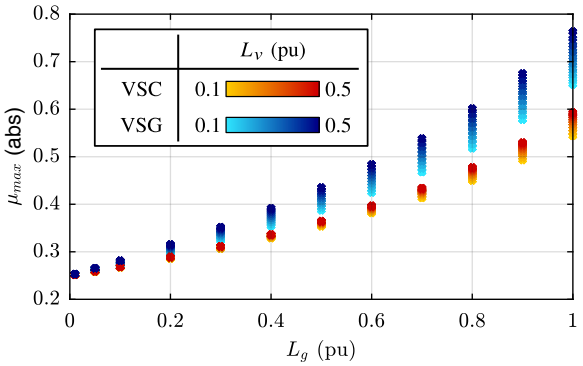

Fig. 6.12 μ_{max} value for different values of L_g (from 0.01 pu to 1 pu) and L_v (from 0.1 pu to 0.5 pu).

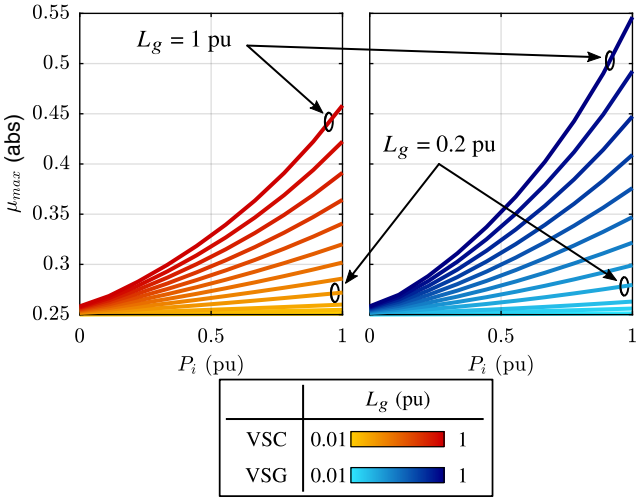

Fig. 6.13 μ_{max} value for different values of L_g (from 0.01 pu to 1 pu) and P_i (from 0 pu to 1 pu).

via power electronic converters. The system is linearized around the nominal operating point of the inverter (P^* = 1 pu) [114].

The results of the μ-analysis for the VSM operating in VSC mode are presented in Fig. 6.9 [114]. At each frequency, the μ value correlates with specific system dynamics. For instance, the virtual electromechanical dynamics of the VSM (e.g., swing equation) predominantly affect μ in the low-frequency range (0.1 Hz to 10 Hz). This observation is validated by repeating the analysis with different values of the virtual inertia constant H, as depicted in Fig. 6.10. Here, μ varies exclusively within the frequency band associated with virtual electromechanical dynamics, while its behavior remains consistent at high frequencies (100 Hz to 10 kHz), primarily influenced by current control and LCL filter

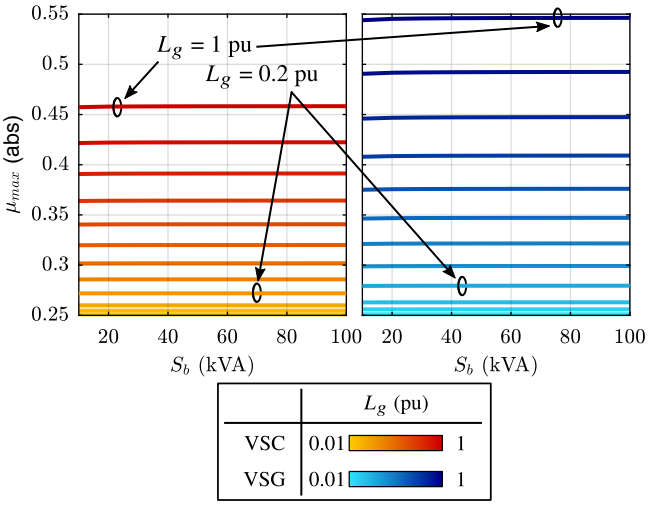

Fig. 6.14 μ_{max} value for different values of L_g (from 0.01 pu to 1 pu) and S_b (from 10 kVA to 100 kVA).

dynamics. Additionally, the excitation VSM dynamic related to the virtual flux λ_e affects μ around the nominal grid frequency (50 Hz).

Subsequently, the μ-analysis is performed for the VSG mode operation. The comparison of results between VSC and VSG modes is illustrated in Fig. 6.11. It is observed that in VSG mode, the peak μ value at low frequencies exceeds that of the VSC case, whereas both modes exhibit similar behavior in the high-frequency range. This distinction indicates that the operational mode of the VSM influences its response primarily in low-frequency phenomena.

In this generalized analysis, the VSM demonstrates greater robustness when operated as a virtual compensator (VSC), as evidenced by $\mu_{max,VSC} < \mu_{max,VSG}$. This implies that under identical conditions, a VSM controlled as a compensator remains stable over a broader range of perturbations (or uncertainties) compared to when operated as a generator (VSG) [114].

This result is obtained under a specific operating condition. To comprehensively highlight the benefits of the VSC over the VSG, the μ-analysis is performed for different:

- virtual inductance values (i.e., different L_v);
- working operating conditions (i.e., different P^*);
- sizes of the converter (i.e., different S_b).

All cases are tested for different values of grid impedance, from a really stiff condition (SCR = 100) to a really weak one (SCR = 1). The nominal values are expressed in per unit in Table 6.2. The analysis is performed considering the uncertainty on the SCR (w_{SCR}=0.25). The results are respectively illustrated in Fig. 6.12, Fig. 6.13 and Fig. 6.14.

Fig. 6.12 shows how μ_{max} almost linearly increases by increasing the grid inductance value L_g along the horizontal axis. The grid resistance R_g is constantly equal to $L_g/10$. Moreover, the analysis is repeated for five reasonable values of virtual impedance (L_v from 0.1 to 0.5 pu, $R_v = L_v/10$). It can be observed that the higher is the virtual inductance, the higher is μ_{max} (i.e., the lower is the robustness). Notably, in all cases the VSC shows a lower μ_{max} value, i.e., the VSC guarantees a higher robustness compared to the VSG.

Next, Fig. 6.13 provides the results obtained by changing the working operating condition of the converter (i.e., the active power reference P^* and therefore the inverter active power P_i) from 0 to 1 pu. At zero power the VSC and VSG show obviously the same robustness. Then, μ_{max} exponentially increases by increasing the working operating point. It can be observed that, under the same conditions, the VSC still shows a lower μ_{max} value compared to VSG.

Finally, the same analysis is performed for several sizes of the converter by changing the base value S_b from 10 to 100 kVA. The results are illustrated in Fig. 6.14. It can be observed that for each grid impedance condition, the value of μ_{max} is almost constant independently of the converter size. Therefore, in per unit values, the robustness of a system is independent of the converter size. Even in this final case, under the same condition, the VSC enhances the robust stability of the grid-tied converter compared to the VSG.

6.4 Robust Stability Analysis of the parallel converters

The same analysis of Section 6.3 is repeated for a system of two parallel converters. The scheme of the system under study is depicted in Fig. 6.15. Two inverters, named Inverter 1 and Inverter 2, share a common ideal dc-source. They are connected to the grid at the PCC through their own LCL filter (Filter 1 and 2), as highlighted in Fig. 6.15. The two filters are equal as the inverters (e.g., same size, switching frequency). All the parameters are collected in Table 6.2 and they are the same of the single converter analysis.:

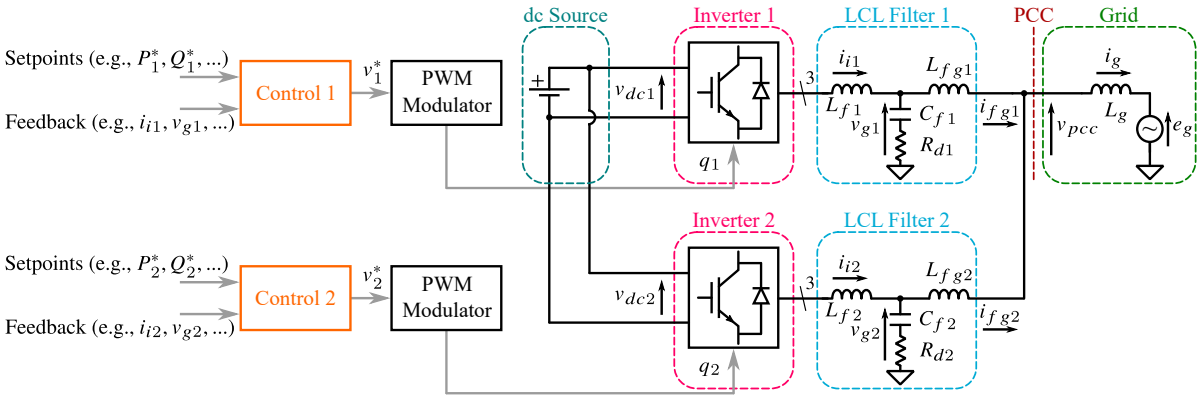

Fig. 6.15 Scheme of the parallel system under study.

- Inverter 1 is the same converter of the previous section. Therefore, the block Control 1 of Fig. 6.15 is the control already described in Fig. 3.34;
- Inverter 2 operates as a grid-forming converter and its control algorithm is described in the following subsection.

6.4.1 Synchronverter model

Inverter 2 operates as a VSG grid-forming converter and it is controlled according to the original version of the Synchronverter [46]. The control scheme is depicted in Fig. 6.16.

The Synchronverter consists of three main parts:

- Swing Equation (highlighted in green in Fig. 6.16): it emulates the mechanical dynamic of the virtual machine. The inputs are the reference active power P^* (from a higher level control unit) and the electrical torque T_e retrieved from the measured active power P_i. This part provides the frequency ω_r and the angle θ_r of the virtual machine;
- Excitation Control (highlighted in blue in Fig. 6.16): it emulates the excitation control of the virtual machine. It receives as inputs the reference reactive power Q^* from a higher level control unit and the measured reactive power Q_i. It provides the virtual flux $M_f i_f$ as output;
- P, Q, V Calculation block: this block calculates the inverter active power P_i, the reactive inverter power Q_i and the voltage amplitude V_g from the measured inverter current i_i and the measured voltage v_g.

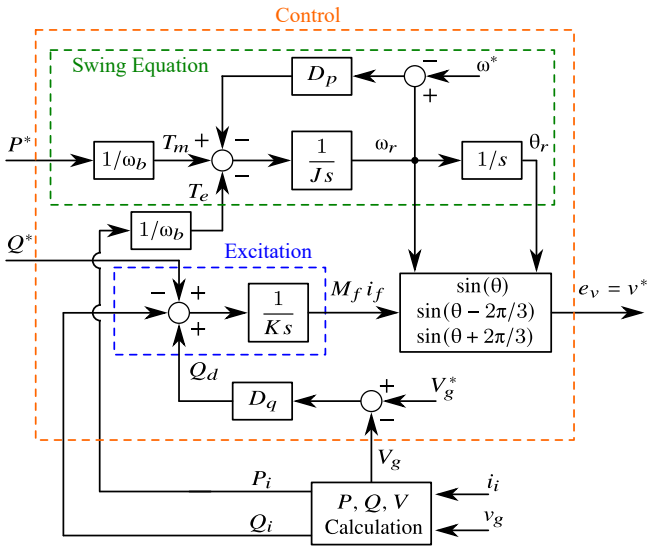

Fig. 6.16 Scheme of the Synchronverter control algorithm.

The flux amplitude $M_f i_f$, the virtual frequency ω_r and the virtual angle θ_r are used to calculated the three-phase virtual electromotive force e_v as follows:

$$e_v = \begin{bmatrix} e_{v,a} \\ e_{v,b} \\ e_{v,c} \end{bmatrix} = M_f i_f \omega_r \begin{bmatrix} \sin(\theta_r) \\ \sin(\theta_r - 2\pi/3) \\ \sin(\theta_r + 2\pi/3) \end{bmatrix} \tag{6.26}$$

The electromotive force is the voltage reference v^* used to retrieve the inverter commands q. Therefore, Inverter 2 operates as a grid-forming because it directly imposes its voltage reference with no current regulator.

6.4.2 State-space model of the parallel converters

The block scheme of the system under analysis is illustrated in Fig. 6.17. For simplicity, the (d, q) quantities are written as vectors, where the generic quantity $\overline{x}$ corresponds to $\overline{x} = [x_d, x_q]^{\mathrm{T}}$. The *C1* block corresponds to the Control block of Fig. 6.5. The *C2* block corresponds to the control block highlighted in orange in Fig. 6.16. It features the following inputs and outputs:

$$\mathbf{u_{C2}} = \left[\Delta P_2^*, \Delta P_{i2}, \Delta Q_2^*, \Delta Q_{i2}, \Delta V_{g2}\right]^{\mathrm{T}} \tag{6.27}$$

$$\mathbf{y_{C2}} = \left[\Delta E_{i2}, \Delta \omega_{r2}, \Delta \theta_{r2}\right]^{\mathrm{T}} \tag{6.28}$$

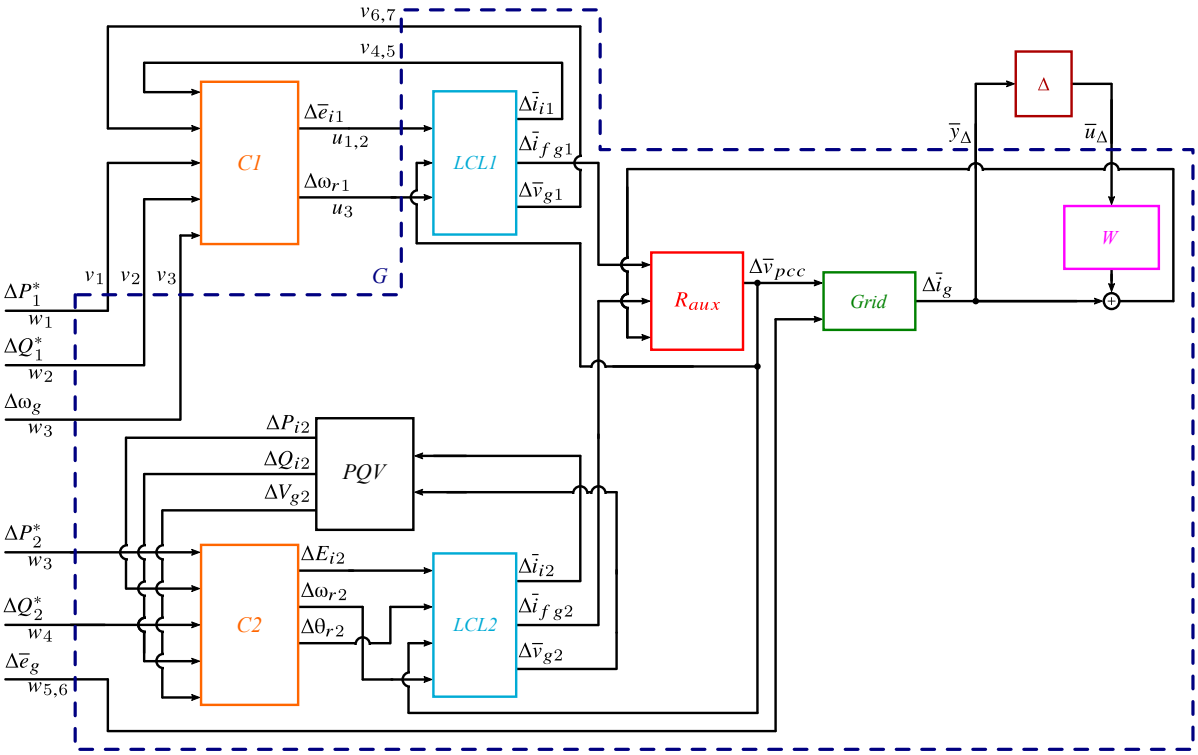

Fig. 6.17 Complete block scheme of the overall parallel system to perform the μ-analysis.

where E_{i2} and θ_{r2} are respectively the amplitude and the phase of the Inverter 2 voltage output, assuming ideal the Synchronverter control (i.e., $e_v = v^* = e_i$).

The *PQV* block performs the P,Q,V Calculation operations. A detailed description of the state-space matrices can be found in [74].

The *LCL1* block is slightly different to the *LCL* block of Section 6.2 as there is no auxiliary resistance. Therefore, it receives the PCC voltage v_{PCC} as input and it provides the grid-side filter current i_{fg1} as output. The entire subsystem features the following inputs and outputs:

$$\mathbf{u_{LCL1}} = \left[\Delta e_{i1d}, \Delta e_{i1q}, \Delta v_{pccd}, \Delta v_{pccq}, \Delta\omega_{r1}\right]^{\mathrm{T}} \tag{6.29}$$

$$\mathbf{y_{LCL1}} = \left[\Delta i_{i1d}, \Delta i_{i1q}, \Delta i_{fg1d}, \Delta i_{fg1q}, \Delta v_{g1d}, \Delta v_{g1q}\right]^{\mathrm{T}} \tag{6.30}$$

Next, *LCL2* is almost the same of *LCL1*. The only difference lies in the input inverter voltage. In the *LCL1* block the inverter voltage e_{i1} is provided in (d,q) components, whereas the *LCL2* block receives the inverter voltage as amplitude E_{i2} and phase θ_{r2}.

$$\mathbf{u_{LCL2}} = \left[\Delta E_{i2}, \Delta\omega_{r2}, \theta_{r2}\right]^{\mathrm{T}} \tag{6.31}$$

$$\mathbf{y_{LCL2}} = \left[\Delta i_{i2d}, \Delta i_{i2q}, \Delta i_{fg2d}, \Delta i_{fg2q}, \Delta v_{g2d}, \Delta v_{g2q}\right]^{\mathrm{T}} \tag{6.32}$$

Finally, the *Grid* block, the uncertainty function W and the perturbation matrix Δ are the same of the analysis of Section 6.3. As for the previous analysis, the *Grid* block has the PCC voltage v_{pcc} and the grid voltage e_g as inputs and the grid current i_g as output. The grid current is a state variable, as the grid-side currents i_{fg1} and i_{fg2} of the two LCL filters. Therefore, i_g cannot be calculated as simply the sum of i_{fg1} and i_{fg2}. To solve this incompatibility, a common practice is to parallel the two LCL filters through an auxiliary shunt resistance R_{aux} connected at the PCC [64]. R_{aux} does not alter the dynamic response of the overall system and it is set to 10^4 pu [115]. As for the *LCL* block of Section 6.2, the PCC voltage v_{pcc} is computed as the voltage drop on R_{aux} as follows:

$$v_{pcc} = R_{aux}(i_{fg1} + i_{fg2} - i_g) \tag{6.33}$$

6.4.3 μ-analysis of the parallel converters

The μ-analysis of the parallel converters system is performed according to the procedure described in Section 6.2 and Section 6.3. First, the robust stability analysis is evaluated for the simplified case of uncertainty only on the SCR (20%). The parameters used for the analysis are the experimental setup 2 parameters listed in Table 6.3. Note that the values are different from the setup 1 parameters because the tests have been performed in two different laboratories. The control parameters of Inverter 1 and 2 are tuned according to [25] and [65], respectively, and listed in Table 6.3. Inverter 1 operates at $P_i = 0.2$ pu, whereas Inverter 2 operates at $P_i = 0.1$ pu.

Fig. 6.18 illustrates the theoretical outcomes. The system of a VSG in parallel to the Synchronverter shows a μ_{max} value of 0.298 at 1.396 Hz, which corresponds to a k_{SCR} equal to 6.2. Therefore, if the grid impedance increases of 6.2 times, the system will diverge at a frequency of 1.396 Hz. The same test is repeated for the VSC in parallel to the Synchronverter. The result demonstrates the superior robustness of the VSC, as μ_{max} is equal to 0.28, which corresponds to a $k_{SCR} = 9.3$. Therefore, the system VSC+Synchronverter is more robust as it needs an higher variation of grid impedance to become unstable. The theoretical instability frequency is equal to 1.285 Hz. This result will be experimentally demonstrated in the following section.

Next, the theoretical analysis is performed for a more generic case as in Section 6.3 using the simulation parameters of Table 6.2 for both Inverter 1 and Inverter 2.

Table 6.3 Experimental setup 2 parameters.

Inverter 1 & 2		**Base Values**			
S_N	15 kVA	S_b	15 kVA	ω_b	314 rad/s
I_N	30 A	V_b	$230\sqrt{2}$ V	Z_b	10.6 Ω
f_{sw}	10 kHz				
LCL Filter 1 & 2		**Grid**			
L_f	2 mH	$\widehat{E}_g$	$230\sqrt{2}$ V	L_g	0.32 mH
L_{fg}	3.3 mH	f_g	50 Hz	R_g	0.04 Ω
C_f	5 µF				
Inverter 1		**Inverter 2**			
R_v	0.02 pu	J	1.2 kg·m^2	D_p	24.4 kg·m^2/s
L_v	0.2 pu	K	75761 A	D_q	241 A
H	4 s				

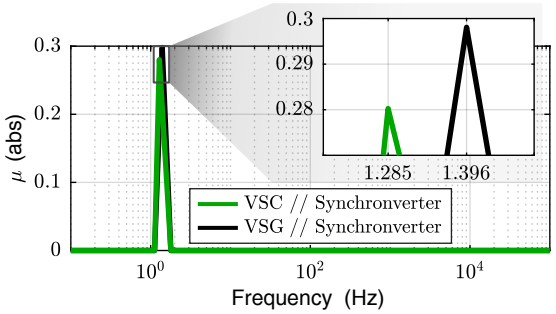

Fig. 6.18 µ-analysis results considering only the SCR as uncertainty: Synchronverter in parallel to the VSC (green) and to the VSG (black).

The Synchronverter parameters used for the simulations are tuned according to [65] and they are equal to:

$$J = 8.1 \text{ kg} \cdot \text{m}^2 \qquad D_p = 205.3 \text{ kg/s} \cdot \text{m}^2$$
$$K = 80487 \text{ A} \qquad D_q = 2562 \text{ A}$$

Both Inverter 1 and Inverter 2 operate at their nominal setpoints, i.e., $P_{i1} = P_{i2} = 1$ pu. As it can be observed in Fig. 6.19, even in the general case the VSC enhances the system robustness compared to the VSG as it features a lower μ_{max} value. The µ profile along the frequency is quite similar to one of the single converter case. There are three different peaks related to the mechanical dynamic of the VSM, the VSM excitation dynamic and the current control dynamic. At high frequency, there are no differences between the VSC and the VSG, as for the single converter case.

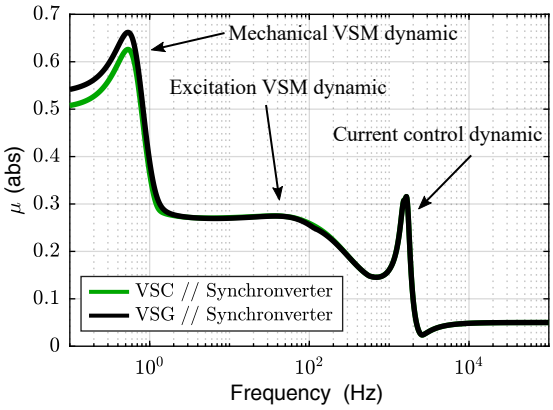

Fig. 6.19 μ-analysis results with the uncertainty **W** for the Synchronverter in parallel to the VSC (green) and to the VSG (black).

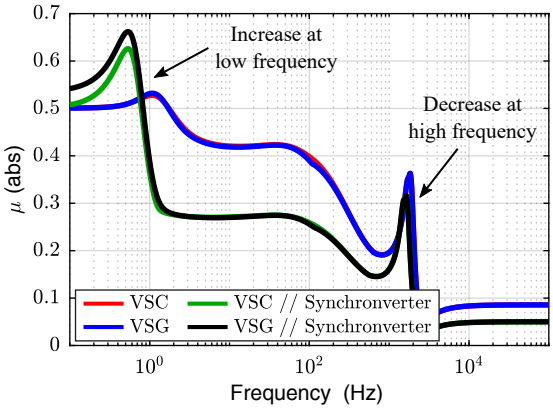

Fig. 6.20 Comparison between the single converter and the parallel converters systems.

To better appreciate the differences between the single converter and the parallel converters cases, the results are compared in Fig. 6.20. It can be noted that μ increases at low frequency and decreases at high frequency. At high frequency the peak decreases because of the mode operations of the two converters. Inverter 1 operates a grid-following converter (independently of the VSG or VSC operation), whereas Inverter 2 is a grid-forming converter. The grid-forming is equivalent to an ideal voltage source connected at the PCC. Therefore, the current regulator of the grid-following converter is connected to an equivalent grid more stiff than the single converter case. Consequently, the high frequency instability condition is reached for an higher increase of the grid impedance, as demonstrated in [74]. At low frequency, instead, the mechanical dynamic of the VSC and VSG interacts with the mechanical dynamic of the Synchronverter, thus resulting in a system more prone to low frequency instabilities (i.e., sub-synchronous oscillation issue among parallel VSMs) [83].

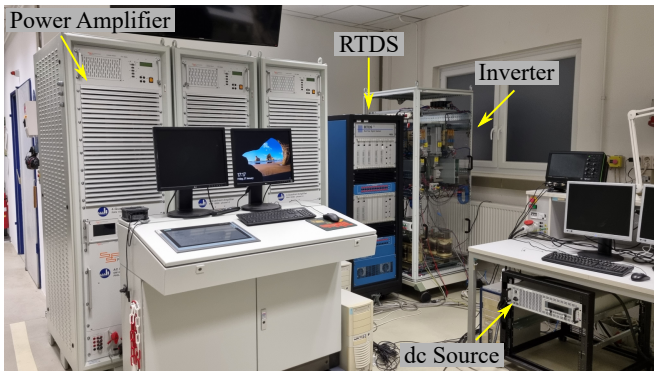

(a)

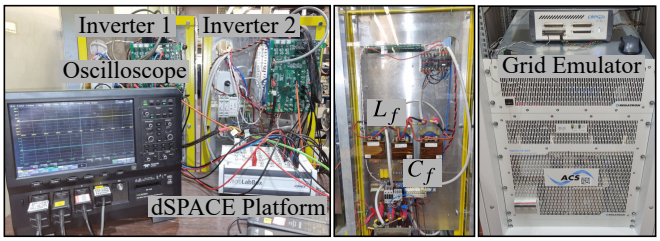

(b)

Fig. 6.21 (a) Picture of the experimental setup 1: single converter connected to the grid [114]; (b) Picture of the experimental setup 2: two converters operating in parallel to the grid.

6.5 Experimental Validation

The single converter system is validated on the experimental setup 1, depicted in Fig. 6.21a [114]. The experimental results for the two parallel converters system are retrieved from the setup 2, shown in Fig. 6.21b.

6.5.1 Single Converter

The experimental setup consists of a three-phase inverter linked to a power amplifier via an LCL filter. The control of the converter is managed through the dSPACE MicroLabBox platform. The power amplifier, simulated by a Real-Time Digital Simulator (RTDS), mimics the grid. Fig. 6.21a provides a visual representation of this setup, while Table 6.1 details its primary data. Two types of experimental tests were conducted to verify the theoretical findings of μ-analysis [114].

The first step is to validate the state-space (S-S) models used in the μ-analysis. For this purpose, step variations of the references are applied and the response of the S-S model, PLECS simulations and the experimental outcomes are compared. Figs. 6.22a and

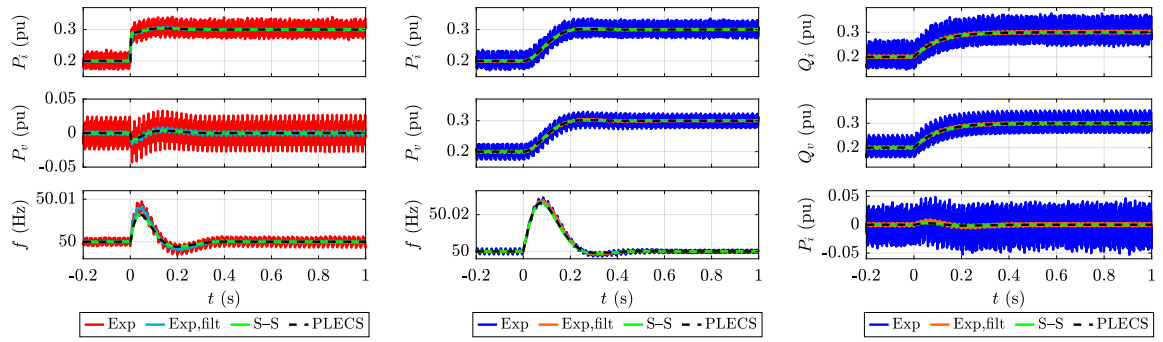

(a) (b) (c)

Fig. 6.22 Test to validate the S-S models. Step variations of (a) active power in VSC mode; (b) active power in VSG mode; (c) reactive power in VSG mode [114].

6.22b illustrate the responses to active power reference steps for the VSM operating as VSC and VSG, respectively. The figures show the trends of P_i, P_v and f, i.e, the inverter active power, the virtual active power, and virtual frequency, respectively. Fig. 6.22c shows the response to a step in virtual reactive power reference. The figure proposes the trends of Q_i, Q_v and P_i, i.e., the inverter reactive power, the virtual reactive power, and inverter active power. These responses consistently match simulations in PLECS and experimental results, confirming the accuracy of the modeling process [114].

The uncertainty function employed for μ-analysis in Section 6.3 reflects a generalized scenario encompassing multiple sources of uncertainty. However, validating such a general case experimentally is impractical. Consequently, the results of μ-analysis were validated under the simplified conditions outlined in subsection 6.2.5. As previously demonstrated, uncertainty solely in the SCR equates to a variation in grid impedance.

The initial test consisted of using a grid impedance seven times bigger than nominal and performing a step change in active power reference from 0 pu to 0.2 pu. The experimental outcomes for the VSG operation are shown in Fig. 6.23a., where nominal inductors and resistors of 2.5 mH and 0.5 Ω were replaced by three inductors of 17.5 mH and three resistors of 3.5 Ω. VSG divergence at 1.101 Hz aligns with theoretical predictions. Under identical conditions, VSC exhibits slower convergence, as depicted in Fig. 6.23b, underscoring the heightened robustness of virtual synchronous compensator operation. Furthermore, when increasing the grid impedance tenfold (inductance of 25 mH and resistance of 5 Ω), VSC gradually diverges around 0.989 Hz, aligning with theoretical findings from μ-analysis, as illustrated in Fig. 6.23c [114].

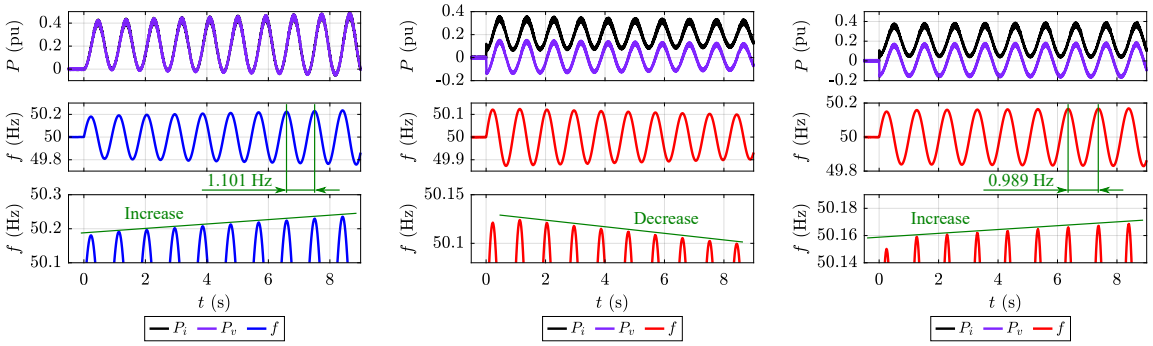

Fig. 6.23 Instability tests for the single converter connected to the grid in: (a) VSG mode with $k_{SCR} = 7$; (b) VSC mode with $k_{SCR} = 7$; (c) VSC mode with $k_{SCR} = 10$ [114].

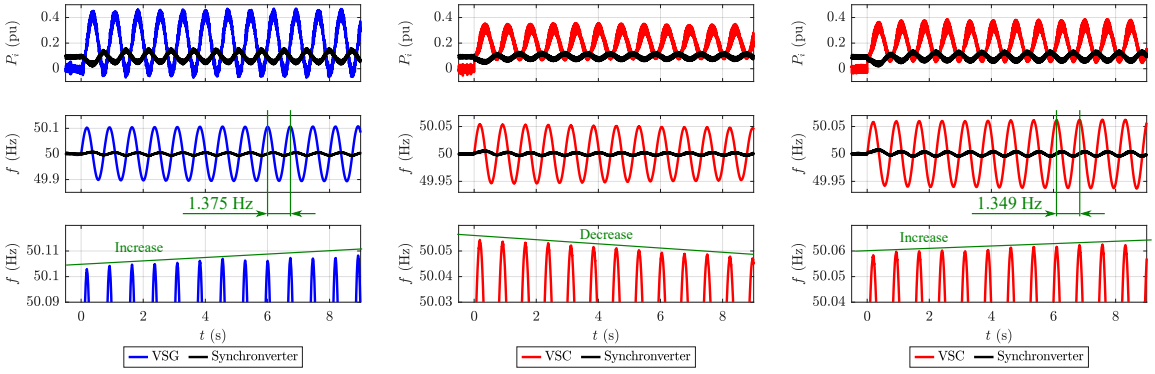

Fig. 6.24 Instability tests for the system of two converters in parallel in: (a) VSG mode with $k_{SCR} = 6.2$; (b) VSC mode with $k_{SCR} = 6.2$; (c) VSC mode with $k_{SCR} = 9.3$.

6.5.2 Parallel Converters

The experimental setup consists of two three-phase converters connected to a grid emulator through their own LCL filter. The converters are connected in parallel at the PCC as illustrated in the scheme of Fig. 6.15. A picture of the experimental is depicted in Fig. 6.21b. The two converters are controlled by the same dSPACE platform. The main data of the two inverters are listed in Table 6.3, where Inverter 1 is the VSM (VSG and VSC) under study and Inverter 2 is the Synchronverter.

As already stated in subsection 6.5.1, the outcome of the μ-analysis is validated for the simplified case of uncertainty on the SCR. According to the theoretical analysis of Section 6.4, the minimum increase of grid impedance to make the system unstable for the VSG mode operation is 6.2 times. Therefore, the first test consists of increasing the nominal

grid impedance of 6.2 times and performing an active power reference variation from 0 pu to 0.2 pu to Inverter 1, while Inverter 2 is injecting an active power of $P_{i2} = 0.1$ pu to the grid. A 2 mH three-phase inductor is inserted as a new grid inductor ($0.32 \cdot 6.2 \approx 2$ mH). Moreover, three resistors of 200 mΩ are added to match the desired increase of grid resistance.

The experimental results for the VSG operating mode are shown in Fig. 6.24a. The active power and the frequency slowly diverge at 1.375 Hz. This first results corroborates the theoretical analysis, according which the system must diverge with a frequency of 1.396 Hz.

Next, the same test is applied while Inverter 1 operates as VSC. The result is illustrated in Fig. 6.24b. In this case, the system is under damped because it is close to the instability condition. However, it slowly converges, as foreseen by the theoretical analysis. Indeed, the minimum instability condition for the VSC operation is matched for an increase of 9.3 times.

Therefore, the test is repeated by increasing the grid impedance of 9.3 times. Two three-phase inductors of 1.25 mH and 1.75 mH are inserted as new grid inductors ($0.32 \cdot 9.3 \approx 2.98$ mH). They feature a total internal resistance of 60 mΩ, so three resistors of 300 mΩ are added to match the desired grid resistance increase ($0.04 \cdot 9.3 \approx 0.37$ Ω). Fig. 6.24c shows the experimental results. It can be observed that the system slowly diverges according to the theoretical analysis with a frequency of 1.349 Hz, close to the theoretical one (1.285 Hz).

6.6 Conclusion & Main Contributions

This chapter proposes a robust stability analysis of a VSM operating in both virtual compensator and generator modes. The theoretical analysis reveals that a VSM functioning as a virtual compensator exhibits greater robustness compared to its operation as a VSG. Specifically, under identical nominal conditions, VSC operation remains stable across a wider range of uncertain plant scenarios [114].

Moreover, the same tests are repeated for a system of two parallel converters. One converter operates as a grid-forming, while the second one can operate as either VSG or VSC. The theoretical and experimental outcomes confirm even in this case that the VSC mode operation enhances the robustness of the system compared to the VSG one. Therefore, in a scenario of multi converters where one operates as a grid-forming, a VSC

approach is preferable to the VSG one to guarantee a higher robustness. In conclusion, the theoretical analysis, supported by experimental results, emphasizes the robustness advantage of operating as a virtual compensator rather than a virtual generator.

Chapter 7

S-VSC integration in Active Front End Converter Control

7.1 VSMs integration in battery chargers

Considering a bidirectional ultra-fast DC charging station equipped with integrated energy storage and distributed DC-bus (as depicted in Fig. 7.1), various solutions have been proposed in literature to enhance grid stability and resilience using ultra-fast chargers (UFCs) [118–120]. Some studies in technical literature suggest providing partial ancillary services, such as frequency support, while others advocate for full Virtual Synchronous Machine (VSM) technology capable of offering both active and reactive support. While these approaches ensure satisfactory performance, they necessitate integrating the VSM model to manage both compensating signals (ancillary services) and the required charging power references.

However, this integrated approach is not strictly necessary. A preferable solution is a plug-in option where the VSM model is solely responsible for ancillary services, while the standard UFC control structure handles power generation. This approach is exemplified by the Simplified Virtual Synchronous Compensator (S-VSC). By emulating a synchronous compensator, the virtual component exclusively provides grid services, allowing the conventional battery charger structure to manage power generation. As a result, the S-VSC consistently operates at a minimal load angle, offering the following advantages [121]:

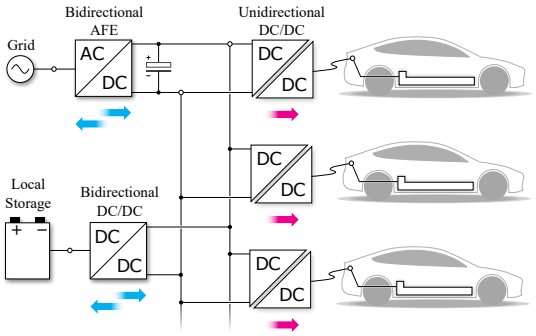

Fig. 7.1 Simplified schematic of a next-generation bidirectional ultra-fast DC charging station with integrated energy storage and distributed dc-bus [121].

- The S-VSC algorithm is a plug-in add-on for standard UFCs, enabling them to support the grid;
- With respect to the early grid supporting UFCs, the VSC-based control is capable of providing both static (permanent) and dynamic (transient during faults) grid support.

This chapter proposes a control strategy that integrate the control of the S-VSC into the conventional control an ultra fast battery charger. The finding of this chapter led to the publication of [121].

The scheme of the system under study is proposed in Fig. 7.2. The primary advantage of the S-VSC solution lies in its capability to directly enable or disable power reference signals originating from the S-VSC. In contrast to other approaches, where the VSM model governs all aspects of power exchange with the grid, this strategy allows for selectively deactivating one or both power channels when they are unnecessary or outside the operational plan of the charging station. For example, if local storage requires recharging, the contribution of the AFE to transient frequency support can be restricted or completely omitted.

The proposed solution operates as a straightforward plug-in control, significantly enhancing the grid-side performance of UFC stations with minimal adjustments to standard control algorithms. The control scheme is depicted in Fig. 7.3 [121].

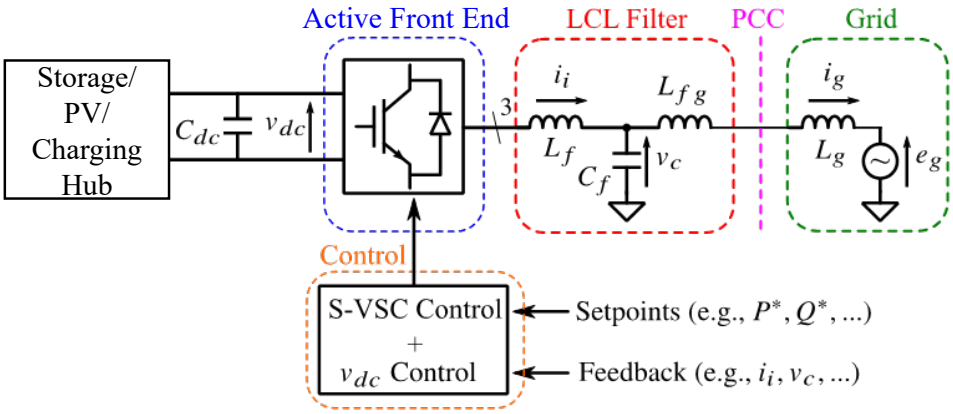

Fig. 7.2 Scheme of the system under study.

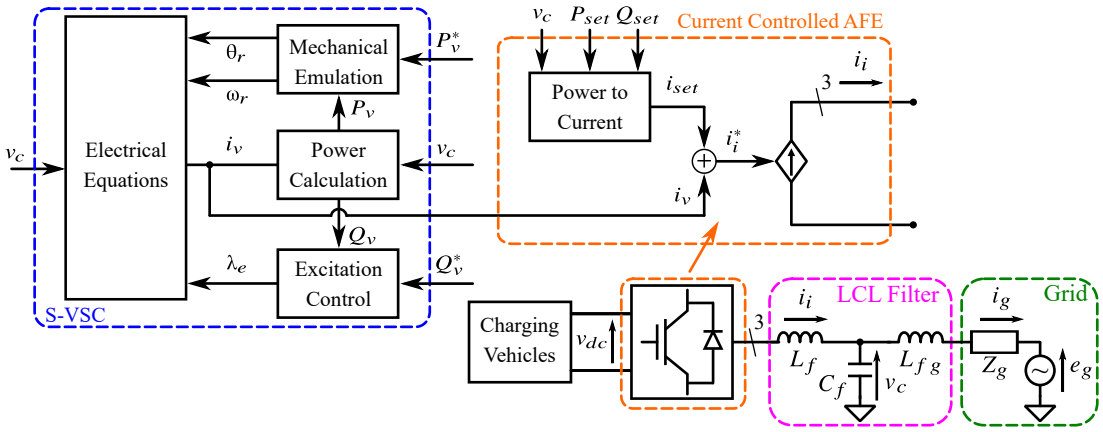

Fig. 7.3 General schematic overview of the ultra-fast charging (UFC) station with the integration of the S-VSC control strategy [122].

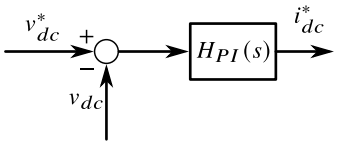

Fig. 7.4 Outer dc voltage control loop.

7.2 AFE Converter

This subsection briefly describes the conventional control of an Active Front End (AFE). The AFE is the input ac/dc stage of a fast battery charger. The dc-side of the system can be considered as ideal. The bidirectional exchange of power between the vehicle and the converter is modeled as an ideal current source. A potential additional backup storage system is modeled as an ideal voltage source. First, the converter must synchronize to the grid operating as a grid-following. A synchronization strategy is necessary to track the grid voltage. One of the most adopted solution available in the literature is the Phase Locked Loop (PLL) [77]. Next, one of the simplest methods proposed in the literature to control an AFE consists of implementing two cascaded control loops [123, 124]: an outer dc voltage control loop and an inner inverter current control loop.

(1) Outer dc Voltage Control

The desired reference voltage v^*_{dc} is compared to the measured voltage v_{dc}. A Proportional-Integral (PI) regulator receives the error $e_{dc} = v^*_{dc} - v_{dc}$ and provides the reference current i^*_{dc} needed to cancel the error in steady state. The scheme is depicted in Fig. 7.4.

(2) Inner Inverter Current Control

The reference current i^*_{dc} is multiplied by the voltage v_{dc} to retrieve the reference power P^*_{dc}. Assuming efficiency equal to unity, the inverter reference power is $P_{set} \approx P^*_{dc}$. The ac inverter reference current i^*_i is finally calculated from P_{set} and the measured voltage v_g. The inverter reference current i^*_i can be calculated either in a stationary frame (α, β) or in a (d,q) reference frame rotating at the grid frequency. In the first case, a Proportional-Resonant (P-RES) regulator tuned at the grid frequency is used to cancel the error between the reference current and the actual value, by providing the voltage reference v^*. The reference v^* is finally used to retrieve the commands for the converter q. In the second case, a PI regulator is used for the same purpose. The control block scheme is depicted in Fig. 7.5 [121].

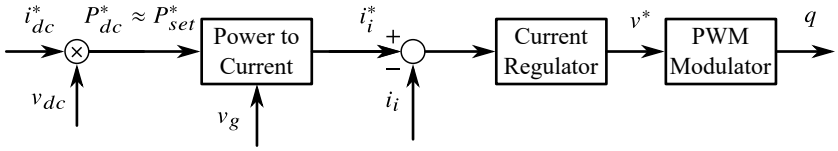

Fig. 7.5 Inner dc current control loop.

7.3 AFE Control with S-VSC

The S-VSC control can be easily integrated into the AFE control preserving the main goal of the AFE control. The reference power P_{set} retrieved from the dc voltage control is the external reference power which can be added to the S-VSC control block depicted in Fig.7.3. The synchronization of the AFE is performed through the S-VSC algorithm and a PLL is no more needed. In normal operating conditions, the converter will work as an AFE by managing the exchange of active power with the grid for both charging the electric vehicle battery and operate in V2G by injecting active power to the grid. The virtual current will be zero and the S-VSC will operate only as a PLL to guarantee the synchronization to the grid. Moreover, if a grid perturbation occurs (e.g., grid frequency variation, voltage dip, harmonic distortion) the S-VSC will automatically react to provide grid services and grid support. The following subsection will show some experimental results. The energy required to guarantee the support can come from the dc-link or a dc backup storage connected in parallel [121].

7.4 Experimental Results

The experimental setup consists of a 15 kVA three-phase inverter connected to the grid emulator through an LCL filter. A picture of the setup is shown in Fig. 7.6. The setup is the same of Chapter 3, where the converter is used as an Active Front End [121].

7.4.1 Inertial behavior + Primary frequency regulation

Considering a frequency reduction due to the loss of a generation source, the battery charger provides inertial support. If the active droop control is enabled, the converter also provides primary frequency regulation, as demonstrated in Fig. 7.7 [121].

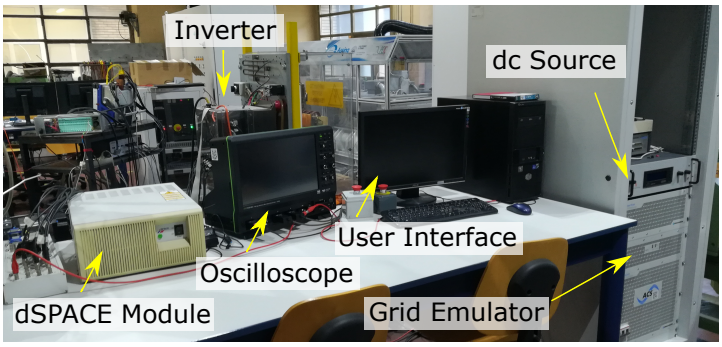

Fig. 7.6 Picture of the experimental setup.

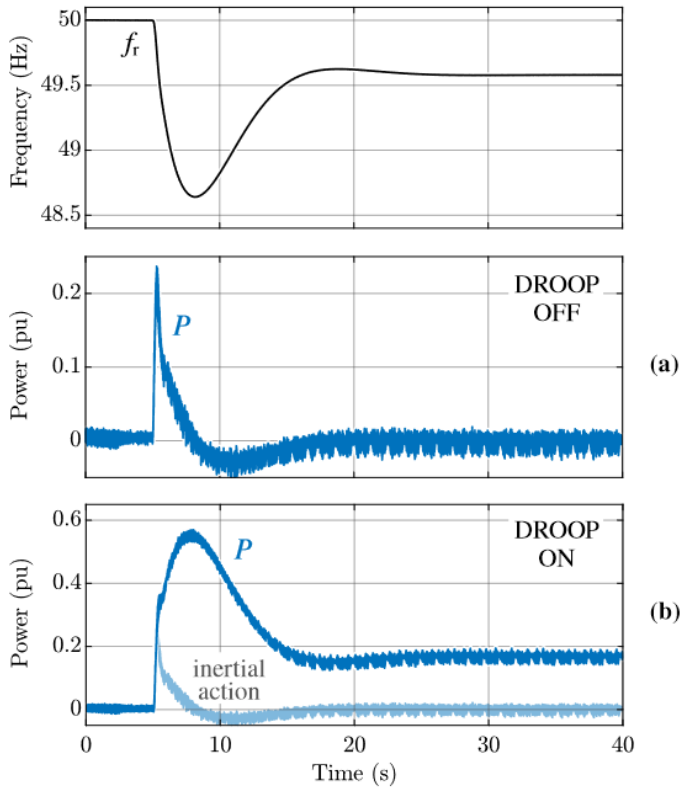

Fig. 7.7 Inertial behavior + Primary frequency regulation results. From top to bottom: virtual frequency f_r (Hz); (a) AFE measured active power (pu) when droop is disabled; (b) AFE measured active power (pu) when droop is enabled [121].

7.4.2 Grid support during faults

Considering a 15% voltage dip, the converter immediately reacts by injecting reactive power Q to support the grid. The result of the test is proposed in Fig. 7.8. The current

is saturated to a predefined value (in this case, 50% of the nominal value) which can be changed according to the operating conditions of the battery charger. The converter can withstand the fault showing a proper Fault Ride-Through Capability, as prescribed by the newest grid codes [121].

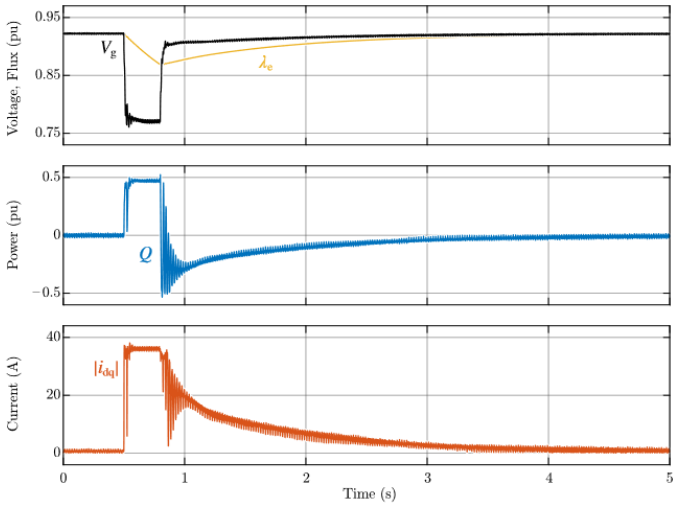

Fig. 7.8 Grid support during faults results. From top to bottom: measured voltage amplitude V_g and virtual excitation flux λ_e (pu); AFE measured reactive power (pu); AFE current amplitude (A) [121].

7.4.3 Harmonic support

Considering a harmonic distortion into the grid voltage, VSMs can support the grid by reducing the voltage distortion at the PCC behaving as harmonic sinks. As shown in Fig. 7.9, by applying a fifth harmonic voltage distortion, if the S-VSC is off, the voltage distortion at the PCC is circa 6 V. If the S-VSC is on, the voltage distortion at the PCC decreases below 4 V.

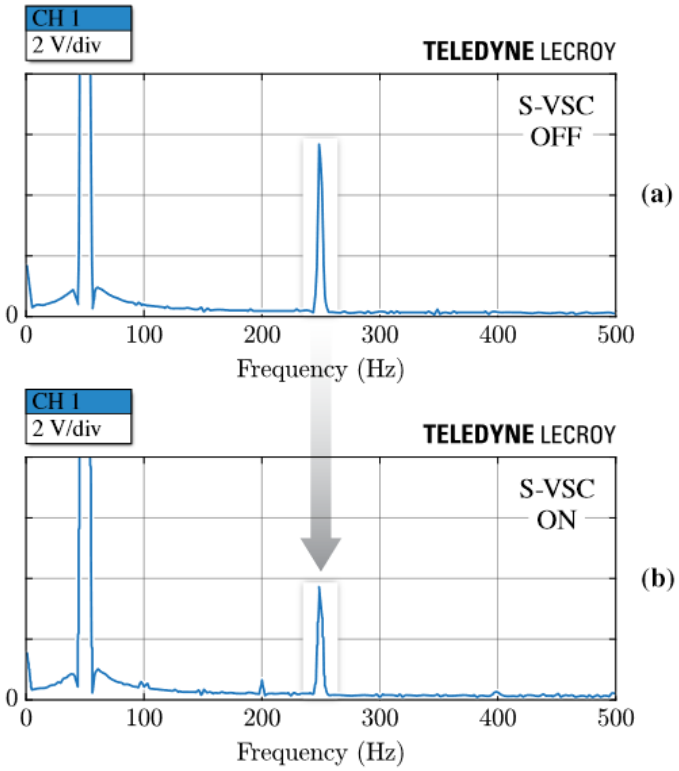

Fig. 7.9 Harmonic support results. DFT of the measured voltage in case of (a) S-VSC OFF; (b) S-VSC ON.

7.5 Conclusions and Main Contributions

This chapter demonstrates how the S-VSC algorithm can be integrated into the traditional control of an Active Front End converter from an ultra-fast charger. The S-VSC allows the charger to transiently provide grid support services for improved grid stability without compromising its primary charging function.

Moreover, this chapter explores the potential of utilizing ultra-fast chargers as active contributors to grid stability as their presence in the power system increases, addressing both the challenges and opportunities posed by this emerging phenomenon [121].

Chapter 8

Conclusions and Future Works

8.1 Conclusions

Virtual Synchronous Machines represent a valid solution to facilitate the penetration of renewable energy sources into the grid.

This PhD thesis has explored the development and implementations of control strategies that integrate the Virtual Synchronous Machine (VSM) concept to provide grid services to support the grid. The research has been divided into two parts, each addressing critical aspects of VSM control and application.

General Aspects of VSMs

- A clear distinction between grid-following, grid-forming, and VSM control strategies was established, addressing common confusion in the literature [C1];
- The most adopted VSM topologies were implemented and compared using a consistent tuning strategy. The comparative experimental analysis highlighted the differences and similarities in their inertial behavior, frequency regulation and grid support during faults [J4], [C1];
- The beneficial effects of inertial response provided by VSMs were demonstrated through dynamic grid experimental tests [T2];
- The response of main VSM typologies to grid harmonics and imbalances was foreseen and analyzed. It was found that some typologies can enhance grid voltage

quality by acting as harmonic/unbalance sinks, while others might deteriorate it [J3];

- The study revealed that the harmonic/unbalance sink capability of grid-forming VSMs is constrained by dead-time effects, emphasizing the necessity for dead-time compensation [J2].

Development of S-VSC

- The S-VSC developed in a previous PhD thesis was extended to operate in grid-forming mode, validating its application for converters in microgrids operating both in grid-connected and islanded modes [J1];
- Robust stability of the S-VSC was evaluated using the μ-analysis, demonstrating that converters operating as compensators are more robust than those functioning as generators, both individually and in parallel configurations. The robust stability is intended as the stability against grid impedance error estimation [C2];
- An innovative implementation of the S-VSC algorithm into battery chargers was proposed, showing that such chargers can provide ancillary services to the grid while preserving the primary function of charging vehicles, thus enhancing their utility and integration into the power system [J8].

In conclusion, this PhD thesis contributes to the body of knowledge on VSMs and their role in modern power systems, providing both theoretical insights and experimentally validated solutions for enhancing grid stability and support with the purpose of facilitating the renewable energy sources spread.

8.2 Future Works

All the findings summarized of the PhD activity opened up potential future research directions:

(1) Grid-forming S-VSC

Chapter 5 demonstrated the grid-forming capability of the S-VSC for the control of an islanded microgrid. However, in island operation, the S-VSC cannot guarantee

proportional-integral frequency and voltage regulations, as it has no access to the status of the breaker interfacing the microgrid to the main grid. The advancement of the proposed solution is to make the S-VSC aware of the breaker status to guarantee: 1) the switch from the proportional regulation in grid-connected mode to the proportional-integral regulation in island mode; 2) resynchronization to the grid after the island operation.

(2) Transient stability analysis of the S-VSC

Chapter 6 demonstrated the higher robustness of the virtual compensator operation over the virtual generator one. As described in previous chapters, the virtual synchronous compensator (VSC) always operates at a very small load angle, implying better performance in terms of transient stability with respect to virtual synchronous generators (VSG). Therefore, future works might focus on the theoretical and experimentaly demonstration that the VSC concept can guarantee a higher transient stability during large grid faults compared to the VSG working principle, highlighting another advantage of adopting this VSM topology.

(3) Subsynchronous oscillations in a multi-S-VSC system

The studies on the S-VSC mainly focused on a system consisting only of a single converter connected to the grid. Only simple experimental outcomes proposed in Chapter 3 and 6 demonstrated the possibility to adopt the S-VSC algorithm to control a multi-converters system with no sub-synchronous oscillations (i.e., one of the main recent issues affecting VSMs operating in a microgrid). However, a detailed theoretical analysis is needed to properly demonstrate the validity of the S-VSC in controlling multi-converters system.

References

[1] International Energy Agency. Electricity generation by fuel and scenario, 2018-2040.

[2] National Grid ESO. A national blueprint for a decarbonised electricity system in Great Britain. Technical report, 2024.

[3] Australian Energy Market Operator (AEMO). Integrated System Plan. Technical report, 2024.

[4] Robert Foster, Majid Ghassemi, and Alma Cota. *Solar Energy: Renewable Energy and the Environment*. 08 2009.

[5] James Manwell, Jon Mcgowan, and A Rogers. *Wind Energy Explained: Theory, Design and Application, Second Edition*, volume 30. 03 2006.

[6] T. Esram and P. L. Chapman. Comparison of photovoltaic array maximum power point tracking techniques. *IEEE Transactions on Energy Conversion*, 22(2):439–449, 2007.

[7] Prabha Kundur. *Power System Stability and Control.* McGraw-Hill Education, January 1994. ISBN: 978-0-07-035958-1.

[8] Australian Energy Market Operator (AEMO). Power system requirements, jul 2020.

[9] IRENA. Innovative ancillary services: Innovation landscape brief. page 24, 2019.

[10] ENTSO-E. High Penetration of Power Electronic Interfaced Power Sources and the Potential Contribution of Grid Forming Converters, January 2020. Technical Report.

[11] Project Inertia Team. Frequency Stability in Long-Term Scenarios and Relevant Requirements. Technical Report, ENTSO-E, 2021.

[12] AEMO. Application of Advanced Grid-scale Inverters in the NEM. Technical Report, August 2021.

[13] Galina Antonova, Massimo Nardi, Alan Scott, and Michael Pesin. Distributed generation and its impact on power grids and microgrids protection. 04 2012.

[14] IEA. Unlocking the Potential of Distributed Energy Resources. Technical report, IEA, May 2022.

[15] Australian Energy Market Operator (AEMO). Application of advanced grid-scale inverters in the nem. *White Paper*, 2021.

[16] UNIFI Consortium. UNIFI Specifications for Grid-Forming Inverter-Based Resources - Version 2. Technical report, March 2024.

[17] Australian Energy Market Operator (AEMO). Analysis of the South Australian Blackout - 28 September 2016. Technical report, 2017.

[18] Terna - Rete Elettrica Nazionale S.p.A. Codice di Rete, 2020. https://download.terna.it/terna/Codice%20di%20rete%20completo_20200424_8d7e8496cd24dd5.pdf.

[19] Terna, July 2020. Pilot Project Fast Reserve.

[20] Fingrid, June 2021. Fast Frequency Reserve.

[21] Jia Liu, Yushi Miura, and Toshifumi Ise. Comparison of dynamic characteristics between virtual synchronous generator and droop control in inverter-based distributed generators. *IEEE Transactions on Power Electronics*, 31(5):3600–3611, 2016.

[22] R.I. Bojoi, G. Griva, V. Bostan, M. Guerriero, F. Farina, and F. Profumo. Current control strategy for power conditioners using sinusoidal signal integrators in synchronous reference frame. *IEEE Transactions on Power Electronics*, 20(6):1402–1412, 2005.

[23] Ujjwol Tamrakar, Dipesh Shrestha, Manisha Maharjan, Bishnu P. Bhattarai, Timothy M. Hansen, and Reinaldo Tonkoski. Virtual Inertia: Current Trends and Future Directions. *Applied Sciences*, 7(7):654, July 2017.

[24] M. Chen, D. Zhou, and F. Blaabjerg. Modelling, Implementation, and Assessment of Virtual Synchronous Generator in Power Systems. *Journal of Modern Power Systems and Clean Energy*, 8(3):399–411, May 2020.

[25] Fabio Mandrile, Enrico Carpaneto, and Radu Bojoi. Grid-Feeding Inverter With Simplified Virtual Synchronous Compensator Providing Grid Services and Grid Support. *IEEE Transactions on Industry Applications*, 57(1):559–569, January 2021.

[26] European Commission. Commission Regulation (EU) 2016/631, 2016. http://data.europa.eu/eli/reg/2016/631/oj.

[27] Terna. Code for Transmission, Dispatching, Development and Security of the Grid, March 2023. Grid Code.

[28] Terna - Rete Elettrica Nazionale S.p.A. Allegato A.17, 2019. https://download.terna.it/terna/Allegato%20A.17_8d787c9c8a17ba6.pdf.

[29] Terna - Rete Elettrica Nazionale S.p.A. Allegato A.68, 2019. https://download.terna.it/terna/Allegato%20A.68_8d787c9e10c227c.pdf.

[30] Terna - Rete Elettrica Nazionale S.p.A. Allegato A.79, 2019. https://download.terna.it/terna/A.79_Accumuli_8da5abbf2fe745c.pdf.

[31] IEEE standard for harmonic control in electric power systems. *IEEE Std 519-2022 (Revision of IEEE Std 519-2014)*, pages 1–31, 2022.

[32] National Grid ESO. Grid Code, 2024. https://dcm.nationalgrideso.com/.

[33] nationalgridESO. GC0137: Minimum Specification Required for Provision of GB Grid Forming (GBGF) Capability (formerly Virtual Synchronous Machine/VSM Capability). Technical Report, March 2021.

[34] Hao Luo, Yi Xiao, Yinxiao Zhu, Yongheng Yang, Nick Peter Papanikolaou, and Marta Molinas. A review of recent requirements for inverter-based resources and grid-forming technologies. In *2023 25th European Conference on Power Electronics and Applications (EPE'23 ECCE Europe)*, pages 1–9, 2023.

[35] Yashen Lin, Joseph Eto, Brian Johnson, Jack Flicker, Robert Lasseter, Hugo Villegas Pico, Gab-Su Seo, Brian Pierre, and Abraham Ellis. Research roadmap on grid-forming inverters, 2020.

[36] IEEE standard for interconnection and interoperability of distributed energy resources with associated electric power systems interfaces. *IEEE Std 1547-2018 (Revision of IEEE Std 1547-2003)*, pages 1–138, 2018.

[37] IEEE standard for interconnection and interoperability of inverter-based resources (ibrs) interconnecting with associated transmission electric power systems. *IEEE Std 2800-2022*, pages 1–180, 2022.

[38] Remus Teodorescu, Marco Liserre, and Pedro Rodriguez. *Grid Converters for Photovoltaic and Wind Power System*. John Wiley & Sons, Ltd, July 2011.

[39] R.I. Bojoi, G. Griva, V. Bostan, M. Guerriero, F. Farina, and F. Profumo. Current control strategy for power conditioners using sinusoidal signal integrators in synchronous reference frame. *IEEE Transactions on Power Electronics*, 20(6):1402–1412, 2005.

[40] Wenhua Wu, Yandong Chen, Leming Zhou, An Luo, Xiaoping Zhou, Zhixing He, Ling Yang, Zhiwei Xie, Jinming Liu, and Mingmin Zhang. Sequence impedance modeling and stability comparative analysis of voltage-controlled vsgs and current-controlled vsgs. *IEEE Transactions on Industrial Electronics*, 66(8):6460–6472, 2019.

[41] Roberto Rosso, Jair Cassoli, Giampaolo Buticchi, Soenke Engelken, and Marco Liserre. Robust Stability Analysis of LCL Filter Based Synchronverter Under Different Grid Conditions. *IEEE Transactions on Power Electronics*, 34(6):5842–5853, June 2019.

[42] R.H. Lasseter and P. Paigi. Microgrid: a conceptual solution. In *2004 IEEE 35th Annual Power Electronics Specialists Conference*, volume 6, pages 4285–4290, June 2004.

[43] Huang Jiayi, Jiang Chuanwen, and Xu Rong. A review on distributed energy resources and MicroGrid. *Renewable and Sustainable Energy Reviews*, 12(9):2472–2483, December 2008.

[44] Daniel E. Olivares, Ali Mehrizi-Sani, Amir H. Etemadi, Claudio A. Cañizares, Reza Iravani, Mehrdad Kazerani, Amir H. Hajimiragha, Oriol Gomis-Bellmunt, Maryam Saeedifard, Rodrigo Palma-Behnke, Guillermo A. Jiménez-Estévez, and Nikos D. Hatziargyriou. Trends in microgrid control. *IEEE Transactions on Smart Grid*, 5(4):1905–1919, 2014.

[45] Joan Rocabert, Alvaro Luna, Frede Blaabjerg, and Pedro Rodríguez. Control of power converters in ac microgrids. *IEEE Transactions on Power Electronics*, 27(11):4734–4749, 2012.

[46] Q. Zhong and G. Weiss. Static synchronous generators for distributed generation and renewable energy. In *2009 IEEE/PES Power Systems Conference and Exposition*, pages 1–6, 2009.

[47] Q. Zhong and G. Weiss. Synchronverters: Inverters That Mimic Synchronous Generators. *IEEE Transactions on Industrial Electronics*, 58(4):1259–1267, April 2011.

[48] Moshe Blau and George Weiss. Synchronverters used for damping inter-area oscillations in two-area power systems. *Renewable Energy and Power Quality Journal*, pages 45–50, 04 2018.

[49] Zeev Kustanovich, Shivprasad Shivratri, Hang Yin, Florian Reissner, and George Weiss. Synchronverters with fast current loops. *IEEE Transactions on Industrial Electronics*, 70(11):11357–11367, 2023.

[50] K. Sakimoto, Y. Miura, and T. Ise. Stabilization of a power system with a distributed generator by a virtual synchronous generator function. In *8th International Conference on Power Electronics - ECCE Asia*, pages 1498–1505, 2011.

[51] Jia Liu, Y. Miura, and T. Ise. Dynamic characteristics and stability comparisons between virtual synchronous generator and droop control in inverter-based distributed generators. In *2014 International Power Electronics Conference (IPEC-Hiroshima 2014 - ECCE ASIA)*, pages 1536–1543, 2014.

[52] H. Beck and R. Hesse. Virtual synchronous machine. In *2007 9th International Conference on Electrical Power Quality and Utilisation*, pages 1–6, 2007.

[53] Ralf Hesse, Dirk Turschner, and Hans-Peter Beck. Micro grid stabilization using the virtual synchronous machine, (VISMA). *Renewable energy & power quality journal*, 1:676–681, 2009.

[54] Yong Chen, Ralf Hesse, Dirk Turschner, and Hans-Peter Beck. Dynamic properties of the virtual synchronous machine (VISMA). *Renewable energy & power quality journal*, pages 755–759, 2011.

[55] Y. Chen, R. Hesse, D. Turschner, and H. Beck. Improving the grid power quality using virtual synchronous machines. In *2011 International Conference on Power Engineering, Energy and Electrical Drives*, pages 1–6, 2011.

[56] Yong P Chen, Ralf Hesse, Dirk Turschner, and Hans-Peter Beck. Comparison of methods for implementing virtual synchronous machine on inverters. *Renewable energy & power quality journal*, pages 734–739, 2012.

[57] P. Rodriguez, I. Candela, and A. Luna. Control of pv generation systems using the synchronous power controller. In *2013 IEEE Energy Conversion Congress and Exposition*, pages 993–998, 2013.

[58] W. Zhang, D. Remon, A. Mir, A. Luna, J. Rocabert, I. Candela, and P. Rodriguez. Comparison of different power loop controllers for synchronous power controlled grid-interactive converters. In *2015 IEEE Energy Conversion Congress and Exposition (ECCE)*, pages 3780–3787, 2015.

[59] J. Driesen and K. Visscher. Virtual synchronous generators. In *2008 IEEE Power and Energy Society General Meeting - Conversion and Delivery of Electrical Energy in the 21st Century*, pages 1–3, July 2008.

[60] M. P. N. van Wesenbeeck, S. W. H. de Haan, P. Varela, and K. Visscher. Grid tied converter with virtual kinetic storage. In *2009 IEEE Bucharest PowerTech*, pages 1–7, 2009.

[61] Yuko Hirase, Kazuhiro Abe, Kazushige Sugimoto, and Yuji Shindo. A grid connected inverter with virtual synchronous generator model of algebraic type. *IEEJ Transactions on Power and Energy*, 132:371–380, 01 2012.

[62] S. D'Arco, J. A. Suul, and O. B. Fosso. Control system tuning and stability analysis of virtual synchronous machines. In *2013 IEEE Energy Conversion Congress and Exposition*, pages 2664–2671, 2013.

[63] Salvatore D'Arco, Jon Are Suul, and Olav B. Fosso. Small-signal modeling and parametric sensitivity of a virtual synchronous machine in islanded operation. *International Journal of Electrical Power & Energy Systems*, 72:3 – 15, 2015.

[64] Vincenzo Mallemaci, Fabio Mandrile, Enrico Carpaneto, and Radu Bojoi. Simplified virtual synchronous compensator with grid–forming capability. *IEEE Transactions on Industry Applications*, 59(5):6203–6219, 2023.

[65] Vincenzo Mallemaci, Fabio Mandrile, Sandro Rubino, Andrea Mazza, Enrico Carpaneto, and Radu Bojoi. A comprehensive comparison of Virtual Synchronous Generators with focus on virtual inertia and frequency regulation. *Electric Power Systems Research*, 201:107516, December 2021.

[66] Vincenzo Mallemaci, Fabio Mandrile, Alessia Camboni, Enrico Carpaneto, and Radu Bojoi. Grid-following virtual synchronous machines: a valid solution fulfilling the newest grid codes regarding the reactive grid support during faults. In *2024 IEEE 22nd Mediterranean Electrotechnical Conference (MELECON)*, pages 1169–1174, 2024.

[67] F. Campanelli. Control of a microgrid based on virtual synchronous machine technology. Master's thesis, Politecnico di Torino, 2023.

[68] Fabio Mandrile, Enrico Carpaneto, and Radu Bojoi. Grid-Feeding Inverter With Simplified Virtual Synchronous Compensator Providing Grid Services and Grid Support. *IEEE Transactions on Industry Applications*, 57(1):559–569, January 2021.

[69] Fabio Mandrile, Vincenzo Mallemaci, Enrico Carpaneto, and Radu Bojoi. Lead-lag filter-based damping of virtual synchronous machines. *IEEE Transactions on Industry Applications*, 59(6):6900–6913, 2023.

[70] Andrés Tarrasó, Cristian Verdugo, Ngoc Bao Lai, Jose Ignacio Candela, and Pedro Rodriguez. Synchronous power controller for distributed generation units. In *2019 IEEE Energy Conversion Congress and Exposition (ECCE)*, pages 4660–4664, 2019.

[71] Jian Guo, Yandong Chen, Shuhan Liao, Wenhua Wu, Leming Zhou, Zhiwei Xie, and Xiangyu Wang. Analysis and Mitigation of Low-Frequency Interactions Between the Source and Load Virtual Synchronous Machine in an Islanded Microgrid. *IEEE Transactions on Industrial Electronics*, 69(4):3732–3742, April 2022.

[72] Chang Li, Yaqian Yang, Nenad Mijatovic, and Tomislav Dragicevic. Frequency Stability Assessment of Grid-Forming VSG in Framework of MPME With Feedforward Decoupling Control Strategy. *IEEE Transactions on Industrial Electronics*, 69(7):6903–6913, July 2022.

[73] Vincenzo Mallemaci, Fabio Mandrile, Enrico Carpaneto, and Radu Bojoi. General method to foresee the behavior of virtual synchronous machines working with distorted and unbalanced voltage conditions. *IEEE Transactions on Industrial Electronics*, 70(10):9709–9719, 2023.

[74] Roberto Rosso, Soenke Engelken, and Marco Liserre. Robust Stability Investigation of the Interactions Among Grid-Forming and Grid-Following Converters. *IEEE Journal of Emerging and Selected Topics in Power Electronics*, 8(2):991–1003, June 2020.

[75] F. Mandrile, E. Carpaneto, and R. Bojoi. Virtual synchronous generator with simplified single-axis damper winding. In *2019 IEEE 28th International Symposium on Industrial Electronics (ISIE)*, pages 2123–2128, 2019.

[76] F. Mandrile, E. Carpaneto, E. Armando, and R. Bojoi. Simple tuning method of virtual synchronous generators reactive control. *In Publication*, 2020.

[77] Remus Teodorescu, Marco Liserre, and Pedro Rodriguez. *Grid Converters for Photovoltaic and Wind Power Systems*. John Wiley & Sons, July 2011. ISBN: 978-1-119-95720-1.

[78] L. Zhang, L. Harnefors, and H. Nee. Power-synchronization control of grid-connected voltage-source converters. *IEEE Transactions on Power Systems*, 25(2):809–820, 2010.

[79] W. Zhang, A. Luna, I. Candela, J. Rocabert, and P. Rodriguez. An active power synchronizing controller for grid-connected power converters with configurable natural droop characteristics. In *2015 IEEE 6th International Symposium on Power Electronics for Distributed Generation Systems (PEDG)*, pages 1–7, 2015.

[80] F. Mandrile, E. Carpaneto, and R. Bojoi. Grid-tied inverter with simplified virtual synchronous compensator for grid services and grid support. In *2019 IEEE Energy Conversion Congress and Exposition (ECCE)*, pages 4317–4323, 2019.

[81] Fabio Mandrile, Enrico Carpaneto, and Radu Bojoi. Grid-Feeding Inverter With Simplified Virtual Synchronous Compensator Providing Grid Services and Grid Support. *IEEE Transactions on Industry Applications*, 57(1):559–569, January 2021.

[82] Fabio Mandrile, Enrico Carpaneto, Eric Armando, and Radu Bojoi. Simple tuning method of virtual synchronous generators reactive control. In *2020 IEEE Energy Conversion Congress and Exposition (ECCE)*, pages 2779–2785, 2020.

[83] Florian Reißner, Vincenzo Mallemaci, Fabio Mandrile, Iustin Radu Bojoi, and George Weiss. Virtual friction subjected to communication delays in a microgrid of virtual synchronous machines. *IEEE Journal of Emerging and Selected Topics in Power Electronics*, 11(4):3910–3923, 2023.

[84] ENTSO-E. High Penetration of Power Electronic Interfaced Power Sources and the Potential Contribution of Grid Forming Converters, January 2020. Technical Report.

[85] Andres Tarrasó, Jose Ignacio Candela, Joan Rocabert, and Pedro Rodriguez. Grid voltage harmonic damping method for spc based power converters with multiple virtual admittance control. In *2017 IEEE Energy Conversion Congress and Exposition (ECCE)*, pages 64–68, 2017.

[86] Leming Zhou, Zhikang Shuai, Yandong Chen, Wenhua Wu, Xiaoping Zhou, Kui Yan, and An Luo. Impedance-Based Harmonic Current Suppression Method for VSG Connected to Distorted Grid. *IEEE Transactions on Industrial Electronics*, 67(7):5490–5502, July 2020.

[87] Eros Avdiaj, Jon Are Suul, Salvatore D'Arco, and Luigi Piegari. A Current Controlled Virtual Synchronous Machine Adapted for Operation under Unbalanced Conditions. In *2020 9th International Conference on Renewable Energy Research and Application (ICRERA)*, pages 263–270, September 2020. ISSN: 2572-6013.

[88] Guannan Lou, Quan Yang, Wei Gu, Xiangjun Quan, Josep M. Guerrero, and Shanlin Li. Analysis and Design of Hybrid Harmonic Suppression Scheme for VSG Considering Nonlinear Loads and Distorted Grid. *IEEE Transactions on Energy Conversion*, 36(4):3096–3107, December 2021.

[89] Thiago Silva Amorim, Daniel Carletti, and Lucas Frizera Encarnação. Comparison of inverter controllers with synthetic inertia and harmonic compensation features. *Electric Power Systems Research*, 197:107344, August 2021.

[90] Jia Liu, Yushi Miura, Hassan Bevrani, and Toshifumi Ise. Enhanced virtual synchronous generator control for parallel inverters in microgrids. *IEEE Transactions on Smart Grid*, 8(5):2268–2277, 2017.

[91] Vincenzo Mallemaci, Fabio Mandrile, Enrico Carpaneto, and Radu Bojoi. Dead-time effect on two-level voltage source virtual synchronous machines. In *2022 IEEE Energy Conversion Congress and Exposition (ECCE)*, pages 01–07, 2022.

[92] Vincenzo Mallemaci, Fabio Mandrile, Enrico Carpaneto, and Radu Bojoi. Dead–time effect on two–level grid–forming virtual synchronous machines. *IEEE Transactions on Industry Applications*, 59(5):6103–6112, 2023.

[93] Vivek Natarajan and George Weiss. Synchronverters With Better Stability Due to Virtual Inductors, Virtual Capacitors, and Anti-Windup. *IEEE Transactions on Industrial Electronics*, 64(7):5994–6004, July 2017.

[94] Xiaodong Liang, Chowdhury Andalib-Bin-Karim, Weixing Li, Massimo Mitolo, and Md Nasmus Sakib Khan Shabbir. Adaptive Virtual Impedance-Based Reactive Power Sharing in Virtual Synchronous Generator Controlled Microgrids. *IEEE Transactions on Industry Applications*, 57(1):46–60, January 2021.

[95] Mingwei Ren, Tong Li, Kai Shi, Peifeng Xu, and Yuxin Sun. Coordinated Control Strategy of Virtual Synchronous Generator Based on Adaptive Moment of Inertia and Virtual Impedance. *IEEE Journal on Emerging and Selected Topics in Circuits and Systems*, 11(1):99–110, March 2021.

[96] Alberto Rodriguez-Cabero, Javier Roldan-Perez, and Milan Prodanovic. Virtual Impedance Design Considerations for Virtual Synchronous Machines in Weak Grids. *IEEE Journal of Emerging and Selected Topics in Power Electronics*, 8(2):1477–1489, June 2020.

[97] Heng Wu and Xiongfei Wang. Small-Signal Modeling and Controller Parameters Tuning of Grid-Forming VSCs With Adaptive Virtual Impedance-Based Current Limitation. *IEEE Transactions on Power Electronics*, 37(6):7185–7199, June 2022.

[98] Xiangjun Quan, Alex Q. Huang, and Hui Yu. A Novel Order Reduced Synchronous Power Control for Grid-Forming Inverters. *IEEE Transactions on Industrial Electronics*, 67(12):10989–10995, December 2020.

[99] John Grainger and William Stevenson. *Power System Analysis*. McGraw Hill, 1994.

[100] Nasser Tleis. *Power Systems Modelling and Fault Analysis*. Elsevier, 2019.

[101] Pedro Rodriguez, Alvaro Luna, Ignacio Candela, Ramon Mujal, Remus Teodorescu, and Frede Blaabjerg. Multiresonant Frequency-Locked Loop for Grid Synchronization of Power Converters Under Distorted Grid Conditions. *IEEE Transactions on Industrial Electronics*, 58(1):127–138, January 2011.

[102] S. Bolognani and M. Zigliotto. Self-commissioning compensation of inverter non-idealities for sensorless AC drives applications. In *2002 International Conference on Power Electronics, Machines and Drives (Conf. Publ. No. 487)*, pages 30–37, June 2002. ISSN: 0537-9989.

[103] L. Ben-Brahim. The analysis and compensation of dead-time effects in three phase PWM inverters. In *IECON '98. Proceedings of the 24th Annual Conference of the IEEE Industrial Electronics Society (Cat. No.98CH36200)*, volume 2, pages 792–797 vol.2, August 1998.

[104] A.R. Munoz and T.A. Lipo. On-line dead-time compensation technique for open-loop PWM-VSI drives. *IEEE Transactions on Power Electronics*, 14(4):683–689, July 1999.

[105] N. Urasaki, T. Senjyu, K. Uezato, and T. Funabashi. An adaptive dead-time compensation strategy for voltage source inverter fed motor drives. *IEEE Transactions on Power Electronics*, 20(5):1150–1160, September 2005.

[106] Gianmario Pellegrino, Paolo Guglielmi, Eric Armando, and Radu Iustin Bojoi. Self-Commissioning Algorithm for Inverter Nonlinearity Compensation in Sensorless Induction Motor Drives. *IEEE Transactions on Industry Applications*, 46(4):1416–1424, July 2010.

[107] Fabio Mandrile, Fausto Stella, Enrico Carpaneto, and Radu Bojoi. Grid fault current injection using virtual synchronous machines featuring active junction temperature limitation of power devices. *IEEE Journal of Emerging and Selected Topics in Power Electronics*, 10(5):6243–6251, 2022.

[108] Vincenzo Mallemaci, Enrico Carpaneto, and Radu Bojoi. Grid-forming inverter with simplified virtual synchronous compensator providing grid services and grid support. In *2021 24th International Conference on Electrical Machines and Systems (ICEMS)*, pages 2323–2328, 2021.

[109] Yanbo Wang, Xiongfei Wang, Zhe Chen, and Frede Blaabjerg. Small-signal stability analysis of inverter-fed power systems using component connection method. *IEEE Transactions on Smart Grid*, 9(5):5301–5310, 2018.

[110] Fabio Mandrile, Salvatore Musumeci, Enrico Carpaneto, Radu Bojoi, Tomislav Dragičević, and Frede Blaabjerg. State-space modeling techniques of emerging grid-connected converters. *Energies*, 13(18), 2020.

[111] Roberto Rosso, Soenke Engelken, and Marco Liserre. Robust stability analysis of synchronverters operating in parallel. *IEEE Transactions on Power Electronics*, 34(11):11309–11319, 2019.

[112] Mohammad Kazem Bakhshizadeh, Changwoo Yoon, Jesper Hjerrild, Claus Leth Bak, Łukasz Hubert Kocewiak, Frede Blaabjerg, and Bo Hesselbæk. The application of vector fitting to eigenvalue-based harmonic stability analysis. *IEEE Journal of Emerging and Selected Topics in Power Electronics*, 5(4):1487–1498, 2017.

[113] Vincenzo Mallemaci, Sante Pugliese, Fabio Mandrile, Enrico Carpaneto, Radu Bojoi, and Marco Liserre. Robust stability analysis of the simplified virtual synchronous compensator for grid services and grid support. In *2023 IEEE Energy Conversion Congress and Exposition (ECCE)*, pages 1188–1195, 2023.

[114] Vincenzo Mallemaci, Sante Pugliese, Fabio Mandrile, Enrico Carpaneto, Radu Bojoi, and Marco Liserre. Robust stability analysis of the simplified virtual synchronous compensator for grid services and grid support. In *2023 IEEE Energy Conversion Congress and Exposition (ECCE)*, pages 1188–1195, 2023.

[115] Yanbo Wang, Xiongfei Wang, Zhe Chen, and Frede Blaabjerg. Small-signal stability analysis of inverter-fed power systems using component connection method. *IEEE Transactions on Smart Grid*, 9(5):5301–5310, 2018.

[116] Kemin Zhou and John C. Doyle. *Essentials of robust control*. Prentice Hall, 1998.

[117] Sigurd Skogestad and Ian Postlethwaite. *Multivariable Feedback Control: Analysis and Design*. John Wiley and Sons, 2001.

[118] Karanveer Dhingra and Mukesh Singh. Frequency support in a micro-grid using virtual synchronous generator based charging station. *IET Renewable Power Generation*, 12(9):1034–1044, 2018.

[119] Jon Are Suul, Salvatore D'Arco, and Giuseppe Guidi. Virtual synchronous machine-based control of a single-phase bi-directional battery charger for providing vehicle-to-grid services. In *2015 9th International Conference on Power Electronics and ECCE Asia (ICPE-ECCE Asia)*, pages 742–749, 2015.

[120] Xiangwu Yan, Jiajia Li, Bo Zhang, Zhonghao Jia, Yang Tian, Hui Zeng, and Zhipeng Lv. Virtual synchronous motor based-control of a three-phase electric vehicle off-board charger for providing fast-charging service. *Applied Sciences*, 8(6), 2018.

[121] Fabio Mandrile, Davide Cittanti, Vincenzo Mallemaci, and Radu Bojoi. Electric vehicle ultra-fast battery chargers: A boost for power system stability? *World Electric Vehicle Journal*, 12(1), 2021.

[122] Alessandro Roveri, Vincenzo Mallemaci, Fabio Mandrile, and Radu Bojoi. Power decoupling method for grid inertial support provided by ultra-fast bidirectional chargers. In *2023 IEEE Energy Conversion Congress and Exposition (ECCE)*, pages 6544–6546, 2023.

[123] M. Liserre, F. Blaabjerg, and S. Hansen. Design and control of an lcl-filter-based three-phase active rectifier. *IEEE Transactions on Industry Applications*, 41(5):1281–1291, 2005.

[124] Davide Cittanti, Matteo Gregorio, and Radu Bojoi. Digital multi-loop control of a 3-level rectifier for electric vehicle ultra-fast battery chargers. In *2020 AEIT International Annual Conference (AEIT)*, pages 1–6, 2020.

[125] Zhe Zhang, Muhammed Ali Gultekin, and Ali M. Bazzi. State-space Modeling of Multi-mode-controlled Induction Motor Drive. In *2021 IEEE International Electric Machines & Drives Conference (IEMDC)*, pages 1–5, May 2021.

[126] Wei Keyin, Liu Dezhi, Ou Yangbing, Zhai Xiaofei, and Yan Ming. State-space average-value model of 3-phase 4-wire diode-bridge rectifier. In *2009 IEEE International Symposium on Industrial Electronics*, pages 1634–1638, July 2009.

Appendix A

State-Space model of the GFM S-VSC

A.1 State-Space Models

In the following, for the generic quantity γ, the term $\Delta\gamma^{dq}$ stands for the row vector $[\Delta\gamma^{d},\Delta\gamma^{q}]$, where $\Delta\gamma^{d}$ and $\Delta\gamma^{q}$ are respectively the d-component and the q-component of $\Delta\gamma$ in the (d,q) reference frame rotating at the virtual speed ω_r.

A.1.1 Loads

Resistive Load

$$\begin{cases} \dfrac{d\mathbf{x_R}}{dt} &= \mathbf{A_R x_R} + \mathbf{B_R u_R} \\ \mathbf{y_R} &= \mathbf{C_R x_R} + \mathbf{D_R u_R} \end{cases} \tag{A.1}$$

$$\mathbf{u_R} = \left[\Delta v_{pcc}^{dq}, P_{load}\right]^{\mathrm{T}}, \mathbf{y_R} = \left[\Delta i_R^{dq}\right]^{\mathrm{T}} \tag{A.2}$$

$$\mathbf{x_R} = 0, \mathbf{A_R} = 0, \mathbf{B_R} = [0]^{1\mathrm{x}3}, \mathbf{C_R} = [0]^{2\mathrm{x}1} \tag{A.3}$$

$$\mathbf{D_R} = \begin{bmatrix} \dfrac{1}{R_R} & 0 & 0 \\ 0 & \dfrac{1}{R_R} & \dfrac{V_{pcc0}^{q}}{R_R} \end{bmatrix} \tag{A.4}$$

where R_R is the resistance of the load, i_R is the load current and P_{load} is a logic flag to emulate the connection or disconnection of the load.

Induction Machine

$$\begin{cases} \dfrac{d\mathbf{x_{IM}}}{dt} &= \mathbf{A_{IM}x_{IM}} + \mathbf{B_{IM}u_{IM}} \\ \mathbf{y_{IM}} &= \mathbf{C_{IM}x_{IM}} + \mathbf{D_{IM}u_{IM}} \end{cases} \tag{A.5}$$

$$\mathbf{x_{IM}} = \left[\Delta\lambda_s^{dq}, \Delta\lambda_r^{dq}, \Delta\omega_{IM}\right]^{\mathrm{T}} \tag{A.6}$$

$$\mathbf{u_{IM}} = \left[\Delta v_{pcc}^{dq}, \Delta\omega, \Delta T_L\right]^{\mathrm{T}} \tag{A.7}$$

$$\mathbf{y_{IM}} = \left[\Delta i_s^{dq}\right]^{\mathrm{T}} \tag{A.8}$$

where λ_s is the stator flux, λ_r is the rotor flux, ω_{IM} is the rotor speed, T_L is the load torque, i_s is the stator current and ω is the grid frequency ω_g in grid-mode operation and the virtual frequency ω_r in island operation. The state-space matrices can be found in [125].

Non-linear load

$$\begin{cases} \dfrac{d\mathbf{x_{NL}}}{dt} &= \mathbf{A_{NL}x_{NL}} + \mathbf{B_{NL}u_{NL}} \\ \mathbf{y_{NL}} &= \mathbf{C_{NL}x_{NL}} + \mathbf{D_{NL}u_{NL}} \end{cases} \tag{A.9}$$

$$\mathbf{x_{NL}} = \left[\Delta i_{dc,NL}, \Delta v_{NL}\right]^{\mathrm{T}} \tag{A.10}$$

$$\mathbf{u_{NL}} = \left[\Delta v_{pcc}^{dq}, \Delta I_{load}\right]^{\mathrm{T}} \tag{A.11}$$

$$\mathbf{y_{NL}} = \left[\Delta i_{dc,NL}, \Delta v_{NL}, \Delta i_{NL}^{q}\right]^{\mathrm{T}} \tag{A.12}$$

The state-space representation refers to the average model of a three phase diode rectifier [126] connected to a capacitor in parallel with a constant current load. The rectifier is connected at the PCC trough an inductive filter with inductance $L_{f,NL}$. $i_{dc,NL}$ is the dc current of the rectifier, v_{NL} is the voltage of the capacitor on the dc-side of the rectifier, I_{load} is the load current and i_{NL}^{q} is the q-component of the ac rectifier current. The state-space matrices are retrieved from [126].

A.1.2 LCL Filter

The LCL filter has a damping resistance R_d. The capacitor voltage is v_c, while the measured voltage v_g is the sum of v_c and the voltage drop on R_d. The subscript "LCL,G"

refers to the state-space representation of the LCL filter in grid-connected operation, while the subscript "LCL,I" refers to the island-mode.

Grid-mode

$$\begin{cases} \dfrac{d\mathbf{x_{LCL,G}}}{dt} &= \mathbf{A_{LCL,G}x_{LCL,G}} + \mathbf{B_{LCL,G}u_{LCL,G}} \\ \mathbf{y_{LCL,G}} &= \mathbf{C_{LCL,G}x_{LCL,G}} + \mathbf{D_{LCL,G}u_{LCL,G}} \end{cases} \tag{A.13}$$

$$\mathbf{x_{LCL,G}} = [\Delta i_i^{dq}, \Delta i_{fg}^{dq}, \Delta i_g^{dq}, \Delta v_c^{dq}]^{\mathrm{T}} \tag{A.14}$$

$$\mathbf{u_{LCL,G}} = [\Delta e_i^{dq}, \Delta e_g^{dq}, \Delta \omega_r, \Delta i_L^{dq}]^{\mathrm{T}} \tag{A.15}$$

where i_L is the total load current.

$$\mathbf{y_{LCL,G}} = [\Delta i_i^{dq}, \Delta i_{fg}^{dq}, \Delta i_g^{dq}, \Delta v_g^{dq}, \Delta v_{pcc}^{dq}]^{\mathrm{T}} \tag{A.16}$$

In the following, R_D, R_F and R_G are equal to, respectively:

$$R_D = R_f + R_d \tag{A.17}$$

$$R_F = R_d + R_{fg} + R_s \tag{A.18}$$

$$R_G = R_s + R_g \tag{A.19}$$

The only non-zero elements of $\mathbf{D_{LCL,G}}$ are:

$$\mathbf{D_{LCL,G}}(9,6) = \mathbf{D_{LCL,G}}(10,7) = -R_s \tag{A.20}$$

$$\mathbf{A_{LCL,G}} = \begin{bmatrix} -\omega_b \frac{R_D}{L_f} & \omega_{r0}\omega_b & \omega_b \frac{R_d}{L_f} & 0 \\ -\omega_{r0}\omega_b & -\omega_b \frac{R_D}{L_f} & 0 & \omega_b \frac{R_d}{L_f} \\ \omega_b \frac{R_d}{L_{fg}} & 0 & -\omega_b \frac{R_F}{L_{fg}} & \omega_{r0}\omega_b \\ 0 & \omega_b \frac{R_d}{L_{fg}} & -\omega_{r0}\omega_b & -\omega_b \frac{R_F}{L_{fg}} \\ 0 & 0 & \omega_b \frac{R_s}{L_g} & 0 \\ 0 & 0 & 0 & \omega_b \frac{R_s}{L_g} \\ \frac{\omega_b}{C_f} & 0 & -\frac{\omega_b}{C_f} & 0 \\ 0 & \frac{\omega_b}{C_f} & 0 & -\frac{\omega_b}{C_f} \end{bmatrix} \tag{A.21}$$

$$\begin{bmatrix} 0 & 0 & -\frac{\omega_b}{L_f} & 0 \\ 0 & 0 & 0 & -\frac{\omega_b}{L_f} \\ \omega_b \frac{R_s}{L_{fg}} & 0 & \frac{\omega_b}{L_{fg}} & 0 \\ 0 & \omega_b \frac{R_s}{L_{fg}} & 0 & \frac{\omega_b}{L_{fg}} \\ -\omega_b \frac{R_G}{L_g} & \omega_{r0}\omega_b & 0 & 0 \\ -\omega_{r0}\omega_b & -\omega_b \frac{R_G}{L_g} & 0 & 0 \\ 0 & 0 & 0 & \omega_{r0}\omega_b \\ 0 & 0 & -\omega_{r0}\omega_b & 0 \end{bmatrix}$$

$$\mathbf{B_{LCL,G}} = \begin{bmatrix} \frac{\omega_b}{L_f} & 0 & 0 & 0 & \omega_b I_{i0}^q & 0 & 0 \\ 0 & \frac{\omega_b}{L_f} & 0 & 0 & -\omega_b I_{i0}^d & 0 & 0 \\ 0 & 0 & 0 & 0 & \omega_b I_{fg0}^q & \omega_b \frac{R_s}{L_{fg}} & 0 \\ 0 & 0 & 0 & 0 & -\omega_b I_{fg0}^d & 0 & \omega_b \frac{R_s}{L_{fg}} \\ 0 & 0 & -\frac{\omega_b}{L_g} & 0 & \omega_b I_{g0}^q & -\omega_b \frac{R_s}{L_g} & 0 \\ 0 & 0 & 0 & -\frac{\omega_b}{L_g} & -\omega_b I_{g0}^d & 0 & -\omega_b \frac{R_s}{L_g} \\ 0 & 0 & 0 & 0 & \omega_b V_{c0}^q & 0 & 0 \\ 0 & 0 & 0 & 0 & -\omega_b V_{c0}^d & 0 & 0 \end{bmatrix} \tag{A.22}$$

$$\mathbf{C_{LCL,G}} = \begin{bmatrix} 1 & 0 & 0 & 0 & 0 & 0 & 0 & 0 \\ 0 & 1 & 0 & 0 & 0 & 0 & 0 & 0 \\ 0 & 0 & 1 & 0 & 0 & 0 & 0 & 0 \\ 0 & 0 & 0 & 1 & 0 & 0 & 0 & 0 \\ 0 & 0 & 0 & 0 & 1 & 0 & 0 & 0 \\ 0 & 0 & 0 & 0 & 0 & 1 & 0 & 0 \\ R_d & 0 & -R_d & 0 & 0 & 0 & 1 & 0 \\ 0 & R_d & 0 & -R_d & 0 & 0 & 0 & 1 \\ 0 & 0 & R_s & 0 & -R_s & 0 & 0 & 0 \\ 0 & 0 & 0 & R_s & 0 & -R_s & 0 & 0 \end{bmatrix} \tag{A.23}$$

Island-mode

$$\begin{cases} \frac{d\mathbf{x_{LCL,I}}}{dt} &= \mathbf{A_{LCL,I}x_{LCL,I}} + \mathbf{B_{LCL,I}u_{LCL,I}} \\ \mathbf{y_{LCL,I}} &= \mathbf{C_{LCL,I}x_{LCL,I}} + \mathbf{D_{LCL,I}u_{LCL,I}} \end{cases} \tag{A.24}$$

$$\mathbf{x_{LCL,I}} = [\Delta i_i^{dq}, \Delta i_{fg}^{dq}, \Delta v_c^{dq}]^{\mathrm{T}} \tag{A.25}$$

$$\mathbf{u_{LCL,I}} = [\Delta e_i^{dq}, \Delta \omega_r, \Delta i_L^{dq}]^{\mathrm{T}} \tag{A.26}$$

$$\mathbf{y_{LCL,I}} = [\Delta i_i^{dq}, \Delta i_{fg}^{dq}, \Delta v_g^{dq}, \Delta v_{pcc}^{dq}]^{\mathrm{T}} \tag{A.27}$$

$$\mathbf{A_{LCL,I}} =$$

$$\begin{bmatrix} -\omega_b\frac{R_D}{L_f} & \omega_{r0}\omega_b & \omega_b\frac{R_d}{L_f} & 0 & -\frac{\omega_b}{L_f} & 0 \\ -\omega_{r0}\omega_b & -\omega_b\frac{R_D}{L_f} & 0 & \omega_b\frac{R_d}{L_f} & 0 & -\frac{\omega_b}{L_f} \\ \omega_b\frac{R_d}{L_{fg}} & 0 & -\omega_b\frac{R_F}{L_{fg}} & \omega_{r0}\omega_b & \frac{\omega_b}{L_{fg}} & 0 \\ 0 & \omega_b\frac{R_d}{L_{fg}} & -\omega_{r0}\omega_b & -\omega_b\frac{R_F}{L_{fg}} & 0 & \frac{\omega_b}{L_{fg}} \\ \frac{\omega_b}{C_f} & 0 & -\frac{\omega_b}{C_f} & 0 & 0 & \omega_{r0}\omega_b \\ 0 & \frac{\omega_b}{C_f} & 0 & -\frac{\omega_b}{C_f} & -\omega_{r0}\omega_b & 0 \end{bmatrix} \tag{A.28}$$

$$\mathbf{B_{LCL,I}} = \begin{bmatrix} \frac{\omega_b}{L_f} & 0 & \omega_b I^q_{i0} & 0 & 0 \\ 0 & \frac{\omega_b}{L_f} & -\omega_b I^d_{i0} & 0 & 0 \\ 0 & 0 & \omega_b I^q_{fg0} & \omega_b\frac{R_s}{L_{fg}} & 0 \\ 0 & 0 & -\omega_b I^d_{fg0} & 0 & \omega_b\frac{R_s}{L_{fg}} \\ 0 & 0 & \omega_b V^q_{c0} & 0 & 0 \\ 0 & 0 & -\omega_b V^d_{c0} & 0 & 0 \end{bmatrix} \tag{A.29}$$

$$\mathbf{C_{LCL,I}} = \begin{bmatrix} 1 & 0 & 0 & 0 & 0 & 0 \\ 0 & 1 & 0 & 0 & 0 & 0 \\ 0 & 0 & 1 & 0 & 0 & 0 \\ 0 & 0 & 0 & 1 & 0 & 0 \\ R_d & 0 & -R_d & 0 & 1 & 0 \\ 0 & R_d & 0 & -R_d & 0 & 1 \\ 0 & 0 & R_s & 0 & 0 & 0 \\ 0 & 0 & 0 & R_s & 0 & 0 \end{bmatrix} \tag{A.30}$$

The only non-zero elements of $\mathbf{D_{LCL,I}}$ are:

$$\mathbf{D_{LCL,I}}(7,4) = \mathbf{D_{LCL,I}}(8,5) = -R_s \tag{A.31}$$

A.1.3 Inverter

The Inverter block is the same proposed in [110] and it is not reported here.

A.1.4 S-VSC Control

The S-VSC control block consists of the Electrical Equations block and the power loops block (i.e., Mechanical Emulation and Excitation Control). The former is the same proposed in [110] and it is not reported here. The latter is slightly different from [110] and it is proposed in the following.

The power loops block changes according to the operating configuration (i.e., grid-mode or island). In the following, f_p and f_q define if the droop references P_d^* and Q_d^* are applied on the inverter references or on the virtual references, are explained in Section 5.2 and shown in Fig. 5.2 with the switch K_{sw}.

Grid-mode

$$\begin{cases} \dfrac{d\mathbf{x_{PW,G}}}{dt} &= \mathbf{A_{PW,G}x_{PW,G}} + \mathbf{B_{PW,G}u_{PW,G}} \\ \mathbf{y_{PW,G}} &= \mathbf{C_{PW,G}x_{PW,G}} + \mathbf{D_{PW,G}u_{PW,G}} \end{cases} \tag{A.32}$$

$$\mathbf{x_{PW,G}} = [\Delta\omega_r, \Delta\delta, \Delta\lambda_e]^{\mathrm{T}} \tag{A.33}$$

where δ is the angle difference between the virtual rotor angle θ_r and the grid voltage angle θ_g.

$$\mathbf{u_{PW,G}} = \Big[\Delta P_v^{ref}, \Delta Q_v^{ref}, \Delta P_d^*, \Delta Q_d^*, \Delta v_g^{dq}, \Delta i_v^{dq}, \Delta\omega_g\Big]^{\mathrm{T}} \tag{A.34}$$

$$\mathbf{y_{PW,G}} = [\Delta P_v, \Delta Q_v, \Delta\omega_r, \Delta\delta, \Delta\lambda_e]^{\mathrm{T}} \tag{A.35}$$

$$\mathbf{A_{PW,G}} = \begin{bmatrix} 0 & 0 & 0 \\ \omega_b & 0 & 0 \\ 0 & 0 & 0 \end{bmatrix} \tag{A.36}$$

$$\mathbf{B_{PW,G}} = \begin{bmatrix} \frac{1}{2H} & 0 & \frac{f_p}{2H} & 0 & -\frac{I^d_{v0}}{2H} \\ 0 & 0 & 0 & 0 & 0 \\ 0 & k_e\frac{1}{V_{g0}} & 0 & k_e\frac{f_q}{V_{g0}} & k_e\frac{I^q_{v0}}{V_{g0}} \\ -\frac{I^q_{v0}}{2H} & -\frac{V^d_{g0}}{2H} & -\frac{V^q_{g0}}{2H} & 0 \\ 0 & 0 & 0 & -\omega_b \\ -k_e\frac{I^d_{v0}}{V_{g0}} & -k_e\frac{V^q_{g0}}{V_{g0}} & k_e\frac{V^d_{g0}}{V_{g0}} & 0 \end{bmatrix} \tag{A.37}$$

$$\mathbf{C_{PW,G}} = \begin{bmatrix} 0 & 0 & 0 \\ 0 & 0 & 0 \\ 1 & 0 & 0 \\ 0 & 1 & 0 \\ 0 & 0 & 1 \end{bmatrix} \tag{A.38}$$

$$\mathbf{D_{PW,G}} = \begin{bmatrix} 0 & 0 & 0 & 0 & I^d_{v0} & I^q_{v0} & V^d_{g0} & V^q_{g0} & 0 \\ 0 & 0 & 0 & 0 & -I^q_{v0} & I^d_{v0} & V^q_{g0} & -V^d_{g0} & 0 \\ 0 & 0 & 0 & 0 & 0 & 0 & 0 & 0 & 0 \\ 0 & 0 & 0 & 0 & 0 & 0 & 0 & 0 & 0 \\ 0 & 0 & 0 & 0 & 0 & 0 & 0 & 0 & 0 \end{bmatrix} \tag{A.39}$$

In (A.37) H is the inertia constant in seconds and k_e is the gain of the excitation control (pu) [81].

Island-mode

$$\begin{cases} \frac{d\mathbf{x_{PW,I}}}{dt} &= \mathbf{A_{PW,I}x_{PW,I}} + \mathbf{B_{PW,I}u_{PW,I}} \\ \mathbf{y_{PW,I}} &= \mathbf{C_{PW,I}x_{PW,I}} + \mathbf{D_{PW,I}u_{PW,I}} \end{cases} \tag{A.40}$$

$$\mathbf{x_{PW,I}} = [\Delta\omega_r, \Delta\lambda_e]^{\mathrm{T}} \tag{A.41}$$

$$\mathbf{u_{PW,I}} = \left[\Delta P_v^{ref}, \Delta Q_v^{ref}, \Delta P_d^*, \Delta Q_d^*, \Delta v_g^{dq}, \Delta i_v^{dq}\right]^{\mathrm{T}} \tag{A.42}$$

$$\mathbf{y_{PW,I}} = \left[\Delta P_v, \Delta Q_v, \Delta \omega_r, \Delta \lambda_e\right]^{\mathrm{T}} \tag{A.43}$$

$$\mathbf{A_{PW,I}} = [0]^{2\mathrm{x}2} \tag{A.44}$$

$$\mathbf{B_{PW,I}} = \begin{bmatrix} \frac{1}{2H} & 0 & \frac{f_p}{2H} & 0 & -\frac{I_{vd0}}{2H} \\ 0 & k_e\frac{1}{V_{g0}} & 0 & k_e\frac{f_q}{V_{g0}} & k_e\frac{I_{vq0}}{V_{g0}} \\ -\frac{I_{v0}^q}{2H} & -\frac{V_{g0}^d}{2H} & -\frac{V_{g0}^q}{2H} & 0 & \\ -k_e\frac{I_{v0}^d}{V_{g0}} & -k_e\frac{V_{g0}^q}{V_{g0}} & k_e\frac{V_{g0}^d}{V_{g0}} & 0 & \end{bmatrix} \tag{A.45}$$

$$\mathbf{C_{PW,I}} = \begin{bmatrix} 0 & 0 \\ 0 & 0 \\ 1 & 0 \\ 0 & 1 \end{bmatrix} \tag{A.46}$$

$$\mathbf{D_{PW,I}} = \begin{bmatrix} 0 & 0 & 0 & 0 & I_{v0}^d & I_{v0}^q & V_{g0}^d & V_{g0}^q \\ 0 & 0 & 0 & 0 & -I_{v0}^q & I_{v0}^d & V_{g0}^q & -V_{g0}^d \\ 0 & 0 & 0 & 0 & 0 & 0 & 0 & 0 \\ 0 & 0 & 0 & 0 & 0 & 0 & 0 & 0 \end{bmatrix} \tag{A.47}$$

A.1.5 Reference Calculation

$$\mathbf{u_{Ref}} = \left[\Delta P_{set}^{ref}, \Delta Q_{set}^{ref}, \Delta i_v^{dq}, \Delta P_d^*, \Delta Q_d^*, \Delta v_g^{dq}\right]^{\mathrm{T}} \tag{A.48}$$

$$\mathbf{x_{Ref}} = 0, \mathbf{y_{Ref}} = \left[\Delta i_i^{*,dq}\right]^{\mathrm{T}} \tag{A.49}$$

$$\mathbf{A_{Ref}} = 0, \mathbf{B_{Ref}} = [0]^{1\mathrm{x}8}, \mathbf{C_{Ref}} = [0]^{2\mathrm{x}1} \tag{A.50}$$

$$\mathbf{D_{Ref}} = \begin{bmatrix} \frac{V_{g0}^d}{V_{g0}^2} & \frac{V_{g0}^q}{V_{g0}^2} & 1 & 0 & (1-f_p)\frac{V_{g0}^d}{V_{g0}^2} & (1-f_q)\frac{V_{g0}^q}{V_{g0}^2} \\ \frac{V_{g0}^q}{V_{g0}^2} & -\frac{V_{g0}^d}{V_{g0}^2} & 0 & 1 & (1-f_p)\frac{V_{g0}^q}{V_{g0}^2} & -(1-f_q)\frac{V_{g0}^d}{V_{g0}^2} \\ \frac{P_{i0}^*(V_{g0}^{2,q}-V_{g0}^{2,d})-2Q_{i0}^*V_{g0}^dV_{g0}^q}{V_{g0}^4} & -\frac{2P_{i0}^*V_{g0}^dV_{g0}^q+Q_{i0}^*(V_{g0}^{2,q}-V_{g0}^{2,d})}{V_{g0}^4} \\ \frac{Q_{i0}^*(V_{g0}^{2,d}-V_{g0}^{2,q})-2P_{i0}^*V_{g0}^dV_{g0}^q}{V_{g0}^4} & \frac{P_{i0}^*(V_{g0}^{2,d}-V_{g0}^{2,q})+2Q_{i0}^*V_{g0}^dV_{g0}^q}{V_{g0}^4} \end{bmatrix} \tag{A.51}$$

A.1.6 High Level Control

$$\begin{cases} \frac{d\mathbf{x_{HL}}}{dt} = \mathbf{A_{HL}}\mathbf{x_{HL}} + \mathbf{B_{HL}}\mathbf{u_{HL}} \\ \mathbf{y_{HL}} = \mathbf{C_{HL}}\mathbf{x_{HL}} + \mathbf{D_{HL}}\mathbf{u_{HL}} \end{cases} \tag{A.52}$$

where:

$$\mathbf{u_{HL}} = \left[\Delta\omega_r, \Delta v_g^{dq}\right]^{\mathrm{T}}, \mathbf{y_{HL}} = \left[\Delta P_d^*, \Delta Q_d^*\right]^{\mathrm{T}} \tag{A.53}$$

$$\mathbf{x_{HL}} = 0, \mathbf{A_{HL}} = 0, \mathbf{B_{HL}} = [0]^{1\mathrm{x}3}, \mathbf{C_{HL}} = [0]^{2\mathrm{x}1} \tag{A.54}$$

$$\mathbf{D_{HL}} = \begin{bmatrix} -\frac{1}{b_p} & 0 & 0 \\ 0 & -\frac{1}{b_q}\frac{V_{g0}^d}{V_{g0}} & -\frac{1}{b_q}\frac{V_{g0}^q}{V_{g0}} \end{bmatrix} \tag{A.55}$$

A.1.7 Grid

The grid block is the same proposed in [110] and it is not reported here.

A.2 Component Connection Method for the loads

Aggregated Matrices

$$\begin{cases} \mathbf{A_L} = \text{blkdiag}\{\mathbf{A_R}, \mathbf{A_{IM}}, \mathbf{A_{NL}}\} \\ \mathbf{B_L} = \text{blkdiag}\{\mathbf{B_R}, \mathbf{B_{IM}}, \mathbf{B_{NL}}\} \\ \mathbf{C_L} = \text{blkdiag}\{\mathbf{C_R}, \mathbf{C_{IM}}, \mathbf{C_{NL}}\} \\ \mathbf{D_L} = \text{blkdiag}\{\mathbf{D_R}, \mathbf{D_{IM}}, \mathbf{D_{NL}}\} \end{cases} \tag{A.56}$$

where "blkdiag" stands for block diagonal.

Aggregated system

$$\begin{cases} \mathbf{u_L} = \mathbf{L_{uy,L}}\mathbf{y_L} + \mathbf{L_{us,L}}\mathbf{u_{s,L}} \\ \mathbf{y_{s,L}} = \mathbf{L_{sy,L}}\mathbf{y_L} + \mathbf{L_{ss,L}}\mathbf{u_{s,L}} \end{cases} \tag{A.57}$$

$$\mathbf{x_L} = \left[\mathbf{x_R^T}, \mathbf{x_{IM}^T}, \mathbf{x_{NL}^T}\right]^{\mathrm{T}} \tag{A.58}$$

$$\mathbf{u_L} = \left[\mathbf{u_R^T}, \mathbf{u_{IM}^T}, \mathbf{u_{NL}^T}\right]^{\mathrm{T}} \tag{A.59}$$

$$\mathbf{y_L} = \left[\mathbf{y_R^T}, \mathbf{y_{IM}^T}, \mathbf{y_{NL}^T}\right]^{\mathrm{T}} \tag{A.60}$$

$$\mathbf{u_{s,L}} = \left[\Delta v_{pcc}^{dq}, \Delta\omega, \Delta T_L, \Delta I_{load}, \Delta P_{load}\right]^{\mathrm{T}} \tag{A.61}$$

$$\begin{aligned} \mathbf{y_{s,L}} = \Big[&\Delta i_s^{dq}, \Delta\lambda_s^{dq}, \Delta\lambda_r^{dq}, \Delta\omega_{IM}, \Delta i_{dc,NL}, \\ &\Delta v_{NL}, \Delta i_{NL}^{q}, \Delta i_R^{dq}, \Delta i_L^{dq}\Big]^{\mathrm{T}} \end{aligned} \tag{A.62}$$

The interconnection matrices $\mathbf{L_{uy,L}}$ and $\mathbf{L_{ss,L}}$ are all zeros matrices.

$$\mathbf{L_{uy,L}} = [0]^{10\text{x}12}, \mathbf{L_{ss,L}} = [0]^{14\text{x}6} \tag{A.63}$$

$$\mathbf{L_{us,L}} = \begin{bmatrix} 1 & 0 & 0 & 0 & 0 & 0 \\ 0 & 1 & 0 & 0 & 0 & 0 \\ 0 & 0 & 1 & 0 & 0 & 0 \\ 0 & 0 & 0 & 1 & 0 & 0 \\ 1 & 0 & 0 & 0 & 0 & 0 \\ 0 & 1 & 0 & 0 & 0 & 0 \\ 0 & 0 & 0 & 0 & 1 & 0 \\ 1 & 0 & 0 & 0 & 0 & 0 \\ 0 & 1 & 0 & 0 & 0 & 0 \\ 0 & 0 & 0 & 0 & 0 & 1 \end{bmatrix} \tag{A.64}$$

The non-zero elements of the matrix $\mathbf{L_{sy,L}} \in [14, 12]$ are:

$$\begin{aligned} &\mathbf{L_{sy,L}}(1:12, 1:12) = [\mathbf{I}]^{12x12} \\ &\mathbf{L_{sy,L}}(13, 1) = \mathbf{L_{sy,L}}(13, 11) = 1 \\ &\mathbf{L_{sy,L}}(14, 2) = \mathbf{L_{sy,L}}(14, 10) = \mathbf{L_{sy,L}}(14, 12) = 1 \end{aligned} \tag{A.65}$$

State-space representation of the Loads Block

$$\begin{cases} \mathbf{A_{s,L}} &= \mathbf{A_L} + \mathbf{B_L L_{uy,L} W_L C_L} \\ \mathbf{B_{s,L}} &= \mathbf{B_L L_{uy,L} W_L D_L L_{us,L} B_L L_{us,L}} \\ \mathbf{C_{s,L}} &= \mathbf{L_{sy,L} W_L C_L} \\ \mathbf{D_{s,L}} &= \mathbf{L_{sy,L} W_L D_L L_{us,L} + L_{ss,L}} \\ \mathbf{W_L} &= \left(\mathbf{I} - \mathbf{D_L L_{uy,L}}\right)^{-1} \end{cases} \tag{A.66}$$

A.3 Component Connection Method for grid-connected operation

The same approach used in Appendix A.2 is applied to obtain the state-state representation of the entire system in case of grid-connected operation. The aggregated system consists of the following blocks: Loads, LCL,G, Inverter, Stator, Power Loops in grid-mode, Reference Calculation, Grid, High Level control. In the following are reported: the input vector $\mathbf{u_{s,G}}$, the output vector $\mathbf{y_{s,G}}$ and the interconnection matrices

$\left[\mathbf{L_{uy,G}}\right]^{44x39}$, $\left[\mathbf{L_{us,G}}\right]^{44x10}$, $\left[\mathbf{L_{sy,G}}\right]^{36x39}$, and $\left[\mathbf{L_{ss,G}}\right]^{36x10}$.

$$\begin{aligned}\mathbf{u_{s,G}} = \Big[&\Delta P_{set}^{ref}, \Delta Q_{set}^{ref}, \Delta\omega_g, \Delta E_g, \Delta\Phi_g,\\ &\Delta T_L, \Delta I_{load}, \Delta P_{load}, \Delta P_v^{ref}, \Delta Q_v^{ref}\Big]^{\mathrm{T}}\end{aligned} \tag{A.67}$$

$$\begin{aligned}\mathbf{y_{s,G}} = \Big[&\mathbf{y_{s,L}}^{\mathrm{T}}, \Delta i_i^{*,dq}, \Delta i_i^{dq}, \Delta i_{fg}^{dq}, \Delta i_g^{dq}, \Delta v_g^{dq}, \Delta v_{pcc}^{dq},\\ &\Delta e_g^{dq}, \Delta\omega_r, \Delta\delta, \Delta P_v, \Delta Q_v, \Delta i_v^{dq}, \Delta P_d^*, \Delta Q_d^*\Big]^{\mathrm{T}}\end{aligned} \tag{A.68}$$

For the interconnection matrices, only the non-zero elements are provided:

$$\begin{aligned}
&\mathbf{L_{us,G}}(1,23) = \mathbf{L_{us,G}}(2,24) = \mathbf{L_{us,G}}(7,25) = 1\\
&\mathbf{L_{us,G}}(8,26) = \mathbf{L_{us,G}}(9,36) = \mathbf{L_{us,G}}(10,37) = 1\\
&\mathbf{L_{us,G}}(11,31) = \mathbf{L_{us,G}}(12,13) = \mathbf{L_{us,G}}(13,14) = 1\\
&\mathbf{L_{us,G}}(14,34) = \mathbf{L_{us,G}}(15,35) = \mathbf{L_{us,G}}(16,15) = 1\\
&\mathbf{L_{us,G}}(17,16) = \mathbf{L_{us,G}}(18,21) = \mathbf{L_{us,G}}(19,22) = 1\\
&\mathbf{L_{us,G}}(20,31) = \mathbf{L_{us,G}}(21,33) = \mathbf{L_{us,G}}(24,38) = 1\\
&\mathbf{L_{us,G}}(25,39) = \mathbf{L_{us,G}}(26,21) = \mathbf{L_{us,G}}(27,22) = 1\\
&\mathbf{L_{us,G}}(28,27) = \mathbf{L_{us,G}}(29,28) = \mathbf{L_{us,G}}(33,27) = 1\\
&\mathbf{L_{us,G}}(34,28) = \mathbf{L_{us,G}}(35,38) = \mathbf{L_{us,G}}(36,39) = 1\\
&\mathbf{L_{us,G}}(37,21) = \mathbf{L_{us,G}}(38,22) = \mathbf{L_{us,G}}(39,32) = 1\\
&\mathbf{L_{us,G}}(42,31) = \mathbf{L_{us,G}}(43,21) = \mathbf{L_{us,G}}(44,22) = 1
\end{aligned} \tag{A.69}$$

$$\begin{aligned}
&\mathbf{L_{us,G}}(3,3) = \mathbf{L_{us,G}}(4,6) = \mathbf{L_{us,G}}(5,7) = 1\\
&\mathbf{L_{us,G}}(6,8) = \mathbf{L_{us,G}}(22,1) = \mathbf{L_{us,G}}(23,2) = 1\\
&\mathbf{L_{us,G}}(30,3) = \mathbf{L_{us,G}}(31,9) = \mathbf{L_{us,G}}(32,10) = 1\\
&\mathbf{L_{us,G}}(40,4) = \mathbf{L_{us,G}}(41,5) = 1
\end{aligned} \tag{A.70}$$

$$
\begin{aligned}
&\mathbf{L_{sy,G}}(1:14,1:14) = [\mathbf{I}]^{14\text{x}14} \\
&\mathbf{L_{sy,G}}(15,34) = \mathbf{L_{sy,G}}(16,35) = \mathbf{L_{sy,G}}(17,15) = 1 \\
&\mathbf{L_{sy,G}}(18,16) = \mathbf{L_{sy,G}}(19,17) = \mathbf{L_{sy,G}}(20,18) = 1 \\
&\mathbf{L_{sy,G}}(21,19) = \mathbf{L_{sy,G}}(22,20) = \mathbf{L_{sy,G}}(23,21) = 1 \\
&\mathbf{L_{sy,G}}(24,22) = \mathbf{L_{sy,G}}(25,23) = \mathbf{L_{sy,G}}(26,24) = 1 \\
&\mathbf{L_{sy,G}}(27,36) = \mathbf{L_{sy,G}}(28,37) = \mathbf{L_{sy,G}}(29,31) = 1 \\
&\mathbf{L_{sy,G}}(30,32) = \mathbf{L_{sy,G}}(31,29) = \mathbf{L_{sy,G}}(32,30) = 1 \\
&\mathbf{L_{sy,G}}(33,27) = \mathbf{L_{sy,G}}(34,28) = \mathbf{L_{sy,G}}(35,38) = 1 \\
&\mathbf{L_{sy,G}}(36,39) = 1
\end{aligned}
\tag{A.71}
$$

A.4 Component Connection Method for island operation

The state-state representation of the entire system in case of island operation is obtained by applying the same procedure shown in Appendix A.2. The aggregated system consists of the following blocks: Loads, LCL,I, Inverter, Stator, Power Loops in island-mode, Reference Calculation, High Level control. In the following are reported: the input vector $\mathbf{u_{s,I}}$, the output vector $\mathbf{y_{s,I}}$ and the interconnection matrices $\left[\mathbf{L_{uy,I}}\right]^{38\text{x}34}$, $\left[\mathbf{L_{us,I}}\right]^{38\text{x}7}$, $\left[\mathbf{L_{sy,I}}\right]^{33\text{x}34}$, and $\left[\mathbf{L_{ss,I}}\right]^{33\text{x}7}$.

$$
\begin{aligned}
\mathbf{u_{s,I}} = \Big[&\Delta P_{set}^{ref}, \Delta Q_{set}^{ref}, \Delta T_L, \Delta I_{load}, \\
&\Delta P_{load}, \Delta P_v^{ref}, \Delta Q_v^{ref}\Big]^{\mathrm{T}}
\end{aligned}
\tag{A.72}
$$

$$
\begin{aligned}
\mathbf{y_{s,I}} = \Big[&\mathbf{y_{s,L}}^{\mathrm{T}}, \Delta i_i^{*,dq}, \Delta i_i^{dq}, \Delta i_{fg}^{dq}, \Delta v_g^{dq}, \Delta v_{pcc}^{dq}, \\
&\Delta\omega_r, \Delta P_v, \Delta Q_v, \Delta i_v^{dq}, \Delta P_d^*, \Delta Q_d^*, \Delta e_i^{dq}\Big]^{\mathrm{T}}
\end{aligned}
\tag{A.73}
$$

For the interconnection matrices, only the non-zero elements are provided:

$$\begin{aligned}
&\mathbf{L_{uy,I}}(1,21) = \mathbf{L_{uy,I}}(2,22) = \mathbf{L_{uy,I}}(3,29) = 1\\
&\mathbf{L_{uy,I}}(7,23) = \mathbf{L_{uy,I}}(8,24) = \mathbf{L_{uy,I}}(9,29) = 1\\
&\mathbf{L_{uy,I}}(10,13) = \mathbf{L_{uy,I}}(11,14) = \mathbf{L_{uy,I}}(12,31) = 1\\
&\mathbf{L_{uy,I}}(13,32) = \mathbf{L_{uy,I}}(14,15) = \mathbf{L_{uy,I}}(15,16) = 1\\
&\mathbf{L_{uy,I}}(16,19) = \mathbf{L_{uy,I}}(17,20) = \mathbf{L_{uy,I}}(18,29) = 1\\
&\mathbf{L_{uy,I}}(19,30) = \mathbf{L_{uy,I}}(22,33) = \mathbf{L_{uy,I}}(23,34) = 1\\
&\mathbf{L_{uy,I}}(24,19) = \mathbf{L_{uy,I}}(25,20) = \mathbf{L_{uy,I}}(26,25) = 1\\
&\mathbf{L_{uy,I}}(27,26) = \mathbf{L_{uy,I}}(30,25) = \mathbf{L_{uy,I}}(31,26) = 1\\
&\mathbf{L_{uy,I}}(32,33) = \mathbf{L_{uy,I}}(33,34) = \mathbf{L_{uy,I}}(34,19) = 1\\
&\mathbf{L_{uy,I}}(35,20) = \mathbf{L_{uy,I}}(36,29) = \mathbf{L_{uy,I}}(37,19) = 1\\
&\mathbf{L_{uy,I}}(38,20) = 1
\end{aligned} \tag{A.74}$$

$$\begin{aligned}
&\mathbf{L_{us,I}}(4,3) = \mathbf{L_{us,I}}(5,4) = \mathbf{L_{us,I}}(6,5) = 1\\
&\mathbf{L_{us,I}}(20,1) = \mathbf{L_{us,I}}(21,2) = \mathbf{L_{us,I}}(28,6) = 1\\
&\mathbf{L_{us,I}}(29,7) = 1
\end{aligned} \tag{A.75}$$

$$\begin{aligned}
&\mathbf{L_{sy,I}}(1:14,1:14) = [\mathbf{I}]^{14\text{x}14}\\
&\mathbf{L_{sy,I}}(15,31) = \mathbf{L_{sy,I}}(16,32) = \mathbf{L_{sy,I}}(17,15) = 1\\
&\mathbf{L_{sy,I}}(18,16) = \mathbf{L_{sy,I}}(19,17) = \mathbf{L_{sy,I}}(20,18) = 1\\
&\mathbf{L_{sy,I}}(21,19) = \mathbf{L_{sy,I}}(22,20) = \mathbf{L_{sy,I}}(23,21) = 1\\
&\mathbf{L_{sy,I}}(24,22) = \mathbf{L_{sy,I}}(25,29) = \mathbf{L_{sy,I}}(26,27) = 1\\
&\mathbf{L_{sy,I}}(27,28) = \mathbf{L_{sy,I}}(28,25) = \mathbf{L_{sy,I}}(29,26) = 1\\
&\mathbf{L_{sy,I}}(30,33) = \mathbf{L_{sy,I}}(31,34) = \mathbf{L_{sy,I}}(32,23) = 1\\
&\mathbf{L_{sy,I}}(33,24) = 1
\end{aligned} \tag{A.76}$$

List of Figures

List of Tables